CARBON NANOFIBER BASED HYBRID MATERIALS FOR PEMFC APPLICATIONS

A THESIS SUBMITTED TO THE
UNIVERSITY OF PUNE

FOR THE DEGREE OF
DOCTOR OF PHILOSOPHY
IN CHEMISTRY

BY
BEENA K. B.

Dr. SREEKUMAR KURUNGOT
(RESEARCH GUIDE)

PHYSICAL AND MATERIALS CHEMISTRY DIVISION
NATIONAL CHEMICAL LABORATORY
PUNE 411 008, INDIA

AUGUST 2013

CERTIFICATE

This is to certify that the work incorporated in the thesis entitled, “**Carbon Nanofiber Based Hybrid Materials for PEMFC Applications”** submitted by **Mrs. Beena K. B.,** has been carried out by her under my supervision at the Physical and Materials Chemistry Division, National Chemical Laboratory, Pune, 411 008, India. All the materials from other sources have been duly acknowledged in the thesis.

Date : **Dr. Sreekumar Kurungot**

Place : **(** Research Guide)

DECLARATION

I, hereby declare that the thesis entitled **“Carbon Nanofiber Based Hybrid Materials for PEMFC Applications”**, submitted for the Degree of Doctor of Philosophy in Chemistry, to the University of Pune, have been carried out by me at Physical and Materials Chemistry Division, National Chemical Laboratory, Pune-411008, India, under the supervision of Dr. Sreekumar Kurungot. The work is original and has not been submitted in part or full by me, for any degree or diploma to this or to any other University.

Date: **Beena K. B.**

Place : Pune

.....Dedicated to

My Family.....

Acknowledgements

There are so many people, whose support, encouragement & inspiration are very much essential to accomplish major achievements in life, especially, if it involves the elements of fulfilling one’s cherished dreams. For me, this thesis is such an important destiny & I am indeed, indebted to lot of people for their well wishes & blessings, for completing this journey.

First of all I would like to express my immense gratitude to my research supervisor Dr. Sreekumar Kurungot for his guidance throughout my research work. I am thankful to him for giving me freedom to carry out multi-disciplinary research work throughout the course of this programme.

I am deeply indebted to Dr. K .Vijayamohanan for his constant inspiration and constructive criticism that helped me a lot to focus my views in proper perspective. His tireless attitude has been an impetus for me throughout the course of this work.

I devote my sincere acknowledgement to Dr. Ulhas K. Kharul for his helping hands and fruitful discussions. I have always been inspired by his systemic approach and realistic views. I am also thankful to his students, Harshal and Pradnaya who helped me in experiments in addition to providing a friendly environment.

I am very much grateful to Dr. Rahul Banerjee for an effective collaboration. My sincere thanks to his student Pradip for his dedicated role in MOF related experiments.

I would also like to convey my admiration to Dr. P. A. Joy for all his help, support, suggestions and advice during the course of this work.

I wish to thank Dr. S. Sivaram, former Director and Dr. Sourav Pal, Director, National Chemical Laboratory, for providing me all infrastructural facilities. I would extend my sincere thanks to Dr. Anil Kumar (Head, Physical Chemistry Division) for allowing me to use all the available facilities in the division & for his persistent encouragement and support.

My heartfelt gratitude to Drs. Anil Kumar, P. A. Joy, S. B. Ogale, B. L. V. Prasad, P. Poddar, and I. S. Mulla for their advice & help. I am highly indebted *to Dr. K.R. Patil, Mr. Gholap, Mr. A. B. Gaikwad, Mr. Ketan and Mrs. Suguna for helping me a lot in characterising my samples. My heartfelt gratitude to Mr. Naren, Mr. Anuj and Mr. Pandiraj for their timely help in characterizing my samples. Thanks are also due to our divisional staff, Mr. Dipak Jori, Mr. Punekar and other office staffs for their willing cooperation. Further, CSIR are gratefully acknowledged for the financial support. Timely help from Mr. Dipak & Mr. Punekar is gratefully acknowledged.*

I am forever indebted to all my former teachers as they built the foundation for this achievement. I have to acknowledge especially my teachers in B.Sc. and M.Sc. class who really nourished my interest in Chemistry.

I am also thankful to Manju madam, Nihara madam, Hari, Keshu, Neerav and Niranjana for giving me cherished moments.

My deepest and heartiest thanks go to all my seniors Mahima, Bhalchand, Bhaskar, Deepali, Kannan, Meera, Vivek and Meenu. I am overwhelmed by the friendly atmosphere and support provided by my labmates Dhanraj, Joyashish, Palani, Bipin, Pritish, Vishal, Hussain, Ashwini, Neeta, Harshitha, Vrushali, Sreekuttan, Bihag, Sanjay, Pravin, Rathod, Neelesh and Ranjit. My sincere thanks to Mahima (Chechi) for her mentoring & care during my initial research days. I can never forget the special support, love & care with constant encouragement extended to me by Bhasku and always being with me in all sorts of situations during my stay in NCL. I take time to convey my gratitude to the project students who worked with me Anu, Bipin, Bhagyesh, Lal, Geethu, Brinda, Aswathy and Aiswarya.

I also acknowledge the homely environment provided by Surendran chettan, Manoj Chettan, Sanyo chettan, Hari chettan, Sony Chechi, Smitha Chechi, Panchami chechi, Shyla, Smitha, Mithra, Jima, Aany, Soumya, Dhanya, Deepashree, Biyas, Sadiq, Rahul, Reji, Rajesh, Arun, Anumon, Renny, Vijaydas and Hari.

Also it gives me immense pleasure to express my sincere thanks to my colleagues of Physical Chemistry Division Khaja, Mangesh, Pankaj, Vijay, Nagesh and other friends in NCL Bhavna, Anita, Rekha, Prajitha, Nisha, Harshal, Majid, Manoj, Chinmay, Pradip, Tamas, Arijit and Sarath.

Innumerable thanks go to my roommates Divya, Nikitha, Neha, Kalyani and subha; the cherished moments with them shall always be remembered.

In this occasion I would like mention my friends Manjusha, Mithra, Asha, Gireesh and Shimji for their constant support and help especially during my toughest time.

I express my deep sense of gratitude to my family for their continuing encouragement and affection. I find no words to express the love of my achan, amma, Divya and Bichu who have always given me the best of everything. Their love, support, blessings has always been my strength. Their patience and sacrifice will remain my inspiration throughout my life. Due adoration to 'Adi' and my nephew 'Devang' for their innocent love and affection.

A very special appreciation is due to my husband Jijil not only for his constant encouragement but also for his patience & understanding throughout. These few words are only a small fraction of my enormous sense of love, appreciation, and thanks. It gives me great pleasure to thank his family members, for their tremendous patience and affection.

Above all, I thank God; the almighty for this most amazing moment.

Though, many have not been mentioned, none is forgotten.

Beena K B

List of Abbreviations

1-D	One-Dimensonal
2-D	Two-Dimensional
AFC	Alkaline Fuel Cells
BE	Binding Energy
BET	Braunauer-Emmett-Teller
BJH	Barrett-Joyner-Halenda
BPtNW	Branched Pt Nanowires
BSE	Backscattered Electrons
BuI	5-tert-butyl isophthalic acid
CB	Carbon Black
CE	Counter Electrode
CNC	Carbon Nanocoil
CNF	Carbon Nanofiber
CNH	Carbon Nanohorns
CNS	Carbon Nanosphere
CNT	Carbon Nanotube
CV	Cyclic Voltammetry
DAB	3,3’-diaminobenzidine
DI	Deionized Water
DMAc	N,Ndimethyl acetamide
DMFC	Direct Methanol Fuel Cells
DOE	American Department of Energy
DTA	Differential thermal analysis
DWCNT	Double-Walled Carbon Nanotubes
ECSA	Electrochemically Active Surface Area
EDAX	Energy Dispersive analysis of X-rays
EG	Ethylene Glycol
EIS	Electrochemical Impedance Spectroscopy
FCNF	Functionalized Carbon Nanofiber
FCNT	Functionalized Carbon Nanotube

FE	Field Emission
GC	Glassy Carbon
GNF	Graphitic Nanofiber
GNP	Graphene Nanoplatelet
GNS	Graphene Nanosheet
GO	Graphene Oxide
HOR	Hydrogen Oxidation reaction
HRTEM	High Resolution Transmission Electron Microscopy
HT-PEMFC	High Temperature Polymer Electrolyte Membrane Fuel Cell
I_b	backward anodic peak current
I_f	forward anodic peak current
K-L	Koutecky-Levich
LSV	linear sweep voltammetry
LT-PEMFC	Low Temperature Polymer Electrolyte Membrane Fuel Cell
MEA	Membrane Electrode Assembly
MOFC	Molten Carbonate Fuel Cell
MOR	Methanol Oxidation Reaction
MPC	Mesoporous Carbon
MWCNT	Multi-Walled Carbon Nanotube
NC	Nanocrystal
NP	Nanoparticle
NPM	Non-precious Metal
OMPC	Ordered Mesoporous Carbon
ORR	Oxygen Reduction Reaction
PAFC	Phosphoric Acid Fuel Cell
PBI	Polybenzimidazole
Pc	Phthalocyanines
PDDA	Poly- (diallyldimethylammonium chloride)
PEMFC	Polymer Electrolyte Membrane Fuel Cell
PGM	Platinum Group Metals
PPA	Polyphosphoric acid
PTFE	Poly (tetrafluoroethylene)
RDE	Rotating Disc Electrode

RE	Reference Electrode
RHE	Reversible Hydrogen Electrode
RT	Room Temperature
SAED	Selected Area Electron Diffraction
SE	Secondary Electrons
SOFC	Solid Oxide Fuel Cell
SWCNHs	Single walled Carbon Nanohorns
SWCNT	Single-Walled Carbon Nanotube
TEM	Transmission Electron Microscopy
TGA	Termogarvimetric Analysis
THH	Tetrahexahedral
TPB	Triple Phase Boundary
UHV	Ultrahigh Vacuum
VA-NCNT	Vertically Aligned Nitrogen-Containing Carbon Nanotubes
WE	Working Electrode
XPS	X-Ray Photoelectron Spectroscopy
XRD	X-ray Diffraction
YSZ	Y_2O_3-Stabilized ZrO_2

Table of Contents

Chapter 1

Introduction

Chapter 4

Pt-RuO_2 Bimetallic Sandwich Type Thin layer Catalyst for Oxygen Reduction Reaction

Chapter 5

On the Importance of Surface Functionalization in the Bimetallic Electrocatalyst Design

Chapter 6

Carbon Nanofiber-Pt-Poly(benzimidazole) Hybrids as Multifunctional Electrocatalyst with Ideal Interfacial Structure

Chapter 7

A Novel Route for Nitrogen Doping Along the Inner and Outer Surfaces of Carbon Nanofiber and its Electrocatalytic Activity

Abstract

An efficient oxygen reduction reaction (ORR) offers the potential to fulfil the energy demand of the world in Polymer Electrolyte Membrane Fuel Cells (PEMFCs). However, the cost of the PEMFC which mainly arises from the Pt based catalyst hinders its widespread applications. Efforts are underway for reducing the total cost by increasing the Pt utilization or by the use of non-noble metal catalysts. In the advent of nanomaterials, the electrocatalyst performance has been considerably benefited and satisfactory performance has been obtained so far. Some of the advances in this direction include low Pt catalysts like core-shell or alloy type materials with various binary and ternary combinations and Pt-free catalysts like nitrogen doped carbon materials, nitrogen containing macrocyclic complexes, transition metal chalcogenides etc. However, still, there are some major challenges to be addressed for their extensive applications. If we consider durability and reliability issues along with the catalyst activity, till now, the best catalyst for ORR is Pt supported on carbon materials. It is interesting to note that the performance and Pt utilization in a fuel cell catalyst is determined by many factors like active catalyst size and shape, dispersion of the catalyst on support material, surface area of support, catalyst-support interaction, proper mass transfer rate, balanced electron and proton conductivity, ionomer-catalyst-gas pore triple-phase boundary (TPB) etc. Therefore, the best way to effectively meet the requirements for an efficient ORR electrocatalyst is to design advanced electrode materials with high level of catalyst utilization by carefully considering all the above mentioned key parameters.

In view of overcoming some of the above mentioned issues, one-dimensional (1D) nanostructures of carbon such as nanotubes (CNTs) and nanofibers (CNFs) have triggered wide interest, mainly due to their exciting features such as anisotropy, unique structure, and surface properties. However, the inherently low surface area possessed by many of these materials restricts the amount of active component such as Pt that can be dispersed on these materials. A catalyst with higher carbon to catalyst ratio leads to a thick layer of catalyst with high mass transfer and electric resistances. A strategic approach to obviate these

issues is to develop Membrane Electrode Assembly (MEA) with thin electrodes by using catalysts possessing high Pt loading and dispersion. Tubular morphologies of some carbon nanomaterials with open tips are interesting in the context of developing low-carbon-loaded, metal-rich catalysts because the morphology offers the possibility to access both inner and outer surfaces of carbon support for metal dispersion.

The genesis of my work is inspired by this concept where the immense scope for the utilization of both the inner and outer walls of a 1-D carbon nanostructure with peculiar morphological characteristics will be unfolded. Since the materials confined inside are expected to show different chemical and electrochemical behaviour due to the change in the intermolecular interactions, first part of my research is focusing on the decoration of catalyst particles, both monometallic and bimetallic, along the inner and outer walls of CNF support. A suitable process is developed by carefully optimizing the surface tension, polarity and surface wettability of the solvent to achieve this goal. As the establishment of TPB around the catalyst nanoparticles with the provision for proton, electron and gaseous reactants is needed to facilitate the electrode reactions, introduction of proton conductivity along the inner cavity as well as the outer wall is also a major issue. Nafion®, which is a perfluorosulfonic acid polymer with high proton conductivity, has proved to be the best binder in forming a TPB in PEMFCs. However, due to its high molecular weight and fibrillar structure, Nafion cannot be incorporated in the inner cavity of CNFs. Therefore, the next goal of my research is to incorporate a low molecular weight proton conducting polymer in the inner cavity as well as on the outer walls of CNF to provide effective pathways for proton conduction and reactant distribution.

Recently, nitrogen doped (N-doped) carbon nanostructures have been demonstrated as low cost alternatives to Pt with their comparable electrocatalytic activity and improved durability. However, there has not been any attempt to induce N-doping along the inner cavity as well as on the outer surfaces of hollow carbon morphologies. Hence, another goal of this thesis is to develop N-doped CNFs with active sites along the inner and outer walls of CNF.

The thesis is presented in eight chapters, a brief summary of which is given here.

The first chapter is a general introduction to fuel cells, describing the history, working principle and the classification. A detailed review about PEMFCs is included with special emphasis on ORR mechanism, electrocatalysts and catalyst supports. General introduction to the field of nanostructured multifunctional materials and their scope as electrocatalysts for PEMFCs are also included. Finally, the importance of nanoconfinement in modulating the electrochemical properties of materials is also discussed.

Chapter 2 presents different methods employed for the synthesis of various electrocatalysts. The basic principle and experimental details of different characterization techniques employed in the present research are also described.

Chapter 3 describes a novel strategy for the selective decoration of Pt nanoparticles only in the inner wall or along both the walls of CNF by a modified polyol process. The pristine CNF, which possesses inherently active inner wall surface and inactive outer surface, led to selective Pt deposition along the inner wall (C-Pt), whereas activation of the outer wall with chemical functionalization resulted into excellent dispersion of Pt along both the inner and outer walls (F-Pt). Structural and morphological characterizations of these materials revealed that when Pt could be dispersed along the inner as well as the outer walls of CNF, the Pt particle size reduces to almost half as compared to the one with Pt decoration only along a single wall. Further, electrochemical studies using CV and RDE measurements revealed enhanced ORR and methanol oxidation properties of F-Pt as compared to the conventional CNT supported catalyst.

In Chapter 4, we discuss the synthesis of a Pt thin layer catalyst supported on an *in-situ* prepared ‘RuO_2-Carbon-RuO_2’ sandwich type hybrid support. While the selective exposure of Pt on the hybrid support surface is confirmed from the HRTEM analysis, the electronic changes effected in the CNF support are evident from the XPS and XRD analyses. Electrochemical evaluation of this catalyst revealed its exceptionally high activity for ORR with three times increase in the electrochemically active surface area (ECSA) and four times improvement in the limiting current density coupled with 80 mV gain in onset potential. Apart from this, a drastic reduction in the CO poisoning is observed for methanol oxidation reaction.

In Chapter 5, we demonstrate the importance of surface functionalization in the design of bimetallic electrocatalysts. When pristine CNF is used to decorate Pt and RuO_2 nanoparticles, mainly phase-separated nanoparticles rich in RuO_2 characteristics is obtained (C-PtRuO_2). In contrast to this, when CNF activated by a simple H_2O_2 treatment to create oxygen-containing surface functional groups are used, a material rich in Pt features on the surface is obtained (F-PtRuO_2). This is achieved because of the preferential adsorption of RuO_2 by the functionalized surface of CNF. Evaluation of the electrochemical properties of these materials indicated that C-PtRuO_2 exhibits a charge storage property whereas F-PtRuO_2 shows an oxygen reduction property. Thus, the results of this study show how important it is to have a clear understanding of the nature of surface functionalities in the processes involving dispersion of more than one component on various carbon materials.

In Chapter 6, we discuss the synthesis of a novel electrocatalyst system with unique multifunctional characteristics originated by the presence of proton conducting polybenzimidazole (PBI-BuI) bound layer and electron conducting hollow CNF substrate with catalytically active Pt nanoparticles. This is achieved by decorating Pt nanoparticles along the inner cavity as well as on the outer walls of the hollow CNF support (F-Pt). In a further extension, the low molecular weight polymer, PBI-BuI is incorporated into the inner cavity and along the outer surfaces of F-Pt. Electrochemical studies using CV and RDE revealed the high activity of this hybrid material with improved ECSA, 70 mV shift in the onset potential and higher current density.

Chapter 7 describes a simple polymer mediated strategy for N-doping along the inner and outer surfaces of CNF and its electrocatalytic activity for ORR. This is achieved by the high temperature treatment (700-1000 °C) of the

PBI-BuI incorporated CNFs. The initial PBI-BuI content and the annealing temperature are also systematically varied to choose the right combination of starting precursors and heat-treatment conditions. These materials are characterized by a host of techniques and electrochemical characterizations of this material using CV, RDE studies and durability analysis demonstrated that this material can act as a metal-free ORR electrocatlyst with improved oxygen reduction kinetics and stability.

Chapter 8 presents an overall conclusion and comparison of the work reported in the earlier chapters on the synthesis and characterization of monometallic, bimetallic and even non-metal (N-doped CNF) electrocatalysts and their electrocatalytic activities for oxygen reduction reaction. The role of surface functionalization and the need for a proper process modification to access the inner cavity as well as the outer surfaces are discussed in detail. Further work required to be carried out to enhance the electrocatalytic activity of these materials, in comparison with the present work as well as the work reported in the literature are also discussed.

Chapter 1

Introduction

This chapter begins with a brief introduction to fuel cells with special emphasis on polymer electrolyte membrane fuel cells (PEMFCs). A brief review on the structure, working principle, major components and challenges for PEMFCs is also included. This is followed by detailed discussions on oxygen reduction reaction (ORR), need for a better electrocatalyst and ORR mechanism. This chapter also describes a critical survey on the current status of electrocatalyst and catalyst support materials for ORR, including the potential benefits and drawbacks of each category. The importance of nanoconfinement and the advantages of nanostructured multifunctional electrocatalysts are also provided. Finally, the objectives and scope of the present thesis, based on the above discussion, are listed toward the end of the chapter.

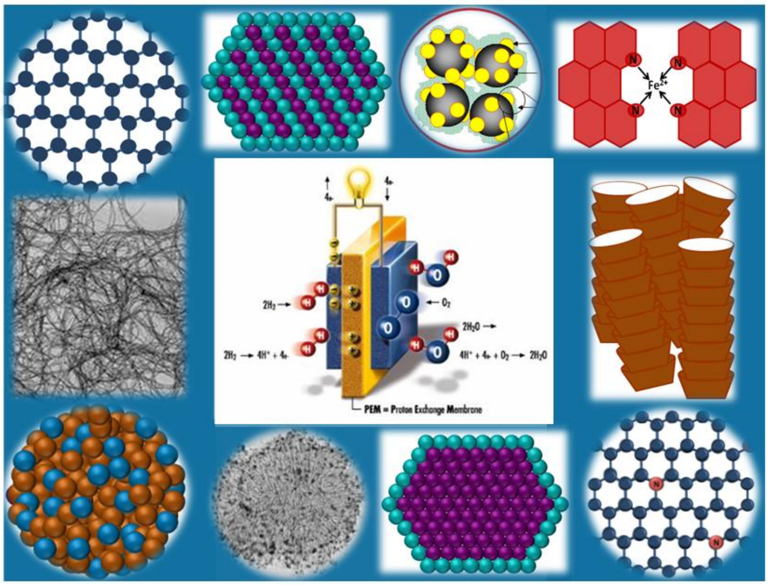

1.1. General Background

Ever increasing demand for energy combined with the depletion of fossil resources and the need for environmental concerns has spurred interest in environmentally friendly, alternative energy systems based on renewable energy [1]. Fuel cells, which convert fuels directly into electrical energy with high efficiencies and produce water as the by-product, have been in the spot light of the environmentally compatible energy systems for the 21st century [2]. The origin of fuel cell can be dated back to the fundamental research carried out by Christian Friedrich Schonbein in the early nineteenth century, where H_2 and O_2 react to produce electricity once connected by electrodes [3]. Later, William Robert Grove designed the first operating fuel cell. He utilized H_2 as fuel and O_2 as oxidant at platinum metal electrodes and sulphuric acid as common electrolyte [4]. Initially, Fuel cells were especially of interest in submarines, space applications and in remote areas where normal combustion engines could not operate. However, in the last few decades, fuel cells have attracted widespread commercial use in the areas of transportation and residential applications.

1.2. Working Principle

The basic structure and the working principle are similar for all fuel cells and are in essence very straightforward. Two electrodes, anode and cathode are electronically separated by electrolyte that provides ionic conduction and circuit is closed externally by electronic conductors. A fuel such as H_2, CH_4, CH_3OH or other hydrocarbons is oxidized at the anode producing electrons, which are transferred to the cathode through an external circuit. While at the cathode, oxygen which is reduced to anion by the electrons, meets with the H^+ diffusing from the anode and forms water [5].

1.3. Classification of Fuel Cells

Fuel cells can be classified by different parameters which include the nature of fuels used, operating temperature and on the basis of electrolytes used.

However, they are customarily classified into five categories according to the electrolyte employed, namely solid oxide fuel cells (SOFCs), molten carbonate fuel cells (MCFCs), phosphoric acid fuel cells (PAFCs), alkaline fuel cells (AFCs) and PEMFCs [5, 6].

The operating temperature of a fuel cell dictates the physicochemical and thermo mechanical properties of the materials used in the cell components (*i.e.*, electrodes, electrolytes, interconnectors, current collectors, etc.). The low temperature fuel cells generally use aqueous electrolytes and hydrogen as a fuel. The operating temperature is limited to 100 °C or lower as the aqueous electrolytes degrade at higher temperature. They typically have compact size, light weight and hence generally are accepted for portable and automobile applications. Apart from these, they are considered to be more environmentally friendly as they do not generate pollutants such as $NO_{x.}$ However, the low temperature fuel cells need noble metals such as Pt to facilitate the electrode reactions which hamper their widespread commercialization.

The high temperature fuel cells such as MCFCs or SOFCs, can utilize CO and even CH_4 as fuels because of the inherently rapid electrode reaction kinetics and the lesser need for high catalytic activity at high temperature. The added advantage of this type of fuel cells is that they do not require noble metal catalysts such as Pt. However, complex components are needed to recover heat generated for steam reforming and thus occupy larger spaces than the low temperature fuel cells.

1.3.1. Solid Oxide Fuel Cells (SOFCs)

SOFC is a highly promising fuel cell, generally used in big, high-power applications including industrial and large-scale central electricity generating stations. SOFCs typically operate in the temperature range of 650-1000 °C and use a hard ceramic material of Y_2O_3-stabilized ZrO_2 (YSZ) that can conduct oxide ($O^{2-)}$ ions at high temperatures, that is $T > 800$ ºC. Typically, the anode is Co-ZrO_2 or Ni-ZrO_2 cermet and the cathode is Sr-doped $LaMnO_3$. Due to the high temperature operation, noble metal catalysts are not required to catalyze the electrode reactions. However, the cathode, anode and the electrolyte should have more or less similar thermal expansion coefficients to be compatible with each other. Another attractive feature of SOFCs is that hydrocarbons can be directly used without any external reformers for hydrogen generation and combined heat and power efficiency (cogeneration) could be as high as 80 %.

1.3.2. Molten Carbonate Fuel Cells (MCFCs)

MCFCs are another class of high temperature fuel cells which operate in the temperature range of 600-650 °C and generate power using a variety of both direct as well as reformed hydrocarbons. The electrolyte in this type of fuel cells is molten Li, Na or K carbonates absorbed in a $LiAlO_2$ ceramic matrix, with carbonate ions providing ionic conduction. Typically, porous nickel and nickel oxide materials are used at the anode and cathode respectively. The operation of MCFCs is based on the shuttle action provided by carbonate ions. Due to the high operation temperature, noble metals are not needed at the electrodes and the added advantages are high system efficiencies and greater flexibility in the use of available fuels. However, higher operating temperature places severe issues such as enhanced corrosion and breakdown of the cell components.

1.3.3. Phosphoric Acid Fuel Cells (PAFCs)

PAFCs are the first fuel cells to be commercially available. Phosphoric acid (H_3PO_4), usually held in a refractory non-conducting matrix like silicon carbide, is used as the electrolyte of these cells. The operating temperature of PAFCs ranges from 150-200 °C and the electrocatalyst in both the anode and the cathode is Pt. Due to the high operation temperature, it can use impure hydrogen as the fuel and the CO tolerance is up to 1.5 %. The other advantages of PAFCs are their simple construction, stability and low volatility of the electrolyte at their operating temperatures. The existing PAFCs have outputs up to 200 kW and they find applications mostly for stationary power plants and on-site generators. However, slow start up due to higher temperature operation and high cost due to the usage of Pt as the electrocatalyst are the major barriers facing the PAFC technology.

1.3.4. Alkaline Fuel Cells (AFCs)

AFCs were long used by NASA in space mission and these cells are too costly for commercial use. AFCs normally operate in the range of 50-70 °C and use an aqueous solution of KOH or NaOH soaked in a matrix as the electrolyte. Typically, AFCs use Pt as the electrocatalyst in both the anode and cathode. One of the main advantages of AFC is that the activation overvoltage of oxygen reduction reaction (ORR) is smaller and hence the efficiency of AFCs is higher. As a result of this improved ORR kinetics, wide range potential materials such as Ni, Ag, metal oxide, spinels, and other non Pt noble metals can also be used as electrocatalysts. However, a major constraint in the AFC operation is that it is easily poisoned by CO_2 which react with the electrolyte to form the respective carbonates. Thus, it only works properly with very pure gases.

1.3.5. Polymer Electrolyte Membrane Fuel Cells (PEMFCs)

PEMFCs were the first type of fuel cells to be employed in space systems, used by the Gemini program. Recently, due to their high achievable power density, flexible design, quick start-up and lower operating temperature, these systems have found great interest in both stationary and portable applications. Based on their operating temperature, PEMFCs can be further classified into two; low temperature PEMFCs (LT-PEMFCs) which operate below 100 °C and high temperature PEMFCs (HT-PEMFCs) operating above 100 °C [7].

Generally, the electrolyte used in LT-PEMFCs is a solid organic polymer poly-perflourosulfonic acid (Nafion®) that depends critically on water for their ionic conduction. This restricts the operating temperature and the LT-PEMFCs operate normally in the temperature range of 30-100 °C under humidified environment. Due to the low operation temperature, electrocatalysts are very important for increasing the ORR kinetics and generally Pt is used as the electrocatalyst in both the anode and cathode. Water management is critical for the efficient performance; the cell must operate under conditions where the by-product water does not evaporate faster than it is produced because the membrane must be hydrated. This type of fuel cell, however, is sensitive to fuel impurities such as CO, as it has a negative effect on the performance due to catalyst-poisoning and it will oxidize to CO_2, which is a greenhouse gas.

HT-PEMFCs are typically designed to overcome some of the above mentioned limitations of LT-PEMFCs. Phosphoric acid doped polybenzimidazole (PBI) membranes are normally used as the proton conducting membrane in HT-PEMFCs. Here, PBI acts as a matrix to hold the phosphoric acid (H_3PO_4), which is responsible for the proton transport and hence can be operative even under dry conditions above 100 °C. Hence, the typical operating temperature of HT-PEMFCs is 120-200 °C. This high temperature operation offers improved kinetics and higher efficiency. Moreover, it prevents CO poisoning of the Pt electrocatalyst. Further, PBI membranes do not rely on water for their proton conductivity thus simplifying the balance of plant components greatly.

1.3.5.1. Structure and Working Principle of PEMFC

The key part of PEMFC is the membrane electrode assembly (MEA), which consists of a proton exchange membrane with anode and cathode catalyst layers attached onto each surface. The electrodes are electronically conducting whereas the proton exchange membrane is an ionic conductor that transports protons. To facilitate the electrochemical reaction at the membrane-electrode interfaces, a catalyst layer is used. The state-of-the-art catalysts for PEMFC consist of Pt or Pt alloy nanoparticles (NPs) supported on high surface area carbon [8]. Typical fuels such as compressed gaseous hydrogen are fed to the anode and an oxidant such as atmospheric oxygen or air is fed to the cathode. At the anode, hydrogen gets oxidised to yield protons and electrons. Protons are then transported across the membrane to the cathode under the influence of the electrochemical potential gradient. Electrons are transported across the external circuit to reduce O_2 at the cathode. This reduced oxygen and protons recombine at the cathode to generate water. Hence the effective formation of triple phase boundary (TPB), where the reactant gases, electrocatalyst and electrolyte membrane meet, is an important criterion for successful PEMFC operation [9]. The product water has to be expelled from the catalyst site to prevent water clogging and better access of reactant gases to the electrocatalyst. The basic half-cell reactions for a hydrogen-powered fuel cell in acidic solutions are given below:

Anode: $H_2 \rightarrow 2H^+ + 2e^-$ E° = 0.00 V (1.1)

Cathode: $1/2O_2 + 2H^+ + 2e^- \rightarrow H_2O$ E° = 1.23 V (1.2)

Overall: $H_2 + 1/2O_2 \rightarrow H_2O$ E_{Cell} = 1.23 V (1.3)

Reaction 1.1 is the hydrogen oxidation reaction (HOR) and the equilibrium potential of the HOR at a Pt electrode in the electrolyte is 0 V by definition [10]. ORR is shown by Reaction 1.2 and the equilibrium potential of ORR on Pt is 1.23 V. ORR has gained significant interest in the past decades as it is currently the efficiency-limiting reaction in a hydrogen-powered PEMFC [11]. The difference in the equilibrium potentials of the HOR and ORR will be the maximum cell voltage. Figure 1.1 shows the schematic illustration of a single cell in a PEMFC stack.

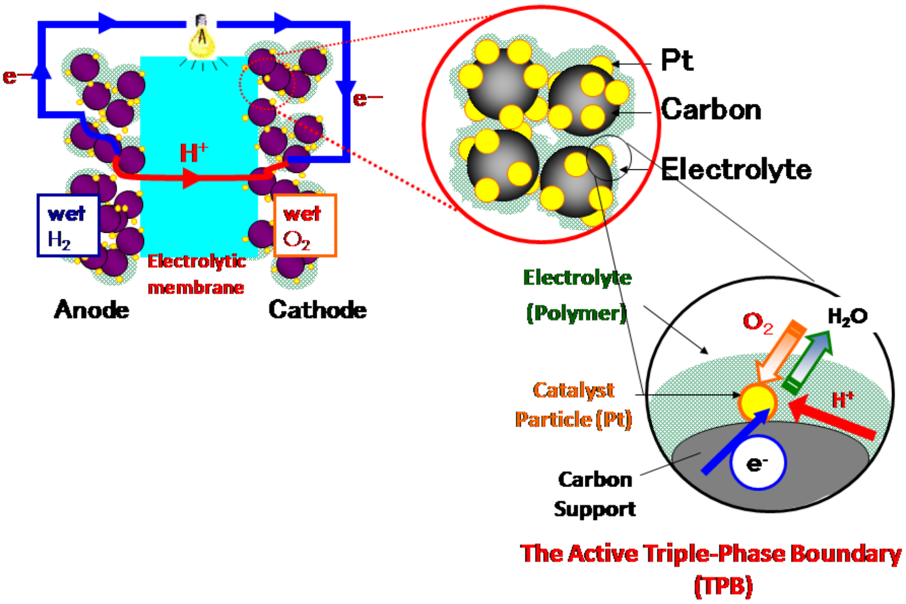

Figure 1.1. Schematic illustration of a single cell in a PEMFC.

1.3.5.2. Challenges of PEMFC

Despite the many attracting features of PEMFCs such as high theoretical efficiency, less pollution etc., the development of commercially viable fuel cell systems faces a number of design, performance and affordability [6, 12]. The present PEMFC technology uses materials such as electrocatalysts, graphite bipolar plates and proton conducting membranes which were selected long back [12]. These materials have exhibited many inadequacies to perform in the present scenario. Hence, constraints on material selection, including electrocatalyst, bipolar plate and electrolyte membrane are the critical challenges in PEMFC.

A major problem is associated with the electrocatalyst. Due to the sluggish kinetics of ORR, the most practical catalysts for ORR are Pt-based catalysts. At present, the state-of-the-art PEMFC stacks use a Pt loading of 0.3 mg/cm^2 which is too expensive for commercialization while American Department of Energy (DOE) target for 2015 lies at 0.03 mg/cm^2 [13]. Another critical issue existing in the electrocatalyst part is CO poisoning, when the PEMFC is operating with a reformate fuel or methanol in the direct methanol fuel cells (DMFCs). Hence a CO tolerant electrocatalyst is needed to overcome this issue. Thus, the main requirement for future is to develop innovative alternative low-Pt loaded materials as electrocatalyst for PEMFCs without compromising performance and durability [6].

The most commonly used membrane in PEMFCs is Nafion developed by DuPont and its conductivity is highly dependent on the bound and free water associated with the active sites. Hence, the operation temperature is limited to 100 °C which necessitates the use of ultrapure H_2 [6]. In addition, reactants such as methanol can readily permeate through existing membrane materials. This reduces the overall efficiency of the cell and it short-circuits the cell. Thus, reactant crossover to the cathode side is another prevailing issue in PEMFCs. Phosphoric acid doped PBI is an alternative membrane material used in PEMFCs especially for high temperature applications. Reduced methanol permeability and better temperature stability of this material direct its potential to use in DMFCs and reformate based fuel cells [14].

1.4. Oxygen Reduction Reaction and Need for Electrocatalysts

HOR under acidic and alkaline conditions is thermodynamically reversible and kinetically less demanding; thus, the overpotential (the potential difference between a thermodynamically determined equilibrium potential and the potential at which the reaction is experimentally observed) loss at the anode during fuel cell operation is minimum [15]. On the other hand, though oxygen is a chemically reactive element, the electrochemical reactions involving oxygen are kinetically slow, resulting in a large overpotential loss under the typical operating conditions. The reaction kinetics is significantly affected by the adsorption process that is governed by the adsorbates, structure, bonding types and energy barriers [16]. Thus, the performance of PEMFC is limited by the sluggish kinetics of ORR. Hence, the choice of an innovative electrocatalyst to improve the rate of the ORR is necessary [17]. Researchers worldwide are trying to design promising catalysts to improve the ORR kinetics. Many electrocatalysts have been tested so far, and that include metal and alloy based nanocrystals, transition metal macrocyclic compounds, transition metal chalcogenides, transition metal carbides, heteroatom-doped (nitrogen, boron, sulphur, phosphorous etc.) carbon compounds and their composite materials, oxides and pervoskites etc. [18]. However, the most practical catalysts for ORR to date are Pt-based catalysts. The design strategies of various nanostructures as ORR catalysts and their performance in PEMFCs are discussed in details in the following section.

1.4.1. ORR Mechanisms

The ORR mechanism is quite complicated and includes several individual reactions and many intermediate compounds, mainly determined by the nature of the electrode material, catalyst and electrolyte [19]. The ORR in acidic and alkaline solution proceeds *via* different pathways. However, either 4-electron reduction or 2-electron reduction pathways are possible in both the conditions. In acidic solution, protons are consumed in the reduction process, while in the alkaline media hydroxyl ions play a dominant role [20]. The catalytically active surface area and the mode of interaction of O_2 with the catalyst's surface are the key factors that determine the reaction pathway. In the 4-electron pathway, the electrocatalytically reduced O_2 combines with protons and H_2O is formed directly. This route is the mostly desired reaction pathway as it produces a high voltage for a H_2-O_2 fuel cell. The overall reaction for this pathway in acid and alkaline solution can be represented as:

a. acidic medium

$$O_2 + 4H^+ + 4e^- \rightarrow 2H_2O \qquad E^o = 1.23\ V \qquad (1.4)$$

b. alkaline medium

$$O_2 + 2H_2O + 4e^- \rightarrow 4OH^- \qquad E^o = 0.401\ V \qquad (1.5)$$

The 2-electron path involves the generation of H_2O_2 as the reaction intermediate and this adsorbed H_2O_2 is further reduced to H_2O. The reaction sequence and E^o in the acid and alkaline solution are given by the following reactions:

a. acidic medium

$$O_2 + 2H^+ + 2\ e^- \rightarrow H_2O_2 \qquad E^o = 0.67\ V \qquad (1.6)$$

$$H_2O_2 + 2H^+ + 2\ e^- \rightarrow 2H_2O \qquad E^o = 1.76\ V \qquad (1.7)$$

or an alternate decomposition pathway is also possible as,

$$2H_2O_2 \rightarrow 2H_2O + O_2 \qquad (1.8)$$

b. alkaline medium

$$O_2 + H_2O + 2e^- \rightarrow HO_2^- + OH^- \qquad E^o = -0.065\ V \qquad (1.9)$$

$$HO_2^- + H_2O + 2e^- \rightarrow 3OH^- \qquad E^o = 0.867\ V \qquad (1.10)$$

or an alternate decomposition pathway is also possible as,

$$2HO_2^- \rightarrow 2OH^- + O_2 \qquad (1.11)$$

The 2-electron reduction pathway which involves the incomplete reduction of O_2 to H_2O_2 leads to low energy conversion efficiency in PEMFCs. Apart from this, H_2O_2, the main intermediate in the 2-electron reduction pathway, is highly undesirable as it causes chemical degradation of the membrane and catalysts [21].

1.4.1.1. ORR Mechanism on Pt

ORR on Pt electrocatalyst has been the most extensively studied mechanism, two mechanisms for ORR on Pt are suggested by theoretical studies based on the electronic structure. One is the dissociative mechanism for reactions taking place in the low current density range; the other is the associative mechanism which is proposed for a high current density range [22, 23]. In the dissociative mechanism, the adsorbed O_2 is dissociated to the adsorbed O atoms on Pt surfaces follows:

$$1/2O_{2(\text{ ads})} \rightarrow O_{(\text{ads})} \qquad (1.12)$$

The adsorbed O atoms then gain two electrons in the two consecutive steps and H_2O is formed and can be expressed by the following equations:

$$O_{(\text{ads})} + H^+ + e^- \rightarrow OH_{(\text{ads})} \qquad (1.13)$$

$$OH_{(\text{ads})} + H^+ + e^- \rightarrow H_2O \qquad (1.14)$$

Since there is no adsorbed O_2 on the Pt surface, H_2O_2 cannot be formed and hence this mechanism can be considered as a detailed form of the direct 4-electron pathway. In the associative mechanism, O_2 is adsorbed without the cleavage of O-O bond. This adsorbed O_2 then reacts *via* reactions as given in 1.15-1.19 and leads to H_2O.

$$O_2 \rightarrow O_{2(\text{ads})} \qquad (1.15)$$

$$O_{2(\text{ads})} + H^+ + e- \rightarrow HO_{2(\text{ads})} \qquad (1.16)$$

$$HO_{2(\text{ads})} + H^+ + e- \rightarrow H_2O + O_{(\text{ads})} \qquad (1.17)$$

$$O_{(\text{ads})} + H^+ + e- \rightarrow OH_{(\text{ads})} \qquad (1.18)$$

$$OH_{(\text{ads})} + H^+ + e- \rightarrow H_2O \qquad (1.19)$$

Since adsorbed O_2 is present on Pt surface, the O-O bond may not be broken in the following steps, resulting in the formation of H_2O_2. The H_2O_2 could either be further reduced to H_2O or be a final product.

In the ORR, electrons are transferred from the metal to the antibonding orbitals of O_2. This decreases the bond order and elongates the O-O bond, and, subsequently, decreases the vibrational frequency of the O-O stretching. However, the adsorption sites and the configuration for the O_2 adsorption on the electrode surface are unclear. The initial O_2 adsorption configuration on the active site significantly affects the subsequent reduction processes. There are three possible O_2 absorption models on metal surfaces, named Griffith, Pauling and Yeager models [19]. O_2 is adsorbed on a single substrate atom with two bonds in the Griffith model, and through a single bond in the Pauling model (end-on configuration), whereas in Yeager model, O_2 is adsorbed on two sites with two bonds (bridge configuration), as shown in Figure 1.2. The two-electron and four-electron reduction may involve the Pauling and Yeager or Griffith model respectively [24].

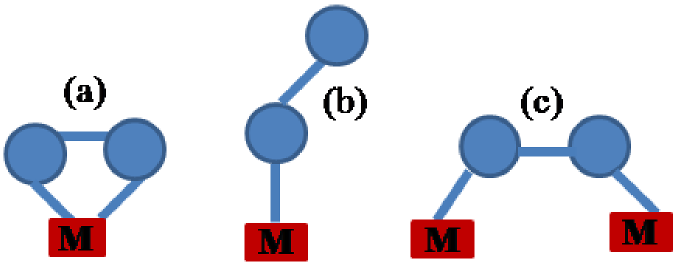

Figure 1.2. Possible adsorption configuration of O_2 on Pt surface: (a) Griffith, (b) Pauling and (c) Yeager models.

1.4.2. Pt Based Electrocatalysts

Fundamental to the electrocatalyst theory is the Sabatier principle that dictates that the adsorbed intermediates should neither adsorb too strongly nor too weakly. To be an efficient electrocatalyst, all the reaction intermediates should remain adsorbed with an optimum binding energy until the final stable product is formed that desorbs into the electrolyte. The key steps involved in ORR is the O-O bond dissociation and the formation of surface-absorbed -OH groups [25]. Based on theoretical calculations, Pt is predicted to have best ORR activity as it has suitable electronic structure (low *d*-band center and *d*-orbital vacancy) and favourable Pt-Pt inter-atomic distance, which has been proven experimentally as well [26]. Since the most active catalyst being Pt, the total capital cost is too high.

Apart from this, even with the best state-of-the-art Pt catalysts, there is still a large overpotential, which reduces the total output. Hence, to reduce the cost and to improve the activity, many approaches have been developed. These include size and shape selective synthesis of Pt, mixing Pt with high-surface area carbon supports, design of low Pt catalysts such as alloys, core-shells etc [27]. The basic designs for Pt based catalysts are summarized in Figure 1.3.

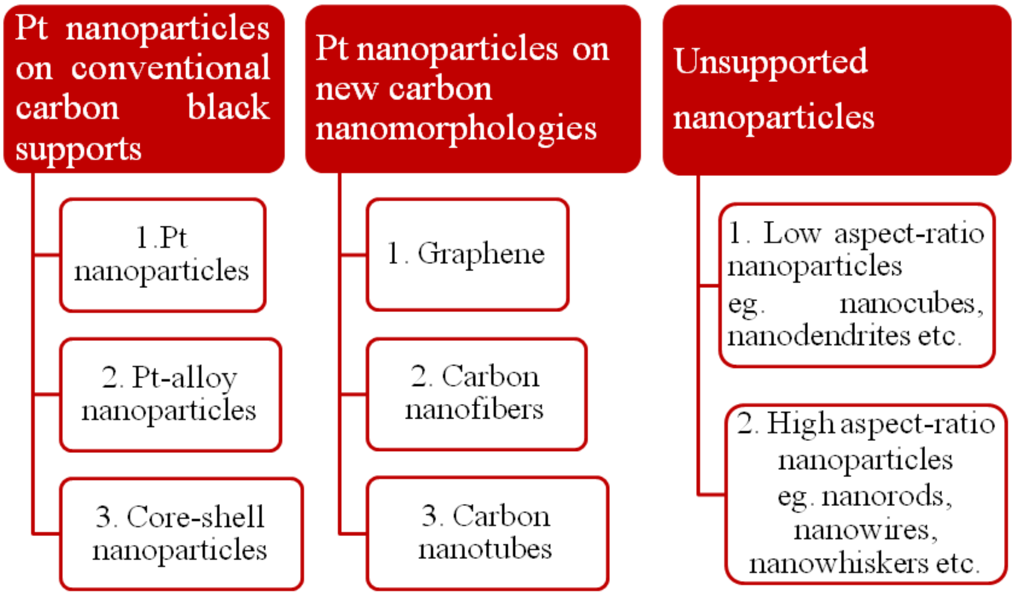

Figure 1.3. Pt-based electrocatalyst approaches (*Ref. 27*).

1.4.2.1. Pt Electrocatalysts

As discussed in the previous section, Pt has been widely considered as the conventional state-of-the-art ORR electrocatalyst. The Pt electrocatalysts in dominant use today consist of Pt NPs with diameters of 2-4 nm, dispersed on high-surface-area carbon supports. The commonly used commercial Pt catalysts such as the catalyst from E-TEK (20 % Pt/C), Pt catalysts supported on TKK porous carbon etc. have surface areas of 80-120 m^2/g, specific activities of 0.15-0.20 mA/cm^2 Pt and mass activities of 0.10- 0.12 A/mg Pt [27]. The electrocatalytic activity of Pt catalysts is dependent on the degree of dispersion on the support materials and the Pt NP sizes. Generally, Pt NPs with smaller sizes provide higher electrochemical activity. However, the particle effect implies that the Pt particle cannot be extremely small and the optimum Pt NP size for the highest ORR activity has been reported to be in the range from 2 to 4 nm [28].

The high index planes with high percentage of atomic steps, edges, corners and kinks can act as active sites for breaking chemical bonds. Therefore, Pt NPs with high-index facets are expected to exhibit higher ORR activity than those bound by low-index facets. This necessitates the shape selective synthesis of NPs which have high density of such active sites. Yang *et al*. synthesized monodisperse Pt nanocubes which exhibited high catalytic activity towards ORR [29]. An electrochemical route for the synthesis of tetrahexahedral (THH) Pt nanocrystals (NCs) bound with high-index facets such as (210), (520), and (730) was reported by Sun *et al*. Electrochemical studies have demonstrated that THH-Pt can act as an efficient electrocatalyst for ethanol and formic acid oxidation [30].

1.4.2.2. Pt Alloys

The catalytic activity of Pt towards ORR strongly depends on many factors such as O_2 adsorption energy, the O-O bond dissociation energy and the binding energy of OH on the Pt surface. The electronic structure of the Pt catalyst and the surface geometric effect are reported to affect these energies [31]. Hence, theoretical calculations have predicted that the intrinsic activity of Pt for ORR can be enhanced by alloying with inexpensive non-noble metals such as Fe, Ni, Co, Cr, Y, Sc etc. [31, 32]. In several such Pt-based systems, both activity and durability are improved and numerous studies have been conducted to understand the origins of the enhancement [31, 32]. It has been recognized that, alloying causes a lattice contraction, leading to a more favourable Pt-Pt distance for the dissociative adsorption of O_2. Apart from this, the *d*-band vacancy can be increased after alloying which weakens the O-O bonds. Thus, the observed activity enhancement in Pt alloys can be attributed to the effects of non-Pt metals on the *d*-band electron level of Pt and the favourable change in the Pt-Pt interatomic distance.

For example, Wang *et al*. have reported the synthesis and ORR activity of size controlled, monodispersed $CoPt_3$ alloy NPs (3-9 nm) supported on carbon. A 3-fold enhancement in the mass activity was obtained for the alloy catalyst at an optimal size, whereas, the specific activity increased monotonically with particle size, as compared to the commercially available Pt/C catalysts [33, 34]. Wu *et al*. demonstrated four times improved mass activity of truncated-octahedral Pt_3Ni particles with predominantly {111} facets as compared to the commercial Pt/C [35]. This ORR activity was much higher than the {100} bounded Pt_3Ni cubes [36]. These results suggest that shape-controlled particles with higher surface coordination (fewer surface defects where oxides preferentially form) or compositional gradients could improve activities.

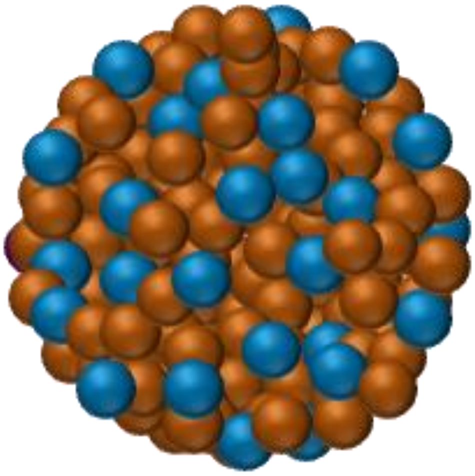

Figure 1.4. Schematic representation of a Pt-based alloy catalyst.

1.4.2.3. Core-Shell Catalysts

It is well-known that only the surfaces of catalysts are involved in electrochemical reactions. Hence, Pt can be eliminated from the inner core and the cost can be reduced to a considerable level. In addition to this, the chemical composition of the core material influences the outer Pt monolayer and optimizes its surface electronic and structural properties. This results into significantly enhanced mass and specific activities of the core-shell type materials [37]. Thus, the core-shell materials comprising of metal core and another metal shell have developed into an increasingly important class of electrocatalysts. In ORR electrocatalysts, a Pt shell or skin layer supported on a non-Pt core are generally used. Typical examples include Pt or Pt-alloy shells on platinum group metals (PGM), non-noble metal or de-alloyed cores [38]. In general, the choice of the core material is based on the segregation properties of the two metals, as well as their electronic and strain-inducing effects on the Pt monolayer. However, a non-noble metal core will be an ideal candidate in the cost perspective. Figure 1.5 shows the schematic representation of the important types of core-shell designs.

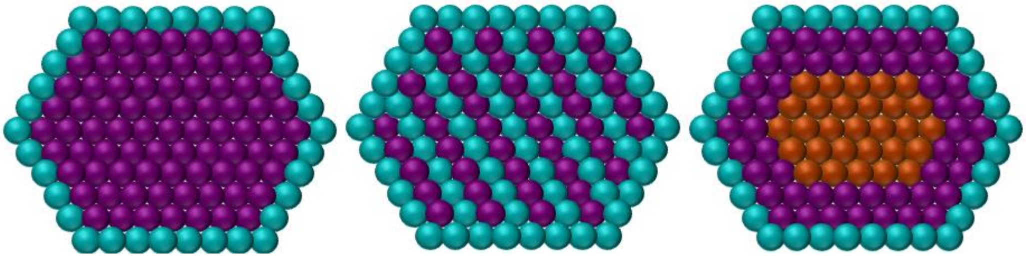

Figure 1.5. Schematic representation of (a) metal core-metal shell, (b) alloy core with enriched metal surface shell and (c) metal core-bimetallic shell designs.

For example, Stamenkovic *et al*. prepared Pt_3M (M stands for Co, Ni and Fe elements) catalysts with Pt-skin surface, which exhibited three to four times higher ORR activity than that of pure Pt [39]. The $Pt_3Ni(111)$ single-crystal catalyst prepared under ultrahigh vacuum (UHV) demonstrated 10 times higher ORR mass activity than the current state-of-the art Pt/C in 0.1 M $HClO_4$ solution. The core-shell design has been further extended to alloys also. Thus, $FePt_3$ bimetallic layer on Au core reported by the same group, exhibited high catalytic activity and prolonged durability [39, 18b]. Strasser *et al.* reported the synthesis and ORR activity of carbon supported, Pt-enriched shell on a PtCu alloy core by an electrochemical dealloying of the non-noble metal Cu atoms. The resultant material exhibited a 4-6 fold improvement in the ORR activity over that of pure Pt. The authors attributed this enhanced activity to the reduced adsorption energy of reactive intermediates on the strained Pt. In CuCoPt ternary catalysts, Cu was preferably removed by voltametrical dealloying process and electrocatalysts having Pt and Co enriched surfaces with compressed surface strain resulted into enhanced ORR activity [40]. Pt-Ag alloy NPs with surface enriched Pt were produced through selective electrochemical removal of Ag atoms under different potentials [41]. In addition, Xia *et al.* synthesized Pd-Pt bimetallic nanodendrites with a core rich in Pd and many arms rich in Pt, which showed improved ORR activity than the state-of-the-art Pt/C catalyst. This was attributed to the presence of high-index Pt surfaces, which exhibited slightly greater ORR activities than the low-index planes in acidic solutions due to the favorable O_2 adsorption [42].

1.4.3. Non-Pt Catalysts

Despite the extensive use of Pt based catalysts in PEMFCs, these classes of catalysts often suffer from multiple competitive disadvantages, including the scarcity and high cost, low selectivity and poor durability. Therefore, it is highly desirable to develop alternative low cost materials as electrocatalysts, which can perform better or equivalent to the Pt standard [43]. Non-precious metal (NPM) catalysts completely eliminate Pt and have recently shown improved ORR activities. Among the wide variety of materials explored, pyrolysis of cobalt and iron-containing heteroatom polymer precursors (for example, porphyrins, phthalocyanins) is one of the dominant routes towards NPM catalysts [44-46]. Nitrogen-containing carbons are another important class of electrocatalyst materials under vigorous study as they have been shown to have good catalytic activity and even better performance and stability when composited with Pt based catalysts [47-52].

1.4.3.1. Transition Metal Macrocyclic Compounds

Transition metal macrocyclic compounds, specific class of compounds containing metal chelates, have been investigated as potential ORR catalysts since the early 1960s [44]. They are reported to catalyse the ORR through a 2-electron or 4-electron transfer pathway to produce either H_2O_2 or H_2O. Sometimes, they can also catalyze ORR through a mixed pathway of 2- and 4-electron transfer reductions. It is reported that the electrocatalytic activity of the transition metal macrocyclic compounds is determined by the nature of transition metal center and the macrocyclic ligand. Among the wide variety of macrocyclic compounds, phthalocyanines (Pc) and porphyrins and their derivatives complexed with various transition metals such as iron, cobalt, nickel and copper are the major class of compounds investigated as the ORR electrocatalysts. The active sites in these classes of materials are believed to be the metal site co-ordinated to several nitrogen atoms and particularly those consisting of M-N_4 macrocycles have attracted particular attention due to their reasonable activity and remarkable selectivity towards ORR. The nature of the active site and the actual mechanisms involved in these catalysts are not well understood till date. However, it is generally believed that nitrogen acts as an n-type dopant, allowing oxygen to adsorb on the edge of the nitrogen-doped carbon surface, which initiates ORR.

Though the pioneering works on transition metal macrocyclic compounds as electrocatalysts for ORR were inspired by Jasinki *et al*., the strategy developed by Dodelet *et al*. has led to the unprecedented increase in the ORR activity [44, 45]. They synthesized microporous, carbon-supported Fe-based catalysts by mixing carbon support, phenanthroline and ferrous acetate by ball-milling followed by two pyrolyzing steps in argon and ammonia respectively [45a]. The resulting material exhibited enhanced catalytic activity and the kinetic activity obtained at 0.8 V was 99 A/cm^3. In a more recent report by Zelenay *et al.*, a high-performance electrocatalyst with relatively high durability was derived from polyaniline, iron and cobalt [46].

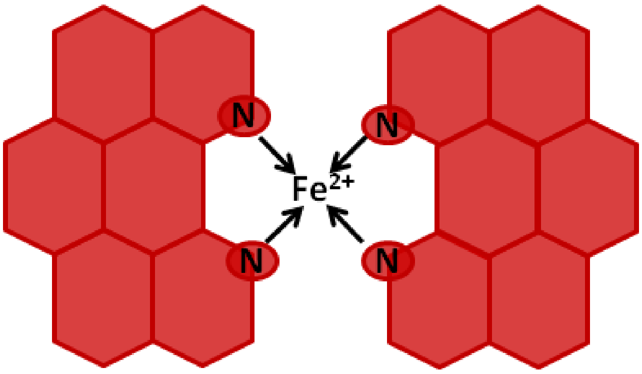

Figure 1.6. Structure of Fe based NPM catalyst (*Ref. 45a*).

1.4.3.2. Nitrogen-doped Carbon Nanostructures

Nitrogen doping in nanostructured carbon materials such as carbon nanotubes (CNTs), carbon nanofibers (CNFs), carbon nanocoils (CNCs), carbon nanospheres (CNSs), ordered mesoporous carbons (OMCs), graphene etc. is another promising strategy to obtain fuel cell catalysts with desirable performance [47]. The introduction of nitrogen into the honeycomb structure of carbon through doping creates unique electronic structure by the conjugation between the nitrogen lone-pair electrons and graphene π system. This results into an n-type semiconductor with localised states above the Fermi level and thus exhibits excellent electrocatalytic activity for ORR. Though, a full understating of the active sites and the role of nitrogen atoms in the nitrogen doped systems are still controversial, the generally accepted mechanism is that due to the electro-negativity difference, a net positive charge is created on the carbon atoms adjacent to nitrogen atoms in the carbon based nanostructures, which facilitates the O_2 adsorption and the ORR process [47]. Figure 1.8 shows the schematic representation of a nitrogen doped graphene.

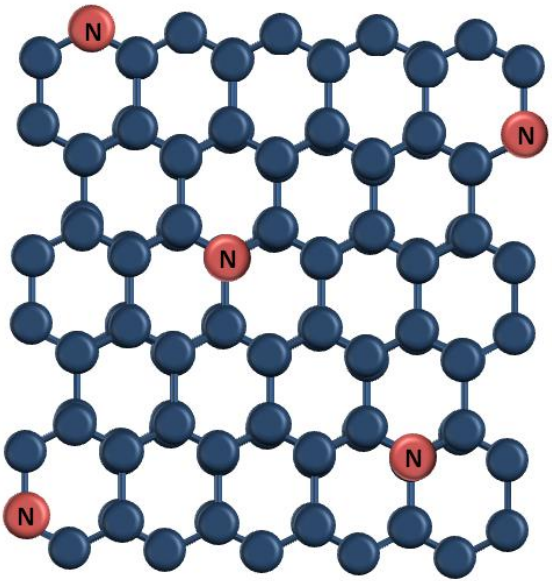

Figure 1.7. Schematic representation of nitrogen doped graphene.

Dai *et al.* synthesized vertically aligned nitrogen-containing CNTs (VA-NCNTs) by pyrolysis of FePc in either the presence or absence of additional NH_3 vapor. The prepared VA-NCNTs had much higher diffusion-limited currents and lower overpotentials than their nitrogen-free counterparts. VA-NCNTs also exhibited better long-term operational stability and tolerance to crossover than that of commercially available Etek-Pt/C catalyst in alkaline electrolytes [48]. In a recent report from the same group, it was demonstrated that intermolecular charge-transfer could also facilitate ORR. They designed polyelectrolyte adsorbed pure CNTs or graphene and the resulting materials exhibited high ORR activity due to the intermolecular charge-transfer from the CNTs or graphene to the adsorbed poly-(diallyldimethylammonium chloride) (PDDA) [49]. Nitrogen doped graphene has been also demonstrated as an excellent metal-free ORR electrocatalyst. For example, Shao *et al*. developed a nitrogen plasma assisted method to synthesize nitrogen-doped graphene (N-Gr). Though, the initial ORR activity of N-Gr was less, it exhibited higher ORR activity with high selectivity than Pt/C after the durability test [50].

Li *et al*. demonstrated the synthesis and electrocatalytic activity of nitrogen doped graphene attached CNTs for ORR. In this method, nanosized graphene sheets were formed from the unzipped part of the outer wall of the nanotubes which remains attached to the intact inner walls of the nanotubes. N-doping in the defect-rich graphene sheets was achieved by annealing in NH_3. The resulting materials exhibited better activity and superior stability in both alkaline and acidic medium [51]. In addition to nitrogen doping, boron, phosphorous and sulphur doping have also been demonstrated to facilitate the oxygen reduction process on carbon surfaces [52].

1.4.4. Carbon Nanomorphologies as Support Material for Electrocatalysts

The catalyst support also plays a crucial role in the performance of electrocatalysts as it provides dispersion and stability for the catalyst particles. More importantly, catalyst supports interplay with catalytic metals and influence the activity and durability of the electrocatalyst. The stability of the catalyst support under the stringent operating conditions of PEMFCs is the major determining parameter of a catalyst support. Apart from this, a large surface area for finely dispersing catalyst particles, high electrical conductivity for providing electrical pathways, highly developed porosity for facile diffusion of reactants and by-products, good corrosion resistance etc. also are equally important in the selection of a catalyst support [53]. Carbon based materials are the most commonly used catalyst supports for PEMFCs as they have many material properties attractive to electrochemical applications, such as high electrical conductivity, good corrosion resistance and mechanical properties [54]. Carbon black materials such as Vulcan XC-72, Ketjen black etc. have been extensively used as the catalyst supports in PEMFCs. In the last decade, a number of novel nanostructured carbon materials such as CNTs, CNFs, CNCs, CNSs, graphene, carbon nanohorns (CNHs), mesoporous carbons (MPCs), etc. have been extensively used as support materials in PEMFCs [55]. As compared to the conventional carbon black materials, these carbon nanomaterials have different properties both at the microscopic and macroscopic levels such as structure, morphology and pore texture. The characteristic properties of some of these new classes of carbon nanomaterials as support materials for PEMFCs are discussed in details in the following section.

1.4.4.1. Carbon Black and Activated Carbons

Standard or graphitized Carbon Blacks (CBs) have been widely used as support materials in PEMFCs [56]. They are easily available, comparatively low cost materials with high surface area. However, they are micro-porous in nature which is difficult to access and hence the fuel supply will not occur smoothly. Moreover, the catalyst NPs remain trapped in these pores and will become inaccessible for the required function [57]. Apart from this, the pores of these types of carbon materials are poorly connected. All these physical properties are directly reflected in the electrochemical activity and hence recently new non-conventional carbon materials have attracted much interest as support materials for PEMFCs.

1.4.4.2. Mesoporous Carbon (MPC)

Mesoporous Carbon (MPC) is constructed of regular arrays of uniform mesopores, with tunable pore sizes of the order of 2 to 50 nm [58]. As compared to CBs, MPCs have large surface area and high pore volume. The high mesoporous surface area gives rise to excellent dispersion of catalyst NPs, which results into high catalytic activity. Apart from this, the mesoporous structure facilitates efficient diffusion and transport of reactants and by-products giving rise to high limiting currents. Thus, MPCs as support materials are expected to be advantageous for the utilization of catalyst particles as well as for efficient mass transport. Many groups have reported the excellent electrochemical performance of Pt NPs loaded MPC for ORR, methanol and formic acid oxidation than that of CB supported catalysts [59]. Shao *et al*. reported the improved durability of Pt loaded, PDDA functionalized highly graphitized MPC [60].

1.4.4.3. Carbon Nanotubes

CNTs are tubular structures of carbon with distinct characteristics such as high surface area, high chemical stability, highest Young’s modulus, electrical conductivity, light weight and easy interfacing capability with many inorganic and organic compounds [55a, 61]. CNTs are made of seamless cylinders of graphene sheets and based on this, CNTs can be broadly classified into two types, single-walled (SWCNTs) and multi-walled (MWCNTs) and some reports are available on double-walled nanotubes (DWCNTs) also [62]. A SWCNT is made by the simple rolling of a single graphene sheet into a cylindrical form whereas MWCNT consists of several coaxially arranged graphene cylinders. The surface areas of the as grown SWCNTs and MWCNTs range between 400-900 m^2/g and 200-400 m^2/g respectively.

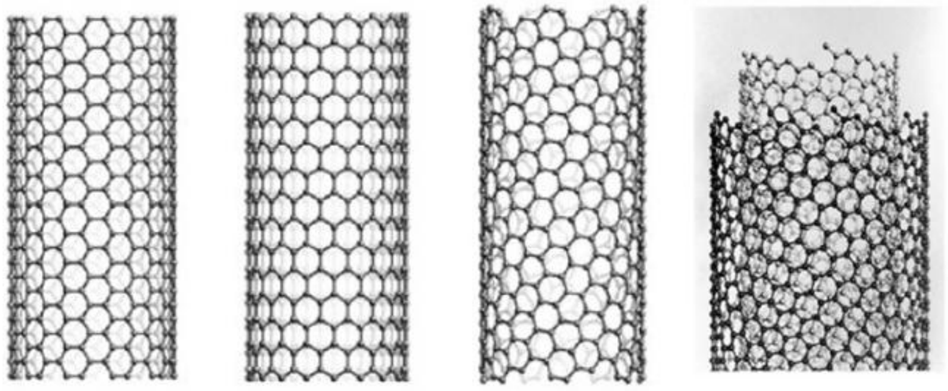

Figure 1.8. Schematic representation for single-walled and multi-walled CNTs.

Many recent reports have demonstrated the use of CNTs as electrocatalyst support for PEMFCs and their overwhelming advantages over Vulcan XC-72 carbon support [63]. This improved activity can be attributed to its fascinating properties such as unique electronic structure with delocalized ‘π’ electrons that helps in enhancing the catalytic activity of the supported metal in addition to providing mechanical integrity. Apart from this, the electrical properties of CNTs provide a high electrical conductivity also. In line with these benefits, due to their high curvature and chemical inertness, NP dispersion on pristine CNTs will result into poor dispersion with a broad particle size distribution, resulting into significantly reduced electrocatalytic activity. Thus, functionalization of CNTs to attach specific functional groups is generally adopted to improve the dispersion of NPs. However, there are many challenges which revolve around the chemical functionalization of CNTs as it introduces structural defects, which in turn reduces the electrical conductivity and the durability of CNTs [64]. The non-covalent functionalization which involves the wrapping of CNTs with surfactants or high molecular weight species such as polymers, DNA and proteins generates high-density and homogenous surface functional groups on CNT surface. These approach maintains the structural integrity of CNTs and thus retains good electrical conductivity [64].

Yan *et al.,* have carried out a pioneering work on the use of CNTs in PEMFC electrodes to improve Pt utilization [65]. Their results have shown improved current and power density in the activation, ohmic and mass transport regions of the polarization curve, presumably due to the intrinsic properties of CNTs to increase the ORR kinetics. A large number of reports are available on preparing CNT based electrodes especially to increase the Pt utilization by means of different experimental conditions. A more recent work by Haddon *et al.*, has demonstrated the high level of performance of ultralow Pt loaded (6 µg Pt/cm^2 and 12 µg Pt/cm^2) MWCNT supported catalysts by a filtration method [66]. Recent advances have shown that the intrinsic activity and durability of Pt catalysts can be improved further by tuning surface geometric and compositional effects. One-dimensonal (1-D) nanostructures of Pt is of particular interest because of the presence of more surface sites located on low-index atomic planes and fewer corner and edge sites than Pt NPs. In this context, Shao-Horn and co-workers have developed a simple synthetic route to create Pt-covered MWNTs (Pt NPs/MWNTs) as promising 1-D Pt nanostructured catalysts for ORR in PEMFCs. The intrinsic activity of the Pt NPs/MWNTs was ∼3-fold higher than that of a commercial Pt/C (40 wt%) catalyst. More significantly, the mass activity of Pt NP/MWNT was also higher as compared to the other 1-D nanostructured catalysts and commercial Pt/C catalysts. They attributed this significantly enhanced intrinsic activity to the weak chemical adsorption energy of OH_{ads}^- species on the surface of the Pt NPs covering MWNTs [67].

1.4.4.4. Carbon Nanofibers

CNFs or graphitic nanofibers (GNFs) are also cylindrical carbon materials like CNTs, first reported by Hughes and Cambers in 1889 [68]. The mechanical and electric properties of CNFs are similar to that of CNTs [69]. The usual diameters of CNF are 2-100 nm and lengths are in the range of few micrometers. CNFs can be grown by catalytic decomposition of certain hydrocarbons over some small metal NPs such as Fe, Co, Ni and their alloys and the diameter of CNF can be tuned by the size of the catalyst NPs [70]. The characteristic feature that differentiates CNFs from CNTs is in the stacking of graphene sheets producing more edge sites on the outer wall of CNFs than CNTs [71]. Depending on the stacking arrangements of graphene sheets in CNFs, they can be classified into three: fishbone (herringbone or cup-stacked), platelet (deck of cards) and parallel (tubular or ribbon-like) type, as shown in Figure 1.9. In fishbone (herringbone) type CNF, graphene layers are arranged at an angle of 45º to the growth axis, whereas in the platelet type and parallel (tubular) type CNFs, the graphene layers are arranged perpendicular and parallel to the growth axis respectively [72]. Such high degree of exposed graphene edges can act as favourable sites for the stabilization of NPs by maintaining their uniform distribution. Apart from this, it is reported that the presence of more edge plane defects facilitate the electron transfer also. These properties, coupled with its low cost as compared to CNTs, have generated intense interest in CNFs as catalyst support materials for fuel cell applications.

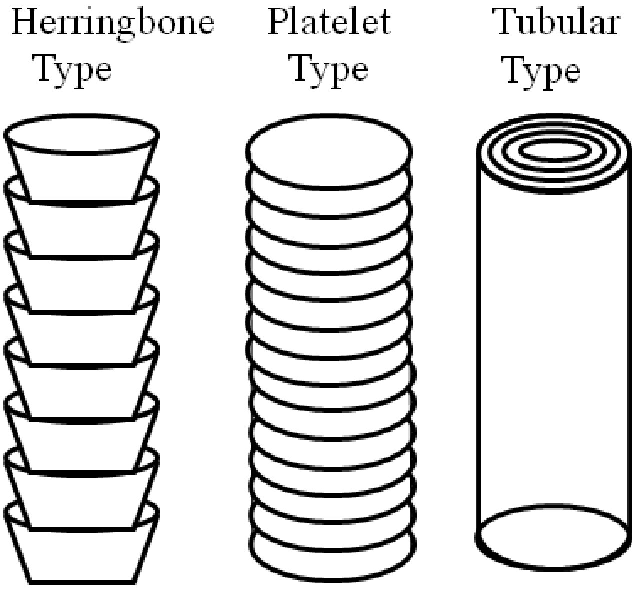

Figure 1.9. Schematic representation of the herringbone, platelet and tubular type CNFs.

Among the three types of CNFs, herringbone type CNFs are of particular interest as they can be synthesized with very small or completely hollow core [73]. Unlike the other CNFs, herringbone type CNFs are made up of truncated conical graphene layers (cups). Because of this peculiar rolling of graphene sheets, CNF exhibits a large central hollow core, which in turn imposes a significant portion of exposed and reactive edges in the inner channel created within CNFs. This peculiar morphology offers a possibility to access both the inner and outer surfaces for NP dispersion. However, NP dispersion along the inner wall of such materials can be accomplished by surmounting the geometry and surface affinity related issues. For example, Endo *et. al*. demonstrated the selective decoration of Pt NPs only on the outer surface, only in the inner surface and both on the outer and in the inner surfaces of CNFs by tailoring the morphology and the chemical reactivity [74]. Alcaide *et. al*. reported the synthesis and electrocatalytic activity of Pt supported on CNFs (Pt-CNF). The Pt-CNF material exhibited an enhancement of *ca*. 94 % in power density at 0.60 V, in comparison with a commercial catalyst supported on conventional carbon black, Pt/Vulcan XC-72R [75].

1.4.4.5. Graphene

Graphene, one atom-thick sheet of sp^2-bonded carbon atoms arranged in a hexagonal lattice, has attracted strong scientific and technological interest since its discovery in 2004 [76]. It is a unique two dimensional (2-D) material with large theoretical specific surface area (2630 m^2/g), graphitized basal plane structure, good optical transparency, high Young’s modulus, good electrical conductivity, high mechanical strength and potentially low manufacturing cost [77]. Recently, many research efforts have been made to take advantage of the unique features of graphene as a PEMFC electrocatalyst support. It has been demonstrated as a promising electrocatalyst support with enhanced activity and increased durability [78]. Figure 1.10 shows the schematic representation of a single layer graphene.

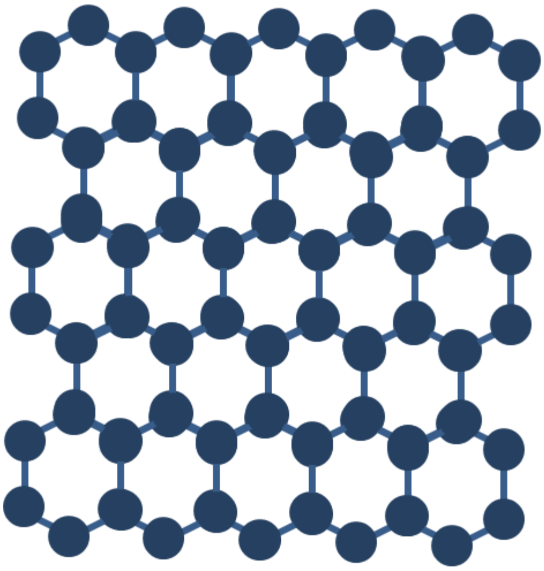

Figure 1.10. Schematic representation of a single layer graphene.

Yoo *et. al*. found that graphene nanosheets (GNS) can assist the formation of sub-nanometre Pt clusters with a size of ~0.5 nm. The resulting Pt-GNS hybrid catalyst exhibited 3 times higher activity for methanol oxidation, as compared to that of the Pt-CB catalyst. Such unusually high activity can be attributed to the well distribution of Pt clusters on the GNS which results from the enhanced interaction between the graphene and Pt and consequently these Pt clusters can remain stable even after the heat treatment at 400 ºC [78a]. Shao *et. al.* employed graphene nanoplatelets (GNPs), which exhibited the advantages of both single-layer graphene and highly graphitic carbon, as a durable alternative support material for Pt NPs [78b]. In a recent report, Choi and his co-workers developed a single step method for the synthesis of Pt NP decorated graphene sheets (Pt-Gr) by a thermal treatment of graphene oxide (GO) with Pt acetylacetonate. Electrochemical studies of the resulting Pt-Gr material reveal the excellent activity and stability towards the methanol oxidation reaction [78c]. Wang *et. al.* reported the synthesis of a new type of high-quality branched Pt nanowires on graphene (BPtNW/G) as an efficient and stable electrocatalyst towards the methanol oxidation reaction than commercial Pt/C catalysts (Hispec4000) [78d]. The improved catalytic activity of graphene supported catalysts can be attributed to the graphene microstructure, including the functional groups, surface defects and voids on the surface as well as to the interaction of Pt particles with graphene. It is reported that the nature of functional groups and the group surface densities on graphene strongly affect the metal-support interaction and therefore, the ORR activity. Thus, hydroxyl- and epoxy-functionalized graphene-supported Pt showed a higher electrochemical activity and stability after 5000 CV cycles than commercial catalysts E-TEK [78e].

1.4.4.6. Other Carbon Nanostructures

CNHs, CNCs and CNSs constitute another important class of new carbon morphologies. The properties of these materials differ significantly from that of other high aspect ratio carbon nanomaterials such as CNTs and CNFs. The CNH is a new type of carbon nanomaterials with a horn-shaped sheath of graphene sheets. Single walled CNHs (SWCNHs) are generally 2-3 nm thick and 30-50 nm long and they form aggregates that resemble either a ‘dahlia flower’ or it takes a ‘bud-like’ form [79]. The structure of CNCs is similar to that of helical MWCNTs [80]. Recently, these materials have been tested as support materials for PEMFCs. The high catalytic activity of CNH, CNC or CNS supported catalysts demonstrates the future potential of these materials as PEMFC catalysts support.

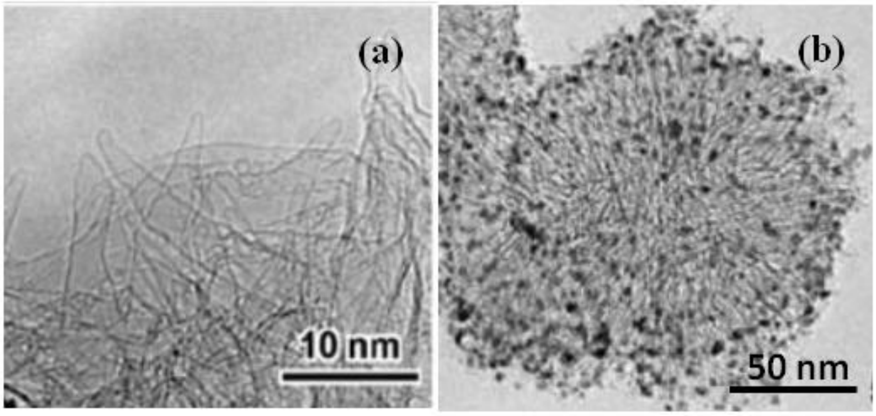

Figure 1.11. TEM images of (a) SWNHs nanostructure and (b) Pt/SWNH catalyst; *(Ref. 79).*

1.4.5. Importance of Nanoconfinement in Electrocatalysis

It is well documented in the literature that the materials confined in a nanocavity exhibit unprecedented behaviour that differs very much from their unconfined counterparts. Numerous studies on confined materials have been reported in the last few decades [81-83]. A wide variety of materials such as CNTs, CNFs, graphene and OMC have been demonstrated as the suitable host materials for encapsulation. Among them, SWCNTs are the widely explored class of hosts. In fact, studies have shown that confinement of certain molecules in CNTs result in unique intermolecular arrangements and lead to lowering of activation barriers for certain reactions [81a]. Remarkable enhancement of the catalytic activities has already been observed over the CNT-confined catalysts due to the tuned properties of active species *via* confinement. It is also revealed that the confinement offers a unique opportunity to protect the materials especially NPs from agglomeration, sintering, dislodgement etc. These effects are dominant while confining inorganic materials as compared to organic materials and polymers.

In fact, the above mentioned benefits of confined systems can be effectively utilized to overcome many of the existing challenges in electrocatalysts. It is well-known that the materials confined in a nanocavity are expected to exhibit different redox behavior as a result of the space restriction and interaction with the walls. Thus, by confining the catalyst NPs in suitable nanocavity, the intrinsic activity can be better tuned. Moreover, catalyst NPs decorated on the outer surface of the support materials are prone to agglomeration and sintering, which reduces the overall efficiency. For example, Joo *et al.* have demonstrated the ORR activity of Pt NPs confined in OMC support [84]. However, the major drawback of that study was the diffusion limitation to the reactants as well as to the ionomer, due to the smaller pore size. Hence, choice of the host material having larger pore sizes (~50 nm) will result into improved ORR activity without transport limitations.

1.4.6. Nanostructured Multifunctional Materials as Electrocatalysts

Multifunctional materials (MFMs) are materials designed to perform multiple functions simultaneously and are formed by integrating different types of materials at the nm to sub-picometer levels. At first glance, these materials are considered as collection of two or more materials. However, it is noteworthy that the properties of the resulting MFMs are not just the combination of the individual components and the synergistic contribution from the individual components results into high level of functional integration [85]. This leads to the formation of a new hybrid material with redefined performance characteristics. Thus, MFMs are potential candidats to provide specific requirements in many fields through tailored properties. Implementation of such materials in various technically and economically demanding fields is expected to reduce the cost along with the advancements in properties. Hence, the design and related processing technologies of MFMs aiming at the high level of functional integration have attracted recent research interest.

The potentiality of the MFMs promises to open up new avenues in the design of advanced electrocatalyst materials, which is the main focus of PEMFC research today. It is well-known that the performance of an electrocatalyst is determined by many factors like active catalyst size and shape, dispersion of catalyst on support material, surface area of support, catalyst-support interaction, proper mass transfer rate, balanced electron and proton conductivity, ionomer-catalyst-gas pore TPB etc. A careful review on the electrocatalysts reveals that much of the progress in this area considers the above mentioned issues independently. Therefore, the best way to effectively meet the requirements for an efficient ORR electrocatalyst is to design advanced electrode materials based on a logical combination of all the aforementioned parameters. To date, practically these types of multifunctional characteristics are imparted by sequential processes and mostly the stringent experimental conditions lead to the loss of the inherent properties as well [86]. Thus, it is worth mentioning that a method based on a logical combination of all the aforementioned approaches by the proper control of the specific interactions will promote better activity of these materials.

1.5. Scope and Objectives of the Present Thesis

Based on the above critical review of current research activities on PEMFCs, it is apparent that the development of commercially viable PEMFC systems still faces a number of design, performance and affordability related challenges. Electrocatalysts, in particular, demand specific attention as they hold a pivotal role in the PEMFC performance. Hence, a proper understanding on critical factors those are central to decide the final activity is important. Efforts are underway to design novel electrocatalyst materials based on this and in the advent of nanomaterials, the performance has been considerably benefited. However, several lacunae are still present impeding their wide utilization. Thus, the main objective of the present thesis is to open up the immense scope of utilizing both the inner and outer walls of a 1-D carbon nanostructure with peculiar morphological characteristics for the design of new electrocatalysts. Development of a suitable process to utilize both the inner cavity as well as the outer wall, by fine tuning the experimental conditions, is another objective. Finally, detailed characterization of the resulting materials using a host of techniques and the exploration of their electrochemical properties for reactions relevant for PEMFC applications are the other important objectives. The specific objectives of the work embodied in this thesis are set out in this perspective as follows:

1. Design of a new electrocatalyst by utilizing both the inner cavity as well as the outer surface of a hollow CNF, wherein the unusual chemical and electrochemical behaviour of materials confined in nanocavity will be unfolded, resulting into a high performing, thin fuel cell electrodes with a desired level of Pt loading at a minimum carbon content.

2. To synthesize a Pt-RuO_2 bimetallic sandwich type thin layer electrocatalyst possessing the exposed features of Pt by exploiting the greater affinity of Ru towards the oxygen moieties present on the substrate surface.

3. To fine tune the Pt-RuO_2 bimetallic catalyst composition to have the best oxygen reduction activity coupled with enhanced CO tolerance.

4. To understand how important it is to have a clear perceptive on the nature of surface functionalities in the processes involving the dispersion of more than one component on various carbon nanomorphologies to achieve a controlled and predictable assembly of the desired NPs. The study will focus onto to demonstrate the importance of chemical functionalization to effectively fine tune the functionality of hybrid systems composed of more than one components.
5. To develop a novel high aspect ratio electrocatalyst system with unique multifunctional characteristics originated by the presence of proton conducting polymer, polybenzimidazole (PBI-BuI) bound layer and electron conducting hollow CNF with catalytically active Pt NPs decorated along its walls. Specific attention will be given to simultaneously take into account the problems of support surface area, surface reactivity and establishment of a proper triple phase boundary, while ensuring pathways for reactant distribution and product dissipation.
6. Evaluation of the effect of viscosity of the proton conducting polymer (PBI-BuI) in the multifunctional catalyst design.
7. To develop a facile and cost-effective method for the fabrication of a non-Pt electrocatalyst by introducing N-doping along the inner and outer surfaces of CNF by a polymer mediated thermal annealing strategy, using polybenzimidazole as the nitrogen precursor
8. To optimize the PBI-BuI content and the annealing temperature to extract best activity.

1.6. References

1 (a) H. I. Karunadasa, C. J. Chang, J. R. Long, *Nature* **2010**, *464*, 1329. (b) J. Tollefson, *Nature* **2010**, *464*, 1262. (c) J. M. Andujar, F. Segura, *Renew. Sust. Energ. Rev.* **2009**, *13*, 2309. (d) M. S. Dresselhaus, I. L. Thomas, *Nature* **2001**, *414*, 332.

2 J. W. Gosselink, *Int. J. Hydrogen Energ.* **2002**, *27*, 1125.

3 C. F. Schçnbein, *Philos. Mag. J. Sci.* **1839**, *XIV*, 43.

4 W. R. Grove, *Phil. Mag. Ser.* **1839**, *314*, 127.

5 (a) W. Vielstich, A. Lamm, H. A. Gasteiger, *Handbook of Fuel Cells: Fundamentals, Technology, Applications,* Wiley **2003**. (b) L. Carrette, K. A. Friedrich, U. Stimming, "*Fuel Cells – Fundamentals and Applications." Fuel Cells* **2001**, *1*, 5.

6 B. C. H. Steele, A. Heinzel, *Nature* **2001**, *414*, 345.

7 (a) J. Zhang, K. Sasaki, E. Sutter, R. R. Adzic, *Science* **2007**, *315*, 220. (b) V. R. Stamenkovic, B. Fowler, B. S. Mun, G. Wang, P. N. Ross, C. A. Lucas, N. M. Markovic, *Science* **2007**, *315*, 493.

8 J. Wu, H. Yang, *Acc. Chem. Res*. DOI: 10.1021/ar300359w, **2013**.

9 R. Subbaraman, D. Strmcnik, V. Stamenkovic, N. M. Markovic, *J. Phys. Chem. C*. **2010**, *114*, 8414.

10 (a) D. Strmcnik, D. Tripkovic, D. van der Vliet, V. Stamenkovic, N. M. Markovic, *Electrochem.Comm.* **2008**, *10*, 1602. (b) B. E. Conway, B. V. Tilak, *Electrochim. Acta* **2002**, *47*, 3571. (c) K. Domke, E. Herrero, A. Rodes, J. M. Feliu, *J. Electroanal. Chem.* **2003**, *552*, 115. (d) S. L. Chen, A. Kucernak, *J. Phys. Chem. B.* **2004**, *108*, 13984. (e) N. M. Markovic, B. N. Grgur, P. N. Ross, *J. Phys.Chem. B.* **1997**, *101*, 5405. (f) A. F. Innocente, A. C. D. Angelo, *J. Power Sources* **2006**, *162*, 151.

11 (a) J. O. Bockris, *Chem. Rev.* **1948**, *43*, 525. (b) S. Barnartt, *J. Electrochem. Soc.* **1952**, *99*, 549. (c) S. Barnartt, *J. Electrochem. Soc.* **1961**, *108*, 102. (d) G. L. Booman, W. B. Holbrook, *Anal. Chem.* **1963**, *35*, 1793. (e) G. S. Popkirov, *J. Electroanal. Chem.* **1993**, *359*, 97.

12 (a) K. Kordesch, G. Simader, *Fuel Cells and their Applications*, VCH, Veinheim, Germany, **1996**. (b) J. Larminie, A. Dicks, *Fuel Cell Systems Explained*, Wiley, Bognor Regis, **2000**. (c) V. Metha, J. S. Cooper, *J. Power Sources* **2003**, *114*, 32. (d) S. Litster, G. McLean, *J. Power Sources* **2004**, *130*, 61.

13 P. Mock, S. A. Schmid, *J. Power Sources* **2009**, *190*, 133.

14 R. Savinell, E. Yeager, D. Tryk, U. Landau, J. Wainright, D. Weng, K. Lux, M. Litt, C. Rogers, *J. Electrochem. Soc.* **1994**, *141*, L46.

15 A. J. Bard, L. R. Faulkner, *Electrochemical Methods*, Wiley New York, **2001**.

16 O. Antoine, Y. Bultel, R. Durand, *J. Electroanal. Chem.* **2001**, *499*, 85.

17 T. J. Schmidt, U. A. Paulus, H. A. Gasteiger, R. J. Behm, *J. Electroanal. Chem*. **2001**, *508*, 41.

18 (a) W. Yu, M. D. Porosoff, J. G. Chen, *Chem. Rev*. **2012**, *112*, 5780. (b) J. Fournier, G. Lalande, R. Cote, D. Guay, J. P Dodelet, *J. Electrochem. Soc*. **1997**, *144*, 218. (c) F. R. Brushett, M. S. Thorum, N. S. Lioutas, M. S. Naughton, C. Tornow, H. -R. M. Jhong, A. A. Gewirth, P. J. A. Kenis, *J. Am. Chem. Soc*. **2010**, *132*, 12185. (d) M. R. Gao, Q. Gao, J. Jiang, C. H. Cui, W. T. Yao, S. H. Yu, *Angew. Chem. Int. Ed.* **2011**, *50*, 4905. (e) D. V. Esposito, J. G. Chen, *Energ. Environ. Sci.* **2011**, *4*, 3900. (f) B. Wang, *J. Power Sources* **2005,** *152*, 1. (g) S. J. May, K. J. Gasteiger, H. A. Goodenough, J. B. Shao-Horn, Y. *Science* **2011**, *334*, 1383.

19 Z. Shi, J. Zhang, Z. -S. Liu, H. Wang, D. P. Wilkinson, *Electrochim. Acta*. **2006**, *51*, 1905.

20 W. Y. Wonga, W. R. W. Daud, A. B. Mohamad, A. A. H. Kadhum, K. S. Loh, E. H. Majlan, *Int. J. Hydrogen Energ.* **2013**, *38*, 9421.

21 J. Wu, X. Z. Yuan, J. J. Martin, H. Wang, J. Zhang, J. Shen, S. Wu, W. Merida *J. Power Sources* **2008**, *184*, 104.

22 (a) J. K. Norskov, J. Rossmeisl, A. Logadottir, L. Lindquvist, *J. Phy. Chem. B* **2004**, *108*, 17886. (b) V. P. Zhdanov, B. Kasemo, *Electrochem. Commun.* **2006**, *8*, 1132. (c) E. Yeager, M. Razaq, D. Gervasio, A. Razaq, D. Tryk, *Proc. Electrochem. Soc.* **1992**, *440*, 92.

23 T. Li, P. B. Balbuena, *Chem. Phys. Lett.* **2003**, *367*, 439.

24 R. A. Sidik, A. B. Anderson, *J. Electroanal Chem*. **2002**, *528*, 69.

25 A. Stassi, C. D'Urso, V. Baglio, A. D. Blasi, V. Antonucci, A. S. Arico, A. M. Castro Luna, A. Bonesi, W. E. Triaca, *J. Appl. Electrochem.* **2006**, *36*, 1143.

26 J. K. Norskov, J. Rossmeisl, A. Logadotir, L. Lindqvist, J. R. Kitchin, T. Bligaard, H. Jónsson, *J. Phys. Chem. B* **2004**, *108*, 17886.

27 M. K. Debe, *Nature* **2012**, *486*, 43.

28 K. Wikander, H. Ekstrom, A. E. C. Palmqvist, G. Lindbergh, *Electrochim. Acta* **2007**, *52*, 6848.

29 W. Yang, X. L. Wang, F. Yang, C. Yang, X. R. Yang, *Adv. Mater*. **2008**, *20*, 2579.

30 N. Tian, Z. Y. Zhou, S. G. Sun, Y. Ding, Z. L. Wang, *Science* **2007**, *316*, 732.

31 W. Yu, M. D. Porosoff, J. G. Chen, *Chem. Rev*. **2012**, *112*, 5780.

32 (a) K. J. J. Mayrhofer, M. Arenz, *Nat. Chem.* **2009**, *1*, 518. (b) J. K. Norskov, J. Rossmeisl, A. Logadotir, L. Lindqvist, J. R. Kitchin, T. Bligaard, *J. Phys. Chem. B* **2004**, *108*, 17886. (c) J. Wu, L. Qi, H. You, A. Gross, J. Li, H. Yang, *J. Am. Chem. Soc*. **2012**, *134*, 11880.

33 C. Wang, D. van der Vliet, K. C. Chang, H. You, D. Strmcnik, J. Schlueter, N. M. Markovic, V. R. Stamenkovic, *J. Phys. Chem. C* **2009**, *113*, 19365.

34 C. Wang, G. Wang, D. van der Vliet, K. C. Chang, N. M. Markovic, V. R. Stamenkovic, *Phys. Chem. Chem. Phys*. **2010**, *12*, 6933.

35 J. Wu, J. Zhang, Z. Peng, S. Yang, F. T. Wagner, H. Yang, *J. Am. Chem. Soc*. **2010**, *132*, 4984.

36 J. Zhang, H. Yang, J. Fang, S. Zou, *Nano Lett*. **2010**, *10*, 638.

37 (a) P. Liu, J. K. Norskov, *Phys. Chem. Chem. Phys*. **2001**, *3*, 3814. (b) J. L. Zhang, M. B. Vukmirovic, Y. Xu, M. Mavrikakis, R. R. Adzic, *Angew. Chem. Int. Ed*. **2005**, *44*, 2132.

38 (a) K. Gong, D. Su, R. P. Adzic, *J. Am. Chem. Soc*. **2010**, *132*, 14364. (b) J. X. Wang, H. Inada, L. Wu, Y. Zhu, Y. Choi, P. Liu, W. P. Zhou, R. R. Adzic, *J. Am. Chem. Soc*. **2009**, *131*, 17298.

39 V. R. Stamenkovic, B. S. Mun, M. Arenz, K. J. J. Mayrhofer, C. A. Lucas, G. F. Wang, P. N. Ross, N. M. Markovic, *Nat. Mater*. **2007**, *6*, 241. (b) C. Wang, D. van der Vliet, K. L. More, N. J. Zaluzec, S. Peng, S. Sun, H. Daimon, G. Wang, J. Greeley, J. Pearson, A. P. Paulikas, G. D. Karapetrov, Strmcnik, N. M. Markovic, V. R. Stamenkovic, *Nano Lett*. **2010**, *11*, 919.

40 (a) S. Koh, P. Strasser, *J. Am. Chem. Soc*. **2007**, *129*, 12624. (b) P. Strasser, S. Koh, T. Anniyev, J. Greeley, K. More, C. Yu, Z. Liu, S. Kaya, D. Nordlund, H. Ogasawara, M. F. Toney, A. Nilsson, *Nat. Chem*. **2010**, *2*, 454. (c) Srivastava, R. Mani, P. Hahn, N. Strasser, P. *Angew. Chem. Int. Ed.* **2007**, *46*, 8988.

41 Z. M. Peng, H. J. You, H. Yang, *Adv. Funct. Mater*. **2010**, *20*, 3734.

42 B. Lim, M. J. Jiang, P. H. C. Camargo, E. C. Cho, J. Tao, X. M. Lu, Y. M. Zhu, Y. N. Xia, *Science* **2009**, *324*, 1302.

43 R. Othman, A. L. Dicks, Z. Zhu, *Int. J. Hydogen Energ*. **2012**, *37*, 357.

44 R. Jasinski, *Nature* **1964**, *201*, 1212.

45 (a) M. Lefevre, E. Proietti, F. Jaouen, J. P. Dodelet, *Science* **2009**, *324*, 71. (b) E. Proietti, F. Jaouen, M. Lefèvre, N. Larouche, J. Tian, J.Herranz, J. P. Dodelet, *Nat. Commun*. **2011**, *2*, 416.

46 G. Wu, K. L. More, C. M. Johnston, P. Zelenay, *Science* **2011**, *332*, 443.

47 (a) R. Liu, D. Wu, X. Feng, K. Mullen, *Angew. Chem. Int. Ed*. **2010**, *49*, 2565. (b) W. Y. Wong, W. R. W. Daud, A. B. Mohamad, A. A. H. Kadhum, K. S. Loh, E. H. Majlan, *Int. J. Hydogen Energ.*, **2013**, *38*, 9370.

48 K. P. Gong, F. Du, Z. H. Xia, M. Durstock, L. M. Dai, *Science* **2009**, *323*, 760.

49 (a) S. Wang, D. Yu, L. Dai, D. W. Chang, J.-B. Baek, *ACS Nano* **2011**, *5*, 6202. (b) S. Wang , E. Iyyamperumal , A. Roy, Y. Xue, D. Yu, L. Dai, *Angew. Chem. Int. Ed.* **2011**, *50*, 11756.

50 Y. Y. Shao, S. Zhang, M. H. Engelhard, G. S. Li, G. C. Shao, Y. Wang, J. Liu, I. A. Aksay, Y. H. Lin, *J. Mater. Chem*. **2010**, *20,* 7491.

51 Y. Li, W. Zhou, H. Wang, L. Xie, Y. Liang, F. Wei, J.-C. Idrobo, S. J. Pennycook, H. Dai, *Nat. Nanotechnol*. **2012**, *7*, 394.

52 (a) B. R. Wang, *J. Power Sources* **2005**, *152*,1. (b) L. Yang, S. Jiang, Y. Zhao, L. Zhu, S. Chen, X. Wang, Q. Wu, J. Ma, Y. Ma, Z. Hu, *Angew. Chem. Int. Ed*. **2011**, *50*, 7132. (c) Z. -W. Liu, F. Peng, H. Wang, H. Yu, W. Zheng, J. Yang, *Angew. Chem. Int. Ed*. **2011**, *50*, 3257. (d) Z. Yang, Z. Yao, G. Li, G. Fang, H. Nie, Z. Liu, X. Zhou, X. Chen, S. Huang, *ACS Nano* **2012**, *6*, 205.

53 H. Chang, S. H. Joo, C. Pak, *J. Mater. Chem*. **2007**, *17*, 3078.

54 K. Chan, J. Ding, J. Ren, S. Cheng, K. Y. Tsang, *J. Mater. Chem*. **2004**, *14*, 505.

55 (a) C. N. R. Rao, B. C. Satishkumar, A. Govindaraj, M. Nath, *Chem. Phys. Chem*. **2001,** *2*, 78. (b). K. P. de Jong, J. W. Geus, *Catal. Rev. Sci. Eng*. **2000**, *42*, 482. (c) R. Ryoo, S. H. Joo, *Stud. Surf. Sci. Catal*. **2004**, *148*, 241. (d) J. Lee, S. Han, T. Hyeon, *J. Mater. Chem*. **2004**, *14*, 478. (e) H. Yang, D. Zhao, *J. Mater. Chem*. **2005**, *15*, 1217. (f) A. H. Lu, F. Schu¨th, *Adv. Mater*. **2006**, *18*, 1793.

56 J. J. Wang, G. P. Yin, Y. Y. Shao, S. Zhang, Z. B. Wang, Y. Z. Gao, *J. Power Sources* **2007**, *171*, 331.

57 (a) S. D. Thompthon, L. R. Jordan, M. Forsyth, *Electrochim. Acta*. **2001**, *46*, 1657. (b) T. Matsumoto, T. Komatsu, K. Arai, T. Yamazaki, M. Kijima, H. Shimizu, Y. Takasawa, J. Nakamura, *Chem. Commun*. **2004**, 840.

58 (a) C. D. Liang, S. Dai, *J. Am. Chem. Soc*. **2006**, *128*, 5316. (b) X. J. Bo, L. D. Zhu, G. Wang, L. P. Guo, *J. Mater. Chem.* **2012**, *22*, 5758.

59 (a) Z. H. Wen, J. Liu, J. H. Li, *Adv. Mater*. **2008**, *20*, 743. (b) X. Ji, K. T. Lee, R. Holden, L. Zhang, J. Zhang, G. A. Botton, M. Couillard, L. F. Nazar, *Nat. Chem.* **2010**, *2*, 286. (c) F. Su, J. Zeng, X. Bao, Y. Yu, J. Y. Lee, X. S. Zhao, *Chem. Mater*. **2005**, *17*, 3960. (d) P. V. Shanahan, L. Xu, C. Liang, M. Waje, S. Dai, Y. S. Yan, *J. Power Sources* **2008**, *185*, 423.

(e) D. Xiang, L. W. Yin, *J. Mater. Chem*. **2012**, *22*, 9584. (f) W.C. Choi, S. I. Woo, M. K. Jeon, J. M. Sohn, M. R. Kim, H. J. Jeon, *Adv. Mater*. **2005**, *17*, 446.

60 Y. Y. Shao, S. Zhang, R. Kou, X. Q. Wang, C. M. Wang, S. Dai, V. Viswanathan, J. Liu, Y. Wang, Y. H. Lin, *J. Power Sources*. **2010**, *195*, 1805.

61 (a) D. Tasis, N. Tagmatarchis, A. Bianco, M. Prato, *Chem. Rev*. **2006**, *106*, 1105. (b) Y. P. Sun, K. Fu, Y. Lin, W. Huang, *Acc. Chem. Res*. **2002**, *35*, 1096.

62 (a) Y. A. Kim, H. Muramatsu, T. Hayashi, M. Endo, M. Terrones, M. S. Dresselhaus, *Chem. Phys. Lett.* **2004**, *398*, 87. (b) K. Liu, W. Wang, Z. Xu, X. Bai, E. Wang, Y. Yao, J. Zhang, Z. Liu, *J. Am. Chem. Soc*. **2009**, *131*, 62. (c) B. Peng, M. Locascio, P. Zapol, S. Li, S. L. Mielke, G. C. Schatz, H. D. Espinosa, *Nat. Nanotechnol*. **2008**, *3*, 626. (d) Brozena, A. H. Moskowitz, J. Shao, B. Deng, S. Liao, H. Gaskell, K. J. Wang, Y. *J. Am. Chem. Soc*. **2010**, *132*, 3932.

63 (a) Y. Y. Shao, G. P. Yin, J. Zhang, Y. Z. Gao, *Electrochim. Acta* **2006**, *51*, 5853. (b) W. Z. Li, C. H. Liang, W. J. Zhou, J. S. Qiu, Z. H. Zhou, G. Q. Sun, Q. Xin, *J. Phys. Chem. B* **2003**, *107*, 6292. (c) Y. Y. Shao, G. P. Yin, H. H. Wang, Y. Z. Gao, P. F. Shi, *J. Power Sources* **2006**, *161*, 47. (d) S. Y. Wang, X. Wang, S. P. Jiang, *Langmuir* **2008**, *24*, 10505. (e) S. Zhang, Y. Shao, Y. Gao, G. Chen, Y. Lin, G. Yin, *J. Power Sources* **2011**, *196*, 9955. (f) D. C. Higgins, J. Y. Choi, J. Wu, A. Lopez, Z. W. Chen, *J. Mater. Chem*. **2012**, *22*, 3727.

64 S. Zhang, Y. Shao, G. Yin, Y. Lin, *J. Mater. Chem. A* **2013**, *1*, 4631.

65 (a) W. Li, X. Wang, Z. Chen, M. Waje, Y. Yan, *Langmuir* **2005**, *21*, 9386. (b) C. Wang, M. Waje, X. Wang, J. M. Tang, R. C. Haddon, Y. Yan, *Nano Lett*. **2004**, *4*, 345.

66 J. M.Tang, K. Jensen, M. Waje, W. Li, P. Larsen, K. Pauley, Z. Chen, P. Ramesh, M. E. Itkis, Y. Yan, R. C. Haddon, *J. Phys. Chem. C* **2007**, *111*, 17901.

67 J. Kim, S. W. Lee, C. Carlton, Y. Shao-Horn, *J. Phys. Chem. Lett.* **2011**, *2*, 1332.

68 T. V. Hughes, C. R. Chambers, *U. S. Patent* **1889**, *405*, 480.

69 V. Vamvakaki, K. Tsagaraki, N. Chaniotakis, *Anal. Chem*. **2006**, *78*, 5538. (b) J. Huang, Y. Liu, T. You, *Anal. Methods* **2010**, *2*, 202.

70 K. Lee, J. Zhang, H. Wang, D. P. Wilkinson, *J. Appl. Electrochem*. **2006**, *36*, 507.

71 S. -U. Kim, K. -H. Lee, *Chem. Phys. Lett.* **2004**, *400*, 253.

72 P. Serp, M. Corrias, P. Kalck, *Appl. Catal. A* **2003**, *253*, 337.

73 M. Endo, Y. A. Kim, T. Hayashi, Y. Fukai, K. Oshida, M. Terrones, T. Yanagisawa, S. Higaki, M. S. Dresselhaus, *Appl. Phys. Lett*. **2002**, *80*, 1267. (b) C. Park, P. E. Anderson, A. Chambers, C. D. Tan, R. Hidalgo, N. M. Rodriguez, *J. Phys. Chem. B* **1999**, *103*, 10572. (c) H. Terrones, T. Hayashi, M. Muñoz-Navia, M. Terrones, Y. A. Kim, N. Grobert, R. Kamalakaran, J. Dorantes-Dávila, R. Escudero, M. S. Dresselhaus, M. Endo, *Chem. Phys. Lett.* **2001,** *343,* 241. (d) W. C. Ren, H. M. Cheng, *Carbon* **2002**, *41*, 1645.

74 M. Endo, Y. A. Kim, M. Ezaka, K. Osada, T. Yanagisawa, T. Hayashi, M. Terrones, M. S. Dresselhaus, *Nano Lett*. **2003**, *3*, 723.

75 F. Alcaide, G. Álvarez , O. Miguel, M. J. Lázaro, R. Moliner, A. López-Cudero, J. Solla-Gullón, E. Herrero, A. Aldaz, *Electrochem. Commun.* **2009**, *11*, 1081.

76 (a) A. K. Geim, *Angew. Chem. Int. Ed*. **2011**, *50*, 2. (b) K. S. Novoselov, A. K. Geim, S. V. Morozov, D. Jiang, Y. Zhang, S. V. Dubonos, I. V. Grigorieva, A. A. Firsov, *Science* **2004**, *306*, 666.

77 (a) X. Huang, X. Qi, F. Boey, H. Zhang, *Chem. Soc. Rev.* **2012**, *41,* 666. (b) N. G. Sahoo , Y. Pan , L. Li , S. H. Chan, *Adv. Mater*. **2012**, *24*, 4203.

78 (a) E. Yoo, T. Okata, T. Akita, M. Kohyama, J. Nakamura, I. Honma, *Nano Lett*. **2009**, *9*, 2255. (b) Y. Y. Shao, S. Zhang, C. M. Wang, Z. M. Nie, J. Liu, Y. Wang, Y. H. Lin, *J. Power Sources* **2010**, *195*, 4600. (c) S. Mayavan, J. -B. Sim, S. -M. Choi, *J. Mater. Chem*. **2012**, *22*, 6953. (d) Z. Luo, L. Yuwen, B. Bao, J. Tian, X. Zhu, L. Weng, L. Wang, **2012**, *22*,

7791. (e) R. Kou, Y. Y. Shao, D. H. Wang, M. H. Engelhard, J. H. Kwak, J. Wang, V. V. Viswanathan, C. M. Wang, Y. H. Lin, Y. Wang, I. A. Aksay, J. Liu, *Electrochem. Commun.* **2009**, *11*, 954. (f) S. Zhang, Y. Shao, H. Liao, M. H. Engelhard, G. Yin, Y. Lin, *ACS Nano* **2011**, *5*, 1785. (g) S. Zhang, Y. Shao, H.-G. Liao, J. Liu, I. A. Aksay, G. Yin, Y. Lin, *Chem. Mater*. **2011**, *23*, 1079. (h) Y. Li, Y. Li, E. Zhu, T. McLouth, C.-Y. Chiu, X. Huang, Y. Huang, *J. Am. Chem. Soc*. **2012**, 12326.

79 (a) D. Kasuya, M. Yudasaka, K. Takahashi, F. Kokai, S. Iijima, *J. Phys. Chem. B* **2002**, *106*, 4947. (b) T. Yoshitake, Y. Shimakawa, S. Kuroshima, H. Kimura, T. Ichihashi, Y. Kudo, D. Kasuya, K. Takahashi, F. Kokai, M. Yudasaka, S. Iijima, *Physica B* **2002**, *323*, 124.

80 X. Chen, S. Zhang, D. A. Dikin, W. Ding, R. S. Ruoff, L. Pan, Y. Nakayama, *Nano. Lett.* **2003**, *3*, 1299.

81 (a) A. N. Khlobystov, D. A. Britz, G. A. D. Briggs, *Acc. Chem. Res.* **2005**, *38*, 901. (b) J. Sloan, A. I. Kirkland, J. L. Hutchison, M. L. H. Green, *Acc. Chem. Res*. **2002**, *35*, 1054.

82 M. Smeu, F. Zahid, W. Ji, H. Guo, M. Jaidann, H. A. -Rachid, *J. Phys. Chem. C* **2011**, *115*, 10985.

83 V. V. Chaban, O. V. Prezhdo, *ACS Nano* **2011**, *5*, 5647.

84 S. H. Joo, C. Pak, D. J. You, S. A. Lee, H. I. Lee, J. M. Kim, H. Chang, D. Seung, *Electrochim. Acta* **2006**, *52*, 1618.

85 (a) P. Judeinstein, C. Sanchez, *J. Mater. Chem.* **1996**, *6*, 511. (b) G. Schottner, *Chem. Mater.* **2001**, *13*, 3422.

86 E. H. Lock, W. M. Merchan, J. D’Arcy, A. V. Saveliev, L. A. Kennedy, *J. Phys. Chem. C* **2007**, *111*, 13655.

Chapter 2

Experimental Methods and Characterization Techniques

This chapter presents a brief description of various synthesis methods used in this work. This follows with the discussion on various experimental techniques employed for the characterization of materials, which includes a detailed study of the morphology, structure, electrochemical properties, etc. In the present work, a modified polyol process was adopted for the synthesis of electrocatalysts with the selective decoration of active catalyst nanoparticles both in the inner cavity as well as on the outer surfaces of a hollow CNF support. The components which govern the characteristic properties of the electrocatalysts under study are characterized as accurately and as broadly as possible, in order to better understand their origin and particular features.

2.1. Experimental Section

2.1.1. Materials

CNF was purchased from Pyrograf Products, Inc., USA. Chloroplatinic acid hexahydrate (H_2PtCl_6), ruthenium chloride ($RuCl_3$), potassium hydroxide (KOH), 5-tert-butyl isophthalic acid (BuI) and 3,3'-diaminobenzidine (DAB) were purchased from Aldrich Chemicals. Polyphosphoric acid (PPA) was purchased from Alfa Aesar. Ethylene glycol (EG), N,N-dimethyl acetamide (DMAc) and sulfuric acid (H_2SO_4) were obtained from Rankem Chemicals. All the chemicals were of analytical grade and used as received without any further purification. A poly (tetrafluoroethylene) (PTFE) filter paper (pore size, 0.45 μm) procured from Rankem was used for the filtration. For the preparation of all solutions for the study, deionized water (DI) obtained from the milli Q system was used.

2.1.2. Functionalization of Carbon Supports

For the functionalization of the carbon supports such as CNT and CNF, H_2O_2 treatment was used. In the typical synthesis, 1 g of the carbon support material was dispersed well in 200 mL of 30% H_2O_2 solution by ultrasonication for 10-15 min. This was then refluxed at a temperature of 50-60 $^{\circ}$C for 5 h. Subsequently, the mixture was filtered, washed with DI water and dried at 100 $^{\circ}$C for 5 h. CNTs and CNFs after the functionalization are designated as FCNTs and FCNFs respectively.

2.1.3. Synthesis of Electrocatalysts by Conventional Polyol Process

In the conventional polyol process, EG was used as the solvent as well as the reducing agent. For the preparation of the electrocatalyst, the required amount of support material (CNF, FCNF, and FCNT) was dispersed well in the solvent by ultrasonication prior to the addition of the active catalyst (Pt, Ru) precursor. In the next step, the precursor dissolved in the same solvent, was added drop by drop with stirring. Subsequently, the mixture was kept for stirring for 5 h at ambient temperature to achieve well dispersion of the components in the mixture. Following this aging process, the mixture was heated up to 140 ºC for 8 h to ensure complete reduction of the precursor ions. The reaction mixture was then cooled and filtered through the filter paper. The wet cake was washed repeatedly with hot water and then with acetone to remove excess solvent. Finally, a few more washings with DI water were performed, and the product was dried at 100 ºC for 5-6 h.

2.1.4. Synthesis of Electrocatalysts by Modified Polyol Process

To facilitate the decoration of the active catalyst NPs along the inner cavity as well as the outer surface of the FCNF, a modified polyol process was adopted. In the modified process, the solvent used was 3:2 v/v mixture of EG and H_2O. This process modification is important for the simultaneous metal ion dispersion and reduction along both the walls of FCNFs because of the peculiar morphology and contrasting differences in the activity characteristics of the inner and outer walls. When EG was used instead of the EG-water mixture, the solvent filling into the tube by capillary action is impeded, leading to the non utilization of the inner wall for NP dispersion. It may be attributed to the high viscosity of the solvent. Both the surface tension of the medium and the contact angle between the liquid and surface play a decisive role to achieve fine metal particle dispersion along the inner wall by significantly eliminating the possibilities of channel blocking which can be caused by any entrapped particles or their aggregates. Thus, by an appropriate manipulation of the polyol to water ratio, the capillary action by the tubes can be properly utilized to suck the solution into the channels of the support material.

For the preparation of the active catalyst loaded carbon material, the required amount of support material (CNF, FCNF, and FCNT) was dispersed well in the solvent mixture by ultrasonication prior to the addition of the Pt precursor. In the next step, the precursor dissolved in the same solvent mixture was added drop by drop with stirring. Subsequently, the mixture was kept stirring for 5 h at ambient temperature to achieve well dispersion of the components in the mixture. Especially in case of CNFs and FCNFs, this aging time is important because the precursor solution has to be reached inside the tubes of the support material. Following this aging process, the mixture was heated up to 140 °C for 8 h to ensure complete reduction of Pt ions. The reaction mixture was then cooled and filtered though the filter paper. The wet cake was washed repeatedly with hot water and subsequently with acetone to remove excess solvent. Finally, a few more washings with DI water were performed, and the product was dried at 100 °C for 5-6 h.

2.1.5. Synthesis of Bimetallic Electrocatalysts by Modified Polyol Process

All the bimetallic catalysts with required active catalyst loading were prepared using the co-reduction of the respective precursors using the modified polyol process. Initially, the FCNFs were dispersed well in an EG-water mixture. In the next step, calculated amount of both the precursors dissolved in the same solvent mixture was added drop by drop with stirring. Sufficient aging time was given for the precursor ions for adsorption on the FCNFs and their reorganization. Following this aging process, the reaction mixture was heated up to 140 °C for 8 h to ensure complete reduction of ions. The reaction mixture was then cooled and filtered though the filter paper. The mixture was then cooled and filtered though the PTFE filter paper. The wet cake was washed repeatedly with hot water and subsequently with acetone to remove excess solvent. Finally, a few more washings with DI water were performed, and the product was dried at 100 °C for 5-6 h.

2.1.6. Synthesis of Poly(benzimidazole)

Poly(benzimidazole) (PBI-BuI) of varying molecular weights were synthesized by systematically changing the conditions of the solution polycondensation reaction of DAB and BuI using PPA as the solvent as given in Table 2.1.

Table 2.1. Effect of reaction parameters in PBI-BuI synthesis

Designation of PBI	**DAB:PPA Ratio**	**DAB:BuI Ratio**	**At 170 °C (h)**	**At 210 °C (h)**	**Inherent Viscosity**
PBI-BuI$_{0.4}$	1:50	1:1.1	5	14	0.4
PBI-BuI$_{0.6}$	1:40	1:1.1	5	14	0.6
PBI-BuI$_{0.8}$	1:20	1:1.1	5	14	0.8
PBI-BuI$_{1.5}$	1:25	1:1	5	5	1.5

In a typical procedure, a three-necked flask equipped with a mechanical stirrer, N_2 inlet and $CaCl_2$ drying tube was charged with 10 g (0.0467 mol) of DAB and the corresponding amount of PPA, as given in Table 1. The temperature was elevated to 140 ºC. After complete dissolution of DAB, either 1.0 or 1.1 equivalent of BuI was added. Thereafter, the temperature of the mixture was slowly raised to 170 ºC and was maintained for 5 h under a constant flow of N_2. The temperature was further raised to 200 ºC and then maintained for the stipulated time as given in Table 2.1. After completion of the reaction, the temperature was lowered and the highly viscous reaction mixture was poured onto the stirred water. The precipitated polymer was crushed and thoroughly washed with water until a neutral pH was reached. The polymer was then kept overnight in 10% aqueous $NaHCO_3$, washed with water until a neutral pH was reached and soaked in methanol for 8 h to extract the water. Dried polymer (100 ºC, 3 days) was further purified by dissolving in DMAc to get a 3 wt% solution, removing undissolved material, if any, by centrifugation at 3000 rpm for 3 h and reprecipitation onto the stirred water. The polymer was kept in methanol for 8 h, filtered, dried at 60 ºC for 24 h and then dried in a vacuum oven at 100ºC for a week. The inherent viscosity (η_{inh}) was determined using 0.2 g/dL of PBI-BuI solution in concentrated H_2SO_4 at 35 ºC.

2.1.7. PBI-BuI Incorporation in CNF and/or Electrocatalysts

A 0.5 wt% solution of the PBI-BuI was prepared by dissolving the calculated amount of the polymer in DMAc. For the incorporation of the polymer, 5 mg of the material (CNF or electrocatalyst) was added to the required volume of the polymer solution. The mixture was then subjected to sonication for 15 min in a bath type sonicator to initiate the PBI-BuI entry into the inner cavity. In the next step, the mixture was kept stirring for 10 h at RT to ensure a homogeneous coverage in the tubular region and along the outer surfaces of the substrate. The same procedure was repeated for the incorporation of PBI-BuI at various PBI/carbon (P/C) ratios also. Phosphoric acid doping was achieved by dipping the electrodes in ortho-phosphoric acid for 24 h. The electrodes were subsequently dried in a vacuum oven at 100 ºC for 48 h.

2.1.8. Electrode Preparation

For the preparation of the working electrode (WE), a glassy carbon (GC) electrode was polished to a mirror finish using 0.3 and 0.05 μm alumina powder. After that, the electrode was washed several times with DI water and ethanol. The WE was prepared as follows: 10 μL aliquot of the slurry made by sonicating 1 mg of the catalyst in 1 mL isopropyl alcohol was drop-coated on the GC electrode. After this, 2 μL of 0.01 wt% Nafion diluted with ethanol was coated on the surface of the catalyst layer to yield a uniform thin film. This electrode was then dried in air and was used as the WE for electrochemical studies.

For the preparation of the WE of PBI-BuI incorporated samples, a 10 μL aliquot of the catalyst ink prepared by dispersing 5mg of the as prepared catalysts in 1mL of the 0.5 wt% PBI-BuI solution in DMAc was drop-coated onto the polished GC electrode surface. After drying, it was dipped in 10 mL of polyphosphoric acid to ensure the doping of PBI-BuI. To record CV with Nafion as the binder for comparing with PBI-BuI incorporated samples, 5 mg of the catalyst material was dispersed in 1 mL DMAc solution and 10 μL was coated on the electrode surface. After drying, 2 μL of the 0.01 wt% Nafion solution was applied on the catalyst layer to ensure better adhesion of the catalyst on the glassy carbon substrate. This electrode was then dried under ambient conditions and was used for the analysis.

2.2. Materials Characterization Techniques

2.2.1. Powder X-Ray Diffraction

Powder X-Ray diffraction (XRD) is the most important and non-destructive analytical technique used for the identification and quantitative determination of the various crystalline compounds in the field of solid state chemistry [1]. When a monochromatic X-ray beam with wavelength 'λ' is projected onto a crystalline material at an angle 'θ', diffraction occurs only when the distance travelled by the rays reflected from successive planes differs by a complete number 'n' of wavelengths. The incident X-radiation strikes the planes (hkl) at an angle 'θ'. The spacing between these planes is 'd'. Relationship between the wavelength 'λ' of the X-ray beam, the angle of diffraction 'θ' and the distance between each set of planes separated with spacing 'd' is given by the Bragg equation:

$$n\lambda = 2d\sin\theta \qquad (2.1)$$

where `n' is the order of the diffraction, 'd' is the spacing between two adjacent lattice planes, 'λ' is the wave length of the X-ray and 'θ' is known as the diffraction angle or Bragg's angle. Figure 2.1 shows incident X-ray beam interacting with the atoms in the two different planes. Therefore, measuring the diffraction pattern allows one to deduce the distribution of atoms in a material and each crystalline solid has its unique characteristic X-ray powder pattern, which may be used as a "fingerprint" for its identification [2]. Thus, this technique gives information on the phase and purity, degree of crystallinity and unit cell parameters of the crystalline materials [2].

It is well known that the width of a diffraction peak increases when the crystallite size is reduced below a certain limit (< 100 nm). Therefore, XRD patterns can be used to estimate the average size of very small crystallites, from the measured width of the peaks in the diffraction patterns. The commonly accepted formula for the determination of crystallite size from XRD line broadening is the Scherrer formula [1]:

$$t = 0.9\lambda/\beta cos\theta \qquad (2.2)$$

where 'λ' the wavelength of X-ray, 'β' is full width at half maximum of the pattern, and 'θ' is the Bragg angle. 'β' is corrected for contribution from instrument line broadening by recording the pattern of a standard sample having very large particle size in the micrometer range. In addition to the calculation of the grain size using the Scherrer equation, the technique can be effectively used in determining the strain and stress induced in the nanostructures. However, a key disadvantage of XRD is that it is highly applicable to crystalline materials. Moreover, it is time-consuming and the analysis requires a large quantity of sample.

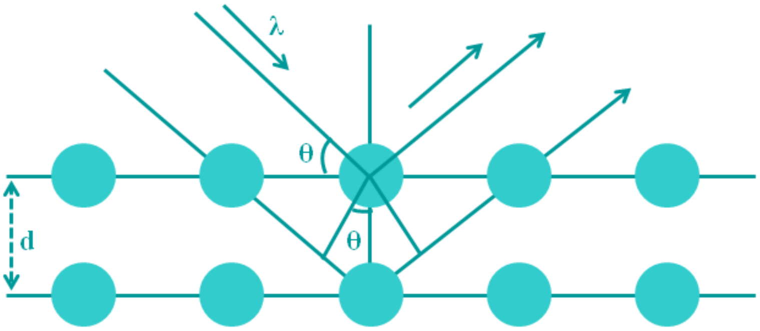

Figure 2.1. Schematic illustration of X-ray reflections from a crystal.

In the present study, XRD analysis of the samples was carried out using a Philips PW 1830 and Panalytical X‟pert Pro diffractometers, using Ni filtered Cu Kα radiation. The wavelength of Cu Kα radiation is 1.5418 Ǻ. The diffractometer was calibrated with reference to standard Si wafer. For the general phase analysis the scan rate used was 10^{o} /minute.

2.2.2. Scanning Electron Microscopy and Energy Dispersive X-ray Analysis

Scanning electron microscopy (SEM) is one of the most widely used techniques for the direct observations of surfaces especially for the characterization of nanomaterials and nanostructures as they offer better resolution and depth of field than optical microscope. The resolution of the SEM approaches a few nanometres, and the instruments can operate at magnifications that are easily adjusted from ~10 to over 300,000. This technique provides topographical information as well as the chemical composition near the surface. A scanning electron microscope can generate an electron beam scanning back and forth over a solid sample. Generally, tungsten or lanthanum hexaboride (LaB_6) thermionic emitters are used as electron gun; alternatively electrons can be emitted *via* field emission (FE) [3].

The interaction between the beam and the sample produces different types of signals providing detailed information about the surface structure and morphology of the sample. The two signals most often used to produce SEM images are secondary electrons (SE) and backscattered electrons (BSE). Most of the electrons are scattered at large angles (from 0 to 180º) when they interact with the positively charged nucleus. Since the scattering angle depends on the atomic number of the nucleus, the primary electrons arriving at a given detector position can be used to produce images containing topological and compositional information [4]. These electrons are detected by a scintillator-photomultiplier device and the resulting signal is rendered into a 2-D intensity distribution that can be viewed and saved as a digital image. Characteristic X-rays, which are also produced by the interaction of electrons with the sample, can also be detected in an SEM if it is equipped for energy dispersive X-ray spectroscopy (EDX) or wavelength dispersive X-ray spectroscopy (EDS). These X-rays are characteristic of the sample and this type of analysis is known as Energy Dispersive analysis of X-rays (EDAX). Despite these advantages, SEM coupled with EDAX has some drawbacks as well: elements below C in the periodic table cannot be detected and this technique cannot be used for precise detection of elements below Na. Moreover, X-ray detection limit is ~ 0.1% depending on the element and samples must be compatible with vacuum.

In the present work, SEM imaging coupled with EDAX and elemental mapping were performed on an FEI, Model Quanta 200 3D instrument equipped with Phoenix energy dispersive spectral analysis setup at an operating potential of 30 kV. For SEM imaging, a small amount of the sample was dispersed well in ethanol by ultrasonication and was mounted on Cu stubs. For comparative studies, the energy of the electron beam was kept constant while analyzing all the samples.

2.2.3. Transmission Electron Microscopy, High-resolution Transmission Electron Microscopy and Selected Area Electron Diffraction

Transmission electron microscopy (TEM) is one of the most powerful and versatile techniques for high resolution imaging of thin sections of solid samples for nanostructural and compositional analysis. Virtually, TEM is useful for determining size, shape and arrangement of the particles which make up the specimen [5]. However, high resolution TEM (HRTEM) provides atomic resolution lattice images as well as chemical information at a spatial resolution of 1 nm or better, allowing direct identification of the chemistry of single nanocrystal [6]. TEM operates on the same basic principles as the light microscope but uses electrons instead of light. In TEM, a thin specimen is illuminated with electrons in which the electron intensity is uniform over the illuminated area [5]. Here, electrons are being used because electrons are smaller than atoms and therefore, it is possible to see details at the atomic level. As electrons travel through the specimen, they are either scattered by a variety of processes or they may remain unaffected. The net result is that a non-uniform distribution of electrons emerges from the exit surface of the specimen that contains all the structural information about the specimen. This non-uniform distribution of electrons results into angular distribution of scattering which can be viewed in the form of scattering patterns usually referred to as diffraction patterns or selected area electron diffraction (SAED). There will be a coherent scattering as a result of elastic scattering occurring from well ordered arrangements of atoms in a crystal. The resultant coherent scattering will give spot patterns in case of single crystals and ring patterns for polycrystalline materials. Spatial distribution of scattering can also be observed as contrast in images of the specimen.

TEM is a unique characterizing tool for the *in-situ* analysis of nanomaterials. Moreover, it is also useful to investigate the faceting, crystallinity and ordering in NCs [7]. Thus TEM coupled with SAED can provide important information on the crystallographic directions in the structures and helpful to understand the growth kinetics [8]. However, despite these advantages, many materials require extensive sample preparation and thinning procedures to make the sample electron transparent, which may result into structural changes. Moreover, the field of view is relatively small, raising the possibility that the region analysed may not be characteristic of the whole sample. Also there is possibility of sample damaging by the electron beam, particularly in the case of biological materials.

In the present work, TEM images were taken by a TECNAI-T 30 model instrument operated at an accelerating voltage of 300 kV and HRTEM analysis was performed using a FEI model TECNAI G2 F30 instrument operating at an accelerating voltage of 300 kV (Cs= 0.6 mm, resolution 1.7 A°). Samples for TEM and HRTEM imaging were prepared by placing a drop of the sample in isopropanol onto a carbon-coated Cu grid (3 nm thick, deposited on a commercial copper grid for electron microscopy), dried in air and loaded into the electron microscopic chamber.

2.2.4. X-Ray Photoelectron Spectroscopy

X-Ray Photoelectron Spectroscopy (XPS) is a surface sensitive technique which has been widely used to characterize materials to get information about the elemental status, nature of interaction with the surroundings through the surface and the physical and chemical composition of these surfaces [9]. XPS is based on the principle of photoelectric effect, emission of electron when X-rays incident on a solid surface [10]. In XPS, the photon is absorbed by an atom in a molecule or solid, leading to ionization and the emission of a core (inner shell) electron. The kinetic energy distribution of the emitted photoelectrons can be measured; from the binding energies (BEs), which depend on the element, one can characterize the materials. Equation 2.3 gives the relationship between the parameters involved in the XPS measurement:

$$KE = h\nu - BE - \varphi \qquad (2.3)$$

where KE, is the kinetic energy of the photo electron, hν is the photon energy, BE is the binding energy of the electron and ‘φ’ is the work function of the solid. Thus, by employing photons with fixed energy hν, and if kinetic energy KE and work function ‘φ’ of the sample are measured, it is possible to measure BE of electron in a solid. BEs being characteristic of atoms, different elements present in the sample under investigation can be easily identified. In addition to this, chemical information can be obtained from the shift in BEs which depends on the chemical bonding of the elements under investigation.

Electrons travelling through a material have a relatively high probability of experiencing inelastic collisions with locally bound electrons as a result of which, they suffer energy loss contributing to the background of the spectrum rather than a specific peak. Due to this inelastic scattering process, the flux of photoelectrons emerging from the sample is much attenuated. Consequently, in some cases the satellite peaks emerge on both the high and low BE side of the main peaks. These peaks give valuable information about the defect complex or the different charge states present, if any. Thus, significant qualitative and quantitative information about the chemical state of elements present in various materials can be obtained from XPS analysis. Apart from this, XPS is a versatile *in-situ* analysis tool for understanding the growth kinetics. However, many limitations are associated with this technique. First, high vacuum condition is needed to run these experiments and hence samples must be dried properly. Sometimes, this drying may impact few subtle systems resulting in many chemical transformations in the sample. Beam-induced damage and carbon contamination from XPS chamber are few other limitations of XPS.

In this work, XPS measurements were carried out on a VG MicroTech ESCA 3000 instrument at a pressure of >1 × 10^{-9} Torr (pass energy of 50 eV; electron takeoff angle 60°) using monochromatic Mg Kα (source, $h\nu$ =1253.6 eV). The overall resolution of the instrument was ~1 eV. Alignment of the BE was carried out using an Au_{4f} BE of 84 eV as the reference. The BE of the C1s peak was fixed to 284.5 eV, and all peaks were calibrated with reference to this graphitic C1s peak. The background was subtracted by the Shirley method. The spectra were fitted using a combined polynomial and Shirley-type background function.

2.2.5. Thermogravimetry and Differential Thermal Analysis

In termogravimetric analysis (TGA) the weight change of a material is monitored as a function of temperature at a controlled rate [11]. Information about any weight changes associated with thermally induced transformations can be obtained from TGA. The loss of weight as a function of temperature is the characteristic features of a material since there will be physical and chemical changes over a wide temperature range. Differential thermal analysis (DTA) involves comparing the precise temperature difference between a sample and an inert reference material, while heating both [11].

Thermogravimetric curves (thermograms) provide information regarding the thermal stability, desorption, absorption, sublimation, vaporization, oxidation, reduction and decomposition of materials under a variety of conditions [12]. Moreover, thermal stability of many materials in presence of moisture, solvent, additives, polymer, filler etc. can be studied along with the kinetics. On the other hand, varied information can be obtained from the DTA namely glass transitions/melting temperatures, phase formations/transitions and reaction kinetics. Interestingly, thermal events under both reactive (e.g. air) and inert conditions (e.g. nitrogen, helium and argon) can be investigated. Thus, valuable information about the growth mechanism of the nanomaterials could be obtained from the TG-DTA when coupled with other suitable analytical tools.

In this work, TGA was performed on a SDT Q600 TG-DTA analyzer and Shimadzu: DTG-60 instrument at a heating rate of 10 ºC/min under normal atmospheric conditions.

2.2.6. Raman Spectroscopy

Raman spectroscopy is a powerful tool to analyze structural, morphological and electronic properties of materials at a local level [13]. When light encounters molecules in air, the predominant mode of scattering is elastic scattering, called Rayleigh scattering [14]. It is also possible for the incident photons to interact with the molecules in such a way that energy is either gained or lost so that the scattered photons are shifted in frequency. Such inelastic scattering is called Raman scattering. Like Rayleigh scattering, the Raman scattering depends upon the polarizability of the molecules. For polarizable molecules, the incident photon energy can excite vibrational modes of the molecules, yielding scattered photons, which are diminished in energy by the amount of the vibrational transition energies. A spectral analysis of the scattered light under these circumstances will reveal spectral satellite lines below the Rayleigh scattering peak at the incident frequency. Such lines are called "Stokes lines". If there is significant excitation of vibrational excited states of the scattering molecules, then it is also possible to observe scattering at frequencies above the incident frequency. These lines, generally weaker, are called anti-Stokes lines, (Figure 2.2). Since the Raman Effect depends upon the polarizability of the molecule, it can be observed for molecules, which have no net dipole moment and therefore produce no pure rotational spectrum. This process can yield information about the moment of inertia and hence the structure of the molecule.

In Raman scattering, an intense monochromatic light source (laser) can give scattered light, which includes one or more "sidebands" that are offset by rotational and/or vibrational energy differences. Since the sideband frequencies contain information about the scattering medium, which could be useful for identification. Moreover, the Raman bands are the characteristics of the structure and give valuable information about the structure, size and crystal surface area. [15]. However, the main limitations of Raman spectroscopy are its inherently low intensity compared to that of the elastically scattered laser intensity and interference from fluorescence due to the electronic excitation of the molecule by the laser.

In the present work, Raman analysis of various nanofiber based samples was performed on a JASCO confocal Raman spectrometer using 532 nm green laser (NRS 1500 W).

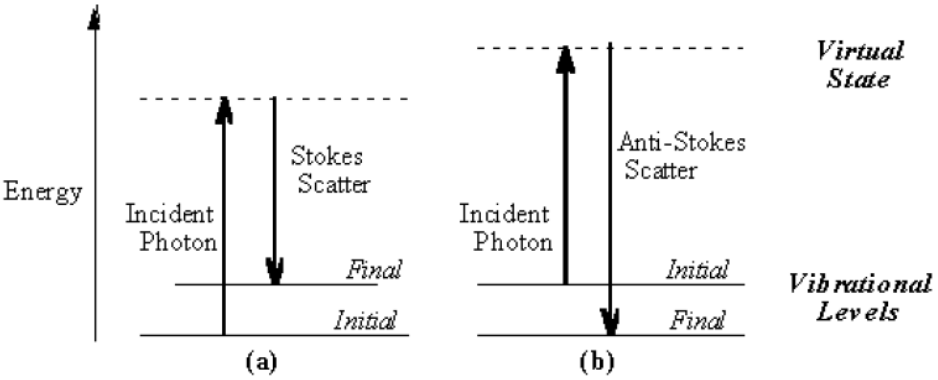

Figure 2.2. Energy level diagram for Raman scattering.

2.2.7. Adsorption Isotherm and Pore Size Distribution Analysis

Gas adsorption measurements are widely used for determining the surface area and pore size of solid materials. Depending on the size of the pores, the solids are classified into macroporous (diameter above 50 nm), mesoporous (diameter 2-50 nm) and microporous (diameter less than 2 nm). The Braunauer-Emmett-Teller (BET) volumetric gas adsorption technique using N_2 is a standard method for the determination of the surface area and pore size distribution of finely divided porous samples [16]. The simple form of this equation can be written as

$$\frac{P}{V_a(P_o - P)} = \frac{1}{CV_m} + \frac{(C-1)P}{CV_mP_0} \qquad (2.4)$$

where ‘P’ is adsorption equilibrium pressure, ‘P_0’ is saturation vapour pressure of the adsorbate at the experimental temperature, ‘V_a’ is volume of N_2 adsorbed at a pressure P, ‘V_m’ is the volume of adsorbate required for monolayer coverage, ‘C’ is a constant that is related to the heat of adsorption and liquefaction, that depends upon adsorbate, adsorbent and temperature. By plotting $P/Va(P_o-P)$ *vs.* P/P_o and determining V_m from the slope of the resultant straight line in the partial pressure range of 0.05 to 0.35, the surface area can be calculated. The specific surface area of the solid material will be obtained by dividing total surface by mass of the solid [17].

The total pore volume is derived from the amount of vapour adsorbed at relative pressure close to unity assuming that all the pores are filled with condensed absorptive in normal liquid state. Pore size distribution is the distribution of pore volume with respect to pore size. The computation of pore size distribution involves a number of assumptions (pore shape, mechanism of pore filling, validity of Kelvin equation etc). It is generally accepted that desorption isotherm is more appropriate than adsorption isotherm for evaluating the pore size distribution of the adsorbent. The mesopore size calculations are made assuming cylindrical pore geometry using Kelvin equation in the form:

$$r_k = \frac{-2\gamma V_m}{RTl_n\left({}^{P}/_{P_0}\right)} \qquad (2.5)$$

where ‘γ’ is surface tension of nitrogen at its boiling point, ‘V_m’ is molar volume of liquid N_2, ‘R’ is gas constant, ‘T’ is boiling point of liquid nitrogen, (P/P_0) is the relative pressure of N_2, and ‘r_k’ is the Kelvin radius of the pore. Several computational procedures are available for the derivation of pore size distribution of mesoporous samples from physisorption isotherms. Most popular among them is the Barrett-Joyner-Halenda (BJH) model, which is based on speculative emptying of the pores by a stepwise reduction of P/P_0, and allowance being made for the contraction of the multilayer in those pores already emptied by the condensate

2.2.8. Electrochemical Characterizations

Several electrochemical techniques, like cyclic voltammetry (CV), linear sweep voltammetry (LSV), and impedance spectroscopy (EIS) are commonly used to study different electrochemical processes (faradaic and non-faradaic) associated with a material [18]. These tools can be effectively used to study the behaviour of electroactive species diffusing to an electrode surface, interfacial phenomena at an electrode surface, and bulk properties of materials in or on the electrodes. However, adequate precautions have to be taken with the cleanliness of the electrode surface and also with the stability of the materials under electric field in order to get correct information.

2.2.8.1. Cyclic Voltammetric Analysis

Cyclic Voltammetry (CV) is the most commonly used potential controlled electrochemical technique which is routinely used to investigate the electrochemical properties of materials [18]. This technique offers a fast location of the redox potentials of electro active species. In CV, generally three-electrode systems are used even though two-electrode systems can also be used. In three-electrode systems, the potential is applied between WE and reference electrode (RE) while the current is measured in between the WE and the counter electrode (CE). To tackle with large currents, normally counter electrode will be with very high surface area. In CV, the potential of the WE is cycled linearly with time between two potential ends at which the oxidation and reduction of the sample occurs. Here, the potential is scanned at a particular scan rate and the current-time curve is plotted. As the scan rate is constant and the initial and switching potential are known, time can be converted into potential. The resulting current-potential plot is known as cyclic voltammogram.

CV is a routinely used technique for characterizing and activating electrocatalysts as it offers important information related to the cleanliness of the electrode surface, mechanism of the charge transfer involved in electrochemical reactions etc. Figure 2.3 shows a typical CV profile of a Pt electrocatalyst supported on a CNT surface, in Ar saturated 0.5 M $HClO_4$ at a scan rate of 50 mV/s. Saturating the electrolyte with an inert gas like Ar allows the study of platinum surface characteristics in a more controlled manner. A typical Pt CV profile can be divided into three regions; H_2 under-potential deposition region (~ 0-0.45 V *vs.* RHE), double layer region (~ 0.45-0.75 V *vs.* RHE) and Pt oxide formation region (above 0.75 V *vs.* RHE). At potentials below 0.45 V, H_2 adsorption/desorption takes place wherein the protons from the electrolyte deposit on the Pt surface up to a monolayer level. In the potential region between 0.45 and 0.75 V, no charge transfer across the electrode/electrolyte interface takes place. In this region, the current is capacitive in nature and is characterized by double layer charging. At potentials above 0.75 V, water in the electrolyte undergoes oxidation on Pt sites and forms Pt-OH species [19].The onset potential for oxygen reduction is typically ~ 1 V on a Pt catalyst. After the subtraction of the capacitive current, electric charge for the desorption of H_2 (Q_H) can be calculated by integrating the area under the desorption region. Assuming that $Q_H = 210\ \mu C/cm^2$ for a smooth polycrystalline Pt, the electrochemically active surface area (ECSA) of the Pt electrocatalyst can be calculated.

In the present study, all CV analyses were performed on an Autolab PGSTAT30 (Eco Chemie) instrument using a conventional three-electrode test cell with a reversible hydrogen electrode (RHE) and a platinum foil as the RE and CE, respectively, unless mentioned specifically. A GC electrode with the sample coated on it was used as the WE. Prior to the CV experiments, the electrolyte was deaerated with N_2 gas.

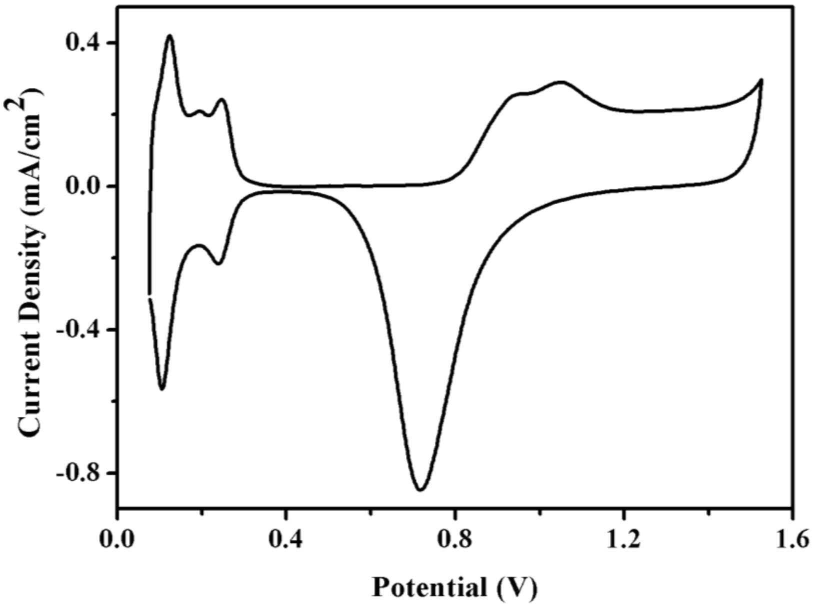

Figure 2.3. Typical cyclic voltammogram of Pt electrocatalyst in Ar saturated 0.5 M H_2SO_4 at a scan rate of 50 mV/s.

2.2.8.2. Rotating Disc Electrode Analysis

The rotating disc electrode (RDE) is a useful tool for following the electrochemical reactions that involves mass transport. This is an effective tool to precisely quantify the electrocatalytic activity of materials, especially electrocatalysts for ORR. In this technique, a WE which can rotate in a predetermined rate is generally used and this rotation brings the reactant gases to the electrode surface in a controlled manner [18]. The flux of the gas to the electrode surface is determined by various parameters such as intrinsic properties of the electrolyte, rotation rate of the WE etc. Thus, in this technique, a convective transport is induced by the rotation of the WE. Here, the total measured current (i) will be the sum of kinetic current (i_k) and mass transport limited current (i_d) and it can be adjusted to the simple Koutecky-Levich equation as [20].

$$\frac{1}{j}=\frac{1}{j_k}+\frac{1}{j_d}=\frac{1}{j_k}+\frac{1}{BC_0\omega^{1/2}}=\frac{1}{j_k}+\frac{1}{0.62nFAD_0^{2/3}C_0^{*}v^{-1/6}\omega^{1/2}} \qquad (2.6)$$

where, ‘n’ is the number of transferred electrons per oxygen molecule, ‘F’ is the Faraday constant, ‘D_O’ is the diffusion coefficient of the electrolyte, ‘C_o*’ is the concentration of dissolved oxygen in the electrolyte, ‘υ’ is the kinematic viscosity of the electrolyte, ‘ω’ is the angular velocity of the electrode. Thus, a plot of 1/j *vs.* $1/\omega^{1/2}$ will give a straight line whose intercept corresponding to $1/j_k$ and slope corresponding to $1/BC_0$. At infinite rotation speeds, current can be considered as kinetic current free from external mass transfer limitation [21]. From the kinetic current, the apparent rate constant ‘k’ can be evaluated using oxygen solubility and diffusion coefficient and from the slope the number of electrons transferred also can be calculated. Apart from this, specific (mA/cm^2_{Pt}) and mass activity (A/mg_{Pt}) can be calculated from the RDE data by normalising the kinetic current with the ECSA obtained from CV and Pt catalyst loading respectively.

All electrochemical studies were performed on an Autolab PGSTAT30 (Eco Chemie) instrument using a conventional three-electrode test cell with a 5 mm diameter GC electrode coated with the sample as the WE, $Hg/HgSO_4$ as the RE and Pt foil as the CE respectively. RDE studies were conducted at a scan rate of 5 mV/s at various rotating speeds *i.e.* 400, 900, 1200, 1600 and 2500 rpm.

2.2.8.3. Electrochemical Impedance Measurements

Electrochemical impedance (EIS) is an important electroanalytical technique based on the measurements of the frequency dependent response of an electrochemically active material after applying a small-amplitude sinusoidal signal under a potentiostatic control. It offers the possibility of obtaining information on important parameters such as ohmic resistance, double layer capacitance and charge transfer kinetics at the electrode/electrolyte interface and also about mass transfer phenomenon. In the present work, electrochemical impedance measurements were done using Autolab PGSTAT30 (ECOCHEMIE) instrument equipped with a frequency response analyzer. MEA impedance was taken, while passing H_2 and O_2 gases at a flow rate of 50 sccm, and ambient pressure at the anode and the cathode respectively. The measurements were taken at an amplitude of 10 mV in the frequency range of 20 kHz to 0.1 Hz.

2.3. References

1 (a) B. D. Cullity, S. R. Stock, *Elements of X-Ray Diffraction*, Addison-Wesley Reading, MA, **1978**. (b) H. P. Klug, L. E. Alexander, *X-Ray Diffraction Procedures*, Wiley New York, **1954**.

2 A. R. West, *Solid State Chemistry and its Applications*, John Wiley & Sons, Singapore, **2003**.

3 J. I. Goldstein, et al., *Scanning Electron Microscopy and X-ray Microananalysis*, Kluwer Academic/ Plenum Publishers, New York, 3rd ed. **2003**.

4 G. Lawes, *Scanning Electron Microscopy and X-ray Microanalysis*, John Wiley and Sons Ltd., Chichester, **1987**.

5 D. B. Williams, C. B. Carter, *The Transmission Electron Microscopy: A Text Book for Materials Science*, Springer 2nd ed. **2009**.

6 (a) G. Thomas, *Transmission Electron Microscopy of Metals*, John Wiley & Sons, Inc, New York, **1962**. (b) D. B. Williams, C. B. Carter, *Transmission Electron Microscopy: A Textbook for Materials Science Vol. I-IV*, Plenum Press, New York, **1996**.

7 J. E. Martin, J. Odinek, J. P. Wilcoxon, R. A. Anderson, P. Provencio, *J. Phys. Chem. B* **2003**, *107*, 430.

8 (a) J. Duan, S. Yang, H. Liu, J. Gong, H. Huang, X. Zhao, R. Zhang, Y. J. Du, *J. Am. Chem. Soc.* **2005**, *127,* 6180. (b) Y. Ding, Z. L. Wang, *J. Phys. Chem. B* **2004**, *108*, 12280.

9 J. F. Watts, J. Wolstenholme, *An Introduction to Surface Analysis by XPS and AES*, John Wolstenholme, **2003**. (b) G. A. Somorjai, A. S. Mujumdar, *Introduction to Surface Chemistry and Catalysis*, Wiley New York, **1994**.

10 (a) C. D. Wagner, W. M. Riggs, L. E. Davis, J. E. Moulder, *Handbook of X-ray Photoelectron Spectroscopy*; Perkin-Elmer Corp. **1979**. (b) P. M. A. Sherwood, *In Surface Analysis by Auger and X-ray Photoelectron Spectroscopy*; Briggs, D., Grant, J. T., Eds. Surface Spectra Ltd. and IM Publications: Chichester, **2003**.

11 D. Dollimore, *Anal. Chem*. **1996**, *68*, 63.

12 (a) W. W. M. Wendlant, *Thermal Methods of Analysis*, 2nd ed. John Wiley & Sons, New York, **1974**. (b) T. Hatakeyama, F. X. Quinn, *Thermal Analysis: Fundamentals and Applications to Polymer Science*, John Wiley & Sons, New York, **1995**.

13 R. Loudon, *Adv. Phys.* **2001**, *50*, 813.

14 D. A. Long, *Raman Scattering*, Mcgraw Hill Book Company, New York, **1977**.

15 (a) M. Fernandez-Garcia, A. Martinez-Arias, J. C. Hanson, J. A. Rodriguez, *Chem. Rev.* **2004**, *104*, 4063. (b) J. L. Anchell, A. C. Hess, *J. Phys. Chem.* **1996**, *100*, 18317.

16 S. Braunauer, P. H. Emmett, E. Teller, *J. Am. Chem. Soc.* **1938**, *60*, 309.

17 S. Lowell, *Characterization of Porous Solids and Powders: Surface Area, Pore Size, and Density*, Springer, **2004**.

18 (a) A.J. Bard, L.R. Faulkner, *Electrochemical Methods*, Wiley New York, **2001**. (b) J.F. Rusling, S.L. Suib, *Adv. Mater.* **2004**, *6*, 922.

19 (a) B. E. Conway, *Progress in Surface Science*, **1995**, *49*, 331. (b). H. Angerstein-Kozlowska, B. E. Conway, W. B. A. Sharp, *J. Electroanal. Chem. Interfacial Electrochem.* **1973**, *43*, 9.

20 (a) V. Komanicky, A. Menzel, H. You, *J. Phys. Chem.* **2005**, *109*, 23550. (b) U. A. Paulus, A. Wokaun, G. G. Scherer, T. J. Schmidt, V. Stamenkovic, N. M. Markovic, P. N. Ross, *Electrochim. Acta* **2002**, *47*, 3787. (c) J. Wang, B. M. Ocko, R. R. Adzic, *Electrochim. Acta* **1995**, *40*, 83.

Chapter 3

Selective Decoration of Pt Nanoparticles on Carbon Nanofiber and its Electrocatalytic Activity for Oxygen Reduction Reaction*

A novel electrocatalyst with excellent Pt dispersion on the inner and outer wall of a CNF was prepared by a modified polyol process. This was achieved by adjusting the surface tension and polarity characteristics of the medium to favor solution entry into the tubular region by capillary filling and homogenous wetting of the inner wall surface by the solvents. The pristine CNF, which possesses inherently active inner wall surface and inactive outer wall surface, led to selective Pt deposition along the inner wall, whereas activation of the outer wall with chemical functionalization resulted into excellent dispersion of Pt NPs along both the inner and outer walls. Structural and morphological characterizations using HRTEM and XRD revealed that when Pt could be dispersed along both the walls of CNF, the Pt particle size reduces to almost half as compared to the one with Pt decoration only along a single wall. Further, electrochemical studies using CV and RDE measurements revealed enhanced methanol oxidation and ORR properties. The ECSA obtained for the catalyst with both inner and outer wall Pt decoration is nearly two times higher as compared to the one with only inner wall Pt decoration. Similarly, the rate constant for ORR displayed by this sample was four times higher in comparison with the sample prepared by utilizing only one wall for Pt decoration.

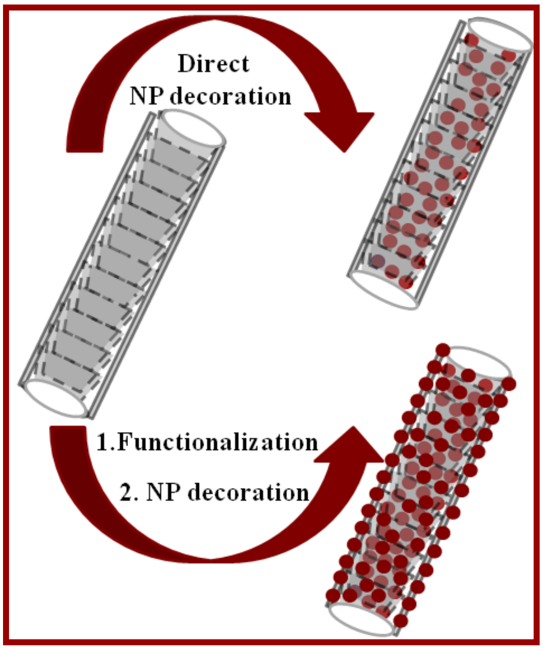

---

* The contents this chapter has been published in “*J. Phys. Chem. C*, **2009,** *113,* 17572-17578”

3.1. Introduction

Platinum supported on carbon has attracted great interest owing to its versatility in catalysis, particularly for fuel cells [1-3]. A great deal of effort has been devoted to improve the performance of Pt in fuel cells. In the advent of nanomaterials, electrode development for fuel cells has considerably benefited and satisfactory performance has been obtained so far with microgram loading of the Pt catalyst [4, 5]. However, the Pt catalysts still suffers from many other drawbacks like ‘cathode thinning’; which is often caused by the carbon corrosion due to the high cathode potential during the PEMFC operation [6, 7]. A carbon weight loss up to 5-8% is observed which influences the mass transport, resulting into a current density loss of 20-60% at 0.5 V [8]. Hence, in looking at the design of the MEAs for PEMFCs from a commercial point of view, apart from controlling the size of Pt and its dispersion, a proper tuning of the mass transfer rate is also important. Moreover, a smooth surface geometry of the carbon support material is always desirable to effectively establish the ionomer-catalyst-gas pore TPB around the Pt NPs and thereby enable the latter to participate in the reaction with a concomitant improvement in the Pt utilization level [9].

In view of overcoming these two prevailing issues on mass transfer and mass activity, 1-D nanostructures of carbon such as CNTs and CNFs have triggered wide interest, mainly due to their exciting features such as anisotropy, unique structure and surface properties [10-12]. However, irrespective of all the much hyped advantages of these classes of materials for fuel cell electrode applications, the inherently low surface area pocessed by many of these materials restricts the amount of active component like Pt dispersible on these materials. A catalyst with higher carbon to Pt ratio leads to thick layer of catalyst and concomitantly higher mass transfer and electric resistances. A strategic approach to obviate the issues related to mass transfer, water management and conductivity is to develop MEAs with thin electrodes by using catalysts pocessing high Pt loading and dispersion. This enables one to achieve a desired level of Pt loading while restricting the carbon content in the minimum possible level. Tubular morphologies of some carbon nanomaterials with open tips are interesting in the context of developing low carbon loaded, metal-rich catalysts since the morphology offers a possibility to access both the inner and outer surfaces of this carbon for metal dispersion. However, metal dispersion along the inner wall of such materials can be accomplished by surmounting the geometry and surface affinity related issues. Even though there have been reports on introducing NPs inside the tubular morphologies of carbon by different strategies, in most of the cases, the NPs exist in the form of nanowires, rods or particle aggregates by blocking the tubular channels of these materials [13]. In this study, we report a novel electrocatalyst based on a hollow tubular morphology with significantly high Pt dispersion and active area formed by successfully utilizing the inner and outer walls of the support material. This catalyst has immense scope as an electrode material for PEMFCs because for a fixed catalyst loading, the available surface area will be doubled leading to better dispersion and a concomitantly low electrode thickness due to the effective utilization of the carbon surface.

In view of utilizing the outer as well as the inner walls for Pt dispersion, a new type of CNF having open tips and comparatively larger inner diameter was purchased and used as the support material for the present study. To facilitate metal dispersion into inner wall of the CNFs, simultaneous metal ion dispersion and reduction was accomplished through a polyol process by carefully optimizing the polyol-water ratio to achieve balanced surface tension and polarity characteristics. The modification of the polyol process by using a proper composition of polyol and water is a critical step to facilitate reactants entry into the tubular region and homogeneous wetting of the inner wall surface by the solvents. To reveal the importance of modifying the polyol process to achieve inner wall Pt deposition, a catalyst was also prepared by adopting traditional polyol process by using the same carbon substrate and EG as the solvent. Further, to utilize the inactive outer surface for decoration of Pt NPs, chemical functionalization was carried out using H_2O_2 and metal dispersion was accomplished by the modified polyol process. Scheme 1 clearly illustrates all these features; before any kind of pretreatment, only the inner walls are active whereas the pretreatment helps to make the outer walls also active by surface functionalization. This opportunity to properly utilize the inherent surface properties of the material and further, to fine tune the surface characteristics by chemical pretreatment enables one to achieve selective inner as well as inner and outer wall Pt decoration. A CNT supported catalyst (FCNT-Pt) also was prepared by the modified polyol process for effectively comparing the activity characteristics.

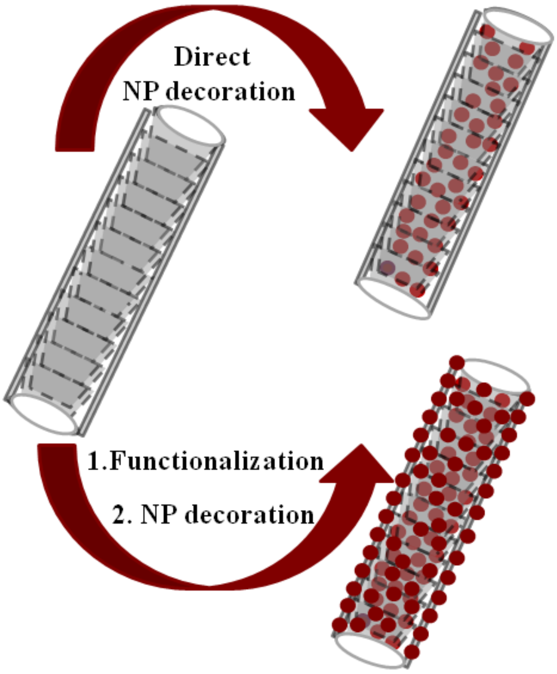

Scheme 3.1. Outline of the steps for the preparation of Pt-decorated CNF

3.2. Experimental Section

3.2.1. Synthesis of Electrocatalysts

For the preparation of 40 wt% Pt loaded catalysts only in the inner cavity and also along both the walls, pristine and H_2O_2 treated CNFs respectively were used. In the typical synthesis, a modified polyol process was adopted and the solvent used was a 3:2 v/v mixture of EG and H_2O. Initially, the required amount of support material (CNF, FCNF, or FCNT) was well dispersed in the solvent mixture by ultrasonication. In the next step, H_2PtCl_6 dissolved in the same solvent mixture was added drop by drop with stirring. Subsequently, the mixture was kept under stirring for 5 h at ambient temperature to achieve good dispersion of the components in the mixture. After this aging process, the mixture was heated up to 140 °C for 8 h to ensure complete reduction of Pt ions. The reaction mixture was then cooled and filtered though a PTFE filter paper. The wet cake was washed repeatedly with hot water and subsequently with acetone to remove excess solvent. Finally, a few more washings with DI water were performed, and the products was dried at 100 °C for 5 h. Catalysts with Pt decoration only along the inner wall and on both the inner and outer walls of CNFs are respectively, denoted as C-Pt and F-Pt.

3.3. Results and Discussion

3.3.1. TEM Analysis

The structure and morphology of the catalyst support as well as the catalyst were explored using TEM analysis. Figure 3.1(a-d) shows the TEM images of CNF support at various magnifications. The low magnification image given in Figure 3.1(a) clearly indicates that the length of these CNFs is in few micrometers. It is clear from Figure 3.1(a and b) that these nanofibers have a large central hollow core and open tips; the open tips are circled in Figure 3.1(a). The inner and outer diameters of the CNFs are *ca.* 50 ±10 and 100±10 nm respectively.

The duplex structure of the system with the edges of the slanting graphene planes in the inner cavity and the smooth outer wall formed due to the stacking on the parallel graphene planes is clearly evident from Figure 3.1(b). Figure 3.1(c), which is the enlarged view of the inner portion of the CNF support, clearly depicts that unlike CNTs, which are made by the simple rolling of graphene sheets, this material is made up of truncated conical graphene layers. Because of this peculiar rolling of graphene sheets, CNF exhibits a large central hollow core, which in turn imposes a significant portion of exposed and reactive edges in the inner channel created within the CNF. However, as evident from Figure 3.1(d), the edge sites on the outer surface of the nanofibers are clearly covered by the deposition of a pyrolitic carbon layer (duplex structure) induced by the high reaction temperature in the synthesis of this material. Tibbetts *et al*. have reported similar kinds of structural features in vapor-grown carbon nanofibers [14]. Deposition of a pyrolytic carbon layer on the outer surface of CNFs during graphitization at high temperatures has been reported by Paredes *et al*. and Carneiro *et al.* [15, 16]. This peculiar morphology of the material leaves its inner wall inherently active and outer wall inert. At the same time, the relatively large inner diameter, open tips, active inner wall and the possibility of activating the inert outer wall by facile chemical treatments make this a potential support material for effectively dispersing Pt [17].

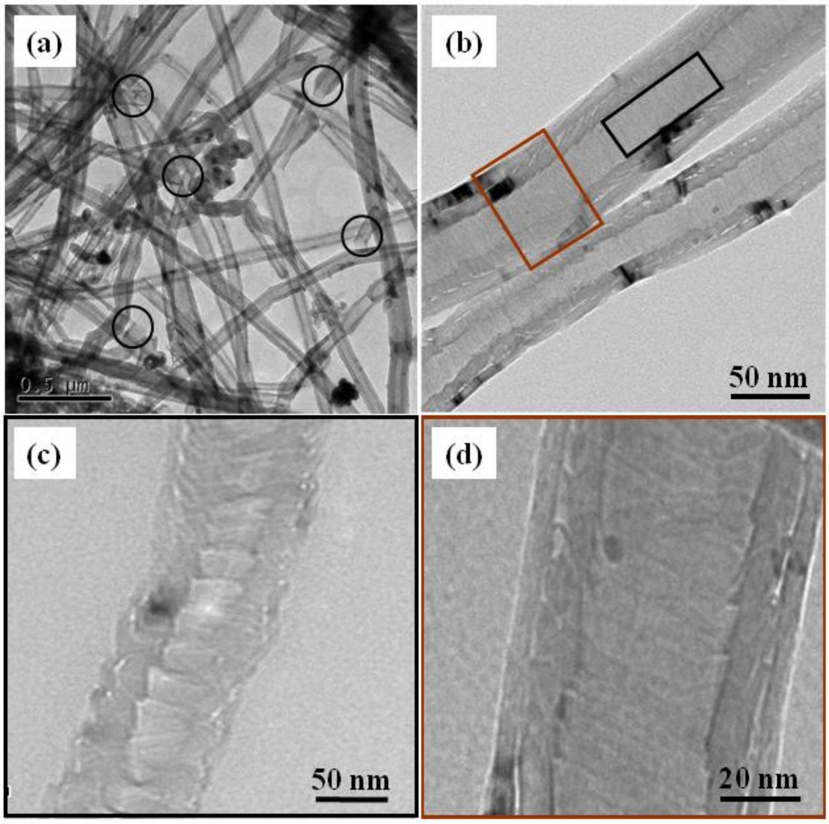

Figure 3.1. TEM images (a) pristine CNF support; circled regions represent the open tips, (b) high magnification image of CNF with a deactivated outer wall due to the deposition of a pyrolitic carbon layer (duplex structure, (c) an enlarged view of inner portion marked by the black box in (b) of CNF, clearly indicating conical graphene layers, (d) enlarged view of the portion marked by the red box in (b) of the CNF with an active inner wall and an inactive outer wall due to the deposition of the pyrolitic carbon layer.

Figure 3.2(a) shows the TEM image of C-Pt where Pt NPs are dispersed on the pristine CNF support. It is evident that the Pt NPs are decorated only on the inner wall of the support and the outer wall is completely empty. As discussed before, in the case of pristine CNF, only the inner wall will be active (due to the presence of the pyrolytic carbon layer on the outer surface) and the metal dispersion by the modified process will result in a selective decoration only on the inner wall. A closer inspection of Figure 3.2(b) reveals that these Pt NPs are randomly dispersed on the CNF support and some of them aggregate to form larger particles or clusters. The average particle size and distribution were also determined from the HRTEM images assuming a spherical shape for the particles. At least 250 particles were selected randomly from different micrographs for each sample. The corresponding particle-size distribution histogram obtained for C-Pt is given in Figure 3.2(c). It is found that the average particle size of the NPs is 5.5 ±0.9 nm.

Interestingly, after the functionalization, Pt NPs are excellently dispersed along both the walls of the CNF (F-Pt), as can be evident from Figure 3.2(d). The high magnification image of F-Pt given in Figure 3.2(e) shows that small nanocrystalline catalyst particles are well separated from each other, and monodispersity of NPs is essentially maintained, indicating that the synthesis method could effectively prevent agglomeration of Pt NPs. The average particle size and distribution were determined here also and the particle size obtained in F-Pt is 2.8 ± 0.4 nm, as presented in Figure 3.2(f). The observed uniformity in size and shape of the NPs could be due to two reasons as follows. First, chemical functionalization leads to the formation of functional group like -OH and -COOH on the outer surface (as evident from XPS analysis given in the latter section), which are known to act as the anchoring sites for the catalyst NPs. Apart from this, after functionalization, the inactive outer surface also becomes active and hence the carbon surface area available for holding the metal species is almost doubled, and in this way, high dispersion quality could be achieved [17]. The SAED pattern [inset of Figure 3.2(b) and 3.2(d)] shows three rings indexed to the (111), (200), and (220) diffraction, respectively. It can be concluded that the as-prepared Pt NPs are crystallized in a face-centered cubic (fcc) structure in both cases [18].

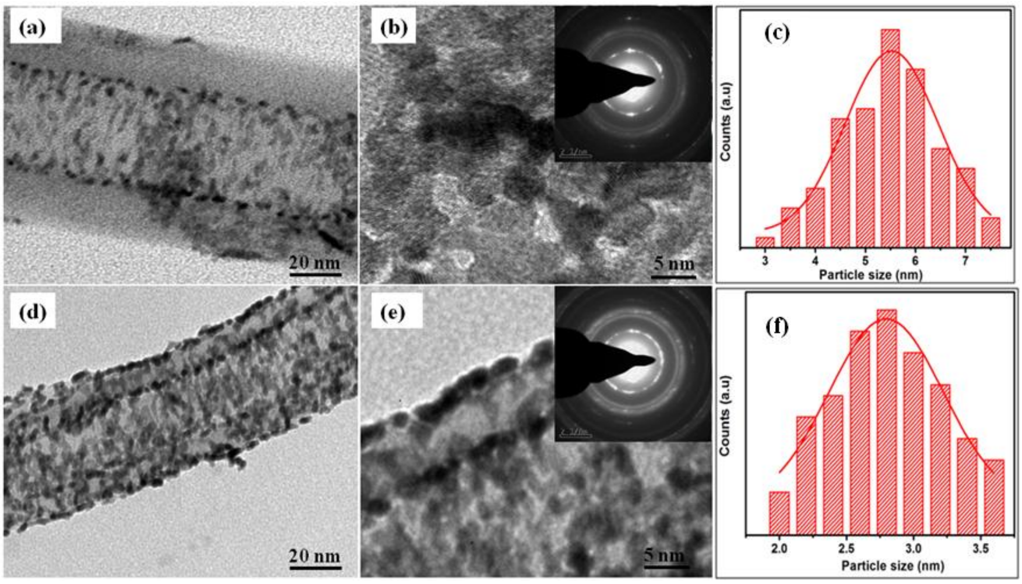

Figure 3.2. TEM images of (a) C-Pt, (b) high magnification image of C-Pt, (d) F-Pt, (e) high magnification image of F-Pt, (c and f) histograms of the particle size for C-Pt and F-Pt respectively. Insets of Figure 3.2(b) and (c) are the diffraction pattern of C-Pt and F-Pt, respectively.

Further, to demonstrate the importance of the modified polyol process, catalysts were prepared using conventional polyol process based on solvent such as ethylene glycol for the metal dispersion. Figure 3.3(a and b) display the images of pristine and functionalized CNF supported catalyst respectively, synthesized using a conventional polyol process. The images clearly indicate that the dispersion of the Pt NPs obtained is very poor, and they form islands of NPs by agglomeration, especially in the case of the catalyst synthesized using pristine CNF, as shown in Figure 3.3(a). In contrast to this, a slightly improved dispersion can be seen in the case of FCNF support.

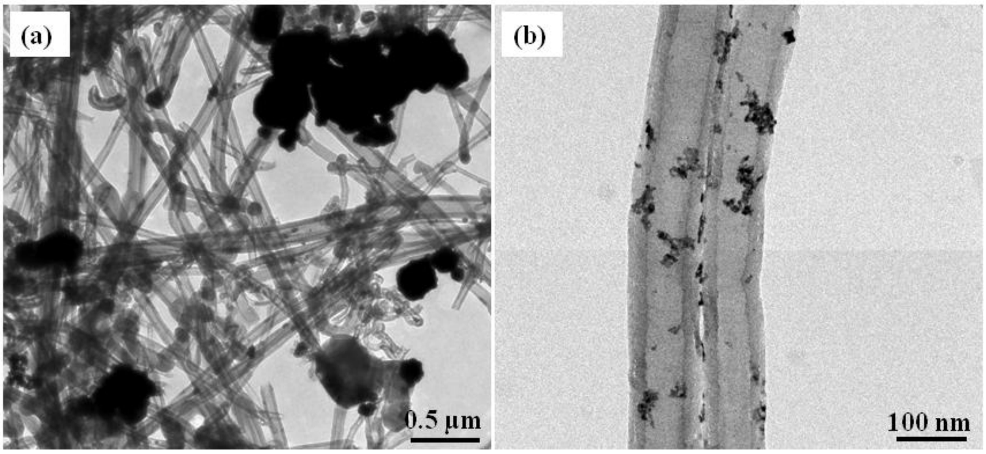

Figure 3.3. TEM images of (a) of pristine and (b) functionalized CNF supported catalyst synthesized using conventional polyol process.

The above results point out that the inner wall of the CNF cannot be accessed using a traditional polyol process. It may be attributed to the fact that because of the high viscosity of the solvent (e.g., EG), the solvent filling in the tube by capillary action is impeded, leading to the non-utilization of the inner wall for Pt dispersion [19]. The above investigations confirm the fact that in this system, because of the peculiar morphology and contrasting differences in the activity characteristics of the inner and outer walls, a process modification is important for the simultaneous metal ion dispersion and reduction. Both the surface tension of the medium and the contact angle between the liquid and surface play a decisive role to achieve fine metal particle dispersion along the inner wall by significantly eliminating the possibilities of channel blocking which can be caused by any entrapped particles or their aggregates. Thus, by an appropriate manipulation of the polyol to water ratio, the capillary action by the tubes can be properly utilized to suck the solution into the channels of the support material. Our detailed investigations reveal that the metal particle size and distribution strongly depend on the amount of water addition. When polyol-water v/v ratio is 3:2, small metal particles are formed whether the metal is supported or unsupported. On the other hand, at still higher water content, even though fine Pt NPs seemed to be formed, their dispersion along the inner and outer walls is poor owing to the increase in the surface tension of the medium. Therefore, the polyol to water ratio of 3:2 has been assigned as the best solvent composition with respect to particle size and dispersion resulting from balanced surface tension and wettability characteristics.

3.3.2. XRD Analysis

XRD was used to characterize the crystal structure of the materials, and Figure 3.4 shows a comparison of the XRD pattern of CNF, C-Pt and F-Pt.

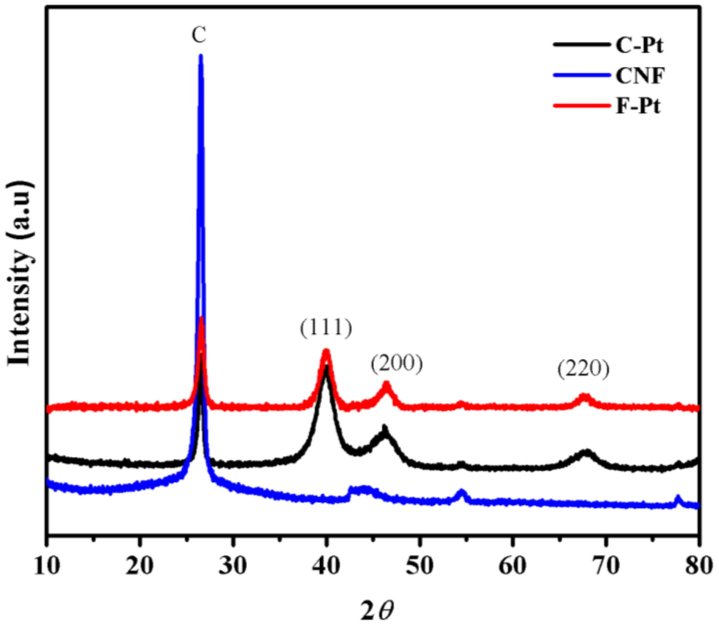

Figure 3.4. Superimposed XRD patterns of CNF, C-Pt and F-Pt revealing reflections from (111), (200) and (220) planes after Pt decoration on CNF.

As shown in Figure 3.4, the pristine CNF has two diffraction peaks: a high intense (002) peak at $2\theta = 26.4°$ and a low intense (100) peak at $2\theta = 43°$. The XRD patterns of both catalysts exhibit strong diffractions at around 2θ of 40.1, 46.4, and 67.7°, which can be indexed as platinum (111), (200) and (220) reflections, respectively. This indicates that the catalysts have face-centered cubic (fcc) structure, which are consistent with previous reports [20]. Moreover, the XRD pattern reveals a high degree of crystallinity in both of the prepared catalysts. Also, the diffraction peaks of F-Pt are broader than those of the C-Pt catalyst. This shows that the average size of the Pt on FCNF is smaller than that on CNF. The average particle sizes of the Pt NPs supported on CNF and FCNF calculated using the Scherrer equation are 6.5 and 3.2 nm, respectively [21]. The size of the Pt NPs calculated using XRD is in good agreement with those obtained from HRTEM results. The diffraction peak at around 2θ of 26.6° of both the samples is attributed to the CNF support.

3.3.3. TG-DT Analysis

TG analyses of C-Pt and F-Pt are conducted in air from RT to 800 °C to study the composition as well as the thermal stability. Accordingly, the TG profile of both catalysts in flowing air (100 sccm) shows interesting differences in the oxidation behavior as shown in Figure 3.5(a and b) for C-Pt and F-Pt, respectively. The slight initial weight loss upto 441 °C, which is more or less similar for both the samples, is expected to be due to the loss of residual water and functional groups [22]. However, from 468 to 800 °C, TGA of C-Pt shows only a single-stage weight loss during heat treatment, whereas F-Pt shows clear two-stage weight loss. Since presence of Pt can facilitate oxidation, a fast decomposition of the Pt-decorated surface can be expected followed by the other parts of the tubes [23]. As the level of Pt dispersion is significantly high on F-Pt, the oxidation of carbon assisted by Pt is fast in this system and accordingly the TGA profile displays a quick weight loss region followed by a tail of the gradual decomposition. Finally, from the residue content, the amount of Pt in case of C-Pt and F-Pt catalyst is quantified to be 39 and 36 wt %, respectively.

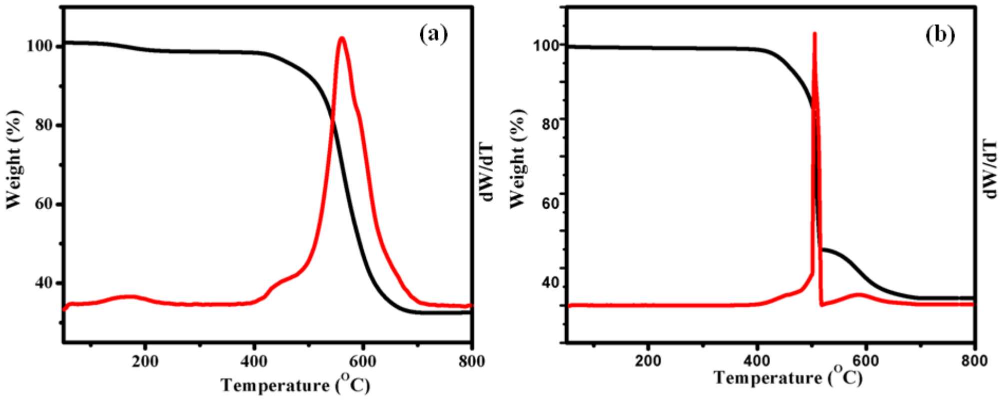

Figure 3.5. Superimposed TG/ DTA curves of (a) C-Pt and (b) F-Pt at a heating rate of 10° C/ min to 800 °C under air atmosphere.

3.3.4. XPS Analysis

The XPS analyses of CNF, C-Pt and F-Pt are conducted to study the CNF-Pt hybrid formation and Figure 3.6 shows the comparison of the full survey XP spectra of CNF, C-Pt and F-Pt. The XPS spectra of CNF show peaks corresponding to C1s, O1s and Fe2p levels whereas in C-Pt and F-Pt an additional doublet corresponding to Pt is also observed. The most intense peak at 284.4 eV corresponds to the C1s sp^2 carbon [24]. The peak at the BE of 531.4 eV indicates the presence of oxygen, and more interestingly, the intensity of this peak is significantly high in F-Pt as compared to that in CNF and C-Pt [25]. This gives a clear evidence for the extent of functionalization effected in CNFs as a result of the H_2O_2 treatment. The Fe2p peak observed at the BE of 702 eV can be attributed to the catalyst used for the CNF synthesis [26]. The clear doublet observed in C-Pt and F-Pt at the BE of 73.4 eV corresponds to Pt and this confirms the formation of CNF-Pt hybrid electrocatalyst [27].

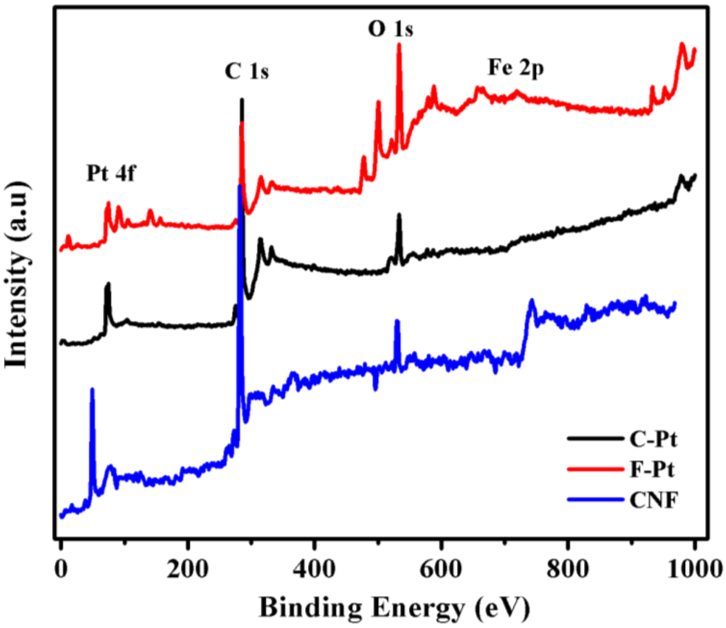

Figure 3.6. Full survey XP spectra for CNF, C-Pt and F-Pt showing the peaks corresponding to C1s, O1s, Fe2p and Pt 4f.

Further, to obtain a detailed insight into the surface chemical composition and the oxidation state of Pt in these hybrids, various parts of the XP spectra of

C-Pt and F-Pt are deconvoluted with respect to Gaussian fitting. Figure 3.7(a-f) shows the deconvoluted narrow scan spectra of C1s, O1s and Pt4f parts.

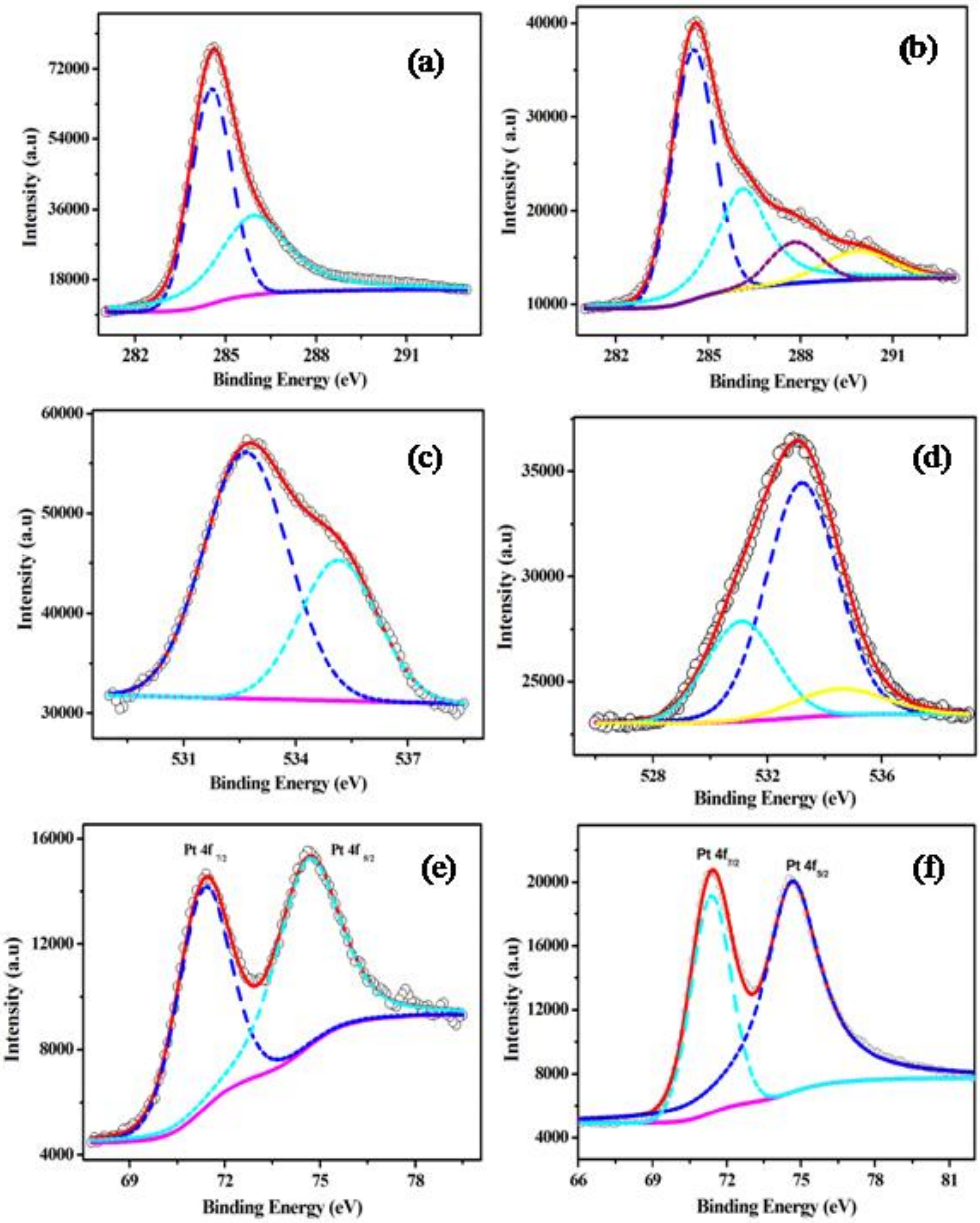

Figure 3.7. Deconvoluted XP spectra of (a) C1s (c) O1s and (e) Pt 4f core levels of C-Pt and (b) C1s (d) O1s and (f) Pt4f core levels of F-Pt, where the circles represent the experimental data, red line represents the fitting data for overall signal, the black lines are the deconvoluted individual peaks for different species present in the sample.

Figure 3.7(a), the C1s part of C-Pt shows two distinct peaks at 284.5 and 286.1 eV corresponding to graphitic carbon and carbon bonded to -OH groups respectively [28]. In case of F-Pt apart from the above mentioned two peaks, two additional peaks at 288.2 and 289.7 eV are also observed as can be evident from Figure 3.7(b). This can be attributed to the carbon atoms attached to oxygen atoms in different environments such as -C=O and -COOH respectively [28]. These peaks confirm the presence of other oxygenated functional groups like -OH, -CO, -COOH on the CNF side walls after functionalization and since, the peak positions are assigned on the basis of the C1s peak at 284.5 eV, all these do not affect the other B.E. values [24(a)].

A comparison of O1s part of both the samples presented in Figure 3.7(c and d) after a similar fitting procedure also confirms the functionalization of CNF support. Figure 3.7(c), the O 1s spectra of C-Pt shows two different peaks; the peak observed at binding energy of 532.4 eV could be due to the presence of small amount of oxygenated species and the peak at 535.5 eV might be due to the adsorbed moisture [25]. However, the XP spectra of F-Pt as shown in Figure 3.7(d) clearly indicate three different functionalities after the functionalization. The peak at 531.2 eV can be attributed to the double bonded oxygenated groups like -COOH [25]. Similarly, a peak at 533.2 eV corresponds to the single bonded oxygenated species like -OH species. In addition, a broad and less intense peak at 535 eV can be assigned to the adsorbed moisture [25].

The Pt4f region in both the catalysts after deconvolution gives one doublet as shown in Figure 3.7(e and f). The peak position, line shape and peak to peak separation are the standard measure of the Pt oxidation state and the observed doublet at the BE of 71.1 and 74.4 eV in both the catalysts corresponds to the $4f_{7/2}$ and $4f_{5/2}$ levels of Pt(0). Hence, it can be concluded that Pt is present in the zero oxidation state and no traces of higher oxidation states are observed in both the catalysts. Apart from this, a slight shift in the BE of the 4f level is also observed which can be attributed to the charge transfer between the CNF support to the Pt NPs [29].

3.3.5. Electrochemical Studies

3.3.5.1. CV Analysis

The electrocatalytic properties of C-Pt and F-Pt are initially evaluated by CV analysis in 0.5 M H_2SO_4 solution. In order to have an effective comparison, CV analysis of FCNT-Pt catalysts is also conducted under similar conditions. The Pt loadings on the electrode surface for C-Pt, F-Pt, and FCNT-Pt catalysts are 0.0195, 0.0180, and 0.0195 mg, respectively. Figure 3.8 shows superimposed CVs of C-Pt, F-Pt and FCNT-Pt in N_2 saturated 0.5 M H_2SO_4 at a scan rate of 50 mV/s in the potential window of 0.15 to 1.5 V at RT. The CV features resemble very much to that of a polycrystalline Pt electrode in acid solution [30]. In the CVs, the H_2 region appeared in the potential range of 0.13 to 0.45 V *vs.* RHE, and oxygen reduction showed a peak at 0.8 V *vs.* RHE for all the three catalysts. Even though the voltammetric profiles look similar for all the three catalysts, significant differences in the current densities can be observed. Further, The ECSA (details of ECSA calculation are provided in chapter 2) obtained for F-Pt is 233 cm^2/mg-Pt, which is almost two times higher as compared to 107 cm^2/mg-Pt obtained for C-Pt [30, 31]. This improvement in the Pt active area when Pt is dispersed by utilizing both the walls is in agreement with the Pt particle size distribution already observed by HRTEM analysis. The conventional FCNT-Pt displayed an active Pt area of 207 cm^2/mg-Pt which was lower than that of F-Pt. It should be mentioned that the Pt dispersion quality was poor on CNT compared to that on CNF, and fine Pt particles appeared as clusters at different locations of this system. Therefore, consistent results were not obtained using this system. Along with the significantly high ECSA of Pt possessed by F-Pt, the high current density obtained also underscores the excellent performance of this catalyst. The current density observed for F-Pt is 640 mA/cm^2 which is ~200 mA/cm^2 and ~100 mA/cm^2 higher than the respective values for C-Pt (420 mA/cm^2) and FCNT-Pt (550 mA/cm^2).

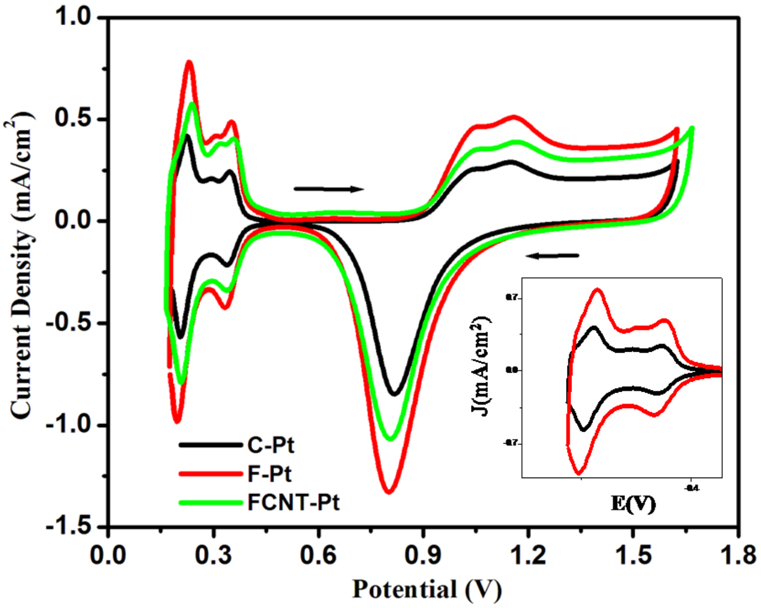

Figure 3.8. Superimposed CVs of C-Pt, F-Pt and FCNT-Pt in 0.5 M in H_2SO_4 using RHE as the RE at RT; sweep rate 50 mV/s. Inset of the figure is the expanded H_2 region of C-Pt and F-Pt, clearly indicating almost double electroactive area of F-Pt; all potentials are quoted *vs.* RHE.

3.3.5.2. Methanol Oxidation Studies

The electrocatalytic performance of F-Pt, C-Pt and FCNT-Pt for methanol oxidation reaction (MOR) was also investigated and accordingly Figure 3.9 compares the methanol oxidation activity of all the three catalysts in 0.5 M methanol solution with 0.5 M H_2SO_4 as the supporting electrolyte. The CV profile obtained for MOR is characterized by well separated anodic peaks in the forward and reverse scans similar to that on Pt-based electrocatalysts in acid media [32]. The peak at 0.90 V in the positive-going scan is attributed to the electro-oxidation of methanol and the anodic peak at 0.72 V in the reverse scan can be associated with the reactivation of oxidized Pt [32]. The magnitude of the anodic peak current in the forward scan is also directly proportional to the amount of methanol oxidized at the respective electrocatalysts. Accordingly, in the forward scan, methanol oxidation produces prominent anodic peaks with current densities 2.2, 1.9, and 1.6 mA/cm^2 for F-Pt, C-Pt, and FCNT-Pt, respectively. Apart from this, the onset potential for MOR on both the CNF supported catalysts is 0.39 V, which is negatively shifted by 200 mV as compared with 0.59 V observed on the

FCNT-Pt system. The reduction in the onset anodic potential shows a significant enhancement in the kinetics of the methanol oxidation reaction. This is important since a direct methanol fuel cell gives only less than 0.5 V output voltages at reasonable current densities.

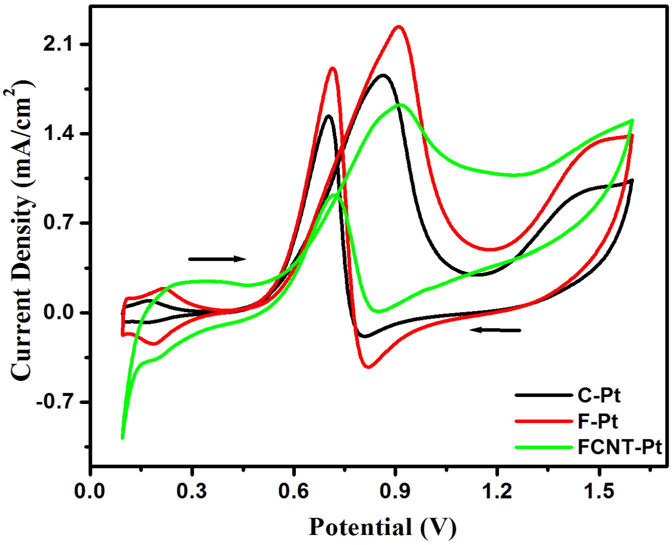

Figure 3.9. Superimposed CVs of for methanol oxidation on C-Pt, F-Pt and FCNT-Pt in 0.5 M CH_3OH + 0.5 M H_2SO_4 at a scan rate of 50 mV/s; all potentials are quoted *vs.* RHE.

Thus, the significantly negatively shifted onset potential and high anodic peak current on the F-Pt electrode confirm that F-Pt exhibits higher electrocatalytic activity as compared to the other two catalysts [33]. It can also be concluded from the above results that CNF supported catalysts have higher electrocatalytic activity for MOR than the conventional CNT supported electrocatalyst. Moreover, in contrast to the observed ORR property of these catalysts, which will be discussed in the following section, better performance of the CNF supported catalysts towards MOR can be explained as follows: in the case of pristine CNF supported catalysts, the Pt NPs are inside the inner cavities of the CNF and the reacting species have to be diffused into the inner cavities so as to be accessible for the reaction. Since the penetration power of methanol is high as compared to H_2SO_4, it is relatively easy for CH_3OH to reach inside the hollow cavity and can effectively be oxidized by Pt deposited along the inner as well as the outer walls.

3.3.5.3. RDE Analysis

As RDE studies allow accurate correction of ohmic and transport overpotentials and therefore yield reliable estimates of upper bounds of intrinsic catalytic activities, the actual ORR activities of these catalysts are demonstrated using RDE studies also [33]. Figure 3.10(a) shows hydrodynamic voltammograms recorded using a RDE electrode at 2500 rpm for ORR on the catalyst modified GC disc electrode in 0.5 M H_2SO_4 at RT. The observed ORR limiting current density is in the order F-Pt > FCNT-Pt > C-Pt. In addition to the limiting current, the onset potential and half wave potentials are also indicative of the performance of an electrocatalyst [33]. In the present case, even though there is only slight difference in the onset potentials, significant difference in the half wave potentials can be observed. The corresponding values are 0.820, 0.806 and 0.801 V for F-Pt, FCNT-Pt and C-Pt, respectively. From these results, the lowest half wave potential displayed by C-Pt can be accounted by a dominant effect of diffusion limitation in the aqueous solution of H_2SO_4. However, because of the high degree of Pt dispersion on F-Pt, this system could manage to display excellent performance irrespective of the diffusion effects that still could act as a limiting factor in accessing the channels of the tube. Thus, it can be clearly concluded from these results that the best catalytic activity is obtained for F-Pt which is in excellent agreement with the CV results. Comparing the above results with the higher MOR activity displayed by the C-Pt, it is clear that a reaction medium with lower surface tension like methanol is more effective in accessing Pt particles inside the tubes.

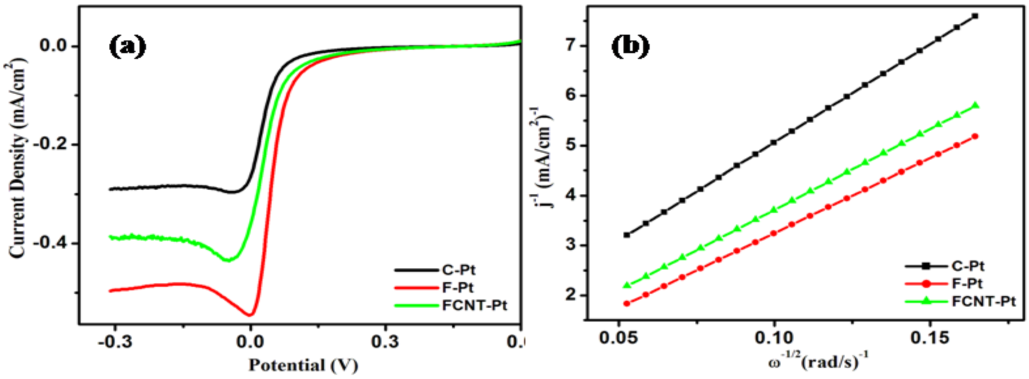

Figure 3.10. a) Polarization curves at a scan rate of 10 mV/s and a rotation rate of 2500 rpm and (b) Koutecky-Levich plots at 0.6 V for the ORR on C-Pt, F-Pt and FCNT-Pt catalysts in O_2-saturated 0.5 M H_2SO_4 at 298 K; all the potentials are quoted *vs.* RHE.

The RDE measurements complemented by the corresponding Koutecky-Levich (K-L) plot (plot of $1/j_{RDE}$ *vs.* *1*/$\omega^{1/2}$, where 'j_{RDE}' is the current density and 'ω' is the rotation speed), can furnish a direct comparison of electrochemical performance in a straightforward manner [34]. Assuming that the resistance of Nafion film coated on the catalyst layer is negligible, kinetic current densities can be adjusted to the simple Koutecky-Levich equation [35] as given below:

$$\frac{1}{j} = \frac{1}{j_k} + \frac{1}{j_d} = \frac{1}{j_k} + \frac{1}{0.62nFAD_0{}^{2/3}C_0{}^{*}v^{-1/6}\omega^{1/2}} \qquad (3.1)$$

where, 'n' is the number of transferred electrons per oxygen molecule, 'F' is the Faraday constant, 'D_O' is the diffusion coefficient of the electrolyte, 'C_o*' is the concentration of dissolved oxygen in the electrolyte, 'υ' is the kinematic viscosity of the electrolyte, 'ω' is the angular velocity of the electrode [35]. Thus, a plot of $1/j_{RDE}$ *vs.* $1/\omega^{1/2}$ will give a straight line whose intercept corresponds to $1/j_k$ and slope corresponds to $1/j_d$. At infinite rotation speeds, current can be considered as kinetic current free from external mass transfer limitation [35]. From the kinetic current, the apparent rate constant 'k' can be evaluated using oxygen solubility and diffusion coefficient of 1.22×10^{-6} mol/cm^3 and 1.04×10^{-5} cm^2/s, respectively obtained in 0.5 M H_2SO_4 at 25 °C [36]. Accordingly, Figure 3.10(b) shows the K-L plots of all the three catalysts at a potential of 0.6 V. The rate constants are respectively 1.91×10^{-3}, 8.46×10^{-3} and 3.88×10^{-3} cm/s for C-Pt, F-Pt and FCNT-Pt. Thus, the four times higher rate constant of F-Pt, compared to C-Pt clearly indicates the superior efficiency for ORR of F-Pt, possibly obtained by the excellent dispersion quality of Pt along the wall surfaces of the substrate.

3.3.5.4. Single Cell Analysis

The single cell analysis of the MEA fabricated using F-Pt is also conducted and the performance is compared with the MEA fabricated using Pt/C catalyst under identical operating conditions. In all the cases, pre-treated Nafion 212 membranes were used and commercially available 40 wt% Pt/C (Johnson Matthey) with a loading of 0.30 mg/cm^2 was used at the anode. A 20 wt% Nafion solution was used as the binder and the Nafion to carbon (N/C) ratio was maintained by 0.45. Accordingly, Figure 3.11 shows the comparison of the H_2/O_2 PEM single cell performances of F-Pt and Pt/C MEAs with a cathode loading of 0.3 mg/cm^2. The polarization curves were recorded at 65 °C under fully humidification at a back pressure of 35 psi. In the low current density region, which is associated with the electrochemical kinetics of ORR, almost similar performance is obtained for both the catalysts. However, in the middle and high current regions a significant difference in the performance is observed. At a fixed cell voltage of 0.6 V, which has been considered as the most desirable operating potential for practical applications, the current density obtained is 0.65 and 0.78 A/cm^2 respectively for Pt/C and F-Pt. The corresponding power densities obtained at 0.6 V is 3.9 and 4.7 W/cm^2 respectively for Pt/C and F-Pt, showing a significant increase in the power density of ~0.8 W/cm^2 at 0.6 V for F-Pt. However, the maximum power density displayed by F-Pt is 7.70 W/cm^2 which is 0.5 W/cm^2 less as compared to the 8.2 W/cm^2 obtained for Pt/C. The comparably low performance of F-Pt can be correlated with the low surface area of the system as compared to that of the Vulcan carbon support.

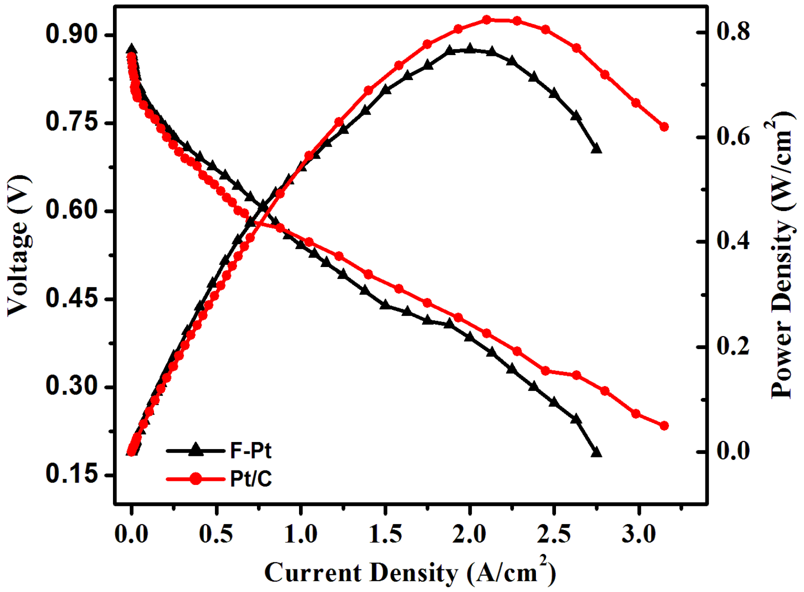

Figure 3.11. Single cell evaluation of the MEAs with the cathode electrodes formed from F-Pt and Pt/C. Commercial 40 wt % Pt/C is used as the anode and a Pt loading of 0.30 mg-Pt/cm^2 are maintained in the cathode and anode.

3.4. Conclusions

In conclusion, we here demonstrated a new strategy for the selective decoration of Pt NPs on the inner and outer walls of CNF by proper tuning of the reaction medium composition to have a balanced surface tension and polarity characteristics. Pt decoration along the inner and outer walls of the substrate with significantly fine Pt particle dispersion could be achieved. The CV and RDE studies demonstrated that the new catalyst prepared with Pt NPs on both the walls showed almost double electrochemical active area and four times higher rate constant as compared to the one with only single wall Pt decoration. The enhanced electrocatalytic activity displayed by these materials opens up great scope in fuel cell electrode fabrication because appropriate Pt loadings can be achieved at significantly low carbon content in the system. Also, the gaseous or vapour atmosphere in PEMFCs based on direct hydrogen or alcoholic fuels is more suited to effectively access the hollow core of the material.

3.5. References

1 Y. H. Lin, X. L. Cui, C. Yen, C. M. Wai, *J. Phys. Chem. B* **2005**, *109*, 14410.

2 W. Li, C. Liang, J. Qiu, W. Zhou, H. Han, Z. Weia, G. Sun, Q. Xin, *Carbon* **2002**, *40*, 791.

3 S. D. Lin, T. C. Hsiao, J. R. Chang, A. S. Lin, J. *Phys. Chem. B* **1999**, *103*, 97.

4 X. Zhang, W. Lu, J. Da, H. Wang, D. Zhao, P. A.Webley, *Chem. Commun.* **2009**, *125*, 195.

5 J. M. Tang, K. Jensen, M. Waje, W. Li, P. Larsen, K. Pauley, Z. Chen, P. Ramesh, M. E. Itkis, Y. Yan, R. C. Haddon, *J. Phys. Chem. C* **2007**, *111*, 17901.

6 C. A. Raiser, L. Bregoli, T. W. Patterson, J. S. Yi, J. D. L. Yang, M. L. Perry, T. D. Jarvi, *Electrochem. Solid-State Lett.* **2005**, *8,* A273.

7 P. T. Yu, W. Gu, R. Makharia, F. T. Wagner, H. A. Gasteiger, *ECS Trans.* **2006**, *3*, 797.

8 H. A. Gasteiger, W. Gu, B. Litteer, R. Makharia, B. Brady, M. Budnski, E. Thompson, F. T. Wagner, S. G. Yan, P. T. Yu, *Mini-Micro Fuel cells: Fundamentals and Applications*. **2008**, 225.

9 M. S. Wilson, S. J. Gottesfeld, *Appl. Electrochem.* **1992**, *22*, 1.

10 G. Zhao, J. He, C. Zhang, J. Zhou, X. Chen, T. Wang, *J. Phys. Chem. C* **2008**, *112*, 1028.

11 X. Wang, W. Li, Z. Chen, M. Waje, Y. Yan, *J. Power Sources* **2006**, *158*, 154.

12 W. Yang, X. Wang, F. Yang, C. Yang, X. Yang, *Adv. Mater.* **2008**, *20*, 2579.

13 X. Pan, X. Bao, *Chem. Commun.* **2008**, *47*, 6271.

14 G. G. Tibbetts, G. L. Doll, D. W. Gorkiewicz, J. J. Moleski, T. A. Perry, C. J. Dasch, M. J. Balogh, *Carbon* **1993**, *31*, 1039.

15 J. I. Paredes, M. Burghard, A. Mart′inez-Alonso, J. M. D. Tasc′on, *Appl. Phys. A: Mater. Sci. Process.* **2005**, *80*, 675.

16 O. C. Carneiro, M. S. Kim, J. B. Yim, N. M. Rodriguez, R. T. K. Baker, *J. Phys. Chem. B* **2003**, *107*, 4237.

17 S. H. Joo, S. J. Choi, I. Oh, J. Kwak, Z. Liu, O. Terasaki, R. Ryoo, *Nature* **2001**, *412*, 169.

18 Y. Mu, H. Liang, J. Hu, L. Jiang, L. Wan, *J. Phys. Chem. B* **2005**, *109*, 22212.

19 Z. Zhou, S. Wang, W. Zhou, G. Wang, L. Jiang, W. Li, S. Song, J. Liu, G. Sun, Q. Xin, *Chem. Commun.* **2003**, 394.

20 S. Mahima, R. Kannan, K. Vijayamohanan, *Langmuir* **2008**, *24*, 3576.

21 H. L. Wang, J. A. Turner. *J. Power Sources* **2008**, *180*, 791.

22 J. Shen, M. Shi, N. Li, B. Yan, H. Ma, Y. Hu, M. Ye, *Nano Res.* **2010**, *3*, 339.

23 Q. Cheng, J. Tang, J. Ma, H. Zhang, N. Shinya, L. Qin, *Carbon* **2011**, *49*, 2917.

24 (a) C. Wang, H. Daimon, *Nano Lett.* **2009**, *9*, 1493. (b) D. Briggs, G. Beamson, *High Resolution XPS of Organic Polymers: The Scienta ESCA300 Database*, John Wiley & Sons Inc, New York, **1992**, 266.

25 M. H. Lee, J. S. Doa, *J. Power Sources* **2009**, *188*, 353.

26 H. Chou, F. Lai, W. Su, K. C. Pillai, L. S. Sarma, B. Hwang, *Langmuir* **2011**, *27*, 1131.

27 (a) E. W. Wang, S. J. Guo, S. J. Dong, *ACS Nano* **2010**, *4*, 547. (b) S. Guo, S. Dong, E. Wang, *Small* **2009**, *5*, 1869.

28 G. P. Yin, S. Zhang, Y. Y. Shao, H. G. Liao, M. H. Engelhard, Y. H. Lin, *ACS Nano* **2011**, *5*, 1785. (b) S. T. Nguyen, S. Stankovich, R. D. Piner, X. Q. Chen, N. Q. Wu, R. S. Ruoff, *J. Mater. Chem.* **2006**, *16*, 155. (c) H. J. Shin, K. K. Kim, A. Benayad, S. M. Yoon, H. K. Park, I. S. Jung, M. H. Jin, H. K. Jeong, J. M. Kim, J. Y. Choi, Y. H. Lee, *Adv. Funct. Mater.* **2009**, *19*, 1987.

29 H. Qiu, X. Huang, *J. Mater. Chem.* **2012**, *22*, 7602.

30 (a) C. Susut, G. B. Chapman, G. Samjeske, M. Osawac, Y. Tong, *Phys. Chem. Chem. Phys.* **2008**, *10*, 3712. (b) X. L. Sun, S. H. Sun, G. X. Zhang,

D. S. Geng, Y. G. Chen, M. N. Banis, R. Y. Li, M. Cai, *Chem.Eur. J.* **2010**, *16,* 829.

31 (a) T. Biegler, D. A. J. Rand, R. Woods, *J. Electroanal. Chem.* **1971**, *29*, 269. (b) T. J. Schmidt, H. A. Gasteiger, G. D. Stab, P. M. Urban, D. M. Kolb, R. J. Behm, *J. Electrochem. Soc.* **1998**, *145*, 2354. (c) H. J. Kim, D.Y. Kim, H. Han, Y.G. Shul, J. *Power Sources* **2006**, *159,* 484.

32 (a) F. Su, J. Zeng, X. Bao, Y. Yu, J. Y. Lee, X. S. Zhao, *Chem. Mater.* **2005**, *17,* 3960. (b) S. P. Jiang, Z. Liu, H. L. Tang, M. Pan, *Electrochim. Acta* **2006**, *51,* 5721.

33 T. J. Schmidt, H. A. Gasteiger, G. D. Stab, P. M. Urban, D. M. Kolb, R. J. Behm, *J. Electrochem. Soc.* **1998**, *145*, 2354.

34 V. Komanicky, A. Menzel, H. You, *J. Phys. Chem. B* **2005**, 109, 23550.

35 (a) U. A. Paulus, A. Wokaun, G. G. Scherer, T. J. Schmidt, V. Stamenkovic, N. M. Markovic, P. N. Ross, *Electrochim. Acta* **2002**, *47*, 3787. (b) J. Wang, B. M. Ocko and R. R. Adzic, *Electrochim. Acta* **1995**, *40*, 83.

36 N. M. Markovic, H. A. Gasteiger, P. N. Ross, *J. Phys. Chem.* **1995**, *99*, 3411.

Chapter 4

Pt-RuO$_2$ Bimetallic Sandwich Type Thin layer Catalyst for Oxygen Reduction Reaction*

This chapter describes the synthesis and ORR acrivity of a Pt thin layer catalyst supported on an *in-situ* prepared ‘RuO$_2$-carbon-RuO$_2$’ sandwich type hybrid support. This is achieved by the extensive functionalization of a hollow CNF support to introduce oxygen containing functional groups (FCNF) with the specific aim to accomplish the exclusive adsorption of Ru ions along its inner and outer surfaces. Preferential adsorption of Ru ions from a mixture of Pt and Ru with sufficient time for adsorption and reorganization of ions on the FCNF surface leads to the *in-situ* renovation of FCNFs to form a hybrid ‘RuO$_2$-carbon-RuO$_2$’ sandwich type support followed by Pt NP decoration. The electrochemical studies using CV and RDE analysis show the improved activity of these materials with a three-fold increase in the ECSA of Pt coupled with a 80 mV gain in onset potential. Further, methanol oxidation studies reveal a drastic reduction in the CO poisoning of this material. Such an exceptionally high performance can be attributed to the strong electronic perturbations occurring in the Pt and the FCNF support due to the presence of a continuous RuO$_2$ layer in between. Such a bimetallic, sandwich type thin layer catalyst design with an unusual enhancement in the Pt utilization establishes the roles of both the hybrid support and active catalyst to address the future challenges in the area of utilization improvement.

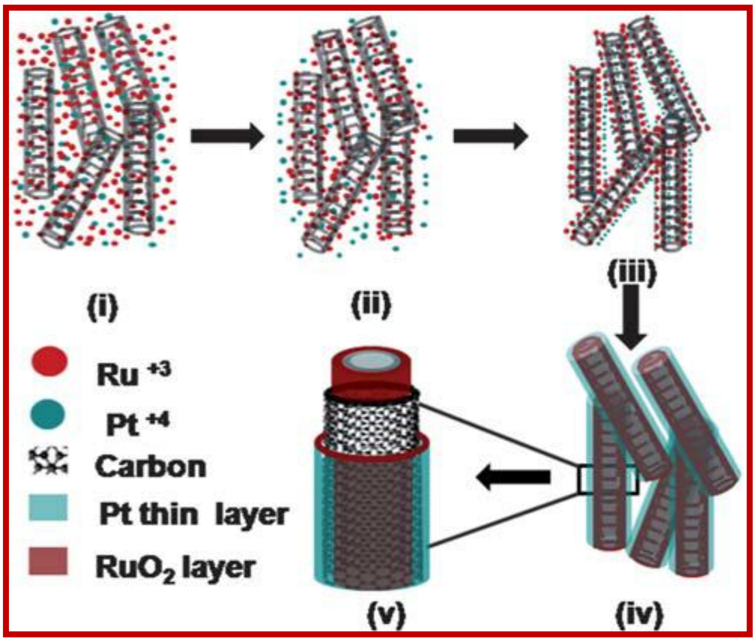

---

* The contents this chapter have been published in “*J. Mater. Chem.* **2011,** *21*, 19039-19048”.

4.1. Introduction

Increasing the utilization of noble metal NPs while maintaining the activity is an interesting challenge in many techno-commercially important fields, particularly in the case of electrocatalysts for ORR [1, 2]. Acquiring fundamental cognizance of the microstructure-to-property origins and engineering nanocatalysts at the atomic and molecular level, especially in the range of 1-10 nm, is particularly important for such catalysts to continue in the decades to follow with current or improved prominence [3, 4]. Recent advances in characterization techniques and first-principle calculations have triggered breakthroughs in materials science and revealed the details of microstructural features of such nanostructures to the material properties [5, 6]. Consequently, it is now possible, through a variety of techniques and fundamental understanding, to produce essentially homogenous nanostructures exhibiting high activity with countable utilization efficiencies, provided suitable processing pathways are chosen. Few prominent processing strategies adopted to significantly enhance the utilization of these ORR electrocatalysts involve new synthesis protocols for developing materials derived from alloys, core-shells, or thin film catalysts of bimetallics or multimetallics [7-11]. Such systems are emerging as a new class of materials for ORR since they are expected to show a combination of properties which are modified to a significant extent due to synergistic effects also [12].

Generally, Pt based systems with transition metals such as Fe, Co, Ni, Cr etc. have been found to be highly active for ORR [13-18]. For example, Mukerjee *et al*. reported enhancement in the ORR activity for Pt/Co, Pt/Ni or Pt-Cr alloy particles supported on carbon as compared to that of Pt/C [16]. Similar improvement in the ORR activity was reported for carbon supported alloy catalysts by other researchers also [17, 18]. Thus, it was found that the ORR activity of Pt can be enhanced to a significant extent by alloying with inexpensive non-noble metals. However, the Pt content in these types of catalysts will be high. Core-shell type materials with noble or non-noble metal core are another important class of ORR electrocatalysts [19-21]. There is ample evidence that the addition of non-noble metal can change the geometric as well as electronic structure of Pt, which weakens the chemisorption of O_2 and improves the ORR [20]. Moreover, by depositing Pt in the form of a thin monolayer, the amount of Pt in the catalyst layer can be reduced. Thus, by proper choice of the core and shell combinations, based on their segregation, electronic and strain inducing properties, the activity and utilization efficiency can be improved.

A review of the property-performance of such catalysts reveals that most of these catalysts are in the form of supported ones [22]. When the catalysts move from the free ones to the supported ones, it is very difficult to implement modifications, like optimization of type, size and shape, at the desired level to strengthen the utilization efficiency. Moreover, the foremost important issue of the supported catalysts is to maintain the finite dispersion of catalyst NPs on the support material. Generally, the weak interaction between Pt and the carbon support result in sintering and agglomeration of Pt nanoparticles [23]. In such a case, there remains an unsatisfactory fit between the free catalysts and the supported catalysts in terms of both performance and utilization [24].

In this context, the focus of the present research is to increase the utilization efficiency of the supported noble metal catalyst (Pt) by modulating its activity by virtue of a supporting RuO_2 layer. This is achieved by making use of the preferential adsorption of a desired metal ion on the support material over the other. Briefly, the utilization of the noble metal catalyst Pt has increased by forming a thin layer of the same on the inner and outer surfaces of an *in-situ* prepared 'RuO_2-carbon- RuO_2' sandwich type hybrid support material. This is effected by the extensive functionalization of CNF to introduce oxygen containing functional groups (FCNF), with the specific aim to accomplish the preferential adsorption of Ru ions from a mixture of Pt and Ru ions. This leads to the *in-situ* renovation of FCNFs to form a hybrid 'RuO_2-carbon-RuO_2' sandwich type support followed by Pt NP decoration. Catalysts with various Pt:Ru compositions supported on FCNF are also synthesized by a simple tuning of the Pt:Ru ratio using the same strategy. Monometallic Pt and RuO_2 NP supported catalysts are also prepared using the same approach. To demonstrate the role of oxygen containing functional groups in achieving the preferential adsorption of Ru ions and thereby in achieving the increased activity of Pt catalysts, control experiments are conducted with pristine CNFs for the best composition. This step is also important because in the absence of any pre-treatment, only the inner walls of CNFs will be active and this will lead to the random adsorption of metal ions on the active terminal graphene edges. Scheme 4.1 shows the major steps involved in the synthesis of the hybrid material. We also present an understanding of the properties of pure Pt, RuO_2 and Pt-RuO_2 bimetallic NPs of various compositions by electrochemical reactions, like ORR and methanol oxidation.

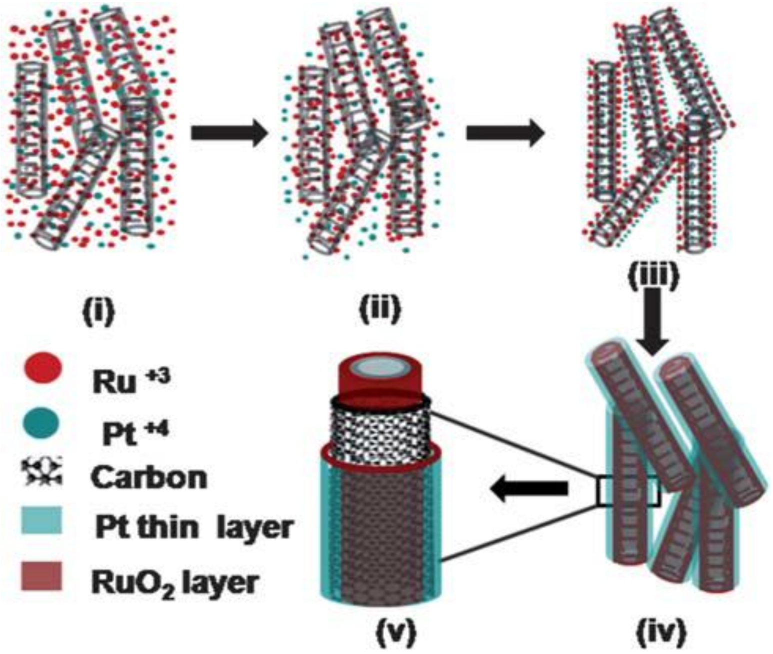

Scheme 4.1. Schematic illustration of the formation of Pt NPs supported on the *in-situ* prepared hybrid support; highlighted portion indicates the Pt thin layer formed on both sides of the RuO_2-carbon-RuO_2 sandwich type hybrid support.

4.2. Experimental Section

4.2.1. Synthesis of Pt-RuO_2 bimetallic catalyst

All the bimetallic catalysts with 20 wt% loading were prepared using the co-reduction of $H_2PtCl_6.6H_2O$ and $RuCl_3$ in the modified polyol process. Initially, the pre-treated CNFs were dispersed well in an EG-water solution containing the required amount of Pt^{4+} and Ru^{3+} ions. In the first step, the ions reorganize in the solution itself because of the affinity of Ru ions towards the oxygen containing functional groups. In the second step, the preferential adsorption of Ru ions on the FCNF occurs. With increase in time, the Pt ions remaining in the solution spontaneously assemble on these adsorbed Ru ions and subsequently primary NPs of both RuO_2 and Pt are formed on the FCNF surface upon increasing the reaction temperature to 140 °C to facilitate the reduction process. Such NPs of RuO_2 spontaneously reassemble to form a hybrid 'RuO_2-carbon-RuO_2' sandwich type support with a thin layer of Pt NPs on these supports. The material after the complete reduction was then collected by filtration and washed with water and dried under vacuum to obtain the NP decorated samples. The bimetallic catalysts having Pt:Ru atomic ratios of 1:5, 1:2, 1:0.5 respectively denoted as F-Pt_1Ru_5, F-Pt_1Ru_2, F-$Pt_1Ru_{0.5}$ were also prepared using the same strategy by changing the concentration of the precursor salts. Bimetallic catalysts with selective inner wall decoration were achieved using pristine CNFs (CPt_1Ru_5). For comparison, monometallic Pt and RuO_2 (F-Pt and F-RuO_2) catalysts supported on FCNFs were also prepared using the respective Pt and Ru precursors.

4.3. Results and Discussion

4.3.1. EDAX Analysis

EDAX analysis of the samples with various Pt:Ru ratios is carried out to find out the total catalyst loading on the CNF. Accordingly, Figure 4.1(a-d) shows the EDAX spectrum of F-Pt, F-$Pt_1Ru_{0.5,}$ F-Pt_1Ru_2 and F-Pt_1Ru_5 respectively and Table 4.1 summarises the EDAX quantification report of these samples. In all the samples, carbon content remains almost same *i.e.* 79-80%. In F-Pt, no trace of Ru is detected and the measured Pt content is 20%. Almost negligible amount of oxygen (~0.6%) is also detected in this sample. For F-$Pt_1Ru_{0.5}$, where the initial Pt:Ru ratio is 15:5, the EDAX quantification gave the Pt:Ru ratio as 14.25:4.72. For the catalyst with the initial Pt:Ru weight ratio 10:10 (F-Pt_1Ru_2), the calculated ratio from EDX is 9.87:8.33. Finally, for F-Pt_1Ru_5, the EDX quantification gives the Pt:Ru ratio as 3.56:12.91. This is slightly less as compared to the initial Pt:Ru ratio of 5:15. More importantly, if we compare the oxygen contents in various bimetallic combinations, there is a progressive increase in the oxygen content with increase in the Ru content.

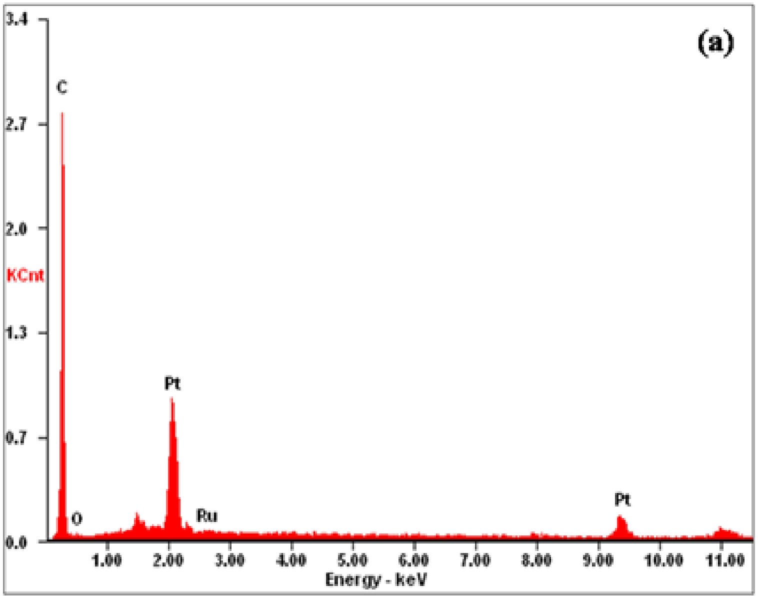

Figure 4.1. (a) EDAX spectrum of F-Pt

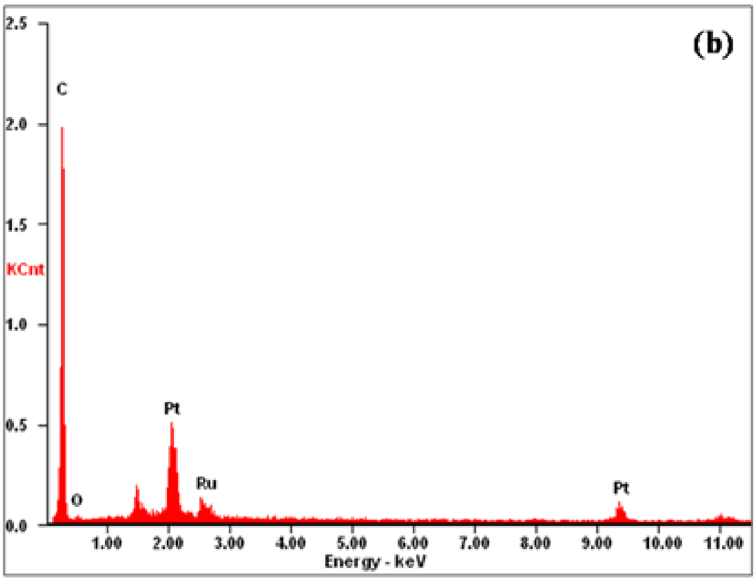

Figure 4.1. (b) EDAX spectrum of F-$Pt_1Ru_{0.5}$

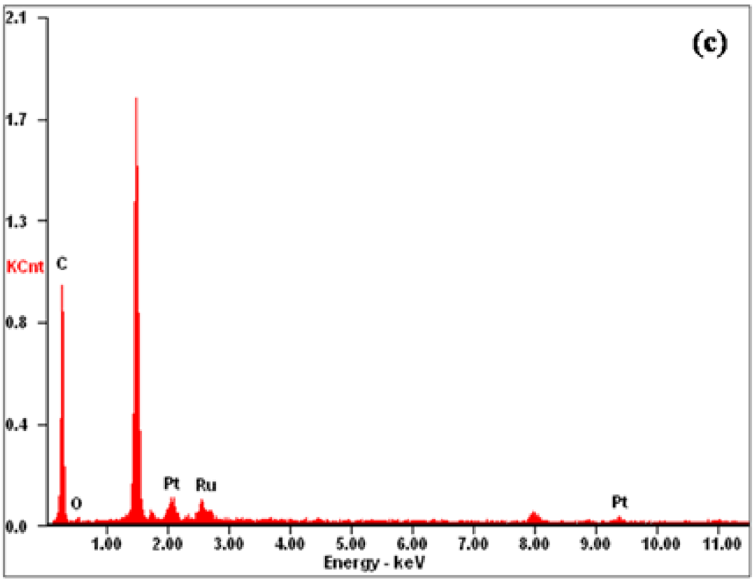

Figure 4.1. (c) EDAX spectrum of F-Pt_1Ru_2

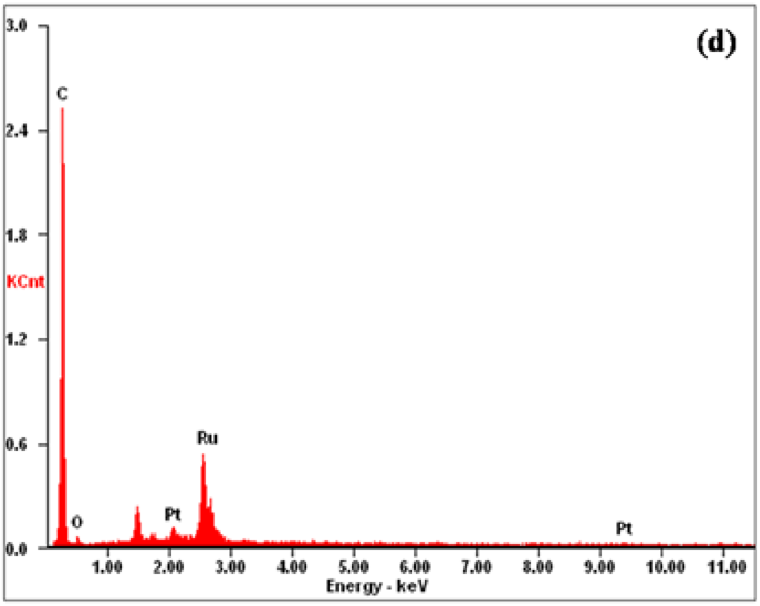

Figure 4.1. (d) EDAX spectrum of F-Pt_1Ru_5

Table 4.1. EDAX quantification of F-Pt, F-$Pt_1Ru_{0.5}$, F-Pt_1Ru_2 and F-Pt_1Ru_5.

Sample	**Carbon**		**Ruthenium**		**Platinum**		**Oxygen**	
	Wt%	**At%**	**Wt%**	**At%**	**Wt%**	**At%**	**Wt%**	**At%**
F-Pt	79.02	97.85	00.00	00.00	20.33	01.55	00.65	00.60
F-$Pt_1Ru_{0.5}$	79.84	97.33	04.72	00.61	14.25	0.97	01.19	01.09
F-Pt_1Ru_2	79.09	95.71	08.33	1.23	09.87	00.70	02.71	02.36
F-Pt_1Ru_5	79.64	94.36	12.91	01.81	03.56	00.26	03.89	03.56

4.3.2. TEM Analysis

The overall morphological and local compositional information of the bimetallic catalysts at various compositions is initially obtained from the TEM analysis. Figure 4.2(a-h) shows the TEM images of F-Pt, F-$Pt_1Ru_{0.5}$, F-Pt_1Ru_2 and F-Pt_1Ru_5 at various magnifications. The low magnification images of all the catalysts clearly show that the bimetallic NPs are uniformly dispersed on the high surface area FCNF support. It is also clear from the images that the individual NPs are anchored in a spatially uniform manner on the inner and outer walls of FCNF. However, a detailed analysis of the samples at various compositions reveals some interesting differences. The striking difference observed while comparing the HRTEM images of F-Pt [Figure 4.2(a and b)], F-$Pt_1Ru_{0.5}$ [Figure 4.2(c and d)], F-Pt_1Ru_2 [Figure 4.2(e and f)] and F-Pt_1Ru_5 [Figure 4.2(g and h)] is in the size of NPs. The average size of the NPs decreases with the increase in RuO_2 contents. An accountable difference in the shape is also observed while changing from pure Pt (F-Pt) to bimetallic Pt-RuO_2 NPs. In the case of F-Pt, as evident from Figure 4.2(b), slightly elongated NPs in the range of 3-4 nm are formed. The particles are well separated with clear boundaries. As the composition changes from pure Pt to bimetallic, spherical NPs with finest dispersion are observed especially in the case of F-$Pt_1Ru_{0.5}$ and F-Pt_1Ru_2, as shown in Figure 4.2(d and f), respectively. Moreover, the boundary between the individual particles becomes indistinguishable with increase in the RuO_2 content.

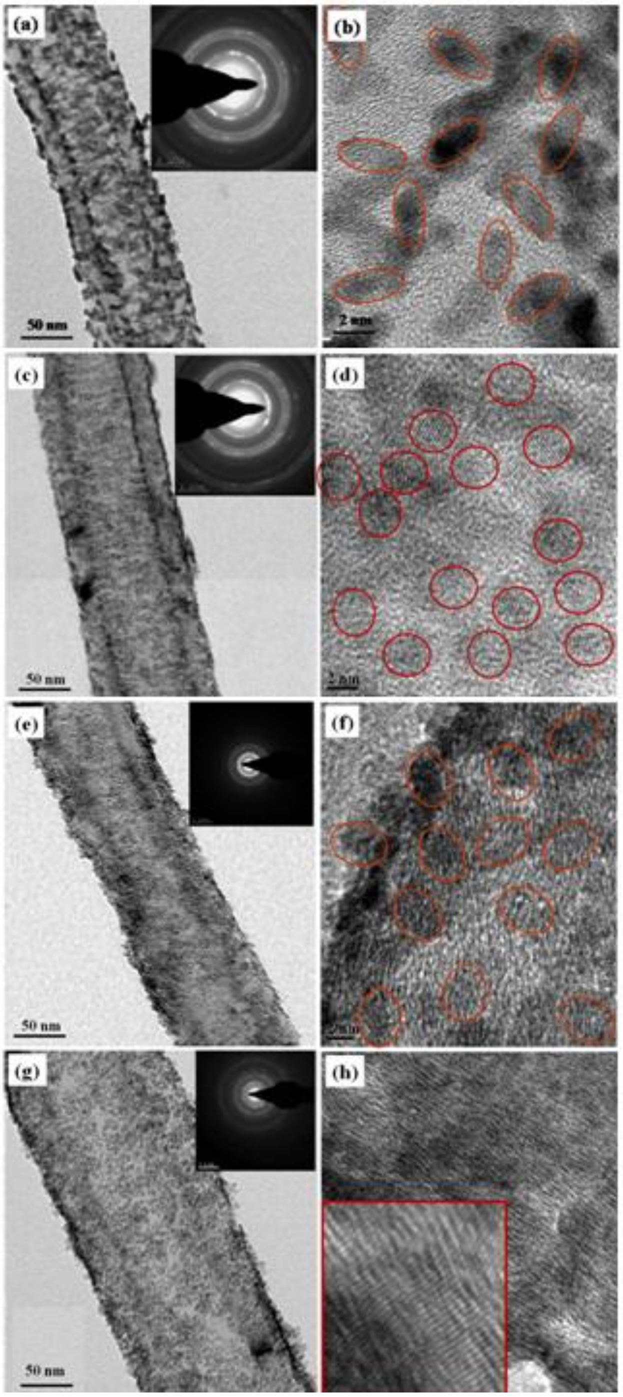

Figure 4.2. (a-h) TEM images of pure Pt and Pt-RuO_2 catalysts supported on FCNF at varying compositions; (a and b) for F-Pt, (c and d) for F-$Pt_1Ru_{0.5}$, (e and f) for F-Pt_1Ru_2 and (g and h) for F-Pt_1Ru_5.

Finally, at the 1:5 composition, the images show a lower contrast between the NPs with an unclear boundary between the crystallites as shown in Figure 4.2(h). This reveals that a continuous layer is formed on the support by a long range assembly and recrystallization of many small primary NPs. These observations suggest that the NPs grow into a thin nanosheet with uniform thickness on the surface of the support in F-Pt_1Ru_5.

A critical analysis of the HRTEM images of F-Pt, F-$Pt_1Ru_{0.5}$, F-Pt_1Ru_2 and F-Pt_1Ru_5 shown in Figure 4.3(a-d) respectively, reveals that all the catalyst compositions show features corresponding to Pt only. For all the catalysts, the *d*-value obtained is *ca.* 0.22 nm which matches with the (111) plane of fcc Pt, as can be evident from their clearly marked interplanar spacing in the inset of the respective figures [25]. The *d*-spacing corresponding to RuO_2 cannot be measured due to its amorphous nature. In F-$Pt_1Ru_{0.5}$ and F-Pt_1Ru_2, the regions with lower contrast correspond to the exposed RuO_2. Interestingly, in F-Pt_1Ru_2, the lattice fringes corresponding to Pt are more resolved as compared to that in F-$Pt_1Ru_{0.5}$. Finally, in F-Pt_1Ru_5 almost straight, continuous atomic fringes with clearly marked interplanar spacings of 0.221 nm are observed, as shown in Figure 4.3(d). The clear lattice image indicates that the NPs are well crystallized. As the catalyst is made of Pt and RuO_2, the chance for the overlap of crystalline planes of RuO_2 and Pt cannot be excluded. Moreover, the interplanar spacing of Pt and RuO_2 does not vary much and it falls within the range of permitted errors in the *d*-value measurement. The angle between two planes of an element, however, is reported to have a fixed value. Therefore, to confirm the composition of NPs, the angle between the observed planes is measured and is 129° [Figure 4.3(d)]. This is in close agreement with 127.28° for the calculated angle between the Pt (111) and Pt (100) planes [25]. This gives a direct indication for the fact that a thin layer made exclusively of Pt is formed in F-Pt_1Ru_5. Thus, the above observations indicate the selective exposure of Pt towards the surface with increase in the Ru content in the bimetallic combinations. As the exposed layer is completely made of Pt in F-Pt_1Ru_5, it can be hypothesized that RuO_2 is present immediately below the Pt layer, which is in intimate contact with the FCNF support. As this kind of layer-by-layer formation is possible in the inner cavity of FCNF also, ultimately it acts like a catalyst with a Pt thin layer exposed in the inner and outer walls of a 'RuO_2-carbon-RuO_2' sandwich type hybrid support. Further evidence for such *in-situ* hybrid support formation is inferred from a combination of TG, XRD, XPS and CV analysis results as given in later sections.

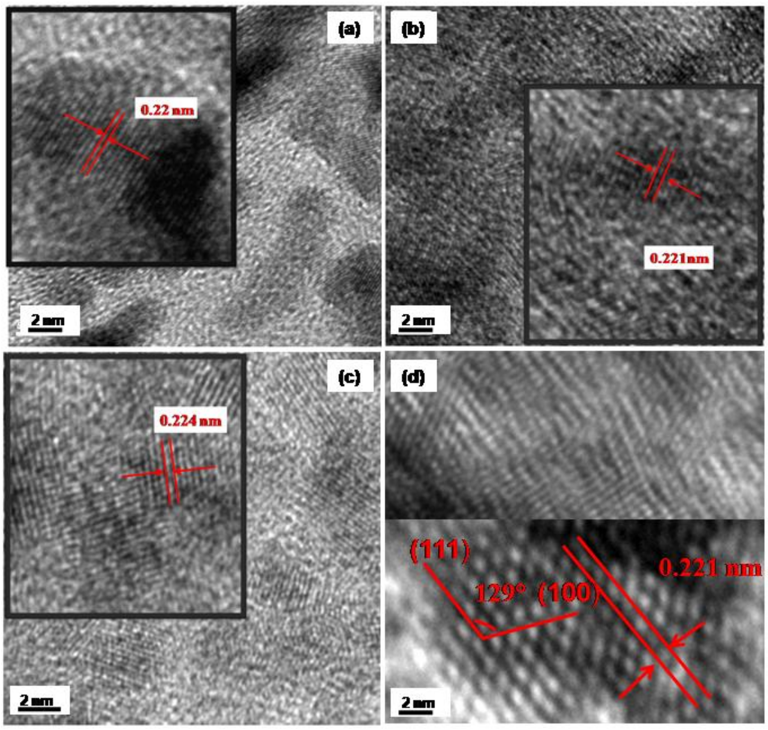

Figure 4.3. HRTEM images obtained for (a) F-Pt, (b) F-$Pt_1Ru_{0.5}$, (c) F-Pt_1Ru_2 and F-Pt_1Ru_5 with clearly marked interplanar spacing in the inset of the respective figures.

4.3.3. XRD Analysis

As HRTEM alone cannot solve the structure of the bimetallic catalyst, augmentation by complementary techniques is necessary for the confirmation of the structures. Therefore, XRD analysis of the catalysts has been carried out. Figure 4.4 shows a comparison of the XRD patterns of F-Pt, F-$Pt_1Ru_{0.5}$, F-Pt_1Ru_2 and F-Pt_1Ru_5. All the patterns show a diffraction peak at 26.5° which corresponds to the graphitic peak of the CNF support. The XRD pattern of F-Pt exhibits a typical face-centered cubic (fcc) lattice structure with strong diffraction peaks at 40.10, 46.49, and 68.08°, corresponding to the (111), (200), and (220) facets of Pt respectively [26]. As the composition of the catalyst moves from pure Pt to $Pt_1Ru_{0.5}$, peak broadening occurs. For the catalyst compositions with still higher RuO_2 contents (F-Pt_1Ru_2), peak broadening becomes more prominent and for the catalyst with the highest RuO_2 content (F-Pt_1Ru_5), only a signature for the presence of Pt (111) is observed. This may be attributed to the lack of sufficient scattering matter (Pt) in the material as it has formed a thin layer over RuO_2 [27]. The observed peak broadening, while moving from pure Pt to Pt_1Ru_x, gives a direct indication of size reduction of NPs and this size reduction may be attributed to the seeding effect of Ru which has lattice parameters smaller than that of Pt. The observed trend in size reduction gives a further confirmation for the observations from HRTEM imaging. Apart from this, the lack of shift in peak position as compared to that of F-Pt completely excludes the chance for alloy formation also [28].

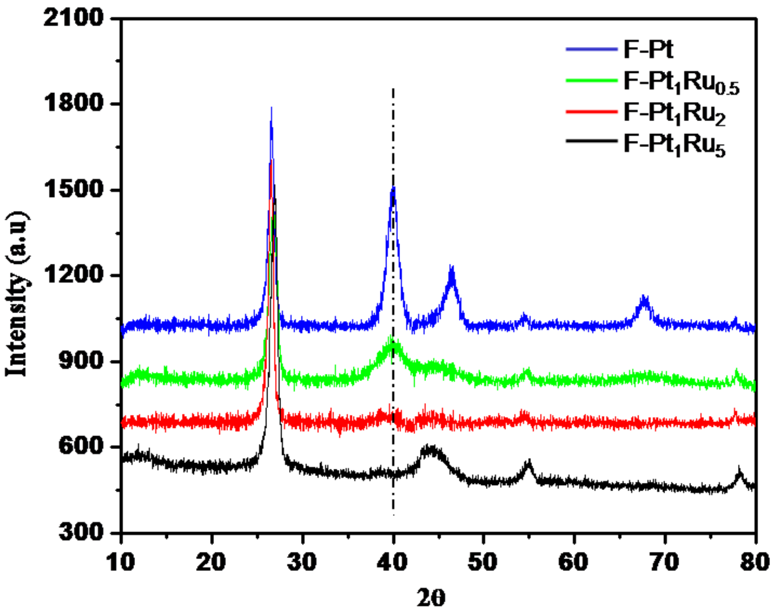

Figure 4.4. XRD patterns obtained for F-Pt, F-$Pt_1Ru_{0.5}$, F-Pt_1Ru_2 and F-Pt_1Ru_5

4.3.4. TG Analysis

TG analysis of F-Pt, F-$Pt_1Ru_{0.5}$, F-Pt_1Ru_2 and F-Pt_1Ru_5 is conducted in air from RT to 1000 °C to calculate the total catalyst loading on the CNF support. For an effective comparison, the TG analysis of pristine CNF is also conducted under similar conditions. Figure 4.5 shows the comparison of the TGA profile obtained for pristine CNF, F-Pt, F-$Pt_1Ru_{0.5}$, F-Pt_1Ru_2 and F-Pt_1Ru_5. All the catalysts show an initial small weight loss corresponding to residual water followed by a continuous weight loss of carbon up to 700 °C. From the residue content, the loading amount (both Pt and RuO_2) is calculated to be 19.8, 19.5, 19.2 and 18.6 wt% for F-Pt, F-$Pt_1Ru_{0.5}$, F-Pt_1Ru_2 and F-Pt_1Ru_5 respectively. It can also be noted from the TGA profile that the metal content present in the pristine CNF is close to zero and can be neglected. Further, it can also be inferred from the TGA profile that Ru is present in the form of RuO_2 only because if Ru is present in the metallic form, in presence of air, TGA profile will show a weight gain corresponding to the formation of RuO_2. This feature gives an interesting evidence for the conclusion that Ru exists exclusively as RuO_2 in the catalyst.

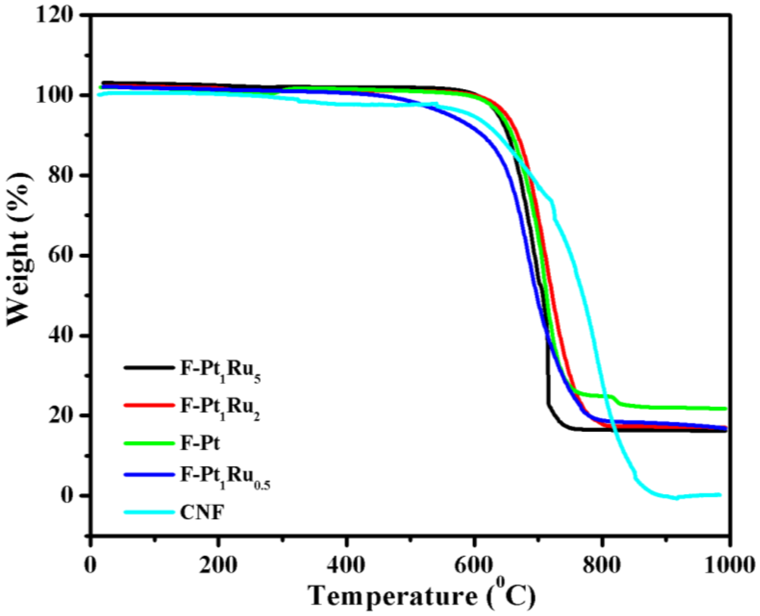

Figure 4.5. TGA profile obtained for CNF, F-Pt, F-$Pt_1Ru_{0.5}$, F-Pt_1Ru_2 and F-Pt_1Ru_5 in air atmosphere; temperature range RT-1000 °C, ramp 10°/min.

4.3.5. XPS Analysis

The insights into the atomic structure and surface chemical composition of the catalysts are obtained from XPS analysis. Accordingly, a comparison of the full survey XP spectra obtained for F-Pt, F-$Pt_1Ru_{0.5}$, F-Pt_1Ru_2, F-Pt_1Ru_5 and

F-RuO_2 before deconvolution is given in Figure 4.6. In all the catalyst compositions, peaks corresponding to C1s, O1s, and Fe2p are observed. The most intense peak observed at the BE of 284.5 eV can be attributed to the overlapped C1s levels in the catalysts [29]. The peaks at 534.5 and 740 eV correspond to the O1s and Fe2p respectively. Moreover, in F-Pt and in all bimetallic catalysts, a clear doublet corresponding to Pt4f levels is observed at a BE of 73.4 eV [27]. In sharp contrast to this, no signatures for Pt is observed in the XP spectra of F-RuO_2. As the most intense 3d levels of Ru overlap with the C1s levels, it is very difficult to perceive its presence before deconvolution. However, the peaks corresponding to Ru3p levels observed in the XP spectra of F-$Pt_1Ru_{0.5}$, F-Pt_1Ru_2, F-Pt_1Ru_5 and F-RuO_2 at the BE of 463.5 eV confirm the presence of Ru in these samples [27].

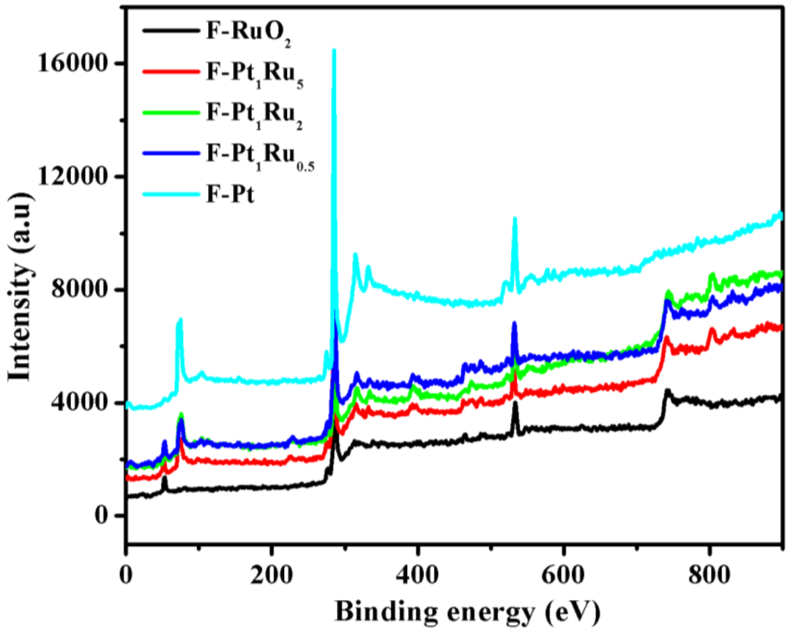

Figure 4.6. Full survey XP spectra obtained for F-Pt, F-$Pt_1Ru_{0.5}$, F-Pt_1Ru_2, F-Pt_1Ru_5 and F-RuO_2.

To gain more insights into the atomic structure and surface chemical composition of the supported catalysts, various parts of the XP spectra are deconvoluted.

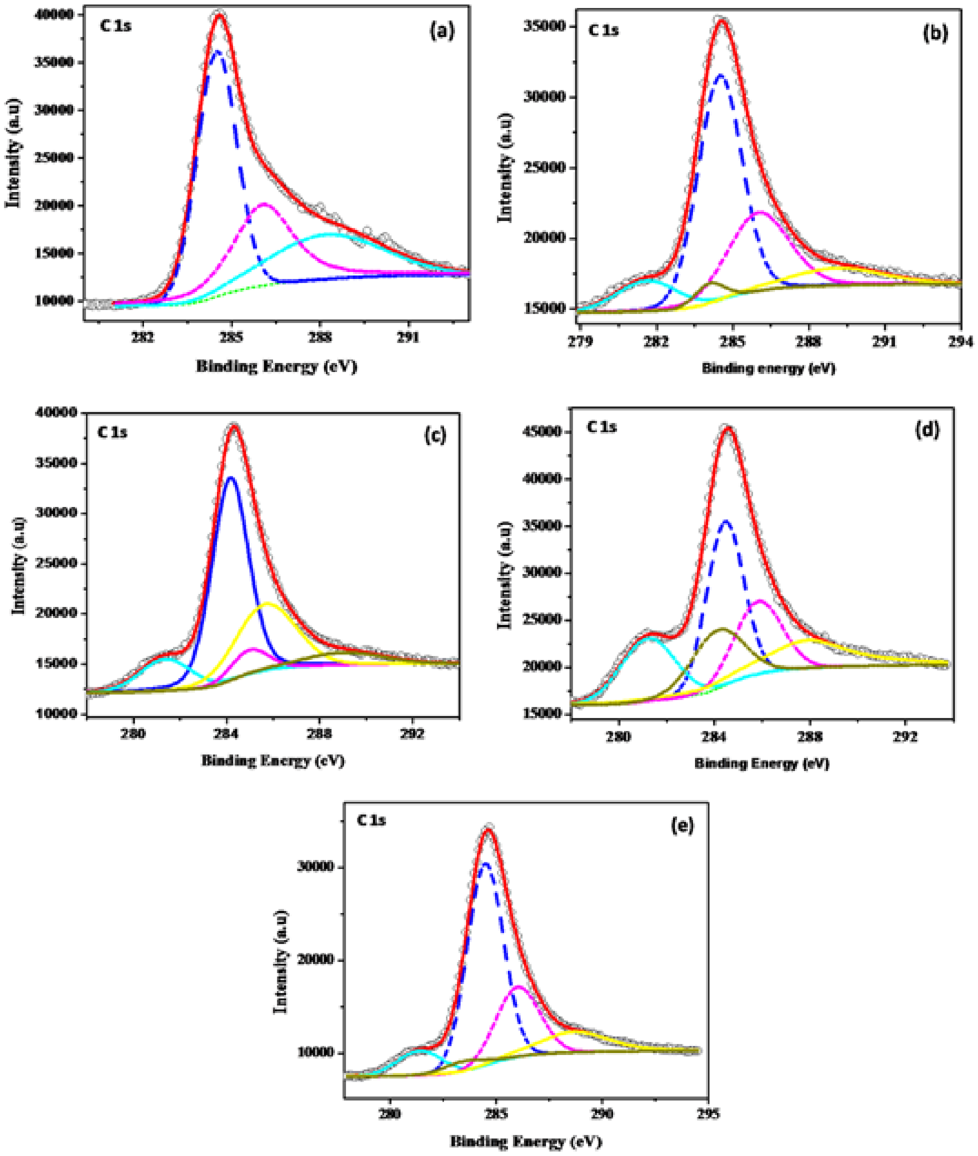

Figure 4.7. XP spectra of the C1s core level of (a) F-Pt and C1s and Ru3d core levels of (b) F-$Pt_1Ru_{0.5}$, (c) F-Pt_1Ru_2, (d) F-Pt_1Ru_5 and (e) F-RuO_2 after deconvolution; the circles represent the experimental data, red line represents the fitting data for the overall signal and the dashed lines are the deconvoluted individual peaks for different species present in the sample.

Figure 4.7(a-e) are the narrow scan spectra for the overlapped C1s and Ru3d core level regions of F-Pt, F-$Pt_1Ru_{0.5}$, F-Pt_1Ru_2, F-Pt_1Ru_5 and F-RuO_2 respectively. The C1s spectrum of F-Pt after deconvolution gives 3 peaks at Bes of 284.5, 286.1 and 288.2 eV corresponding to graphitic carbon and carbon bonded to -OH and -COOH groups respectively [29]. Interestingly, all the bimetallic combinations and pure RuO_2 catalyst after deconvolution give two additional peaks at BEs of 281.6 and 284 eV respectively, corresponding to the $3d_{1/2}$ and $3d_{3/2}$ levels of Ru. From the peak position, it is evident that Ru is in the form of RuO_2 in all the catalysts and no metallic Ru is detected. Apart from this, as can be seen from Figure 4.7, for all the catalysts, a considerable intensity of the peaks corresponding to C-OH and C-COOH are observed, which clearly confirms the presence of various oxygenated functional groups on the carbon surface. This reveals the extent of functionalization happening in the CNF.

The Pt4f levels of F-Pt, F-$Pt_1Ru_{0.5}$, F-Pt_1Ru_2 and F-Pt_1Ru_5 presented in Figure 4.8(a-d) respectively after deconvolution shows some interesting features. The Pt4f region of F-Pt gives one doublet at 71.1 and 74.4 eV corresponding to the $4f_{7/2}$ and $4f_{5/2}$ levels of Pt(0), as shown in Figure 4.8(a) [29]. However, in all bimetallic combinations, the deconvolution of the Pt region shows two doublets. This is indicative of the presence of Pt in two oxidation states [29]. This implies that, in the case of F-Pt, the Pt is exclusively in the Pt(0) state whereas in all the bimetallic combinations, Pt(0) as well as PtO are observed [29]. For the pure RuO_2 catalyst, no traces of Pt are detected. A comparison of the ratio of Pt:PtO in various catalyst compositions reveals some peculiarities. The Pt:PtO ratios are 76:24, 66:33 and 59:41 respectively for F-$Pt_1Ru_{0.5}$, F-Pt_1Ru_2 and F-Pt_1Ru_5 catalysts. The increase in the fraction of PtO with an increase in Ru content and the absence of PtO in F-Pt catalyst give a direct evidence for the prediction that Pt is directly attached to RuO_2 via Pt-O-Ru linkages. The observed shift in the binding energy to higher values in the case of PtO relative to the monometallic Pt NPs indicates the electronic changes effected in the system as a result of the interactions with the RuO_2 modifier [27, 29].

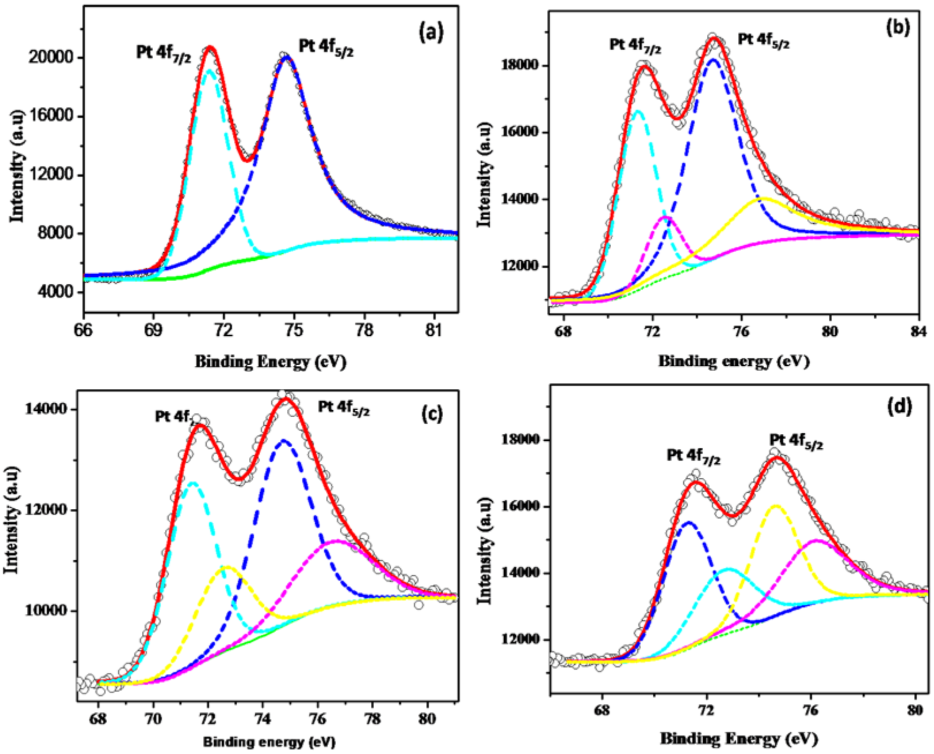

Figure 4.8. Deconvoluted XP spectra of Pt4f levels in (a) F-Pt, (b) F-Pt$_1$Ru$_{0.5}$, (c) F-Pt$_1$Ru$_2$ and (d) F-Pt$_1$Ru$_5$, clearly indicating the presence of Pt(0) and PtO species in all bimetallic combinations and pure Pt(0) in the F-Pt catalyst. The circles represent the experimental data, the red lines represent the fitting data for the overall signal and the dotted lines are the deconvoluted individual peaks for different species present in the sample.

The total loading of the NPs on to the carbon support cannot be determined from XPS because the support has a larger particle size than the sampling depth of the X-rays. Therefore, the XPS analysis gives the compositional information of the region closer to the surface. Accordingly, the surface atomic composition of all the monometallic and bimetallic catalysts obtained from XPS is shown in Table 4.2. For Pt, the 4f levels are selected because its high sensitivity factor of 4.4. For Ru, the 3d levels are used for the composition evaluation. Though the sensitivity factor of 3d levels is high, it overlaps with the intense C1s peak. In such a case, deconvolution and analysis may lead to inaccuracy. Therefore, the composition calculation is confirmed using the 3p levels also; which have a sensitivity factor of 1.3.

Table 4.2. Surface composition evaluation from XPS analysis.

Sample	Carbon	Ruthenium	Platinum	Pt:Ru (wt%)	Pt:Ru atomic ratio
F-Pt	284.5 286.1 288.2	-	71.1 74.4	100% Pt	Pure Pt
F-$Pt_1Ru_{0.5}$	284.5 286 289.1	281.6 284	71.3 74.6 72.4 76.8	3	$Pt_1Ru_{0.5}$
F-Pt_1Ru_2	284.5 285.9 289.3	281.6 285	71.4 74.8 72.6 76.7	1.22	$Pt_1Ru_{1.7}$
F-Pt_1Ru_5	284.4 286 288	281.2 284.1	71.2 74.5 72.6 76.2	0.43	Pt_1Ru_4
F-RuO_2	284.5 286 288.6	281.4 283.5	-	100% Ru	Pure Ru

From the XPS quantification given in Table 4.2, it is found that in some catalyst compositions, especially those with the high Ru contents, the actual Pt:Ru ratios are slightly higher than those expected. Accordingly, $Pt_1Ru_{0.5}$ reveals a Pt:Ru atomic ratio of 3 and thus gives a surface concentration (within the penetration depth of XPS) of Pt versus Ru as 75-25%. In this composition, the Pt:Ru atomic ratio is exactly retained as per the original composition maintained during the synthesis. However, for F-Pt_1Ru_2 and F-Pt_1Ru_5 catalyst compositions, the Pt:Ru ratios obtained are 1.22 and 0.43, respectively, giving a corresponding surface composition of 55-45% and 30-70%. It is exciting to note the 22% and

30% enrichment in the surface Pt contents compared to the initial Pt:Ru atomic ratios of 1 and 0.33 respectively in F-Pt_1Ru_2 and F-Pt_1Ru_5. This gives unambiguous evidence for the selective exposure of Pt to the surface due to the preferential adsorption of Ru on the functional groups.

The XPS quantifications of F-Pt and F-$Pt_1Ru_{0.5}$ are in excellent agreement with the EDAX results and the initial Pt:Ru ratio calculated from the precursor amounts. However, for the catalyst combinations with higher Ru contents, a significant difference is observed in the Pt:Ru ratio obtained from the XPS and EDAX quantifications. This discrepancy can be attributed to the limitation of XPS in depth profiling. In F-Pt and F-$Pt_1Ru_{0.5}$, the surface and bulk concentrations are almost same and consequently both the EDAX and XPS results appeared to be matching. However, in the case of F-Pt_1Ru_2 and F-Pt_1Ru_5, the surface and bulk concentrations are distinctly different due to the surface enrichment of Pt, which leads to a difference in the quantification obtained from the two methods. But the trend observed in the increase of the fraction of oxygen content with increases in the Ru content from the XPS analysis is exactly similar to that obtained from the EDAX analysis.

4.3.6. Probable Mechanism of Morphology Evolution

The probable mechanism of the formation of NP assembly at various compositions is schematically depicted in Scheme 4.2. In the case of NP decoration on FCNF, irrespective of monometallic or bimetallic systems, adsorption of ions on the anchoring sites followed by reduction occurs. In the present case, as Ru has a greater affinity for oxygen containing functional groups (here the anchoring sites), preferential adsorption of Ru occurs [30]. When the amount of Ru is less than that required for monolayer coverage on FCNF, Pt ions act as fillers and the remaining Pt forms a second layer on Ru. This happens when the catalyst compositions are $Pt_1Ru_{0.5}$ and Pt_1Ru_2. When the amount of Ru increases in the compositions, the fraction of Pt exposed to the surface also increases concomitantly and when the Ru content is more than the threshold for monolayer coverage, a structure as shown in Scheme 4.2 for the composition

Pt_1Ru_5 is formed. Here, Ru forms a complete layer on FCNF, leading to the *in-situ* modification of FNCF to a hybrid type support material. It is also important to note that Ru is showing characteristics of RuO_2 as it is directly attached to O_2 containing functional groups (from XPS analysis). Now the primary Pt NPs self-assemble and reorganize to form a uniform thin layer on this hybrid support material. The Pt NP decoration on the RuO_2 platform is also facilitated by the high degree of lattice miscibility as is evident from its tendency for alloy formation over a wide composition and temperature range [31]. Moreover, it is also reported that even in the case of Pt-Ru core-shell formation, a thin RuO_2 shell covering the Ru(0) core is required for Pt coating and Ru particles prepared under rigorous anaerobic conditions do not provide good seeds for core-shell particle growth, resulting in the formation of phase-separated monometallic mixtures [27]. Thus, in the present case, the uniform RuO_2 layer formed on the FCNF support acts as the platform for the growth of the continuous monolayer of Pt, as depicted in the figure for the F-Pt_1Ru_5. Interestingly, when pristine CNF is used for NP decoration, where such anchoring sites are absent, a random adsorption of ions followed by reduction occurs. This is schematically shown for the catalyst C-Pt_1Ru_5.

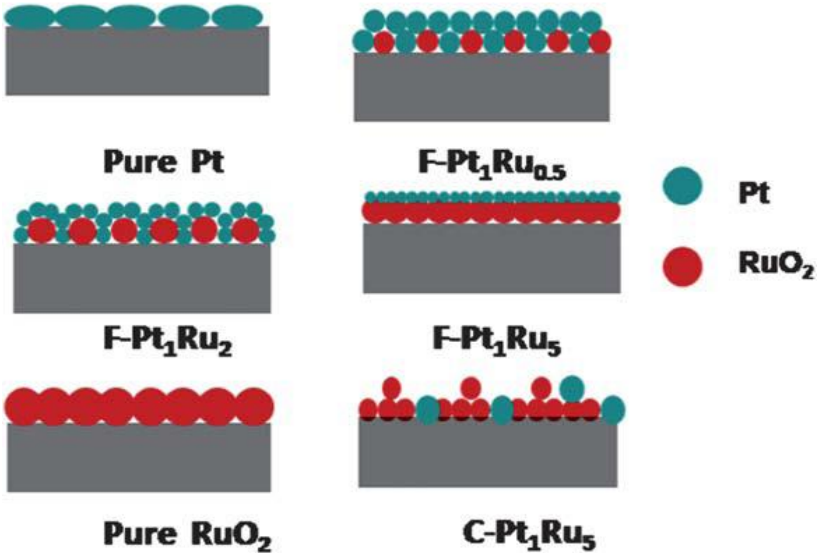

Scheme 4.2. Schematic representation of the morphology evolution at various catalyst compositions.

4.3.7. Electrochemical Studies

4.3.7.1. CV Analysis

To probe the electrochemical activity of the bimetallic catalysts, ORR and methanol oxidation reactions of all the bimetallic combinations are performed and compared with the performance characteristics of pure Pt catalysts. Accordingly, Figure 4.9 summarizes the activity of F-Pt_1Ru_5, F-Pt_1Ru_2, F-$Pt_1Ru_{0.5}$ and F-Pt for ORR. In the CVs obtained in a 0.5 M H_2SO_4 electrolyte solution, the peaks in the region of 0.15-0.45 V originate from hydrogen adsorption/desorption on a polycrystalline Pt electrode [32]. The ECSA of F-Pt_1Ru_5 (at a loading of 0.013 mg/cm^2) determined (as discussed in Chapter 2) by calculating the charge associated with an adsorbed monolayer of hydrogen is 384 cm^2/mg-Pt [32]. The current density and ECSA obtained for F-Pt_1Ru_2, F-$Pt_1Ru_{0.5}$ and F-Pt catalysts are 25 mA/mg-Pt and 224 cm^2/mg-Pt, 12 mA/mg-Pt & 105 cm^2/mg-Pt and 14 mA/mg-Pt and 142 cm^2/mg-Pt respectively. The best activity as evident from the 3-fold higher ECSA and the highest current density obtained for F-Pt_1Ru_5 is further emphasized by the 100 mV onset potential gain for ORR when compared to the rest of the catalysts.

A closer inspection of the H_2 region in the CV indicates that the features of F-Pt and F-Pt_1Ru_5 are exactly similar with the highest intensity peak around 0.22 V, which corresponds to the (110) plane of Pt [33]. This increased intensity reflects that more (110) planes are exposed in these catalysts. However, decreased intensity corresponding to the (110) plane is observed in the case of F-$Pt_1Ru_{0.5}$ and F-Pt_1Ru_2. This can be attributed to the suppression in the activity of this plane. This peculiar resemblance in the CV of F-Pt_1Ru_5 with that of F-Pt further strengthened the claim that a major fraction of Pt is present on the surface of the *in-situ* prepared hybrid support.

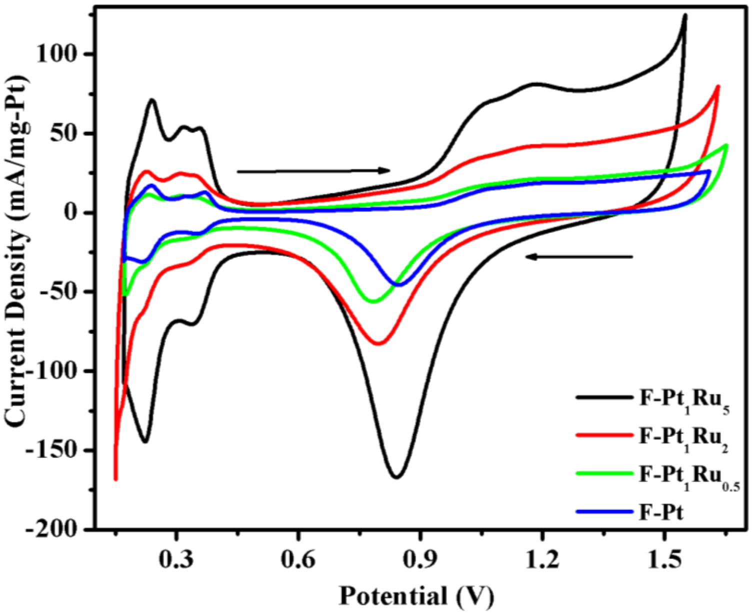

Figure 4.9. Superimposed CVs for the ORR of F-Pt, F-$Pt_1Ru_{0.5}$, F-Pt_1Ru_2 and F-Pt_1Ru_5; electrolyte 0.5 M H_2SO_4, scan rate 50 mV/s; all the potentials are quoted *vs.* RHE.

Further, to demonstrate the role of oxygen containing functional groups in achieving the preferential adsorption of Ru ions and thereby achieving the increased activity of Pt catalysts, the electrochemical activity of a catalyst having the best composition supported on pristine CNF (C-Pt_1Ru_5) is also evaluated. Accordingly, Figure 4.10 shows the CV profile obtained for the C-Pt_1Ru_5 in 0.5 M H_2SO_4 at different scan rates in the range of 5-150 mV/s. The CVs exhibit almost rectangular shape, the typical capacitive behaviour exactly similar to that reported for hydrous RuO_2 [34]. Apart from this, the capacitance current of the electrode increases with increasing the scan rate and the rectangular shape of the CV is also maintained even at various scan rates, which indicates excellent capacitance behavior [34]. Thus, F-Pt_1Ru_5 shows CV features similar to that of a polycrystalline Pt electrode whereas the C-Pt_1Ru_5 shows typical capacitive behaviour. This transition from the characteristic oxygen reduction behaviour of Pt to the characteristic capacitive features of RuO_2 clearly indicates that Pt is selectively exposed to the surface in F-Pt_1Ru_5 due to the preferential adsorption of Ru ions by virtue of the surface functional groups. In sharp contrast to this, in the case of C-Pt_1Ru_5 most of the Pt is merged in the RuO_2 layer and hence suppressing its activity. The above results confirm the role of oxygen containing functional groups in the design of the new catalyst for improving the Pt utilization.

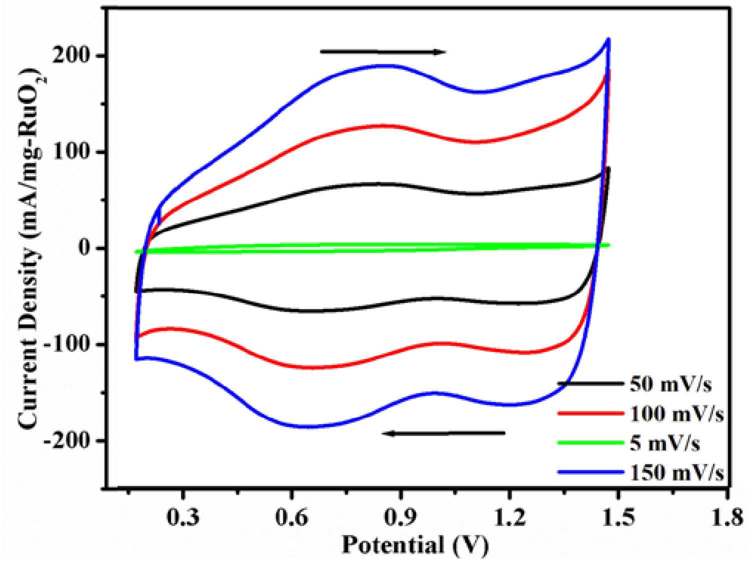

Figure 4.10. Superimposed CVs of C-PtRuO$_2$ in 0.5 M H_2SO_4 at the scan rates of 5, 50, 100 and 150 mV/s.

4.3.7.2. Methanol Oxidation Studies

As the addition of Ru and/or RuO$_2$ to Pt is highly beneficial in increasing the carbon monoxide (CO) tolerance, the MeOH oxidation study is also carried out using the bimetallic catalysts of various compositions and is compared with F-Pt. As shown in Figure 4.11, the CV shows typical characteristics of MeOH oxidation with two main features. F-Pt shows the forward peak at 0.9 V which moves to a more negative potential on RuO$_2$ addition. This is consistent with the observations on nanoscale bimetallic Pt-RuO$_2$ catalysts [5].

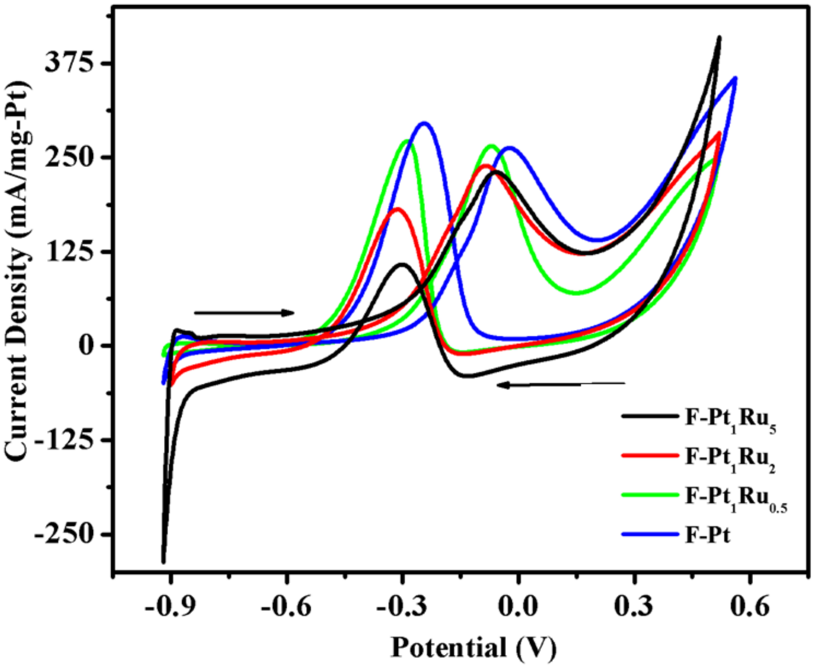

Figure.4.11. Superimposed CVs for the MeOH oxidation reaction of F-Pt, F-$Pt_1Ru_{0.5}$, F-Pt_1Ru_2 and F-Pt_1Ru_5. Electrolyte: 0.5 M H_2SO_4 + 1 M MeOH; scan rate: 50 mV /s; all the potentials are quoted *vs*. RHE.

The tolerance factor (I_f/I_b); *i.e.* the ratio of forward anodic peak current (I_f) to the reverse anodic peak current (I_b); is another important index generally used for evaluating the catalyst tolerance towards CO poisoning during the MOR [33]. A high I_f/I_b value indicates relatively lower poisoning of the catalyst with high CO tolerance. The forward currents generated in the MeOH reaction on all the catalysts are almost identical (260 mA/mg-Pt) but a drastic reduction in the backward current density is observed with increase in the RuO_2 content, which are 300, 268, 181 and 112 mA/mg-Pt for F-Pt, F-$Pt_1Ru_{0.5}$, F-Pt_1Ru_2 and F-Pt_1Ru_5 respectively, as presented in Table 4.3. The tolerance factor calculated for the various catalyst compositions, *i.e*. 0.87, 0.97, 1.38 and 2.21 respectively for F-Pt, F-$Pt_1Ru_{0.5}$, F-Pt_1Ru_2 and F-Pt_1Ru_5, clearly demonstrates the role of RuO_2 in reducing the CO poisoning effect. A 2.5-fold reduction in the backward current density of F-Pt_1Ru_5 when compared with that of F-Pt indicates the high tolerance of this catalyst for CO in the methanol stream. In fact, all the bimetallic catalysts displayed CO tolerance better than that of F-Pt. Overall, the improved performance of F-Pt_1Ru_5 for ORR is further emphasized by its better tolerance and favourable onset potential for the MeOH oxidation reaction [35].

Table 4.3. Comparison of methanol oxidation activities.

Sample	**MeOH Oxidation**		
	I_f (mA/mg-Pt)	**I_b (mA/mg-Pt)**	**I_f/I_b**
F-Pt	260	300	0.87
F-$Pt_1Ru_{0.5}$	260	268	0.97
F-Pt_1Ru_2	250	181	1.38
F-Pt_1Ru_5	247	112	2.21

4.3.7.3. RDE Analysis

As RDE studies allow accurate correction of ohmic and transport overpotentials and therefore yield reliable estimates of upper bounds of intrinsic catalytic activities, the actual oxygen reduction activities of these catalysts are demonstrated using RDE studies also [32]. Figure 4.12(a) shows the polarization curves obtained for the ORR in 0.5 M H_2SO_4 at a scan rate of 5 mV/s and at a rotating speed of 1600 rpm for all the bimetallic combinations and pure Pt catalyst. The ORR could be divided into the kinetic, mixed and mass transfer controlled regions in an ORR polarization curve and the limiting current, onset potential and half wave potentials are indicative of the performance of an electrocatalyst [36]. In the present case, the sigmoidal shape of the ORR characteristic is shifted to more positive potentials in all bimetallic compositions as compared to that of F-Pt indicating ORR activity at much lower overpotentials. The respective onset potentials observed are 0.84, 0.81, 0.73 and 0.76 V for F-Pt_1Ru_5, F-Pt_1Ru_2, F-$Pt_1Ru_{0.5}$ and F-Pt. There is a substantial gain in the onset potential by *ca.* 80 mV for F-Pt_1Ru_5 as compared to pure Pt catalyst. The limiting current region, where the ORR is controlled by the diffusion of dissolved oxygen from bulk to the electrode surface (at a potential less than 0.7 V), also unambiguously shows a significant difference. The limiting current density is progressively increased and it follows the order F-Pt_1Ru_5 > F-Pt_1Ru_2 > F-Pt > F-$Pt_1Ru_{0.5}$. The limiting current obtained for F Pt_1Ru_5, presented in Table 4.4, is almost 4 times higher compared to the pure Pt catalyst. The half wave potentials of the corresponding catalysts are 0.72, 0.63, 0.62 and 0.68 V respectively for F-Pt_1Ru_5, F-Pt_1Ru_2, F-$Pt_1Ru_{0.5}$ and F-Pt. Therefore, a comparison of the onset potential, limiting current and half wave potential reveals an unprecedented improvement in the ORR activity of F-Pt_1Ru_5 as compared to the pure Pt catalyst.

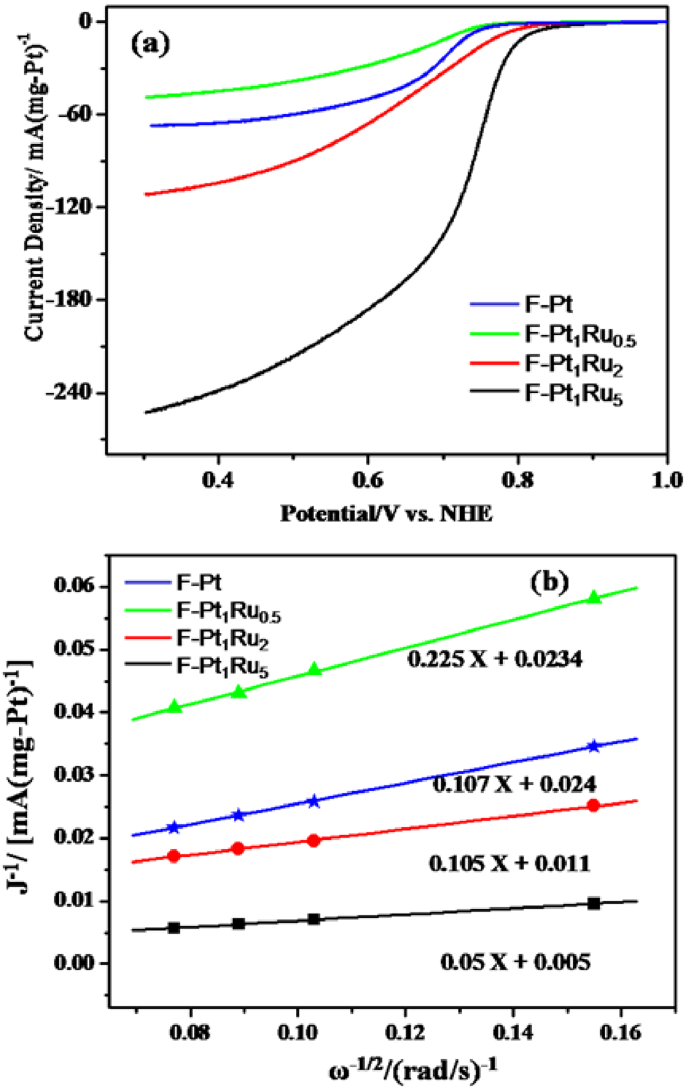

Figure 4.12. (a) Polarization curves at a scan rate of 5 mV/s and a rotation rate of 1600 rpm and (b) Koutecky-Levich plots at 0.72 V for the oxygen reduction reaction on different Pt-RuO_2 catalysts with comparisons to pure Pt in 0.5 M H_2SO_4 at 298 K; all the potentials are quoted *vs.* RHE.

Table 4.4. Comparison of oxygen reduction activities from RDE.

Sample	Onset Potential (V)	Half Wave Potential (V)	Limiting Current density (mA/mg-Pt)
F-Pt	0.76	0.68	46
F-$Pt_1Ru_{0.5}$	0.73	0.62	65
F-Pt_1Ru_2	0.81	0.63	110
F-Pt_1Ru_5	0.84	0.72	250

In order to obtain a more detailed insight into the mechanistic aspects of the ORR on these catalysts, K–L plots of all the four catalysts are also analysed at 0.72 V and the results are given in Figure 4.12(b) (details about the K-L plot are given in Chapter 3). Both the slope and intercept of the K-L plot have greater implications in the ORR mechanisms and the inverse of the slope of the K-L plot gives insight into the mechanistic aspects of the ORR on catalysts. On a closer inspection of the K-L plots obtained for the various catalyst compositions, it is evident that the plots are not parallel and there is an accountable difference in the slopes obtained for different catalysts. The slopes obtained are 0.05, 0.105, 0.225 and 0.107 for F-Pt_1Ru_5, F-Pt_1Ru_2, F-$Pt_1Ru_{0.5}$ and F-Pt respectively. These variations in the slopes suggest some possible differences in the reaction mechanisms based on the active sites available in the catalyst compositions and it can be explained as follows. In Pt-RuO_2 bimetallic systems, due to the entirely different bulk crystal structure of the two metals (Pt with fcc and Ru with hcp) and the presence of a slight difference in the atomic distance corresponding to the bulk phase for Pt and Ru ($d_{\text{Ru-Ru}}$ = 2.705 A°, $d_{\text{Pt-Pt}}$ = 2.774 A°), there will be strong electronic perturbations in order to achieve a minimum energy relaxed state [37]. Such modifications strongly depend on the nature of the neighbouring atoms and the extent of the interaction between them. As a result of this, the changes will be maximum at the bimetallic interfaces and as the distance from such interface increases, the resultant effects decrease. In the present study, when the Pt:Ru ratio changes, there are obvious changes in the RuO_2 environment, where Pt atoms nestle comfortably and hence the electronic changes transpired will also vary significantly from one composition to another. In $FPt_1Ru_{0.5}$, where the RuO_2 content is the least, such changes will be minimum whereas in the other bimetallic compositions with higher RuO_2 contents, the interfacial area will also increase accordingly, thus leading to a prominent difference in such changes. Thus, the catalyst with the highest Pt:Ru ratio and a concomitantly larger interfacial area (F-Pt_1Ru_5) will show the maximum electronic changes and accordingly this composition displayed maximum deviation in the slopes obtained from the K-L plot as compared to that of F-Pt. This indirectly gives evidence for the synergistic effect of RuO_2 in modulating the activity of Pt by electronic changes in the system.

The unusual enhancement in the performance characteristics of F-Pt_1Ru_x catalysts can be explained as follows. When Ru is added to the catalyst system, due to its tendency for preferential adsorption, Pt is selectively exposed to the surface. When the amount of Ru increases, the fraction of Pt exposed also increases concomitantly and once a catalyst bed made of RuO_2 is formed on the FCNF support, a major fraction of Pt is exposed to the surface. As in the case of conventional core-shell type systems, here also the utilization of Pt increases. This feature gives an enhancement in terms of the active area of Pt and subsequently to its ORR activity. Generally, the increase in the CO tolerance observed for the bimetallic systems can be ascribed to the bifunctional mechanism of spilling over the hydroxyl species from RuO_2 to Pt in close proximity. However, the unusual enhancement in the CO tolerance displayed by F-Pt_1Ru_5 can be attributed to multiple factors. The diffusion of electro-active species is different on pure Pt, pure RuO_2 and Pt sites around the periphery of RuO_2. In F-Pt_1Ru_5, a major fraction of Pt is in direct contact with the RuO_2 layer which greatly modifies the diffusion of the species in and out of the surface [5]. Apart from this, the bifunctional pathway for the reduction in CO poisoning is also enhanced as there is a continuous supply of -OH to the Pt sites by virtue of the Pt-O-Ru linkages. It is also possible that the continuous RuO_2 layer can also bring about strong electronic perturbations in the Pt phase [38]. In the present study, long-range modifications in the electronic structure of the support are also evident.

4.4. Conclusions

Pt-RuO_2 bimetallic catalysts with atomic compositions 1:0.5, 1:2 and 1:5 supported in the inner cavity as well as on the outer walls of a functionalized, hollow CNF have been prepared using a modified polyol process. It is observed that when the amount of Ru in the composition increases, due to its preferential adsorption on the oxygen containing functional groups, Pt is selectively exposed to the surface. Apart from this, strong electronic perturbations are also brought about in the system due to the strong interaction between the catalyst support and RuO_2. Finally at the 1:5 composition, a uniform, thin layer of Pt supported on an *in-situ* prepared 'RuO_2-carbon-RuO_2' sandwich type hybrid is formed. Electrochemical evaluation of these catalysts for ORR and methanol oxidation reactions revealed exceptionally high activity at the 1:5 composition. In fact, all the bimetallic catalysts except F-$Pt_1Ru_{0.5}$ displayed activity higher than the pure Pt catalyst. Such an unusual enhancement in the performance of F-Pt_1Ru_5 for both ORR and MeOH oxidation can be attributed to the formation of a high aspect ratio sandwich type catalyst supplemented with electronic and structural modifications in the catalyst and catalyst support phases. The sensible improvement in the utilization of Pt catalyst illustrates the concept that the hybrid support material plays a crucial role in the property improvement by synergistic and electronic effects. The markedly different activity of F-Pt_1Ru_5 firmly establishes the role of both hybrid support and catalyst to address the future challenges in the area of utilization improvement.

4.5. References

1 D. Zhao, B. Xu, *Angew. Chem. Int. Ed.* **2006**, *45*, 4955.

2 J. Zeng, J. Y. Lee, J. Chen, P. K. Shen, S. Song, *Fuel Cells* **2007**, ***4***, 285.

3 C. S. H. Joo, S. J. Choi, I. Oh, J. Kwak, Z. Lui, O. Terasaki, R. Ryoo, *Nature* **2001**, *412*, 169.

4 M. S. Nashner, A. I. Frenkel, D. Somerville, C. W. Hills, J. R. Shapley, R. G. Nuzzo, *J. Am. Chem. Soc.* **1998**, *120*, 8093.

5 Y. Tong, H. S. Kim, P. K. Babu, P. Waszczuk, A. Wieckowski, E. Oldfield, *J. Am. Chem. Soc.* **2002**, *124*, 468.

6 V. R. Stamenkovic, B. S. Mun, M. Arenz, K. J. J. Mayrhofer, C. A. Lucas, G. Wang, P. N. Ross, N. M. Markovic, *Nat. Mater.* **2007**, *6*, 241.

7 S. Zhou, G. S. Jackson, B. Eichhorn, *Adv. Funct. Mater*. **2007**, *17*, 3099.

8 S. Zhang, Y. Shao, G. Yin, Y. Lin, *Angew. Chem. Int. Ed.* **2010**, *49*, 2211.

9 Z. Liu, G. S. Jackson, B. W. Eichhorn, *Angew. Chem. Int. Ed.* **2010**, *49*, 3173.

10 V. M. Dhavale, S. M. Unni, H. N. Kagalwala, V. K. Pillai, K. Sreekumar, *Chem. Commun.* **2011**, *47*, 3951.

11 B. Wickman, Y. E. Seidel, Z. Jusys, B. Kasemo, R. J. Behm, *ACS Nano* **2011**, *5*, 2547.

12 D. Wang, Y. Li, *Adv. Mater.* **2011**, *23*, 1044.

13 V. R. Stamenkovic, B. S. Mun, M. Arenz, K. J. J. Mayrhofer, C. A. Lucas, G. F. Wang, P. N. Ross, N. M. Markovic, *Nat. Mater.* **2007**, *6*, 241.

14 Z. Liu, G. S. Jackson, B. W. Eichhorn, *Angew. Chem. Int. Ed.* **2010**, *49*, 3173

15 A. Oezaslan, M. Heggen, P. Strasser, *J. Am. Chem. Soc.* **2012**, *134*, 514.

16 (a) S. Mukerjee, S. Srinivasan, *J. Electroanal. Chem.* **1993**, *357*, 201. (b) S. Mukerjee, S. Srinivasan, M. P. Soriaga, J. Mcbreen, *J. Phy. Chem.* **1995**, *99*, 4577.

17 C. Wang, H. Daimon, T. Onodera, T. Koda, S. H. Sun, *Angew. Chem. Int. Ed.* **2008**, *47*, 3588.

18 S. Chen, P. J. Ferreira, W. C. Sheng, N. Yabuuchi, L. F. Allard, Y. Shao-Horn, *J. Am. Chem. Soc.* **2008**, *130*, 13818.

19 K. J. J. Mayrhofer, V. Juhart, K. Hartl, M. Hanzlik, M. Arenz, *Angew. Chem. Int. Ed.* **2009**, *48,* 3529.

20 (a) K. D. Beard, D. Borrelli, A. M. Cramer, D. Blom, J. W. Van Zee, J. R. Monnier, *ACS Nano* **2009**, *3*, 2841. (b) S. J. Hwang, S. J. Yoo, S. Jang, T.-H. Lim, S. A. Hong, S.- K. Kim, *J. Phys. Chem. C* **2011**, *115*, 2483. (c) V. R. Stamenkovic, B. S. Mun, M. Arenz, K. J. Mayrhofer, C. A. Lucas, G. Wang, P. N. Ross, N. M. Markovic, *Nat. Mater.* **2007**, *6*, 241.

21 M. Oezaslan, M. Heggen, P. Strasser, *J. Am. Chem. Soc.* **2012**, *134*, 514.

22 (a) J. M. Thomas, B. F. G. Johnson, R. Raja, G. Sankar, P. A. Midgley, *Acc. Chem. Res.* **2003**, *36*, 20. (b) K. C. Park, I. Y. Jang, W. Wongwiriyapan, S. Morimoto, Y. J. Kim, Y. C. Jung, T. Toyad, M. Endo, *J. Mater. Chem.* **2010**, *20*, 5345.

23 (a) M. Tada, S. Murata, T. Asakoka, K. Hiroshima, K. Okumura, H. Tanida, T. Uruga, H. Nakanishi, S.-i. Matsumoto, Y. Inada, M. Nomura, Y. Iwasawa, *Angew. Chem. Int. Ed.* **2007**, *46*, 4310. (b) F. A. de Bruijn, V. A. T. Dam, G. J. M. Janssen, *Fuel Cells* **2008**, *8*, 3.

24 V. Mazumder, S. Sun, *J. Am. Chem. Soc.* **2009**, *131*, 4588.

25 T. Kijima, Y. Nagatomo, H. Takemoto, M. Uota, D. Fujikawa, Y. Sekiya, T. Kishishita, M. Shimoda, T. Yoshimura, H. Kawasaki, G. Sakai, *Adv. Funct. Mater.* **2009**, *19*, 545.

26 L. Li, Y. Xing, *J. Phys. Chem. C* **2007**, *111*, 2803.

27 S. Alayoglu, A. U. Nilekar, M. Mavrikakis, B. Eichhorn, *Nat. Mater.* **2008**, *7,* 333.

28 (a) Z. Liu, X. Yi Ling, X. Su, J. Y. Lee, *J. Phys. Chem. B* **2004**, *108*, 8234. (b) Z. Liu, E. T. Ada, M. Shamsuzzoha, G. B. Thompson, D. E. Nikles, *Chem. Mater.* **2006**, *18,* 4946.

29 H. Darmstadt, C. Roy, S. Kaliaguine, S. J. Choi, R. Ryoo, *Carbon* **2002**, *40*, 2673.

30 C. Iwakura, K. Hirao, H. Tamura, *Electrochim. Acta* **1977**, ***22***, 329.

31 Z. Liu, X. Y. Ling, X. Su, J. Y. Lee, *J. Phys. Chem. B* **2004**, *108,* 8234.

32 T. J. Schmidt, H. A. Gasteiger, G. D. Stab, P. M. Urban, D. M. Kolb, R. J. Behm, *J. Electrochem. Soc*. **1998**, *145*, 2354.

33 V. R. Stamenkovic, B. Fowler, B. S. Mun, G. Wang, P. N. Ross, C. A. Lucas, N. M. Markovic, *Science* **2007**, *315*, 493.

34 Q. Cheng, J. Tang, J. Ma, H. Zhang, N. Shinya, L. Qin, *Carbon* **2011**, *49*, 2917.

35 S. Jones, K. Tedsree, M. Sawangphruk, J. S. Foord, J. Fisher, D. Thompsett, S. C. E. Tsang, *Chem. Cat. Chem.* **2010**, *2*, 1089.

36 M. H. Lee, J. S. Doa, *J. Power Sources* **2009**, *188*, 353.

37 H. Chou, F. Lai, W. Su, K. C. Pillai, L. S. Sarma, B. Hwang, *Langmuir* **2011**, *27*, 1131.

38 W. E. O’Grady, P. L. Hagans, K. I. Pandya, D. L. Maricle, *Langmuir* **2001**, *17*, 3047.

Chapter 5

On the Importance of Surface Functionalization in the Bimetallic Electrocatalyst Design*

In the present chapter, we discuss the importance of chemical functionalization in the design of a Pt-RuO_2 bimetallic electrocatalyst supported on CNF. When pristine CNF is used to decorate Pt and RuO_2 NPs, random dispersion occurs on the CNF surface (C-PtRuO_2). This results in mainly phase separated NPs rich in RuO_2 characteristics. In contrast to this, when functionalized CNF is used, a material rich in Pt features on the surface is obtained (F-PtRuO_2). This architectural tuning is a result of the controlled and predictable assembly of ions based on the preferential adsorption of one metal ion over the other. Better affinity of the oxygen containing functional groups towards RuO_2 mobilizes relatively faster adsorption of this moiety. This leads to a well-controlled segregation of Pt NPs towards the surface. The electrochemical studies of these materials using CV, galvanostatic charge-discharge and RDE analysis indicate that C-PtRuO_2 shows charge storage property, the typical characteristic of hydrous RuO_2, whereas F-PtRuO_2 shows oxygen reduction property which is the characteristic feature of Pt. The results confirm a functionalization induced switch in the property from charge storage to electrocatalysis. Thus, the present study shows how important it is to have a clear understanding on the nature of surface functionalities in the processes involving dispersion of more than one component on various substrates including carbon nanomorphologies.

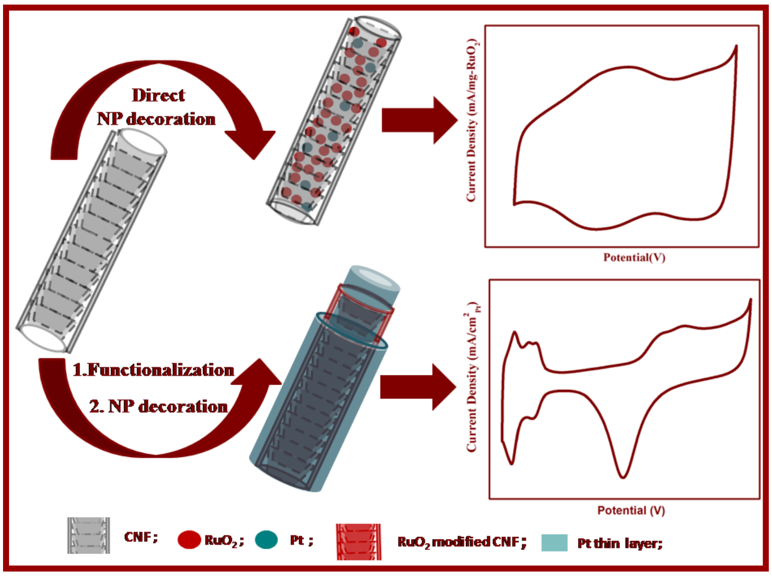

---

* The contents of this chapter have been published in "*Inorg. Chem.* **2012**, *51*, 9766-9774."

5.1. Introduction

Imparting surface sensitive functions in 1-D carbon nanostructures like CNTs and CNFs is a demanding challenge considering their myriad applications in a variety of fields such as nano-electronics, energy, biomedical, catalysis etc. [1-6]. The urge for such modifications originates from their inherent limitations like poor processibility, reactivity and solubility [7, 8]. In a broad way, the approaches commonly adopted to put up such improvements can be classified into two: endohedral or functionalization from inside and exohedral or functionalization from outside [9, 10]. Even though, from a basic chemistry point of view, functionalization is a simple means of recuperating the physico-chemical properties of CNTs or CNFs, the probable utility of functionalization commences from the simple unroping of the nanotube bundles to the highly specific grafting of single-stranded DNA for the selective and sensitive recognition of complementary DNA [11, 12].

Nanostructured materials, in general have great advantages over their bulk counterparts. Single-phased nanomaterials however may not be able to fulfill all the requirements. Assembling several functional nanomaterials into single material is a logical way to surpass the above limitations as the collective interaction between the constituents result into novel and unique properties [13, 14]. But, the success of such a hybrid design, in fact, depends on the selection of the proper individual components and the choice of the suitable methods to assemble the nanocomponents into the desired nanostructures.

In view of the growing importance of designing nanostructured hybrid materials, herein we discuss the significance of simple covalent functionalization in the design of a Pt-RuO_2 bimetallic electrocatalyst. Briefly, Pt and RuO_2 NPs are decorated on the CNF support by a modified polyol process using an EG-water solution containing Pt^{4+} and Ru^{3+} ions, as discussed in the Chapter 4. In a second approach, these NPs are decorated on FCNF adopting the same experimental strategy. In Chapter 4, we have demonstrated that, at a Pt:Ru atomic composition of 1:5, RuO_2 forms a complete layer in the inner cavity as well as on the outer walls and consequently in the present study, we have used the Pt:Ru atomic composition 1:5 in both the cases. When, pristine CNF is used, mainly monometallic, phase separated NPs rich in RuO_2 characteristics are obtained. In contrast to this, with the FCNF preferential adsorption of the Ru ions through the oxygen-containing functional group occurs. Since we have used an optimized composition (from Chapter 4), a thin layer of Pt selectively exposed to the surface of FCNF with a RuO_2 layer in between is formed during the reduction process. The different steps involved in the synthesis of both the materials are systematically represented in Scheme 5.1.

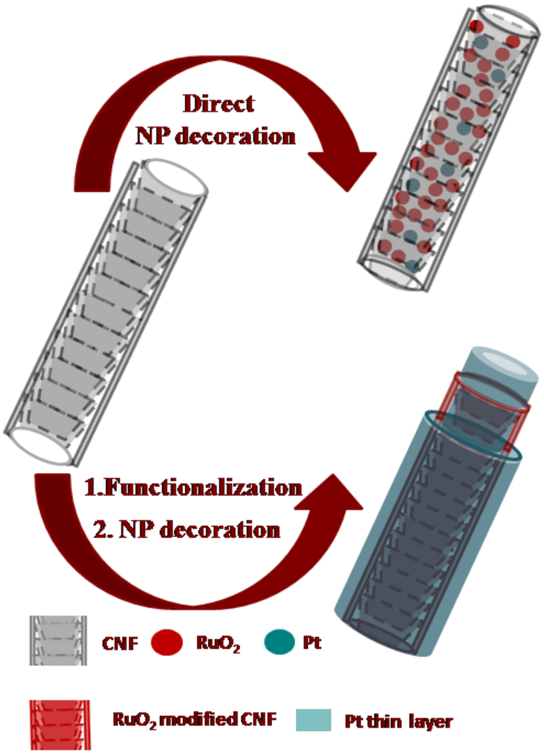

Scheme 5.1. The formation mechanism of Pt-RuO_2 bimetallic NPs on pristine and functionalized CNF.

Thus, with the same composition of Pt and RuO_2, two distinctly different distribution characteristics could be achieved. When pristine CNF is used to assemble the NPs, a material rich in RuO_2 characteristics is obtained whereas FCNF leads to a material rich in Pt features. The electrochemical analyses of these samples using CV, galvanostatic charge-discharge and RDE studies show a switch in the property from charge storage to electrocatalysis while moving from pristine CNF to FCNF.

5.2. Experimental Section

5.2.1. Synthesis of the Pt-RuO_2 bimetallic materials

Both the materials, (*i.e.* by using CNF and FCNF respectively as the supports) with 20 wt% loading (15 wt% RuO_2 and 5 wt% Pt) were prepared using the co-reduction of ($H_2PtCl_6.6H_2O$) and $RuCl_3$ in the polyol-water mixture (detailed experimental procedure is given in chapter 2 and 4). The Pt-RuO_2 bimetallic materials supported on CNF and FCNF are denoted as C-PtRuO_2 and F-PtRuO_2, respectively. For comparison, pure Pt and pure RuO_2 catalysts supported on FCNF and RuO_2 supported on CNF were also prepared using the corresponding Pt and Ru precursors and these are respectively denoted as F-Pt, F-RuO_2 and C-RuO_2.

5.3. Results and Discussion

5.3.1. TEM Analysis

TEM analysis is used for the morphological characterization of the CNF/FCNF-Pt-RuO_2 hybrid materials and to confirm the NP decoration on CNF and FCNF. Figure 5.1(a), which corresponds to the low magnification TEM image of F-PtRuO_2, clearly indicates the uniform and excellent distribution of NPs on the outer wall as well as in the inner cavity of FCNF. Interestingly, the low magnification image of C-PtRuO_2 given in Figure 5.1(b) confirms that the NPs are exclusively present in the inner cavity only and the outer wall is completely free. Though the low magnification image displayed almost similar features in terms of dispersion, on moving to higher magnification, some differences are observed in the assembly of the NPs. F-PtRuO_2 displayed a continuous layer formed by the assembly of large number of fine NPs as can be seen from Figure 5.1(c). In contrast to this, C-PtRuO_2 displayed separate NPs with a distinct boundary as shown in Figure 5.1(d). The average particle size and distribution were also determined from the HRTEM images assuming spherical shape for the particles. The corresponding particle size distribution histogram obtained for F-$PtRuO_2$ and C-$PtRuO_2$ is given in Figure 5.1(e) and (f), respectively. It is found that the average particle size of the NPs in F-$PtRuO_2$ is 2.6±0.9 nm whereas this is almost doubled in case of C-$PtRuO_2$ which is 5.5±0.9 nm. This observed reduction in the size of NPs while moving from pristine to pre-treated CNF can be attributed to almost double surface area (both the inner cavity and outer walls) made available for NP dispersion in FCNFs as a result of the functionalization.

Apart from this, the lattice spacing of NPs are measured and the average *d*-spacing obtained in the case of F-$PtRuO_2$ is 2.2 Å [see inset of Figure 5.1(c)], which corresponds to the (111) plane of fcc Pt [15]. In addition to the *d*-spacing, the angle between the observed planes is also measured which is *ca.*127.8°. This value is in close agreement with that reported for the angle between the Pt (111) and Pt (100) planes [16]. The absence of the lattice fringes corresponding to RuO_2 supplemented by the measured angle between the observed planes indicate that Pt is selectively exposed to the surface in F-$PtRuO_2$. Similarly, the *d*-value calculated for C-$PtRuO_2$ is 2.2 Å, as highlighted by the red circles and in the inset of Figure 5.1(d). The lattice spacing corresponding to RuO_2 cannot be measured because of its amorphous nature and the vague contrast as shown in the blue circles in Figure 5.1(d). These features clearly indicate the formation of phase separated monometallic NPs. Apart from this, the extent of atomic level resolution observed in F-$PtRuO_2$ is extraordinarily high as compared to that in C-$PtRuO_2$. This is evidenced by the coexistence of two lattice planes, *i.e.* (111) and (100), in F-$PtRuO_2$ while in C-$PtRuO_2$, only the fringes corresponding to (111) plane are observed. This observation also validates the fact that a thin layer of Pt is formed in the case of F-$PtRuO_2$.

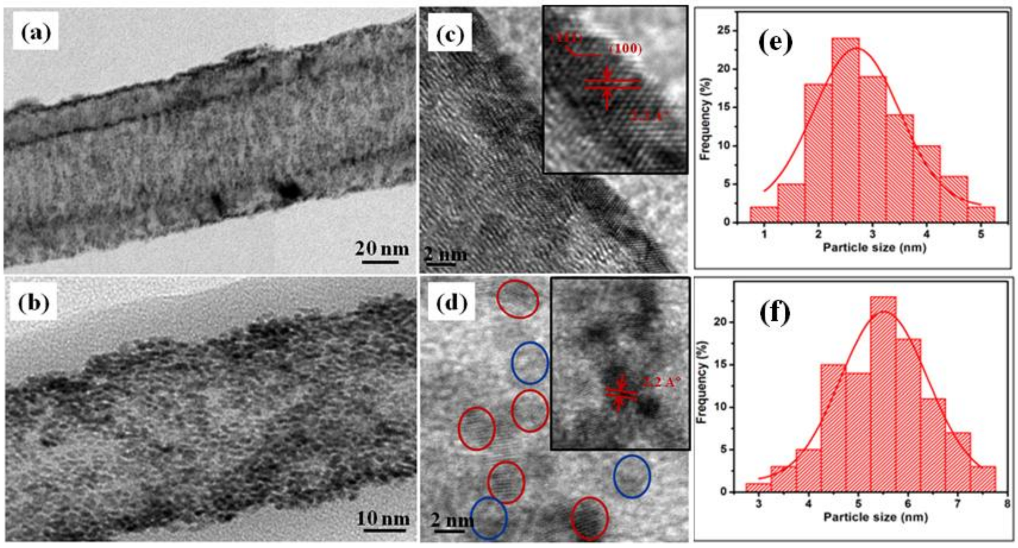

Figure 5.1. TEM images of (a) F-PtRuO$_{2}$, (b) C-PtRuO$_2$, (c) high magnification image of F-PtRuO$_2$ clearly indicating the formation of a thin layer of Pt with highly oriented grains, (d) image of C-PtRuO$_2$ showing the fine distribution of phase separated monometallic NPs and the insets of (c) and (d) show the *d*-spacing and angle between the planes, (e) and (f) are the histograms of particle size for F-PtRuO$_2$ and C-PtRuO$_2$, respectively.

5.3.2. TG Analysis

TG analysis is conducted in air from RT to 1000 °C to study the thermal stability of the materials. Figure 5.2 shows the comparison of the TGA profile obtained for CNF, F-PtRuO$_2$ and C-PtRuO$_2$. All the materials display almost similar TGA profile, *i.e.* an initial small weight loss followed by a continuous decay. The slight initial weight loss observed up to 600 °C can be attributed to the loss of residual water and functional groups. The second stage weight loss starting from 600 °C corresponds to the thermal degradation of the CNF in air. The total metal loading calculated from the residue content is close to zero in CNF whereas the contents in C-PtRuO$_2$ and F-PtRuO$_2$ are *ca.* 17.5 and 17.0 wt% respectively.

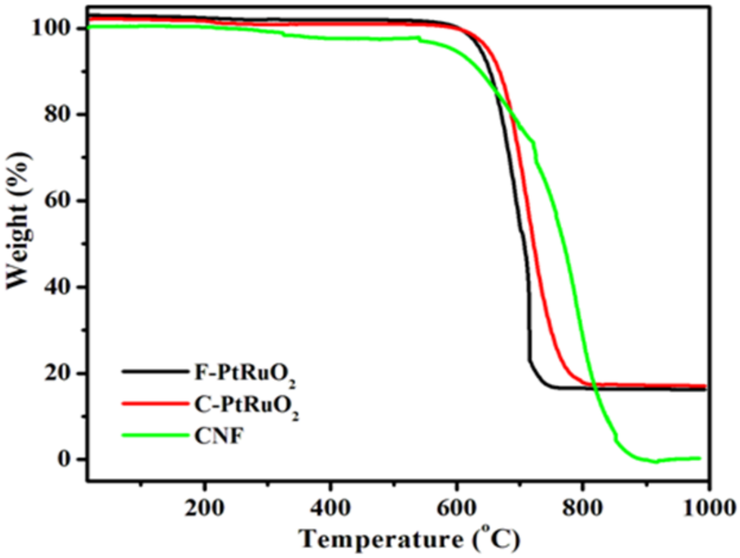

Figure 5.2. Comparison of TGA profiles obtained for C-$PtRuO_2$, F-$PtRuO_2$ and CNF in air from RT to 1000 °C.

5.3.3. XPS analysis

The surface chemical composition of these materials is evaluated by XPS analysis. Figure 5.3 shows the comparison of the full survey XP spectrum obtained for C-$PtRuO_2$ and F-$PtRuO_2$. A sharp peak observed at a BE of 284.6 eV in both C-$PtRuO_2$ and F-$PtRuO_2$ is attributed to the C1s of the CNF. The peak at the BE of 531.4 eV indicates the presence of oxygen. Moreover, the intensity of this peak is significantly high in F-$PtRuO_2$ as compared to that in C-$PtRuO_2$. This gives a lucid evidence for the extent of functionalization effected in CNF as a result of the H_2O_2 treatment [17]. As the most intense 3d signals of Ru merge with the intense C1s peak in the spectrum, it is very difficult to perceive its presence before deconvolution. Apart from all these observations, a remarkable discrepancy is observed in the Pt 4f region. In F-$PtRuO_2$, a clear doublet corresponding to Pt is observed at a BE of 73.4 eV [18]. In sharp contrast to this, no signatures for Pt are observed in the XP spectra of C-$PtRuO_2$. Hence, from a combination of the XPS and TGA results, it can be inferred that Pt and RuO_2 are present close to the calculated amounts from the initial precursors in both the materials. The incongruity observed in the Pt region may be due to the selective exposure of Pt to the surface in F-$PtRuO_{2,}$ as a result of the preferential adsorption.

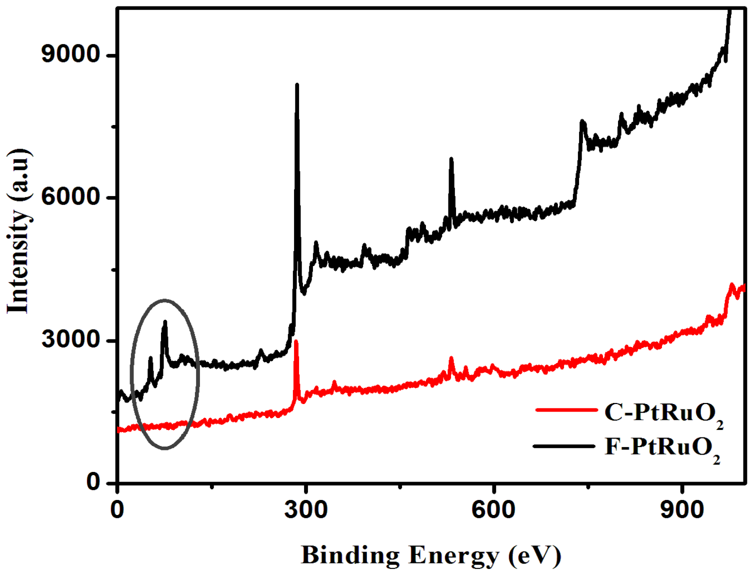

Figure 5.3. Superimposed full survey XP spectra of C-$PtRuO_2$ and F-$PtRuO_2$ before deconvolution.

To gain more insights into the surface structures and the mode of interaction between the individual components, various parts of the XP spectra of both the samples are deconvoluted. In C-$PtRuO_2$, the carbon region can be deconvoluted into four individual peaks as shown in Figure 5.4(a). The peaks observed at 284.6, 285.9, 281.6 and 284.0 eV in C-$PtRuO_2$ can be assigned to the graphitic carbon, carbon bonded to -OH groups and $3d_{1/2}$ and $3d_{3/2}$ levels of Ru respectively. However, in F-$PtRuO_2$, the respective peaks are observed at 284.5, 285.9. 281.3 283.9 eV as can be evident from Figure 5.4(b). Apart from this, one additional peak is also observed at the binding energy of 287.8 eV in F-$PtRuO_2$, which corresponds to the carbon bonded to -COOH groups. From the observed peak positions, it is evident that Ru is present in the form of RuO_2 in both the hybrids and no pure metallic Ru is detected [19]. The intensity of the peak corresponding to C-OH is also enhanced to a noticeable extent in F-$PtRuO_2$ as compared to that in C-$PtRuO_2$. The occurrence of an additional peak respective of -COOH groups and the enhancement in the intensity of the peak corresponding to C-OH groups corroborate the extent of functionalization effected in CNF as a result of the H_2O_2 treatment.

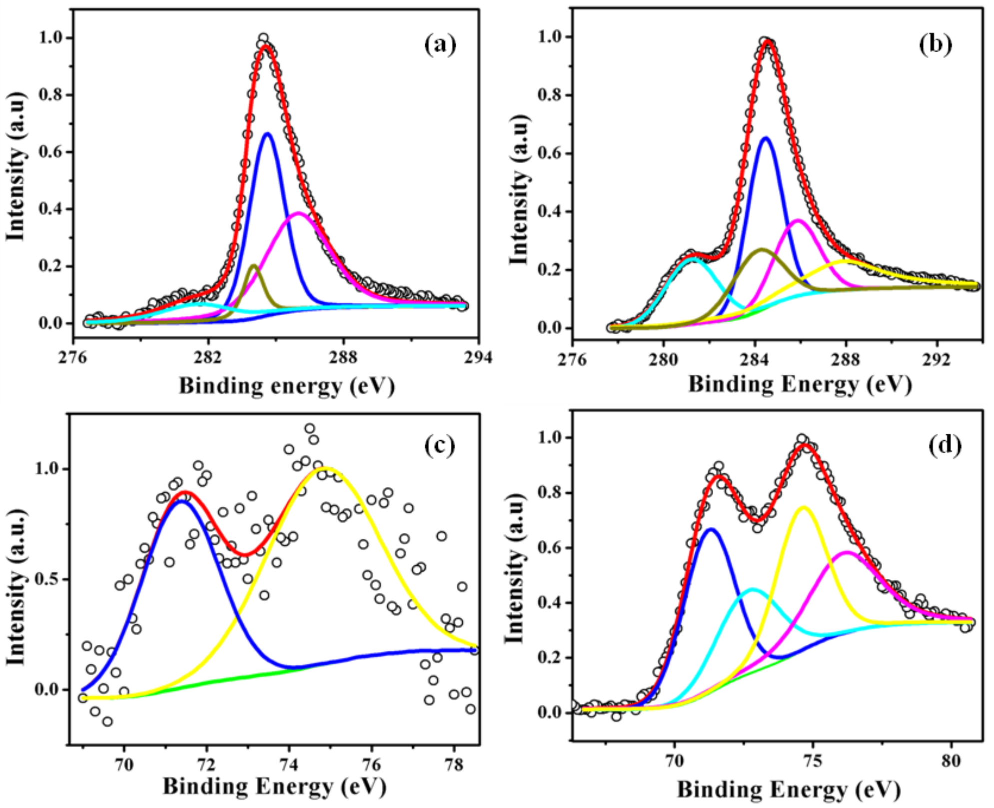

Figure 5.4. Representative XP spectra of C1s and Ru3d core levels in (a) C-$PtRuO_2$ and (b) F-$PtRuO_2$ and Pt4f levels in (c) C-$PtRuO_2$ and (d) F-$PtRuO_2$ after deconvolution. The circles represent the experimental data, the red line represents the fitting data for the overall signal, and the lines are the deconvoluted individual peaks for different species present in the sample.

The Pt4f levels in C-$PtRuO_2$, after deconvolution, give one doublet at BEs of 71.3 and 74.8 eV, corresponding to the $Pt4f_{7/2}$ and $Pt4f_{5/2}$ levels, respectively, as shown in Figure 5.4(c). From the peak position and the peak-to-peak separation, it can be concluded that Pt is present in the zero oxidation state in C-$PtRuO_2$. Interestingly, from Figure 5.4(d), it can be clearly manifested that deconvolution of the Pt4f levels of F-$PtRuO_2$ results in two doublets. The doublet at 71.2 and 74.5 eV corresponds to the regular peaks with respect to Pt in the zero oxidation state. The additional doublet observed at 72.6 and 76.2 eV corresponds to Pt in the higher oxidation states. However, it is interesting to note that this high-BE doublet matches neither with the Pt in the zero oxidation state nor with the pure platinum oxide and falls somewhere between these two. This observed intermediate value of the BE indicates that the doublet is a result of the slight oxidic character imparted to the Pt. Consequently, the peaks corresponding to the Pt in the zero as well as in the higher oxidation states and the perceived shift in its peak position compared to the reported values indicate the possible interaction between Pt and RuO_2 in F-$PtRuO_2$ [20, 21]. In contrast to this, the peaks corresponding to Pt in the higher oxidation state are absent in C-$PtRuO_2$, hence this excludes any strong interaction between Pt and RuO_2. This observation is in excellent agreement with the HRTEM results, where well-separated, monometallic Pt and RuO_2 NPs are observed in C-$PtRuO_2$, whereas a highly oriented, thin layer of Pt is detected in F-$PtRuO_2$. Moreover, from the signal-to-noise ratio of the Pt spectra, it is evident that the Pt peaks are attenuated from the higher RuO_2 content in C-$PtRuO_2$, while intense Pt peaks are observed for F-$PtRuO_2$.

Further, the surface atomic composition of C-$PtRuO_2$ and F-$PtRuO_2$ is also calculated from the XPS results (as discussed in Chapter 4) and is given in Table 5.1. It is evident from Table 5.1 that the Pt:Ru atomic percentages obtained for C-$PtRuO_2$ and F-$PtRuO_2$ are respectively 1:4.7 and 1:4.0, resulting in a surface composition of 26.6% Pt and 73.4% Ru in C-$PtRuO_2$ and 30.5% Pt and 69.5% Ru in F-$PtRuO_2$. The surface composition calculated from the XPS data for C-$PtRuO_2$ is close to the initial composition of 25% Pt and 75% Ru calculated from the precursor amounts. However, it is important to note that the surface composition obtained for F-$PtRuO_2$ shows a slight increase in the Pt% as compared to the initial composition. This could be due to the selective exposure of Pt to the surface in F-$PtRuO_2$. Accordingly, on the basis of a combination of the results from HRTEM, XRD, XPS, and TGA, it can be concluded that Pt is selectively exposed to the surface in F-$PtRuO_2$, while well separated monometallic NPs are present in C-$PtRuO_2$ and such a desirable nanoscale architectural tuning is a result of the preferential adsorption of one metal ion over the other.

Table 5.1. Surface composition quantification from XPS.

Sample	Peak Position			Relative Weight Percentage		Pt:Ru atomic Ratio
	C (eV)	Ru (eV)	Pt (eV)	Ru (Wt%)	Pt (Wt%)	
F-PtRuO$_2$	284.5 285.9 287.8	281.3 283.9	71.2 74.5 72.6 76.2	69.5	30.5	1:4
C-PtRuO$_2$	284.6 285.9	281.6 284	71.3 74.8	73.4	26.6	1:4.7

5.3.4. Electrochemical Studies

5.3.4.1. CV Analysis

To investigate the influence of such architectural tuning on the property modulation, electrochemical responses of these materials are initially evaluated using CV analysis in aqueous 0.5 M H_2SO_4 as the supporting electrolyte. Accordingly, Figure 5.5 shows the comparison of the cyclic voltammograms obtained for C-PtRuO$_2$ at different scan rates in the range of 5-150 mV/s. The cyclic voltammograms exhibit almost rectangular shape, which is the typical characteristic of a capacitor like material with low contact resistance in the system [22, 23]. The presence of RuO$_2$ in the material is supposed to contribute pseudocapacitance according to the following electrochemical process inside the electrode-electrolyte interface:

$$RuO_2 + H^+ + e^- \leftrightarrow RuO(OH) \qquad (5.1)$$

As expected, wide redox peaks which are the distinctiveness of the hydrous ruthenium oxide are observed in the CV [22]. Further, it is interesting to note that the rectangular shape of the CV is maintained even at various scan rates. Apart from this, the capacitance current of the electrode increases with increasing the scan rate which indicates excellent capacitance behavior and low contact resistance in the material. Of interest, no specific features respective of Pt is observed in the CV loop.

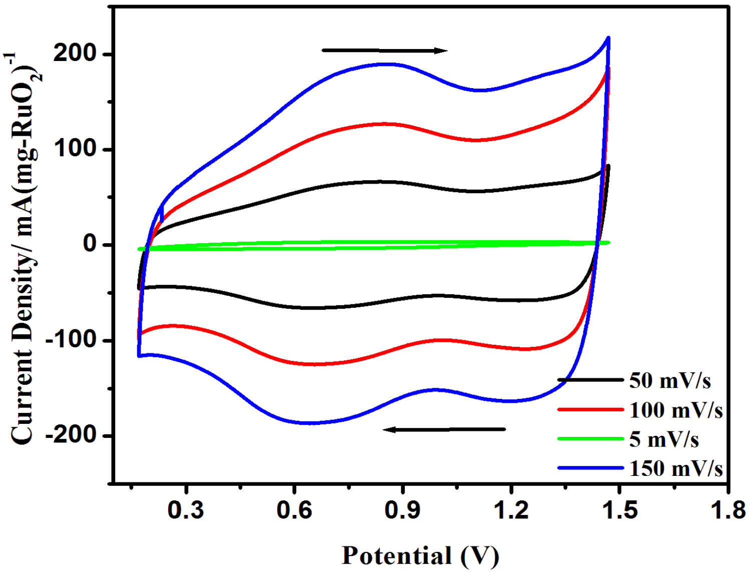

Figure 5.5. Superimposed CVs of C-PtRuO$_2$ in 0.5 M H_2SO_4 at the scan rates of 5-150 mV/s.

Further, to have an effective evaluation of the electrochemical activity, the CVs of C-PtRuO$_2$ and F-PtRuO$_2$ are compared at a scan rate of 50 mV/s as given in Figure 5.6. The CV response of C-PtRuO$_2$ given in Figure 5.6(a) exhibits almost a rectangular shape as discussed in the previous section. The specific capacitance of this material was calculated at a scan rate of 50 mV/s, using the equation,

$$C = Q/V \qquad (5.2)$$

where 'Q' is the cathodic charge and 'V' is the discharge voltage [24]. The capacitance obtained with respect to the RuO$_2$ loading was 1100 F/g. On the other hand, the CV response of F-PtRuO$_2$ presented in Figure 5.6(b) shows distinctly different features. The cyclic voltammogram obtained is similar to that of a polycrystalline Pt electrode with characteristic current peaks that can be ascribed to the hydrogen adsorption-desorption and peaks corresponding to surface oxide formation and reduction [25]. The ECSA, which decides the actual catalytic activity of a material, was calculated by measuring the coulombic charge for desorption of the monolayer of hydrogen (as discussed in the previous chapters 3 and 4). The ECSA obtained for F-PtRuO$_2$ is 384 cm^2/ mg-Pt, which is comparable to the ECSA values reported for Pt based systems in the literature [26].

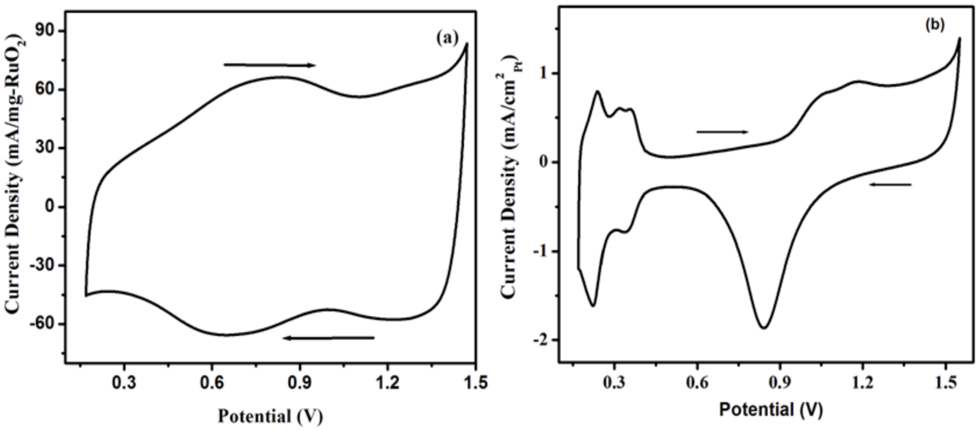

Figure 5.6. Comparison of CVs of (a) C-PtRuO$_2$ and (b) F-PtRuO$_2$ at the scan rate of 50 mV/s; electrolyte 0.5 M H_2SO_4 solution and all the potentials are quoted *vs*. RHE.

Further, to demonstrate the promotional effect of the second counterpart in the performance characteristics of the single phase-pure analogue, CV analysis of pure Pt (F-Pt) and pure RuO$_2$ catalysts (C-RuO$_2$ and F-RuO$_2$) are carried out and the resulting performances are compared with F-PtRuO$_2$ and C-PtRuO$_2$ respectively. A comparison of the CVs of C-PtRuO$_2$, C-RuO$_2$ and F-RuO$_2$ is displayed in Figure 5.7(a). All the materials display a rectangular CV loop with wide redox peaks. The specific capacitance values obtained (with respect to RuO$_2$ loading) for C-RuO$_2$ and F-RuO$_2$ are 520 and 640 F/g respectively, which are less compared to 1100 F/g obtained for C-PtRuO$_2$. Moreover, it can also be observed that the CV corresponding to F-RuO$_2$ is slightly distorted, and it shows a deviation from the perfect rectangular shape. It is already reported in the literature that larger resistance distorts the loop, resulting in a narrower loop with an oblique angle [23]. It can be inferred that the presence of Pt in the material reduces the resistance in the system and thereby increases the charge storage capability.

F-PtRuO$_2$ also shows a remarkable enhancement in the electrochemical activity as compared to F-Pt. Although similar specific activities are obtained for both systems as evidenced by the CV response given in Figure 5.7(b), the mass activity obtained for F-PtRuO$_2$ is considerably higher. The ECSA reaches 384 cm^2/mg of Pt for F-PtRuO$_2$ compared to 145 cm^2/ mg of Pt obtained for F-Pt, which translates into an improvement factor of 2.6 for the bimetallic combination. Such an enhancement in the mass activity is reminiscent of the performance improvement brought about in the system by the addition of RuO$_2$, which could induce the preferential exposure of Pt to the surface coupled with the modifications in the atomic distributions resulting in a modified electronic structure of Pt in F-PtRuO$_2$ [27].

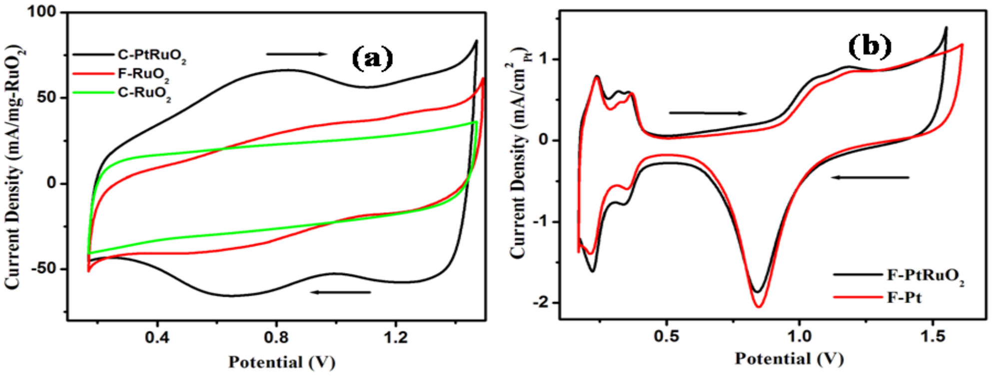

Figure 5.7. Comparison of CVs of (a) C-PtRuO$_2$, C-RuO$_2$ and F-RuO$_2$ and (b) F-PtRuO$_2$ and F-Pt in 0.5 M H$_2$SO$_4$ at a scan rate of 50 mV/s *vs.* RHE.

5.3.4.2. Methanol Oxidation Studies

To give an additional evidence for effect of architectural tuning on the property modulation, methanol oxidation studies of C-PtRuO$_2$ and F-PtRuO$_2$ are also carried out in a 1 M CH$_3$OH solution using 0.5 M H$_2$SO$_4$ as the supporting electrolyte. Figure 5.8(a and b) shows the comparison of the CV profiles obtained for C-PtRuO$_2$ and F-PtRuO$_2$ respectively at a scan rate of 50 mV/s. As shown in the CV profile presented in Figure 5.8(a), C-PtRuO$_2$ retains the rectangular shape of the CV even after the addition of CH$_3$OH. This indicates that C-PtRuO$_2$ is inactive toward methanol oxidation. This can be due to the increased capacitance contribution from the RuO$_2$ which suppresses the methanol oxidation current.

However, F-PtRuO$_2$ shows distinct peaks which can be assigned to the oxidation of methanol as can be evident from the CV profile presented in Figure 5.8(b) [28]. The tolerance factor, *i.e.* the ratio of the forward current to the backward current, calculated for this catalyst is 2.2, which shows the high tolerance of this material for CO poisoning [28]. These findings are in line with the observations from the CV analysis in 0.5 M H_2SO_4, and it is thus assured that, in F-PtRuO$_2$, electrochemical attributes corresponding to Pt are obtained whereas C-PtRuO$_2$ sustained the characteristics of RuO$_2$.

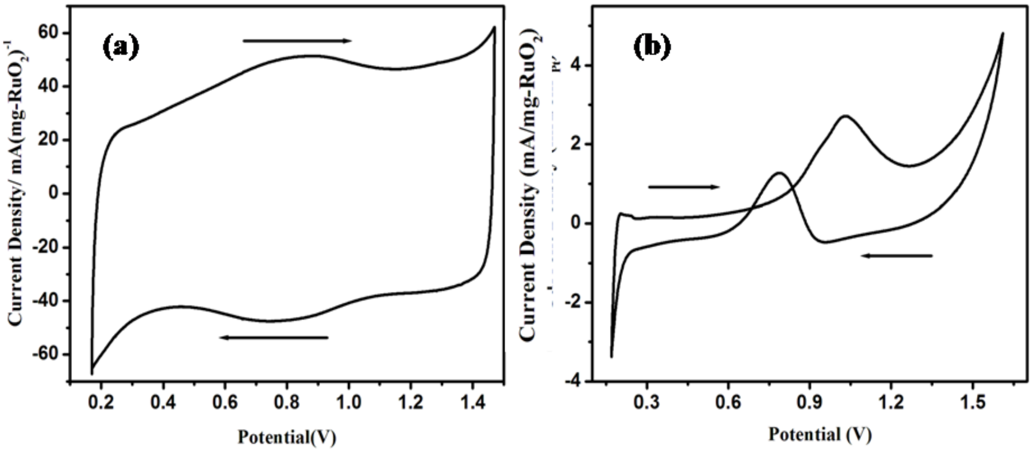

Figure 5.8. CVs for methanol oxidation reaction of (a) C-PtRuO$_2$ and (b) F-PtRuO$_2$; electrolyte 0.5 M H_2SO_4 + 1 M CH_3OH, scan rate 50 mV/s; all the potentials are quoted *vs.* RHE.

5.3.4.3. Galvanostatic Charge -Discharge Analysis

Galvanostatic charge-discharge studies are also conducted in 0.5 M H_2SO_4 in the potential window of 0-1 V to confirm the capacitive behavior of C-PtRuO$_2$. Accordingly, the charge-discharge profile obtained at different charging currents *i.e.* 1, 2, 3 and 5 A/g is shown in Figure 5.9.

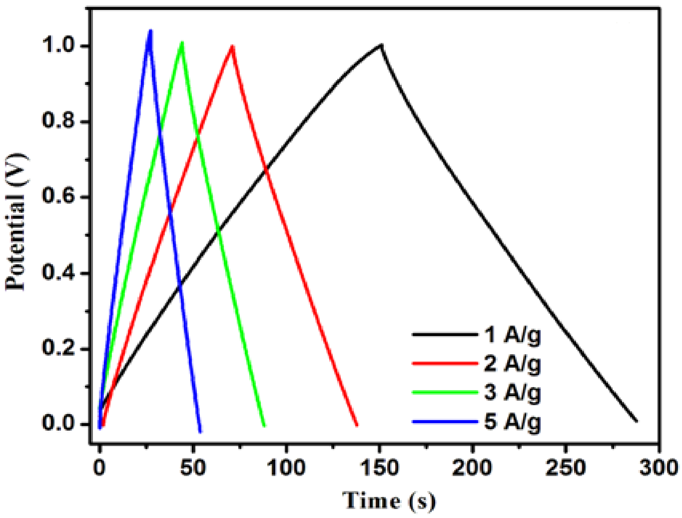

Figure 5.9. Galvanostatic charge-discharge curves of the C-PtRuO$_2$ electrode at different charging current from 1 to 5 A/g; electrolyte 0.5 M H_2SO_4, potential window 0-1 V.

A linear voltage-time profile with highly symmetric charge-discharge characteristics is observed at all current densities, which indicates capacitive behavior of the material [29]. The specific capacitance of C-PtRuO$_2$ is calculated from the discharge line using the formula,

$$C = I*t/\Delta V \tag{5.3}$$

where, ‘I’ is the discharge current, ‘t’ is the discharge time and ‘ΔV’ is the corresponding voltage drop. The mass specific capacitance (with respect to the RuO$_2$ loading) obtained for the C-PtRuO$_2$ from the charge-discharge data at the current density of 1 A/g is 1020 F/g. This value is in excellent agreement with the capacitance value obtained from the CV results.

5.3.4.4. RDE Studies

RDE studies of F-PtRuO$_2$ are also performed to confirm the electrocatalytic activity for ORR. Accordingly, Figure 5.10 shows the polarization curves obtained for the ORR in 0.5M H_2SO_4 solution with various rotating rates at a scan rate of 5 mV/s. The results indicate that the limiting current densities are progressively increased with the rotating rate. It can be ascribed to the increase in the mass transfer rate of the dissolved oxygen from bulk solution to the electrode surface [30]. Apart from this, the onset potential for ORR obtained for F-PtRuO$_2$ is 0.84 V *vs*. RHE. This value is also comparable with other Pt based catalysts reported in the literature [31]. All these features indicate the ORR activity of the F-PtRuO$_2$ material.

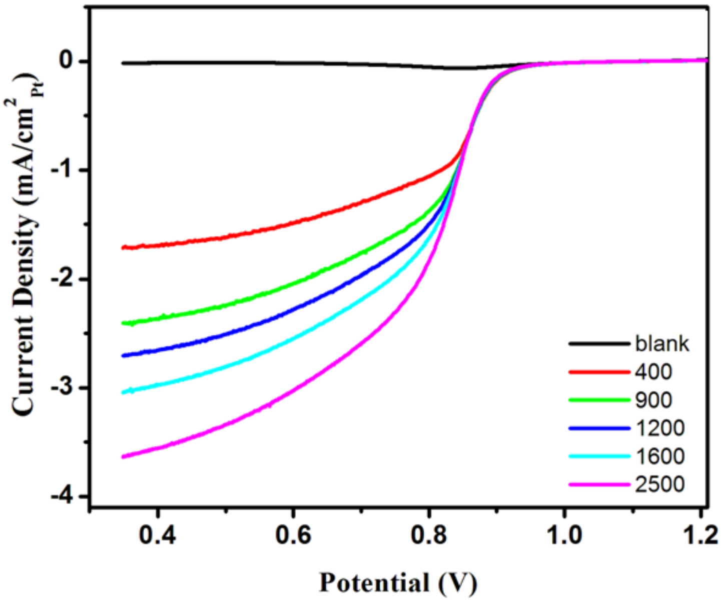

Figure 5.10. Superimposed RDE polarization curves for F-PtRuO$_2$ in 0.5 M H$_2$SO$_4$ solution at a sweep rate of 5 mV/s at various rotation rates; all the potentials are quoted *vs*. RHE.

Therefore, the results of the above electrochemical studies manifest a transition from the typical capacitance characteristic of RuO$_2$ to the typical electrocatalytic behavior respective of polycrystalline Pt. Hence, the above observations confirm that Pt is selectively exposed to the surface in F-PtRuO$_2$ while in C-PtRuO$_2$, mainly phase separated, monometallic NPs are formed. This unambiguous transition from the characteristic behaviour of an electrocatalyst to the characteristic capacitive features for the same Pt:RuO$_2$ composition is a result of the controlled and predictable positioning of each component by virtue of the surface functional groups created during the pre-treatment process.

5.4 Conclusions

We have demonstrated the importance of chemical functionalization to effectively tune the functionality of a hybrid material composed of Pt, RuO_2 and CNF from charge storage to electrocatalysis. This is achieved by a controlled and predictable assembly of the desired NPs based on the fundamental concept of preferential adsorption of ions. The microscopic characterization strongly points toward this architectural tuning effected in the system which is supported by the XPS analysis also. The clear transition from the characteristic capacitor behavior to the typical electrocatalytic activity is demonstrated using electrochemical analysis. Such a switchover in the property while moving from the pristine CNF to functionalized CNF, for the same composition of Pt and RuO_2, is by virtue of the predetermined positioning of the individual components on the CNF support. This is achieved based on the preferential adsorption of one metal ion over the other due to the presence of functional groups created after the activation process. As functionalization of carbon nanostructures is well documented in literature to create various functional groups like -SH, $-NH_2$, $-SO_3H$ etc., we envision that this strategy can be potentially extended for organizing various NPs at our desire.

5.5. References

1 Z. Wei, M. Kondratenko, L. H. Dao, D. F. Perepichka, *J. Am. Chem. Soc.* **2006**, *128*, 3134.

2 P. Qi, O. Vermesh, M. Grecu, A. Javey, Q. Wang, H. Dai, *Nano. Lett.* **2003**, *3*, 347.

3 J. Wang, G. Liu, M. R. Jan, *J. Am. Chem. Soc.* **2004**, *126*, 3010.

4 (a) F. Leroux, K. Metenier, S. Gautier, E. Frackowiak, S. Bonnamy, F. Beguin, *J. Power Sources* **1999**, *81*, 317. (b) A. S. Claye, J. E. Fischer, C. B. Huffman, A. G. Rinzler, R. E. Smalley, *J. Electrochem. Soc.* **2000**, *147*, 2845. (c) W. Lu, D. D. L. Chung, *Carbon* **2001**, *39*, 493.

5 (a) E. Frackowiak, F. Beguin, *Carbon* **2001**, *39*, 937. (b) R. Z. Ma, J. Liang, B. Q. Wei, B. Zhang, C. L. Xu, D. H. Wu, *J. Power Sources* **1999**, *84*, 126. (c) C. Niu, E. K. Sichel, R. Hoch, D. Moy, H. Tennet, *Appl. Phys. Lett.* **1997**, *70*, 1480.

6 J. N. Wang, Y. Z. Zhao, J. J. Niu, *J. Mater Chem.* **2007**, *17*, 2251.

7 S. Niyogi, M. A. Hamon, H. Hu, B. Zhao, P. Bhowmik, R. Sen, M. E. Itkis, R. C. Haddon, *Acc. Chem. Res.* **2002**, *35*, 1105.

8 K. Balasubramanian, M. Burghard, *Small* **2005**, 1, 180.

9 A. Hirsch, *Angew. Chem. Int. Ed.* **2002**, *41*, 1853.

10 H. Peng, L. B. Alemany, J. L. Margrave, V. N. Khabashesku, *J. Am. Chem. Soc*. **2003**, *125*, 15174.

11 M. Okamoto, T. Fujigaya, N. Nakashima, *Adv. Funct. Mater.* **2008**, *18*, 1776.

12 K. A. Williams, P. T. M. Veenhuizen B. G. Torre, R. Eritja, C. Dekker, *Nature* **2002**, *420*, 761.

13 P. L. Taberna, S. Mitra, P.Poizot, P. Simon, J. M. Tarascon, *Nat. Mater.* **2006**, *5*, 567.

14 R. Liu, S. B. Lee, *J. Am. Chem. Soc.* **2008**, *130*, 2942.

15 J. V. Zoval, J. Lee, S. Gorer, R. M. Penner, *J. Phys. Chem. B* **1998**, *102*, 1166.

16 T. Kijima, Y. Nagatomo, H. Takemoto, M. Uota, D. Fujikawa, Y. Sekiya, T. Kishishita, M. Shimoda, T. Yoshimura, H. Kawasaki, G. Sakai, *Adv. Funct. Mater.* **2009**, *19*, 545.

17 B. Gebhardt, Z. Syrgiannis, C. Backes, R. Graupner, F. Hauke, A. Hirsch, *J. Am. Chem. Soc.* **2011**, *133*, 7985.

18 R. Fu, H. Zeng, Y. Lu, S.Y. Lai, W. H. Chan, C. F. Ng, *Carbon* **1995**, *33*, 657.

19 A. Foelske, O. Barbieri, M. Hahn, R. Kötz, *Electrochem. Solid-State Lett.* **2006**, *9*, A268.

20 X. Li, S. Park, B. N. Popov, *J. Power. Sources* **2010**, *195*, 445.

21 C. R. Parkinson, M. Walker, C. F. McConville, *Sur. Sci.* **2003**, *545*, 19.

22 R. R. Bi, X. L. Wu, F. F. Cao, L.Y. Jiang, Y. G. Guo, L. J. Wan, *J. Phys. Chem. C* **2010**, *114*, 2448.

23 M. M. Shaijumon, F. S, Ou, L. Ciab, P. M. Ajayan, *Chem. Commun.* **2008**, *20*, 2373.

24 W. Xiao, H. Xia, J. Fuh, L. Lu, *J. Electrochem. Soc.* **2009**, *156*, A627.

25 C. Susut, G. B. Chapman, G. Samjeske, M. Osawac, Y. Tong, *Phys. Chem. Chem. Phys.* **2008**, *10*, 3712.

26 J. Kim, S. W. Lee, C. Carlton, Y. Shao-Horn, *J. Phys. Chem. Lett.* **2011**, *2*, 1332.

27 (a) J. Greeley, I. E. L. Stephens, A. S. Bondarenko, T. P. Johansson, H. A. Hansen, T. F. Jaramillo, J. Rossmeisl, I. Chorkendorff, J. K. Nørskov, *Nat. Chem.* **2009**, *1*, 552.(b) R. Srivastava, P. Mani, N. Hahn, P. Strasser, *Angew. Chem. Int. Ed.* **2007**, *46*, 8988

28 S. P. Jiang, Z. Liu, H. L. Tang, M. Pan, *Electrochim. Acta* **2006**, *51*, 5721.

29 L. Yuan, X. Lu, X. Xiao, T. Zhai, J. Dai, F. Zhang, B. Hu, X. Wang, L. Gong, J. Chen, C. Hu, Y. Tong, J. Zhou and Z. L. Wang, *ACS Nano* **2012**, *6*, 656.

30 Y. Zhang, K. Fugane, T. Mori, L. Niu and J. Ye, J. *Mater. Chem.* **2012**, *22*, 6575.

31 K. A. Kuttiyiel, K.Sasaki, Y.Choi, D.Su, P.Liu, R. R. Adzic, *Energ. Environ. Sci.* **2012**, *5*, 5297.

Chapter 6

Carbon Nanofiber-Pt-Poly(benzimidazole) Hybrids as Multifunctional Electrocatalyst with Ideal Interfacial Structure*

The present chapter demonstrates the synthesis of a novel electrocatalyst system with unique multifunctional characteristics originated by the presence of proton conducting PBI-BuI bound layer and electron conducting hollow CNF with catalytically active Pt NPs. This is achieved by decorating Pt NPs along the inner cavity as well as on the outer walls of the CNF support (F-Pt). In a further extension, a low molecular weight PBI synthesized by optimizing the experimental parameters is incorporated into the inner cavity and along the outer surfaces of F-Pt. The amount and the viscosity of the PBI-BuI in the electrode material are systematically varied to study the influence on the electrochemical performance. Electrochemical studies using CV and RDE reveal the exceptionally high activity of this hybrid material with improved ECSA. The significant improvement for the ORR is further confirmed by the single cell analysis. The high power density displayed by the PBI-BuI based system as compared to the Nafion based system validates the conceptualization of the well controlled TPB in the system. These results demonstrate that PBI-BuI has a constructive effect in tuning the electrochemical activity at an optimum amount and at a favorable viscosity.

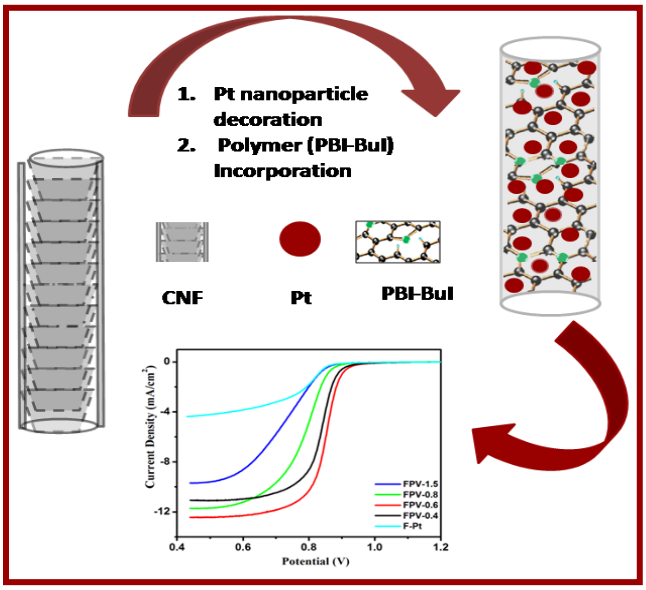

---

* The contents of this chapter have been published in "*Chem. Commun.* **2010**, *46*, 5590-5592 and *J. Mater. Chem. A*, **2013**, *1*, 4265-4276".

6.1. Introduction

The main focus of the PEMFC research today is to design an advanced electrode material to improve the commercialization aspects of the systems. A new electrode material with high level of catalyst activity and utilization, proper mass transfer rate with balanced electron and proton conductivity is needed to effectively meet these requirements [1]. A careful approach considering all the key parts including catalyst supports, catalyst particles and ionomer-catalyst-gas pore TPB is necessary towards the realization of this goal [2]. Major concern in this respect is given to modify the catalyst and/or catalyst support and consequently a sizeable improvement could be achieved so far [3-18]. Generally, the active sites in the MEA will be created by the establishment of the TPB around the catalyst particles with the provision for proton, electron and gaseous reactants to reach simultaneously to facilitate the electrode reactions [19]. While there are various well-known carbon morphologies existing with adequate electronic conductivity and porosity to ensure reactant distribution, establishment of proton conductivity can, in general, be achieved by carefully blending proton conducting ionomer in the system for generating the TPB in the catalyst layer. Nafion®, which is a perfluorosulfonic acid polymer with high proton conductivity, has proved to be the best binder in forming a TPB in PEMFCs [20]. However, the use of this binder is limited to low-temperature applications only, as its conductivity reduces at higher temperature [21]. Moreover, the size mismatch between Nafion and catalyst particles leads to the formation of secondary grains where many primary catalyst particles aggregate together by an outer wrapping of Nafion. This makes the primary particles chemically isolated with a reduction in the Pt utilization [22].

One of the methods adopted to solve this problem is the use of acid-doped PBI with high proton conductivity as a binder in PEMFC [21, 23-26]. Here, PBI acts as a matrix to hold the phosphoric acid (H_3PO_4), which is responsible for the proton transport and hence can be operative even under dry conditions above 100 °C [27]. Even though there are some reports which demonstrate PBI as a potential binder for fuel cells, most of the progresses in this area are limited to Vulcan carbon and CB supports. For example, Lobato *et. al*. reported the effect of catalyst ink preparation on the elctrochemical performance of PBI based catalyst layer in Vulcan carbon support [21]. Similarly, Kim *et. al.* and Lobato *et. al.* have demonstrated the influence of the PBI ionomer content in the electrode layer on the fuel cell performcance [23, 24]. Apart from this, very few studies are also available on 1-D support materials like CNTs or CNFs [25, 26]. Nakashima *et. al*. reported the use of a MWCNT, PBI and Pt nanoparticle composite as an efficient electrocatayst for PEMFC [25]. Apart from this, a recent report from the same group demonstrated the use of KOH doped PBI as the ionomer in the catalyst layer for AEMFCs. It was revealed that MWNT/KOH-PyPBI/Pt hybrid exhibits the highest performance reported so far [26]. However, all these reports consider the amount of PBI, electrode preparation strategy etc. as the variables.To the best of our knowledge, there is no study which describes the variation in the electrochemical activity by controlling the viscosity of PBI to achieve a modulated performance characteristics.

In an earlier chapter (Chapter 3), we have addressed the issues related to surface area of one dimensional carbon supports, where the fundamental idea was based on the concept of utilization of all the available surface area of such materials. By a logical choice of the support material with a hollow tubular morphology and by a proper process modification, both the inner and outer surfaces were utilized for Pt nanoparticle dispersion (F-Pt). The F-Pt catalyst involved in the aforementioned study surpassed the activity of conventional CNT based catalyst in many respects. This achievement was purely the outcome of the enhancement in the total available surface area of the support material resulting into a proper tuning of mass transfer and total resistance of the system. However, some of the issues like introduction of proton conductivity and formation of a proper TPB inside the cavity are still at their infancy. If we could deal with these issues, the overall activity can be further improved, leading to an innovative electrode material with balanced property characteristics to simultaneously address most of the prevailing issues in the fuel cells.

In this context, we describe a novel strategy for developing an electrocatalyst material possessing multifunctional characteristics required to simultaneously address all the aforementioned issues currently existing in this area. The procedure is based on a simple modification of our previous catalyst, F-Pt with a low molecular weight proton conducting polymer which satisfies all the necessary requirements to act as a binder in PEMFCs. Briefly, H_3PO_4 doped PBI-BuI, which is the proton conducting polymer, is incorporated into the inner cavity as well as on the outer surface of F-Pt. Thus, this catalyst combines the properties of a catalyst support which can ensure nearly double active surface area of Pt due to its dispersion along the inner as well as the outer walls along with high electron conductivity maintained by the micro network of the CNF support. At the same time, the polymer binder coverage formed along the inner cavity as well as on the outer wall provides effective TPB around the active sites to facilitate the proton transport while ensuring nearly homogeneous proton distribution. The amount and the viscosity of the PBI-BuI in the electrode material are systematically varied to study the influence on the electrochemical performance. Rather than using a conventional PBI, we employed PBI-BuI for the present work in view of its 16.7 times higher oxygen diffusion and 19.6 times higher hydrogen diffusion rate than that of conventional PBI [27]. These characteristics would allow faster approach of reactant gases towards the active surface area of the catalyst. Moreover, its improved solvent solubility was thought to be crucial for manipulating TBP. Its higher H_3PO_4 doping capability than the conventional PBI is anticipated to provide high ionic conductivity.

To date, most of the reports which addresses the incorporation of materials in the innner cavity of carbon nanostruructres adopt complicated experimental conditions like gas-phase diffusion, filling from molten media or by using supercritial CO_2 [28]. The present approach receives much attention due to the simplicity in the method used for the polymer insertion. It is accomplished by virtue of optimizing the synthesis parameters of PBI-BuI to obtain low viscosity and by manipulating the solution concentration of the PBI to facilitate its entry into the inner cavity of CNF through the open tips. The molecular weight and viscosity of PBI can be easily tuned by simple means. This feature together with the capillary filling effect originated by the nano-straw type structure of CNF help PBI entry into the hollow cavity of CNF without any external force. Doping could be subsequently achieved by dipping the material in polyphosphoric acid. Thus, overall, this catalyst design enables the system to simultaneously take into account the problems of support surface area, proper Pt dispersion and establishment of a proper TPB. The conceptual design of this novel electrocatalyst material with imparted features is given in Scheme 6.1.

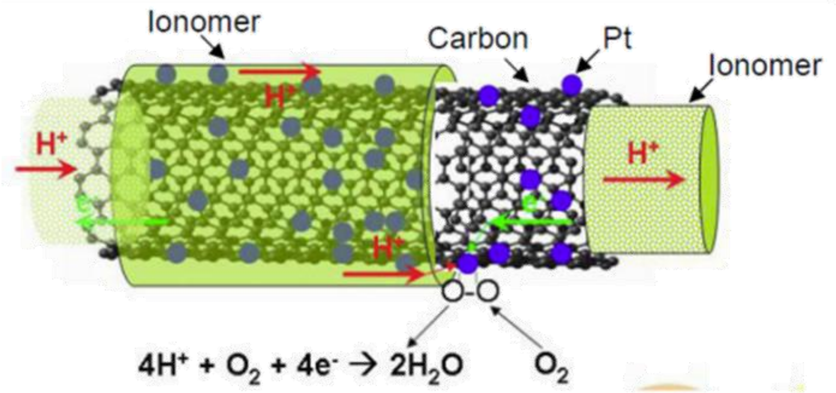

Scheme 6.1. Schematic of the novel catalyst design based on the multifunctional approach.

6.2. Experimental Section

6.2.1. PBI-BuI Incorporation in F-Pt

A 0.5 wt% solution of the PBI-BuI was prepared by dissolving the calculated amount of the polymer in DMAc. For polymer incorporation in the catalayst (F-Pt), 5 mg of F-Pt was added to the required volume of the polymer solution having a viscosity of 0.6 dL/g. The mixture was then subjected to sonication for 15 min in a bath type sonicator to initiate the PBI-BuI entry into the inner cavity. In the next step, the mixture was kept for stirring at RT for 10 h to ensure a homogeneous coverage in the tubular region and along the outer surfaces of the substrate. The same procedure was repeated for the incorporation of PBI-BuI at various PBI/carbon (P/C) ratios also. H_3PO_4 doping was achieved by dipping the electrodes in orthophosphoric acid for 24 h. The electrodes were subsequently dried in a vaccum oven at 100 °C for 48 h. The F-Pt materials after the PBI-BuI incorporation and at the P/C ratios of 0.25, 0.50, 0.75 and 1.0 are respectively denoted as FP-0.25, FP-0.5, FP-0.75 and FP-1. PBI-BuI with different viscosities (0.4, 0.6, 0.8 and 1.5 dL/g) and at a constant P/C ratio of 0.50 were also incorporated in F-Pt by adopting the same procedure and are denoted as FPV-0.4, FPV-0.6, FPV-0.8 and FPV-1.5 respectively.

6.2.2. ORR polarization and impedance studies

The polarization studies of the catalysts were carried out using an FCT Technologies, Inc. fuel cell test station under PEMFC operating conditions. For the catalyst slurry preparation using PBI-BuI based binders, the PBI-BuI incorporated catalysts were subjected to ultrasonication in DMAc. A PBI to carbon (P/C) ratio of 0.5 was maintained in the slurry. The slurry was coated on a gas diusion layer (GDL-35CC, SGL) by the brushing method until the total catalyst loading of 0.20 mg/cm^2 was reached. For preparing Nafion based electrodes, commercially available 20 wt% Nafion solution was used. The Nafion to carbon (N/C) ratio was maintained as 0.50. The catalyst ink was made by mixing the catalyst, Nafion and DMAc at an appropriate ratio and sonicating for 2 min. In all the cases, a commercially available 40 wt% PtC (Johnson Matthey) was used at the anode with a loading of 0.20 mg/cm^2. The cathode and anode electrodes of 6.25 cm^2 were pressed uniaxially with phosphoric acid doped PBI membranes at 130 ºC and 0.5 metric tonne pressure for 3 min. to fabricate the MEA. Fuel cell testing was carried out in a single cell with serpentine flow channels in the monopolar graphite plates. The polarization measurements were conducted with a flow rate of 0.1 slpm using H_2 and O_2. The testing was conducted at three different temperatures *i.e*. 120, 140 and 160 ºC with ambient gas pressure. MEA impedance was taken, while passing H_2 and O_2 gases at a flow rate of 50 sccm, and ambient pressure at the anode and the cathode respectively. The measurements were taken at an amplitude of 10 mV in the frequency range of 20 kHz to 0.1 Hz.

6.3. Results and Discussion

6.3.1. TEM Analysis

TEM imaging of the samples are carried out as it can directly determine the morphology transformations of materials in nanospace. Accordingly, the TEM images of the polymer incorporated CNF at different P/C ratios are given in Figure 6.1(a-h). All the images indicate the incorporation and coating of the PBI-BuI in the inner cavity and the outer surfaces of CNF. When P/C ratio is 0.25, a discontinuous filling of the polymer in the inner cavity of CNF is observed as can be seen from Figure 6.1(a and b). The polymer coating formed along the outer surface is also of different uniformity, with the typical coating thickness ranging from 1- 5 nm. It is also observed that a major part of the inner space is untenanted from the polymer incorporation, which is evident from the vacant spaces present in the images. In fact, such vacant space provides an additional possibility to demarcate the PBI-BuI layer formed in the curved inner surface. At higher P/C ratios [0.50 and 0.75 presented in Figure 6.1(c and d) and (e and f), respectively] CNF appears to be covered by a rather uniform and smooth coating of *ca.* 7-8 nm thickness. A marked decrease in the presence of the vacant spaces in the inner cavity is observed when the P/C ratio is 0.50 as shown in Figure 6.1(c and d). Based on the high magnification image in Figure 6.1(d), it can be inferred that CNF is roughly in the half filled state. The vacant spaces are almost vanished at the P/C ratio of 0.75 as evident from Figure 6.1(f), suggesting that CNF is close to a completely filled state. Finally, at the highest PBI-BuI content (P/C =1.0), CNF is completely merged in the polymer matrix as presented in Figure 6.1(g and h).

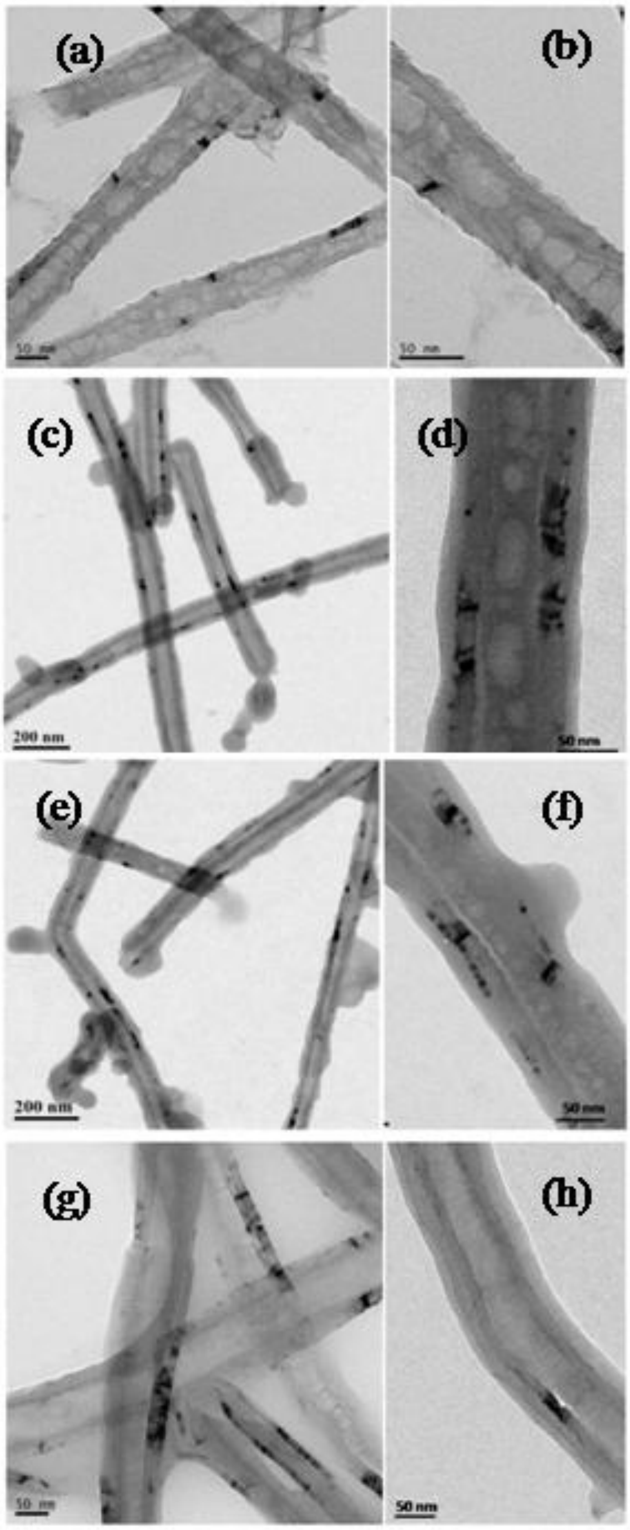

Figure 6.1. TEM images of PBI-BuI incorporated CNF at different P/C ratios; (a and b), (c and d), (e and f) and (g and h) correspond to the images at P/C ratios 0.25, 0.50, 0.75 and 1.0 respectively.

Though the aforementioned TEM results explicitly demonstrate the polymer wrapping on the outer surfaces, the same results are not adequate to confirm the incorporation of the polymer in the inner cavity. As CNF and PBI-BuI are basically carbon materials, distinguishing the contrast between PBI-BuI and CNFs, especially in the inner cavity, using HRTEM analysis will be difficult. Therefore, we have carried out some minor modifications based on the genuine fact that there is a prominent contrast difference between metal and carbon. Prior to executing polymer insertion, we have mixed the PBI-BuI solution with Rh NPs prepared by an in-house process. Here, Rh NPs can act as a tracer to follow the entry of PBI-BuI in the inner cavity of CNFs and accordingly Figure 6.2(a-c) illustrate the concept.

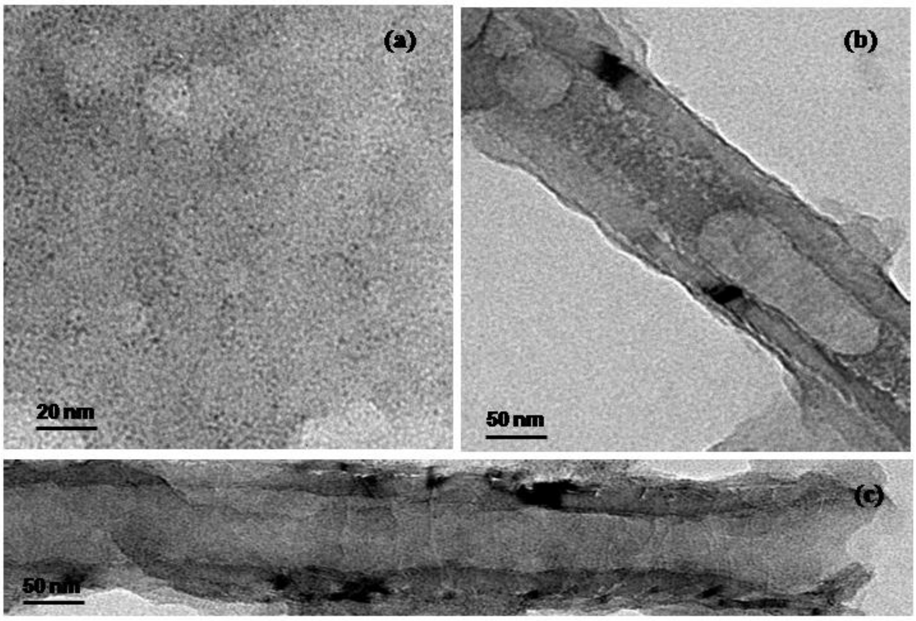

Figure 6.2. HRTEM images of (a) PBI-BuI with Rh NPs, (b) PBI-BuI inserted single CNF along with Rh nanoparticle as a tracer in the polymer phase and (c) CNF with Rh tracer in PBI-BuI matrix showing the one dimensional confinement of PBI phase inside the CNFs.

Figure 6.2(a) is the HRTEM image of the PBI solution with Rh NPs before incorporating into CNF. The image clearly shows the presene of Rh NPs of size *ca.* 2 ± 0.5 nm homogeneously dispersed in the polymer matrix. Figure 6.2(b and c) are the HRTEM images of the Rh-PBI incorporated CNFs. The image in

Figure 6.2(a) and the interior of the CNFs in Figure 6.2(b) have the same contrast, indicating that PBI-BuI is incorporated inside the cavity. Finally, the image of a single CNF given in Figure 6.2(c) demonstrates the one dimensional confinement of PBI-BuI inside the CNF.

TEM imaging of the F-Pt and FP-0.5 materials is also carried out and the corresponding images are given in Figure 6.3(a-f). The low magnification image of F-Pt shown in Figure 6.3(a) indicates the uniform dispersion of Pt NPs along the inner and outer surfaces of the FCNF support. The average size of the Pt NPs is *ca.* 3 ± 0.5 nm, as can be evident from the high magnification images given in Figure 6.3(b and c). The catalyst material after the PBI-BuI incorporation is also imaged and the respective images are given in Figure 6.3(d-f). The main difference observed after the PBI-BuI incorporation is in the contrast of the images. The images obtained after the PBI-BuI incorporation are hazy in nature [Figure 6.3 (d and e)] rather than the sharp contrast obtained for the F-Pt samples [Figure 6.3 (a and b)]. Such a hazy nature in the images is previously reported for the presence of polymer on the outer surface of CNTs also [29]. Moreover, in F-Pt, the NPs are protruding from the FCNF surface resulting into a fairly rough surface, as can be observed in Figure 6.3(b and c). After the PBI-BuI incorporation, the surface appears comparatively smoother, indicating that the NPs are wrapped with a polymer layer. Thus, the existence of a thin coating of the polymer on the F-Pt surface can be concluded from the above observations. Apart from this, the image given in Figure 6.3(f) clearly shows the presence of a skin layer expanding above the nanoparticle surface. The coating thickness of this skin layer is *ca*. 3-4 nm above the nanoparticle layer. This gives an unambiguous evidence for the polymer wrapping on the F-Pt surface. It is noteworthy that the FCNF backbone and the overall dispersion of the Pt NPs on the support material are retained as such even after the polymer incorporation.

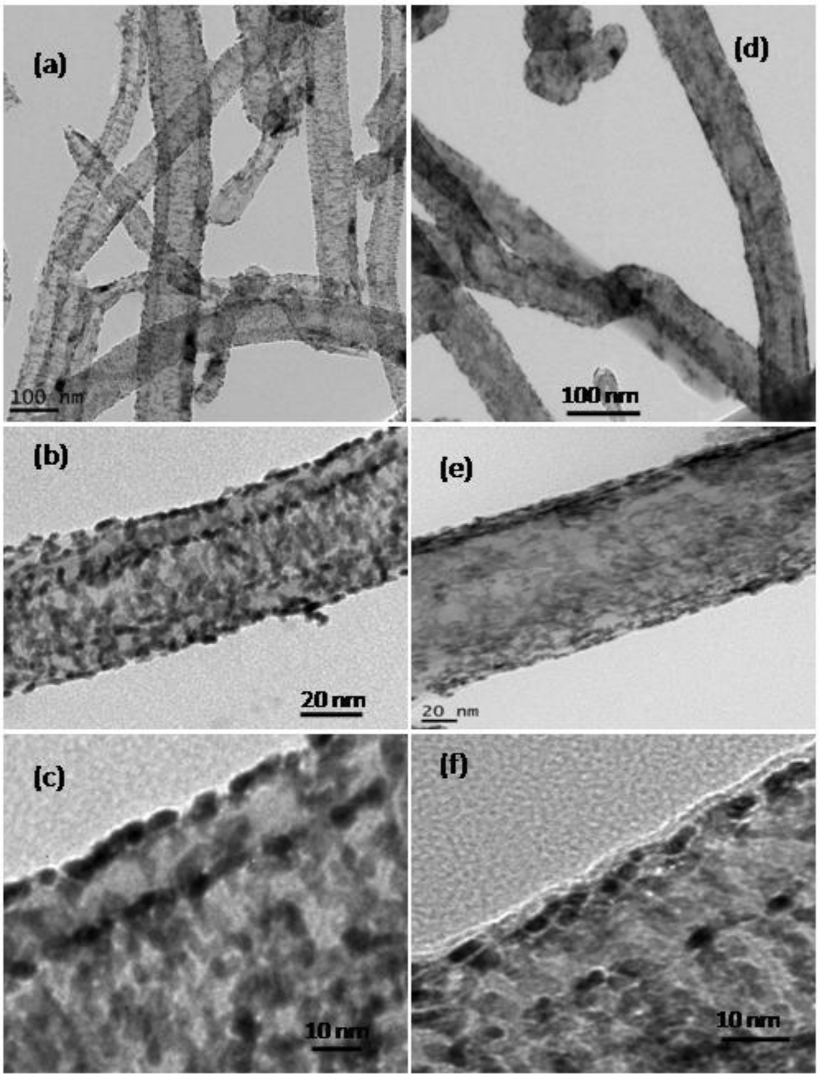

Figure 6.3. TEM images of (a-c) F-Pt and (d-f) FP-0.5 at various magnifications, (a) and (d) are the low magnification images of F-Pt and FP-0.5 depicting the overall dispersion of Pt NPs on the FCNF support; (b) and (e) are the representative images of F-Pt and FP-0.5, respectively, showing the difference in the image contrasts after the PBI incorporation, (c) shows the enlarged view of the presence of a rough surface in F-Pt and (f) a skin layer of PBI-BuI extending from the nanoparticle surface in FP-0.5.

In order to give an additional evidence for the possible utilization of the inner cavity for nanoparticle decoration, TEM image of a catalyst material wherein the NPs are present only in the inner cavity (C-Pt) is also given in Figure 6.4(a). This is easily achievable with the pristine CNF where the outer wall is inherently inactive due to its peculiar morphological characteristics. As expected, the existence of Pt NPs in the inner cavity and the completely empty outer wall is clear from this image. HRTEM imaging of the C-Pt material after the polymer incorporation is also conducted and the resulting image is shown in Figure 6.4(b). A uniform coating of the polymer of approximately 7-8 nm thickness on the outer surface (marked in the black lines) of the CNF is clear from the image. The overall dispersion of the NPs in the inner cavity is also maintained as in the case of F-Pt. This highlights the uniqueness of our approach in obtaining effective polymer incorporation without any rupture to the starting material, especially by following such a mild protocol.

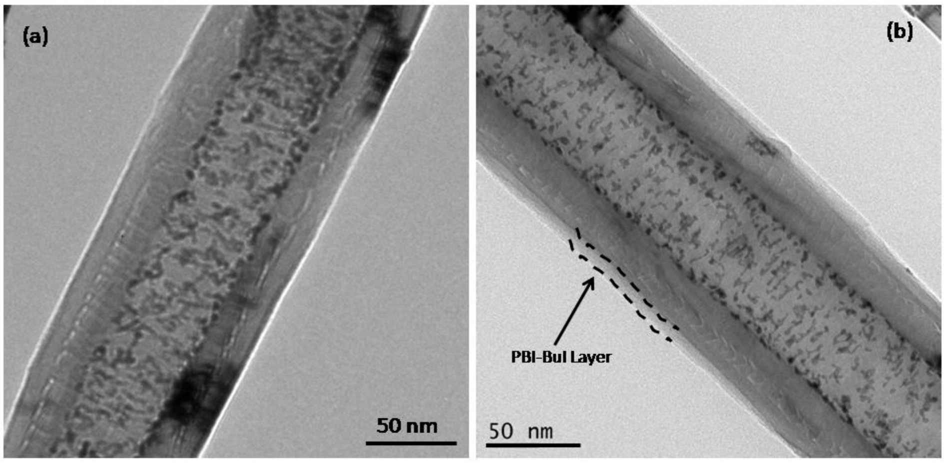

Figure 6.4. TEM image of (a) C-Pt showing the selective decoration of Pt NPs in the inner cavity and (b) CP-0.5 indicating the presence of the PBI-BuI layer on the outer surface.

6.3.2. TG Analysis

TG analysis is conducted to confirm the composition as well as the thermal stability of the F-Pt samples after the PBI-BuI incorporation. Figure 6.5(a) compares the TGA profile obtained for F-Pt, FP-0.25, FP-0.50 and FP-0.75. The TGA profile of F-Pt shows a negligible initial weight loss up to 400 °C which can be attributed to the loss of residual water and functional groups. A fast second stage weight loss due to the oxidation of CNF is observed from 400-500 °C. The Pt loading on FCNF calculated from the residue content is 18.2 wt%. Interestingly, the F-Pt materials after the PBI-BuI incorporation shows a clear three-step weight loss. The first weight loss observed till 300 °C can be attributed to the loss of trapped solvents. The second weight loss observed in the temperature range of 300-500 °C corresponds to the thermal degradation of the incorporated PBI-BuI in the materials. The weight loss occurs at lower temperature as compared to those reported in the literature and it may be due to the lower molecular weight of the PBI used [24, 25]. Moreover, the inner hollow cavity of CNF may provide an intriguing one-dimensional confinement of PBI-BuI leading to limited intermolecular H_2 bonding [24, 25]. This effect also supports the above observation of weight loss at low temperature. The third step weight loss around 500-700 °C can be assigned to that of CNF. It is also revealed from the TGA profiles that the final Pt loadings in the FP-0.25, FP-0.50 and FP-0.75 samples are 14.5, 10.9 and 8.8 wt% respectively. This is in close agreement with the calculated Pt loading in the respective samples considering the PBI-BuI loading also (Table 6.1).

Table 6.1. Calculated Pt loading in various catalyst materials after PBI-BuI incorporation.

Sample Name	P/C	Initial Carbon (Wt%)	Initial Pt Loading (Wt%)	PBI-BuI (Wt%)	Final Carbon (Wt%)	New Pt Loading (Wt%)
FP-0.25	0.25	81.8	18.2	20	101.8	14.62
FP-0.5	0.50	81.8	18.2	40	121.8	12.22
FP-0.75	0.75	81.8	18.2	60	141.8	10.49
FPV-0.4	0.5	81.8	18.2	40	121.8	12.22
FPV-0.8	0.5	81.8	18.2	40	121.8	12.22
FPV-1.5	0.5	81.8	18.2	40	121.8	12.22

TGA analysis of the PBI-BuI incorporated samples with various viscosities is also conducted and the TGA profiles of FPV-0.4, FPV-0.8, FPV-1.5 and F-Pt are shown in Figure 6.5 (b). All the materials show a similar three stage weight loss pattern. However, it is interesting to note that the weight loss corresponding to the PBI-BuI in FPV-1.5 occurs at a lower temperature as compared to that in FPV-0.4 and FPV-0.8. In FPV-1.5, a major part of the polymer remains unbound to the outer surface of CNF leading to its decomposition at a lower temperature. Hence, it can be inferred that the incorporation of the polymer in CNF results into its improved thermal stability as a result of the interaction between CNF and the polymer [24, 25]. Finally, the Pt loadings in FPV-0.4, FPV-0.8 and FPV-1.5 are calculated to be 12.1, 11.4 and 7.6 wt% respectively. The residual weight obtained for FPV-0.4 and FPV-0.8 are close to the calculated values. However, in FPV-1.5, the observed Pt loading after the PBI-BuI incorporation is significantly less as compared to the calculated values.

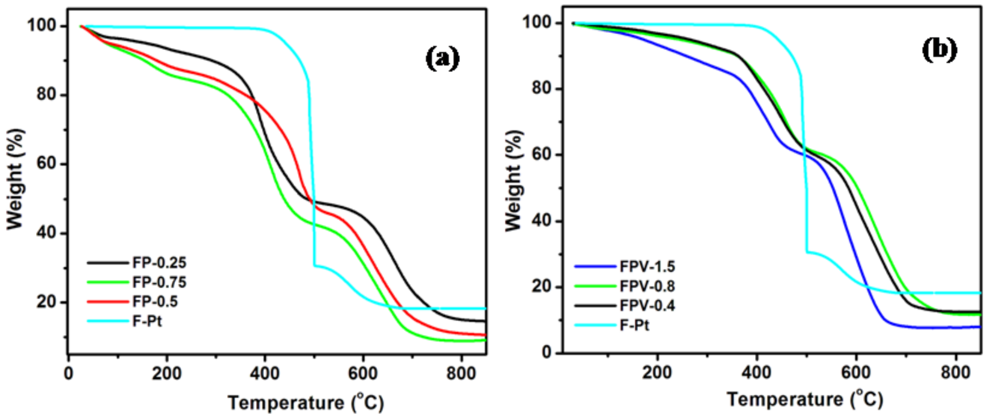

Figure 6.5. TGA profile obtained for (a) F-Pt, FP-0.25, FP-0.50, FP-0.75 and (b) FPV-0.4, FPV-0.8, FPV-1.5, F-Pt in air atmosphere; temperature range RT-1000 °C, ramp 10°/min.

6.3.3. Pore Size Distribution Analysis

The microstructural properties of a catalyst material such as pore size and agglomerate size are strongly reflected in its electrochemical performance also [23]. Hence, the pore size distributions of the various electrode materials are measured. Accordingly, Figure 6.6(a-d) show the pore-size distribution obtained for the various electrode materials. Generally, a catalyst material mixed with the binder exhibits two distinct pore size distributions. The pores which are present in between the primary particles in the agglomerates, usually defined as primary pores occur in the range of 0.01-0.04 µm. The secondary pores correspond to the spaces between the agglomerates and are formed between 0.04 and 1.0 µm [20, 21]. From the comparison of the pore size distribution obtained for FP-0.25, FP-0.50, FP-0.75, FP-1.0 and F-Pt given in Figure 6.6(a and b), it is obvious that the pore volume of the primary and secondary pores decreases with increase in the PBI-BuI content, except in the case of FP-1.0. This behaviour is in accordance with the earlier reports on PBI based binder in PEMFC [30, 31]. Since the PBI-BuI based binder is in the solution state, it can penetrate into both types of pores. Thus the pore volume corresponding to the primary as well as secondary pores decreases. In contrast to this, since Nafion type binders are used in the colloidal form, it cannot penetrate into the primary pores. Hence, with increase in the ionomer content, only the secondary pore volume decreases [30, 31]. The discrepancy observed in FP-1.0 (increase in the primary pore volume and decrease in the secondary pore volume) can be attributed to the formation of the porous agglomerate of the excess polymer itself. This is in accordance with the TEM observation also where the excess PBI-BuI is present as agglomerates.

The effect of the viscosity of PBI-BuI on the microstructure of the catalyst is also analysed. Figure 6.6 (c and d) show the pore size distribution obtained for FPV-0.4, FPV-0.6, FPV-0.8 and FPV-1.5. The results are compared with that of F-Pt also. From the pore size distribution curves, it is clear that specific pore volume corresponding to the primary pores vary with viscosity. Of interest, the specific pore volume of the secondary pores remains almost constant. On a detailed analysis of the region corresponding to the primary pores, it can be observed that the largest decrease in the primary pore volume is observed for PBI-BuI with the lowest viscosity (0.4 dL/g). In case of PBI-BuI with intermediate viscosities (0.6 dL/g and 0.8 dL/g), almost similar decrease in the pore volume is observed. Finally, for PBI-BuI with the highest viscosity selected (1.5 dL/g), the pore volume remains unchanged as compared to that of F-Pt.

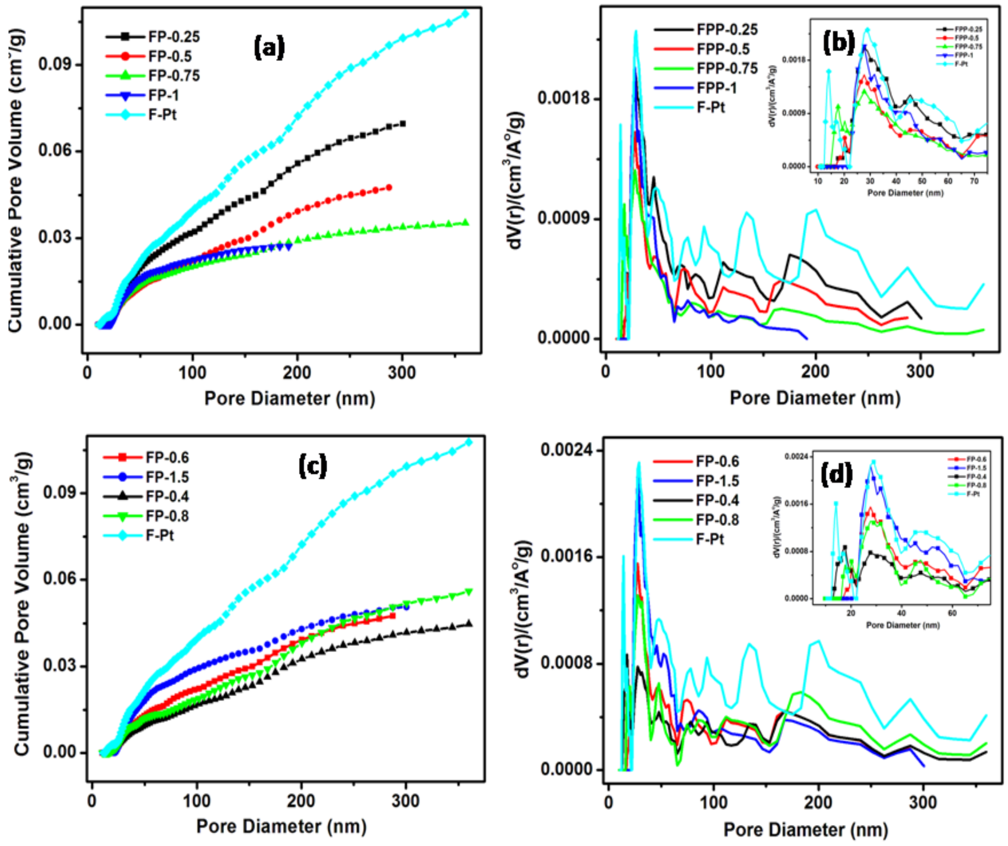

Figure 6.6. Cumulative and specific pore volume distribution of F-Pt, FP-0.25, FP-0.5, FP-0.75 & FP-1 (a and b) and FPV-0.4, FPV-0.6, FPV-0.8 & FPV-1.5 & F-Pt (c and d) electrodes. The insets of (b) and (d) show the magnified portion of the specific pore volume distribution.

The above results can be explained as follows: PBI with lower viscosity can easily penetrate into the small primary pores and hence lowest specific pore volume is obtained for the FPV-0.4 electrode. As the viscosity increases, it impedes the entry of the polymer into the primary pores due to increase in the chain length, resulting into higher pore volume as obtained for FPV-0.6 and FPV-0.8 electrodes. When the viscosity is still higher (highest chain length among the series), it cannot enter into the primary pores. Thus, the pore volume remains same as that of the initial material (F-Pt) even after the attempted PBI-BuI incorporation. Hence, from the above results, it can be deduced that viscosity of PBI-BuI has a strong relation in defining the microstructure.

6.3.4. Electrochemical Studies

6.3.4.1. CV Analysis

The electrocatalytic activity of the F-Pt materials after the PBI-BuI incorporation toward the ORR is primarily evaluated using CV analysis in aqueous 0.5 M $HClO_4$ solution. It is well reported in the literature that an optimum amount of the binder is necessary to extract the best performance from a catalyst. Inadequate amount of the binder cannot form effective TPB and an excess of the same can lead to a blocking effect resulting into a reduction in the actual performance [32]. Hence, to find out the optimum amount of the PBI-BuI needed, the catalyst to PBI-BuI ratios (by weight) are varied as 0.25, 0.35, 0.50, 0.75, 0.85 and 1.0. Formation of the TPB is monitored through CV studies by looking at the characteristic peaks in the hydrogen adsorption-desorption region where the ionomer interfaces are established. ECSA calculated from the CV (assuming that the charge associated with the desorption of a monolayer of hydrogen is 210 $\mu C/cm^2$) for each composition is plotted against the corresponding PBI ratio [33] and is shown in Figure 6.7. As it is clearly evident from the plot, initially, the performance is lower when the ratio is 1:0.25 and 1:0.35. The maximum performance is obtained when the ratio is 1:0.5. However, with further increase in the PBI-BuI content (1:0.75, 1:0.85 and 1:1), a progressive reduction in the performance is observed. This trend obtained for the ECSA with respect to the catalyst to polymer ratio itself is a clear indication of the efficiency of PBI-BuI in its appropriate amount to establish the ionomer network required for the TPB formation in the system. Initially, when the PBI-BuI content is low (0.25 and 0.35), very few Pt NPs might be covered by a skin layer of the binder. It is well known that only those Pt NPs with an effective TPB gives better electrocatalytic activity. Hence due to the incomplete TPB formation, maximum performance could not be displayed by the system. However, an increase in the ratio to 1:0.5 offers an ionomer concentration level well enough to establish the most effective TPB, leading to the observed maximum performance characteristics. With a further increase in the binder content to 1:0.75, the binder layer above the Pt NPs can become thicker resulting into a reverse effect on the reactant distribution at the active Pt sites. Finally, when the ratio is 1:0.85 and 1:1, instead of acting as a layer, PBI-BuI blocks most of the Pt NPs and pores for reactant distribution resulting into a drastic decrease in the performance. The drastic difference in the performance observed with the change in the catalyst to ionomer ratio is a clear indication for the fact that an optimum amount of the ionomer is a crucial part in attaining better performance. This is in accordance with the earlier reports also [23, 24]. Therefore, for further studies, a catalyst:PBI-BuI ratio of 1:0.5 has been taken as the standard composition.

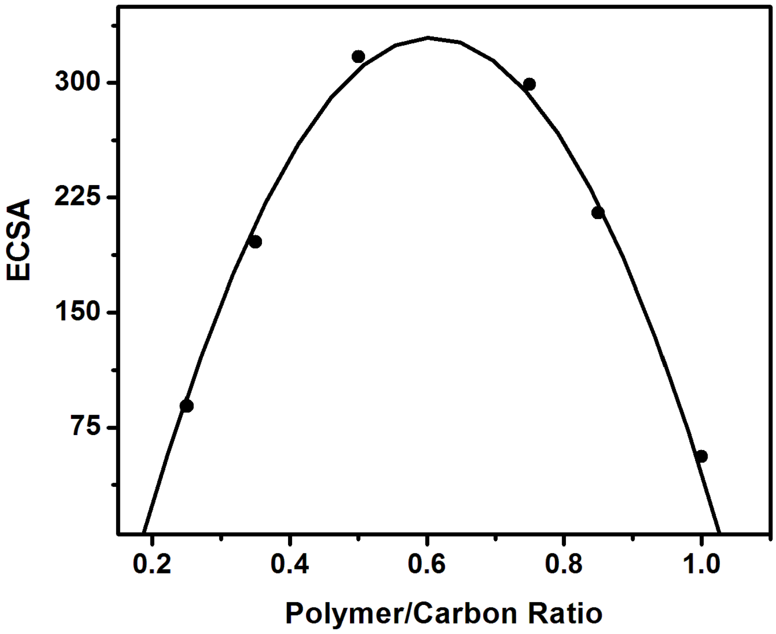

Figure 6.7. Plot showing the variation of the electrochemical active area with the PBI/C ratios.

From the pore size distribution analysis, it is revealed that viscosity of PBI-BuI plays a key role in defining the microstructure of the electrode material. Hence, to investigate the effect of viscosity variation on the ORR performance, the CV response of FPV-0.4, FPV-0.6, FPV-0.8 and FPV-1.5 in 0.5 M $HClO_4$ is analysed. Figure 6.8 compares the CV profile obtained for FPV-0.4, FPV-0.6, FPV-0.8 and FPV-1.5. The voltamogram of F-Pt, where the conventional Nafion binder is used, is also shown for comparison. In all the cases, the catalyst to binder ratio is kept as 0.5 and the potential is scanned positively from 0.2 to 1.6 V and then negatively to 0.2 V (with respect to the RHE) at a sweep rate of 50 mV/s. The voltamograms exhibit the characteristic hydrogen adsorption-desorption and the features corresponding to the surface oxide formation and reduction [33]. The ECSA calculated for FPV-0.4, FPV-0.6, FPV-0.8, FPV-1.5 and F-Pt are 51, 63, 48, 17 and 19 m^2/g-Pt respectively (Table 6.2). FPV-0.6 has the highest performance as is evident from the ECSA values, which is three times more than that of F-Pt. The ECSA value obtained for the FPV-0.6 is higher as compared to that reported for the other PBI based electrodes also [21-24].

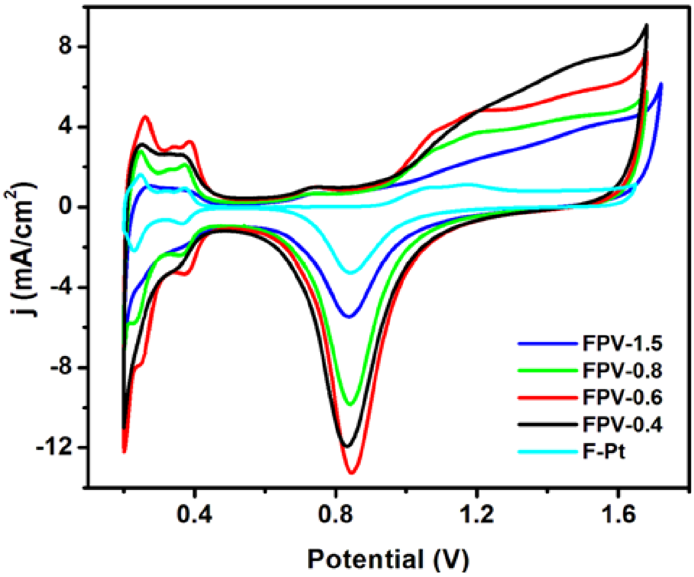

Figure 6.8. Superimposed CV curves for FPV-0.4, FPV-0.6, FPV-0.8, FPV-1.5 and F-Pt electrodes in 0.5 M $HClO_4$ solution; scan rate 50 mV/s; all the potentials are quoted *vs.* RHE.

The low ECSA obtained when Nafion is used as the binder in comparison to the samples prepared by incorporating H_3PO_4 doped PBI-BuI can be accounted on the basis of the higher equivalent weight and the complex fibrillar structure of Nafion. Due to these constrains, Nafion cannot be filled effectively into the inner cavity of CNFs. As a result of this, the Pt NPs present in the inner cavity of CNFs remain unutilized, resulting into a lower ECSA value. An interesting experimental study carried out recently demonstrated that a kinetic hurdle is created for the incoming molecule due to the shielding of CNT walls. Due to this, diffusion inside the nanotube and the reaction with the adsorbate become difficult, resulting into suppressed activity [34]. This effect was observed in the case of the reaction between 1-heptane and hydrogen atoms. Considering the above observation, the same can be expected, sometimes more prominently, in the case of Nafion entry into CNF cavity because of its size effects. Moreover, since the tips of CNF are expected to be more active as compared to the surface, more Nafion will be segregated on the tips, resulting into a blocking effect.

6.3.4.2. RDE Analysis

Since ORR is a complex combination of charge transfer and mass transport processes, RDE studies are best suited to provide additional insight on the performance of electrocatalysts [35]. Hence, to compare the activity characteristics effectively and to investigate the potential effect of PBI-BuI in improving the ORR activity, LSV is also conducted using a rotating-disk electrode in O_2-saturated 0.5 M $HClO_4$. The ORR polarization curves for F-Pt, FPV-0.4, FPV-0.6, FPV-0.8 and FPV-1.5 at a constant rotating rate of 1600 rpm are given in Figure 6.9(a).

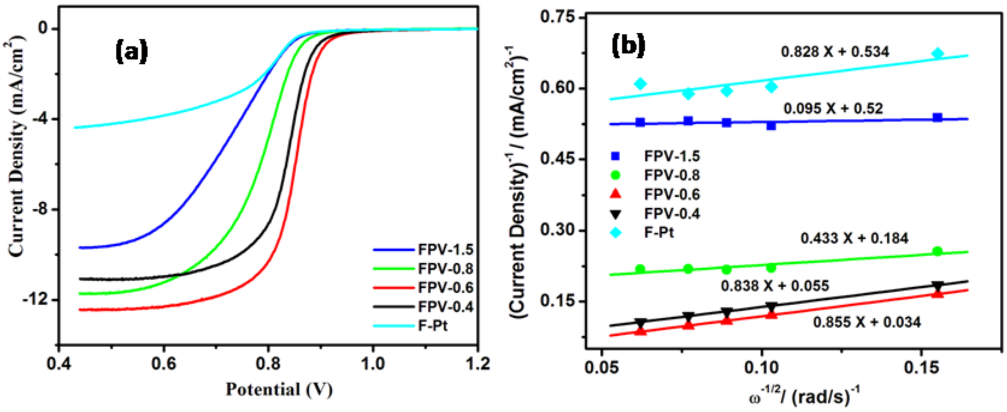

Figure 6.9. (a) ORR polarization curves in O_2 saturated 0.5 M $HClO_4$, rotation rate 1600 rpm, scan rate 5 mV/s and (b) K-L plots at 0.8 V for FPV-0.4, FPV-0.6, FPV-0.8, FPV-1.5 and F-Pt electrodes; all the potentials are quoted *vs*. RHE.

The ORR polarization curves of all the F-Pt-PBI hybrid materials except FPV-1.5 are shifted to more positive potentials as compared to that of F-Pt. This indicates the much more active ORR at lower overpotentials. Detailed analyses of the ORR polarization curves of all the electrode materials based on the half wave potential, specific activity, mass activity and limiting current density etc. are summarised in Table 6.2. The following order is obtained for the ORR activity: FPV-0.6 > FPV-0.4 > FPV-0.8 > FPV-1.5 > F-Pt. It is evident from the above data that the best ORR activity is obtained for FPV-0.6 with the highest kinetic current, favourable onset potential and 70 mV more positive half wave potential than F-Pt. In fact, all the F-Pt-PBI-BuI systems except FPV-1.5 displayed improved activity. This indicates the improved utilization of the F-Pt material for ORR after the PBI-BuI incorporation. The FPV-1.5 catalyst displays a negative effect on the ORR activity with lower half wave potential. This trend is in accordance with the CV results also, where the ECSA obtained for FPV-1.5 system is actually lower than that attained for F-Pt. The present study indicates that the change in the viscosity will result into drastic variation in the electrochemical activity. It is also revealed that the amount as well as the viscosity of the binder are crucial parameters in tuning the electrochemical activity. More importantly, to the best of our knowledge, this is the first sucessful study wherein the effect of the viscosity of the inomer on the electrochemical performance is reported.

Table 6.2. Comparison of the electrochemical activity of various materials

Sample	**ECSA for ORR from CV (m^2/g-Pt)**	**Half-wave Potential for ORR (V)**	**Specific Activity at 0.85 V (mA/cm^2)**	**Mass Activity at 0.85 V (mA/mg-Pt)**	**Limiting Current Density (mA/cm^2)**
F-Pt	19	0.78	0.5	9.8	4.4
FPV-0.4	51	0.84	4.0	78.4	11.0
FPV-0.6	63	0.85	6.3	123.5	12.5
FPV-0.8	48	0.79	1.2	23.5	11.7
FPV-1.5	17	0.73	0.5	9.8	9.7

In order to obtain detailed mechanistic information about the ORR, K-L plots at different potential values are also analysed [32]. Figure 6.9(b) shows the K-L plots corresponding to FPV-0.4, FPV-0.6, FPV-0.8, FPV-1.5 and F-Pt catalysts at 0.85 V. On a closer inspection, it can be observed that the K-L plots corresponding to F-Pt, FPV-0.4 and FPV-0.6 are parallel to each other whereas FPV-0.8 and FPV-1.5 show a deviation from the parallelism. Linearity and parallelism in the K-L plots are indicative of the similar ORR mechanism in the materials. Hence, it can be concluded that the F-Pt, FPV-0.4 and FPV-0.6 systems follow similar mechanism for ORR whereas the FPV-0.8 and FPV-1.5 catalysts show a mechanistic difference in the pathway followed. This observation clearly indicates that the viscosity of the PBI-BuI has a crucial role in modulating the ORR activity. The observed variation in the ORR activity with the viscosity of the polymer binder can be attributed to the following facts. When the viscosity of the polymer is higher, it cannot be effectively incorporated into the inner cavity of the CNFs. This is unambiguously revealed from the pore-size distribution analysis, where the pore volume corresponding to the primary pores remains unchanged at higher viscosity. Hence, at the same P/C ratio, the thickness of the binder layer on the outer surface of F-Pt will be higher as compared to that at a lower viscosity. This will create diffusional limitation to the reactants to reach at the active sites. Such diffusional limitation is evident from the ORR polarization curves corresponding to the hybrid materials at higher viscosities (FPV-0.8 and FPV-1.5) also, where the diffusion plateau is achieved slowly as compared to the other catalysts. Similar kind of kinetic hurdle to the diffusion of the incoming molecule into the inner cavity of nanotubes is demonstrated due to the shielding of CNT walls [34]. Taking into consideration of the above observation, the same can be expected, sometimes more prominently, in the case of PBI-BuI with high viscosity.

6.3.4.3. Impedance Analysis

To understand the reason for the improved performance, impedance analyses of the FPV-0.6 and F-Pt catalysts (optimised from the CV and RDE studies) are conducted. Accordingly, Figure 6.10 shows the Nyquist plot of MEA impedance measurements at different temperatures (120, 140 and 160 °C). From the Nyquist plot, it is clear that the charge transfer resistance (R_{ct}) decreases with increse in the temperature in the FPV-0.6 system. This is a clear indication of the faster kinetic process at high temperatures. However, in F-Pt, a reverse trend is observed. The R_{ct} increases with increase in temperature. This may be due to the dehydration of Nafion binder at high temperature [21]. On a comparison of the Nyquist plot for FPV-0.6 and F-Pt electrodes at same temeprature, it is clear that the R_{ct} is lower for the Nafion based systems. This is due to the low inherent conductivity of PBI-BuI as compared to that of Nafion. However, it is worth mentioning that for high temperature applications PBI-BuI can be a better option as compared to Nafion.

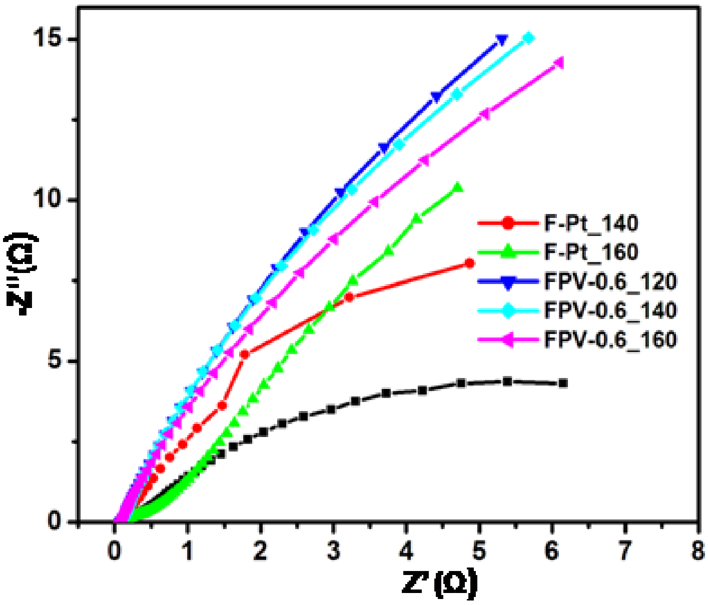

Figure 6.10. Impedance Nyquist plots obtained for F-Pt and FPV-0.6 at various temperatures by passing hydrogen and oxygen to the anode and cathode respectively.

6.3.4.4. Single Cell Analysis

The single cell performance evaluation of the FPV-0.6 and F-Pt catalysts is also conducted to demostrate the real fuel cell performnce of these materials. Inorder to compare the activity characteristics in a more effective manner, polarization studies are conducted with commercial Pt/C also. In all the cases, H_3PO_4 doped PBI membranes are used and commercially available 40 wt% Pt/C (Johnson Matthey) with a loading of 0.20 mg cm^{-2} is used at the anode. The comparison of the H_2/O_2 fuel cell polarization measurements at 160 °C presented in Figure 6.11 shows that the power density obtained for FPV-0.6 and F-Pt electodes are 305 and 230 mW/cm^2 respectively. It is clear that there is 70 mW/cm^2 increase in the power density in the MEA corresponding to the PBI-BuI based binder. This improvement in the activity is maintained in the entire polarization plot including the activation, ohmic and mass transfer controlled regions. Since the analysis is carried out with the same kind of catalyst and membrane, under similar test conditions, the improvement in the activity obtained can be transelated in terms of the PBI-BuI binder.

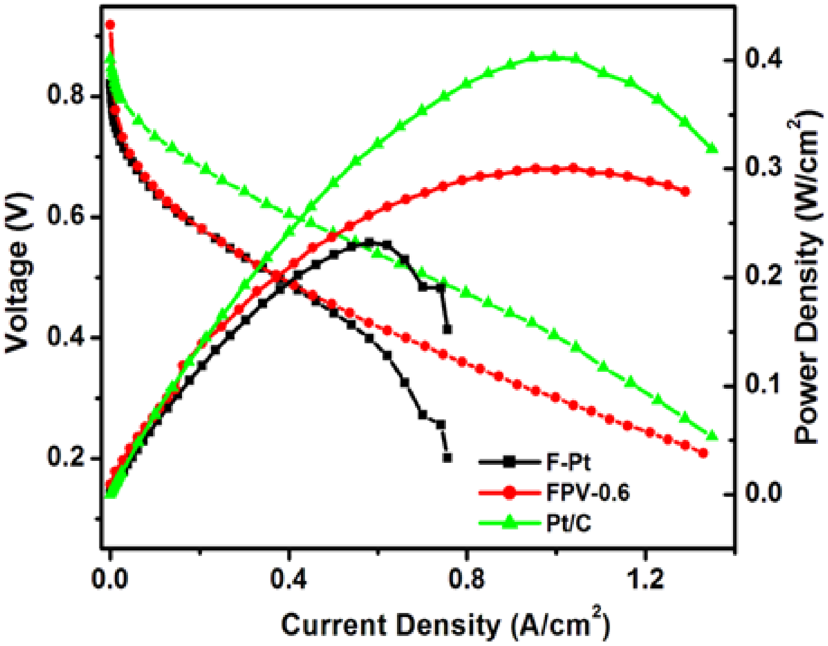

Figure 6.11. Single cell evaluation of the MEAs with the cathode electrodes formed from F-Pt, FPV-0.6 and Pt/C. Commercial 40 wt% Pt/C is used as the anode and a Pt loading of 0.20 mg-Pt/cm^2 is maintained in the cathode and anode.

Apart from this, the single cell analysis is also carried out at various temperatures (140, 150 and 160 °C) and the results are presented in Figure 6.12. It is clear that the FPV-0.6 based MEA dispalys a constant increase in the performance with temperature and it is stable upto a temperature of 160 °C. This result indicates that PBI-BuI binder can be a better counterpart to the PBI membranes for high temperature applications. However, the power density obtained for Pt/C based MEA is higher (400 mW/cm^2) as compared to the FPV-0.6 electrode. This may be due to the low surface area of CNF as compared to that of the vulcan carbon support. However, the possibility of extending this approach to other high surface area carbon supports indicates the possibility of a significant improvement in the activity especially for high temperature applications.

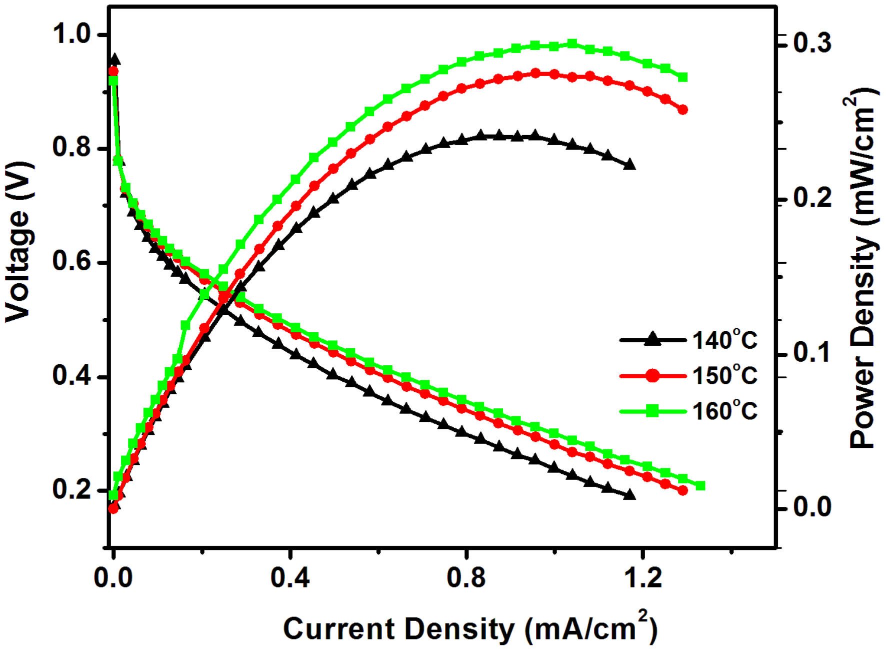

Figure 6.12. Single cell evaluation of the MEAs with the cathode electrodes formed from FPV-0.6 at temperatures 120, 140 and 160° C. Commercial 40 wt% Pt/C is used as the anode and a Pt loading of 0.20 mg-Pt/cm^2 is maintained in the cathode and anode.

6.4. Conclusions

We have developed a new electrode material by imparting the required features to enable the system to simultaneously address multiple functions such as proton and electron conductivity and surface reactivity while ensuring pathways for reactant distribution and product dissipation. This is achieved by decorating Pt NPs along the inner cavity as well as on the outer walls of the hollow CNF support (F-Pt). In a further extension, a low molecular weight PBI synthesized by optimizing the experimental parameters is incorporated into the inner cavity and along the outer surfaces of F-Pt. The key part in the present strategy is the synthesis of a low molecular weight PBI-BuI which satisfies all the necessary requirements to act as a binder in PEMFCs with accurate control on the viscosity. Along with this, the controlled interplay of the choice of the proper solvent and the solution concentration helps the low molecular weight polymer solution to be carried inside the narrow cavity of the substrate. The resulting F-Pt-PBI-BuI hybrid system, with the unique combination of almost double support surface area, proper Pt dispersion and establishment of an efficient TPB, shows the exceptionally high activity as can be evident from the CV, RDE, EIS and single cell analyses. Moreover, our study strongly indicates that PBI-BuI as a binder has a positive effect in tuning the electrochemical activity at an optimum concentration and at a favourable viscosity. The excellent oxygen reduction property displayed by the system offers intriguing possibilities of the present concept in effectively utilizing materials and creating new avenues in system developments.

6.5. References

1 M. K. Debe, *Nature* **2012**, *486*, 43.

2 H. A. Gasteiger, S. S. Kocha, B. Sompalli, F. T. Wagner, *Appl. Catal. B* **2005**, *56*, 9.

3 J. Greeley, I. E. L. Stephens, A. S. Bondarenko, T. P. Johansson, H. A. Hansen, T. F. Jaramillo, J. Rossmeisl, I. Chorkendorff, J. K. Nqrskov, *Nat. Chem.* **2009**, *1*, 552.

4 S. Yang, X. Feng, X. Wang, K.Mullen, *Angew. Chem. Int. Ed.* **2011**, *50*, 5339.

5 E. Antolini, *Appl. Catal. B* **2009**, *88*, 1.

6 Y. Shao, J. Liu, Y. Wang, Y. Lin, *J. Mater. Chem.* **2009**, *19*, 46.

7 R. Borup, J. Meyers, B. Pivovar, Y. S. Kim, R. Mukundan,N. Garland, D. Myers, M. Wilson, A. Nishikata, Z. Siroma, Y. Uchimoto,K. Yasuda, K. I. Kimijima, N. Iwashita, *Chem. Rev.* **2007**, *107*, 3904.

8 N. M. Marković, T. J. Schmidt, V. Stamenković, P. N. Ross, *Fuel Cells* **2001**, *1*, 105.

9 Y. Shao, J. Sui, G. Yin, Y. Gao, *Appl. Catal. B* **2008**, *79*, 89.

10 W. Zhang, P. Sherrell, A. I. Minett, J. M. Razal, J. Chen, *Energ. Environ. Sci.* **2010**, *3*, 1286.

11 W. Li, M. Waje, Z. Chen, P. Larsen, Y. Yan, *Carbon*, **2010**, *48*, 995.

12 F. Alcaide, G. Álvarez, O. Miguel, M. J. Lázaro, R. Moliner, A. López-Cudero, J. Solla-Gullón, E. Herrero, A. Aldaz, *Electrochem. Commun.* **2009**, *11*, 1081.

13 G. G. Wildgoose, C. E. Banks, R. G. Compton, *Small* **2006**, *2*, 182.

14 V. Georgakilas, D. Gournis, V. Tzitzios, L. Pasquato, D. M. Guldi, M. Prato, *J. Mater. Chem.* **2007**, *17*, 2679.

15 M. Tsuji, M. Kubokawa, R. Yano, N. Miyamae, T. Tsuji, M. S. Jun, S. Hong, S. Lim, S. H. Yoon, I. Mochida, *Langmuir* **2007**, *23*, 387.

16 J. Lee, J. Kim, T. Hyeon, *Adv. Mater.* **2006**, *18*, 2073.

17 Y. Y. Shao, G. P. Yin, J. J. Wang, Y. Z. Gao, P. F. Shi, *J. Power Sources* **2006**, *161*, 47.

18 V. Mehta, J. S. Cooper, *J. Power Sources* **2003**, *114*, 32.

19 R. Subbaraman, D. Strmcnik, V. Stamenkovic, N. M. Markovic, *J. Phys. Chem. C* **2010**, *114*, 8414.

20 S. J. Shin, J. K. Lee, H. Y. Ha, S. A. Hong, H. S. Chun, I. H. Oh, *J. Power Sources* **2002**, *106*, 146.

21 J. Lobato, M. A. Rodrigo, J. J. Linares, K. Scott, *J. Power Sources* **2006**, *157*, 284.

22 M. Uchida, Y. Aoyama, N. Eda, A. Ohta, *J. Electrochem. Soc.* **1995**, *142*, 4143.

23 J. H. Kim, H. J. Kim, T. H. Lim, H. I. Lee, *J. Power Sources* **2007**, *170*, 275.

24 J. Lobato, P. Canizares, M. A. Rodrigo, J. J. Linares, F. J. Pinar, *Int. J. Hydrogen Energ.* **2010**, *35*, 1347.

25 K. Matsumoto, T. Fujigaya, H. Yanagi, N. Nakashima, *Adv. Funct. Mater.* **2011**, *21*, 1089.

26 M. Okamoto, T. Fujigaya, N. Nakashima, *Small* **2009**, *5*, 735.

27 S. C. Kumbharkar, P. B. Karadkar, U. K. Kharul, *J. Membr. Sci.* **2006**, *286*, 161.

28 (a) P. M. Ajayan, S. Iijima, *Nature* **1993**, *361*, 333. (b) Skoulidas, D. S. Sholl, J. K. Johnson, *J. Chem. Phys.* **2006**, *124*, 1.

29 E. H. Lock, W. M. Merchan, J. D’Arcy, A. V. Saveliev, L. A. Kennedy, J. Phys. Chem. C **2007**, *111*, 13655.

30 T. J. Schmidt, H. A. Gasteiger, G. D. Stab, P. M. Urban, D. M. Kolb, R. J. Behm, *J. Electrochem. Soc.* **1998**, *145*, 2354.

31 M. H. Lee, J. S. Doa, *J. Power Sources* **2009**, *188*, 353.

32 E. Passalacqua, F. Lufrano, G. Squadrito, A. Patti, L. Giorgi, *Electrochim. Acta* **2001**, *46*, 799.

33 A. L. M. Reddy, S. Ramaprabhu, *J. Phys. Chem. C* **2007**, *111*, 16138.

34 P. Kondratyuk, J. T. Yates, *Acc. Chem. Res.* **2007**, *40*, 995.

35 T. J. Schmidt, H. A. Gasteiger, G. D. Stab, P. M. Urban, D. M. Kolb, R. J. Behm, *J. Electrochem. Soc*. **1998**, *145*, 2354.

Chapter 7

A Novel Route for Nitrogen Doping Along the Inner and Outer Surfaces of Carbon Nanofiber and its Electrocatalytic Activity*

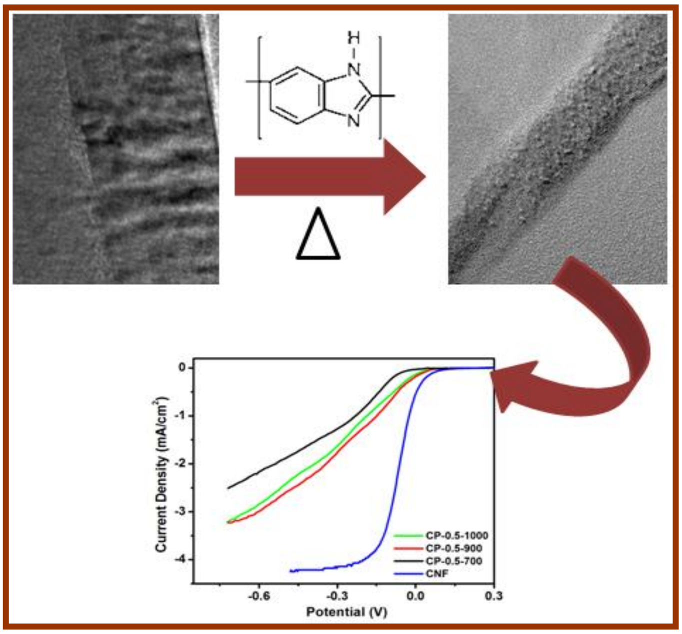

This chapter describes a simple polymer mediated strategy for nitrogen-doping (N-doping) along the inner and outer surfaces of a hollow CNF and its electrocatalytic activity for ORR. This was achieved by incorporating nitrogen containing polymer precursor PBI-BuI, along the inner and outer walls of CNF by synthesizing a low molecular weight polymer. The high temperature treatment (700-1000 °C) of the resulting CNF-PBI material decomposes the polymer and induces N-doping along the inner and outer surfaces of CNF. The initial PBI-BuI content and the annealing temperature are also systematically varied to choose the right combination of starting precursors and heat-treatment conditions. Electrochemical characterizations of this material using CV and RDE studies and durability analysis demonstrated that this material can act as a metal-free oxygen reduction electrocatlyst with improved oxygen reduction kinetics and stability.

***** The contents of this chapter have been published in "*J. Mater. Chem.* **2012**, *22*, 23668-23679"

7.1. Introduction

The sluggish kinetics of ORR is one of the major stumbling blocks in the energy conversion efficiency of PEMFCs [1]. So far, fuel cell technology has relied almost exclusively on Pt and Pt-based materials as the best cathode catalysts for ORR [2]. However, the high cost of the PEMFCs resulting from the Pt based catalysts hamper the wide-scale acceptance of PEMFCs as clean energy source and their large scale commercialization. Apart from this, Pt suffers from multiple problems like limited reserves, susceptibility to CO poising, poor durability etc [3]. Therefore, exploration of non precious metal or metal-free catalysts which have the potential to rival the Pt-based catalysts in terms of activity and durability; will have a long term impact on the fuel cell technologies [4]. Recent reports have demonstrated that N-doped carbon nanostructures show excellent electrocatalytic activity toward the ORR [5]. A full understating of the active sites and the role of nitrogen atoms in N-doped systems is still controversial. The generally accepted mechanism on the basis of the experimental studies and quantum-mechanical calculations is that due to the electro-negativity difference, a net positive charge is created on the carbon atoms adjacent to nitrogen atoms in the carbon based nanostructures, which facilitates the O_2 adsorption and the ORR process [6]. For example, Dai et al. demonstrated that vertically aligned N-containing carbon nanotubes (VA-NCNTs) can act as an efficient metal-free electrode with high durability and tolerance to crossover [5b]. However, an additional purification step was needed for the removal of the residual Fe catalyst. Mullen *et al*. reported the electrocatalytic activity of graphene based carbon nitride nanosheets [5c]. In another approach, Qiao and co-workers have designed a three-dimensionally ordered macroporous graphitic-C_3N_4/carbon composite catalyst with outstanding ORR performance [7]. Both the materials exhibited excellent electrocatalytic activity; however, multiple steps were involved in the preparation of the catalysts using a solid silica template.

Till now, the methods adopted for the synthesis of N-containing carbon materials can be broadly categorized into two groups; the direct doping during synthesis by the high temperature pyrolysis of precursors containing nitrogen and carbon [5d, 8] and the post synthetic treatment of carbon materials in the presence of N-containing precursors such as ammonia, melamine, imidazole, PBI, amino acids etc. [9-13]. Some groups have reported the synthesis of N-doped graphene without high temperature pyrolysis as well [14]. However, the direct N-incorporation in these structures introduces a large number of defect sites resulting in a less stable structure. Hence, the post-treatment approach should be more advantageous as we can restrict the doping on the outer surfaces, thus retaining the stability of the core. Apart from this, post-treatment offers a tantalizing means of controlling the content and nature of the N-centers in a well defined manner by simply changing the chemical structure of the precursor compound [12]. Moreover, there is a large possible combination of carbon nanostructures and nitrogen precursors available with a handful of experimental variables such as temperature, reaction time, precursor nature and content, etc. This suggests that there is still considerable room for cost-effective preparation of various metal-free catalysts for ORR, and even new catalytic materials for applications beyond fuel cells.

Our studies (Chapter 6) have demonstrated that the physical adsorption of PBI-BuI can enhance the individual dispersion of CNTs and/or CNFs by exfoliating the strong bundles [15]. It is also observed that there exists a strong π-π interaction between the CNF/CNT with PBI-BuI which modulates the electronic properties of the CNT/CNF [15]. These findings persuaded us to develop N-doped, Pt-free ORR electrocatalyst by the simultaneous incorporation and wrapping of PBI-BuI in the inner cavity as well as on the outer walls of CNF followed by thermal annealing. CNF is selected as a promising carbon nanomaterial because it can be a low cost alternative to CNT with its high aspect-ratio and unique structure resulting from the stacking of individual graphene cups. Furthermore, plenty of exposed graphene edges are present in the inner cavity which can be utilized through the open tips for N-doping [16]. Such terminal edges of the graphene planes can act as the active sites for N-incorporation, leading to strong confinement effects. Apart from this, since the graphene edges of CNF are more active, the incorporated N-atoms are reported to be concentrated more on these edges. Such nitrogen enrichment may result into higher electrocatalytic activity as compared to that of CNT, where the N-atoms will be distributed on the entire surface [5d]. In addition to this, the possibility of utilization of the outer surface for N-doping is still there as in the case of many other carbon nanostructures. Briefly, the simultaneous wrapping and encapsulation of the PBI-BuI in the CNF is achieved by optimizing the synthesis parameters of PBI-BuI to obtain low viscosity and by manipulating the solution concentration; as discussed in chapter 6. This CNF-PBI hybrid material is then subjected to thermal annealing in Ar atmosphere to obtain the N-doped CNF. The initial PBI-BuI content and the annealing temperature are also systematically varied to choose the right combination of the starting precursors and the heat-treatment conditions. Though, the polymer mediated synthesis of N-containing CNTs and their activity as ORR electrocatalysts are reported in the literature, to the best of our knowledge, there is no attempt which addresses the polymer incorporation followed by N-doping in the inner cavity as well as on the outer walls of CNF. Since a controlled coverage of the polymer along the inner and outer surfaces of CNF has been accomplished by carefully optimizing various process parameters, more uniform and controlled N-doping could be achieved by effectively utilizing the available surface of CNF. The resultant N-doped CNF exhibited superior electrocatalytic activities towards ORR with improved kinetics.

7.2. Experimental Section

7.2.1. Synthesis of N-doped CNF

N-doped CNF was synthesized by the post treatment of CNF using PBI-BuI as the nitrogen precursor. In the typical synthesis, 10 mg of the CNF was added to the calculated volume of the 0.5 wt% PBI-BuI solution in DMAc. The total volume of the slurry was then made up to 5 mL by adding DMAc. The mixture was initially sonicated using a probe sonicator (30 sec pulse for 5 times) to facilitate the PBI-BuI entry into the nanocavity as well as to obtain a uniform dispersion. Subsequently, this reaction mixture was kept stirring for 12 h at RT to attain a homogeneous coverage along the inner and outer surfaces. The CNF-PBI material with different polymer/carbon (P/C) ratios (P/C-0.25, 0.5, 1 and 2), respectively, designated as CP-0.25, CP-0.5, CP-1 and CP-2 were also prepared using the same procedure. The resulting material was then subjected to solvent evaporation by simultaneous heating and stirring at 100 °C till a solid material was obtained. This solid material was then ground well in a mortar using pestle, and was then annealed for 2 h at 700 °C temperature with an Ar flow of 0.5 sccm. After this process, the reaction was cooled down to RT. Finally, the N-doped CNF material was collected from the furnace. Any unwanted impurities present in the sample were removed by successive washing with ethanol several times. The final material was filtered, dried and was used for the further characterizations and electrocatalytic studies. Further, the N-doped CNF was synthesized at different pyrolyzing temperatures also (700, 900 and 1000 °C) using the same procedure. The N-doped CNF synthesized at P/C ratios of 0.25, 0.5, 1.0 and 2.0 at the annealing temperatures of 700, 900 and 1000 °C are respectively denoted as CP-0.25-700, CP-0.5-700, CP-1-700, CP-2-700, CP-0.5-900 and CP-0.5-1000.

7.3. Results and Discussion

7.3.1. TEM and HRTEM Analysis

The morphological changes occurred in the CNF as a result of the PBI-BuI incorporation and subsequent N-doping is followed using TEM imaging. Figure 7.1(a-d) shows the representative TEM images of CNF at the P/C ratios of 0.25, 0.50, 1.0 and 2.0 respectively. Figure 7.1(a), the TEM image of CP-0.25, clearly shows a discontinuous filling of the polymer in the inner cavity along with an uneven coating of the same on the outer surface. In CP-0.5, the coating is rather uniform and the image indicates almost continuous filling in the inner cavity as well [Figure 7.1(b)]. However, at higher P/C ratios, as can be evident from Figure 7.1(c-d), the entire CNF is immersed in the polymer matrix with the individual tubes interconnected by a thick polymer layer. These results indicate that the uniformity as well as the extent of the polymer incorporation varies with the P/C ratios. It is also important to note that at the P/C ratio of 0.5, a uniform coating on the outer surface along with its continuous filling in the inner cavity is formed in

CNF. Moreover, at higher P/C ratios, the excess polymer is deposited as agglomerates in the regions away from the CNF surface.

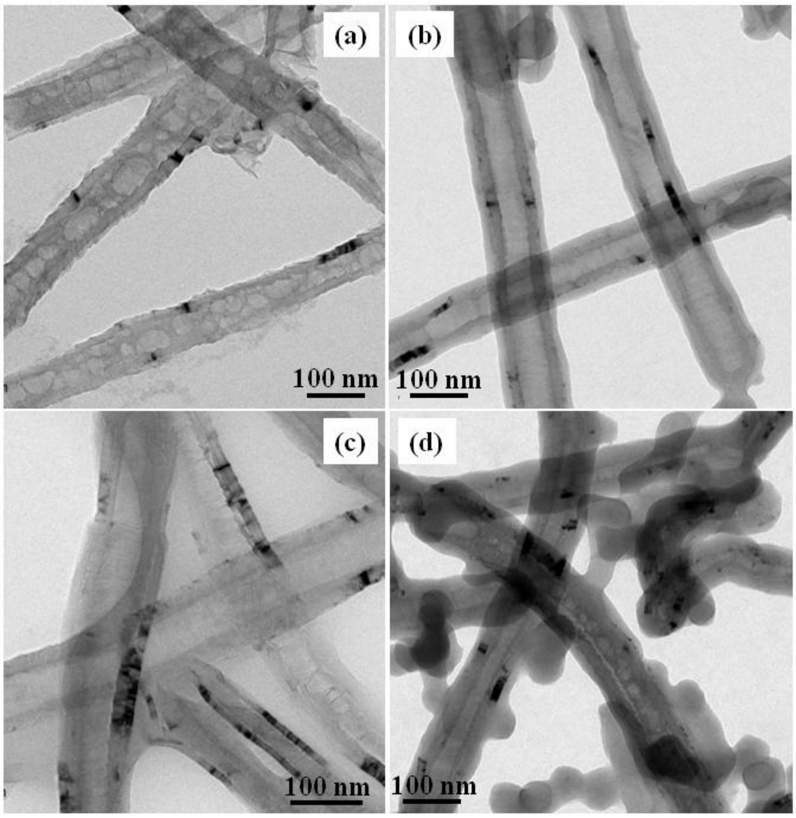

Figure 7.1. TEM images of (a) CP-0.25, (b) CP-0.5, (c) CP-1 and (d) CP-2 clearly depicting the variation in the extent of the polymer incorporation with different P/C ratios.

As HRTEM is one of the best tools to analyze the structural and morphological changes in the samples with atomic level precision, it can be effectively used to follow the N-doping in CNF. Figure 7.2(a-f) displays the representative TEM images of CNF and N-incorporated samples prepared by pyrolysis at 900 °C at various magnifications. On a comparison with the undoped CNF as given in Figure 7.2(a and b), it can be inferred that the length, diameter and the hollow interior of the tubes are retained as such even after the N-incorporation, as can be evident from Figure 7.2(d and e). However, prominent differences in the arrangement of the graphene layers along the walls of the CNF are observed after the N-doping [Figure 7.2(c and f)]. In the undoped CNF, uniform and parallel stacking of the graphene layers are observed [Figure 7.2(c)] whereas the N-incorporation has created more disruptions in the parallel graphene stacking of CNF, which results into buckled and curved arrangement [Figure 7.2(f)].

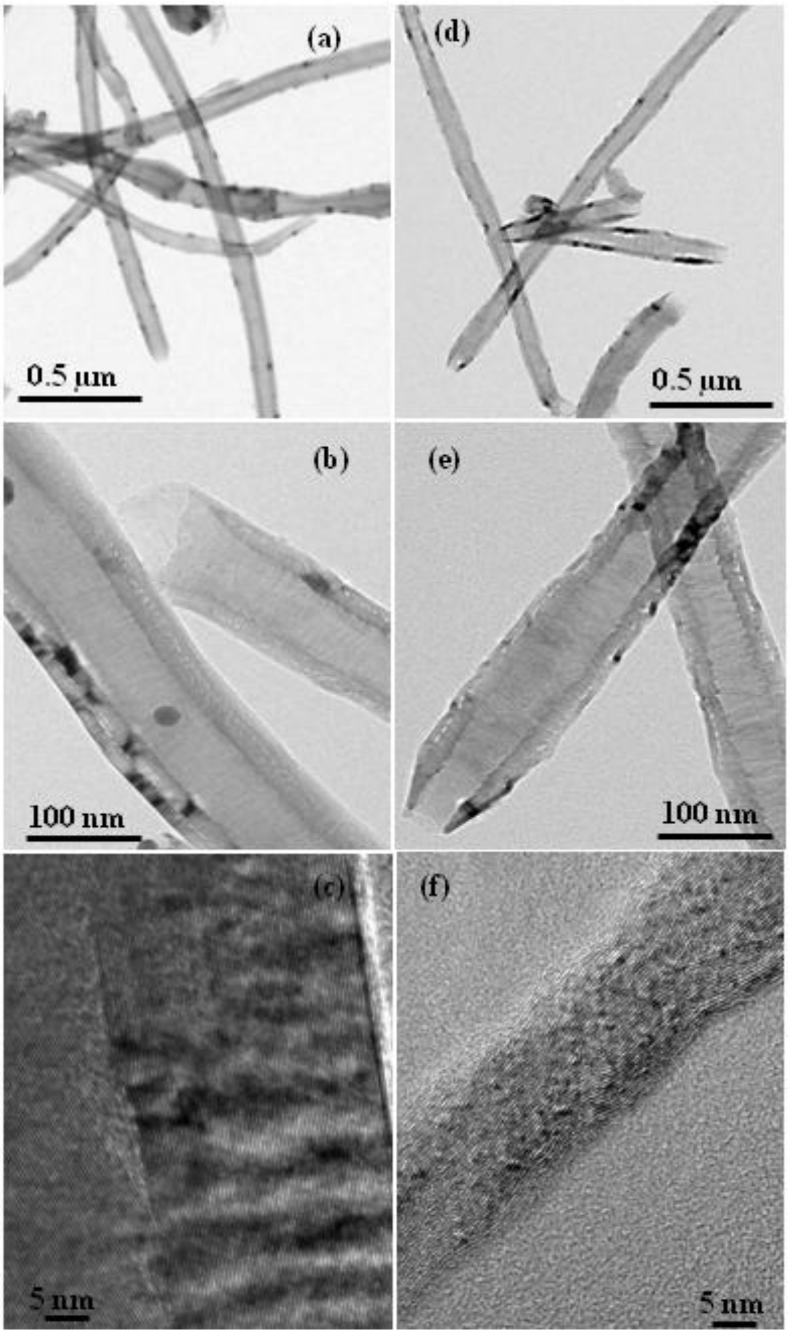

Figure 7.2. TEM images of (a, b and c) hollow CNF and (d, e and f) CP-0.5-900 at various magnifications.

Such ‘turbostatic disorders’ with more dislocations and disruptions in the graphene stacking exhibited by the N-doped CNF are consistent with earlier reports [17]. Such disruptions and irregular curvature in graphene stacking are due to the tendency of the incorporated nitrogen to form pentagonal defects in the graphene sheets. This disrupts the planar hexagonal arrangement of carbon atoms, leading to the buckling of the graphene layers, and resulting in the fluctuation of the interlayer distances. Generally, N-doping in MWCNTs results into bamboo like structure where the nanotube contains a regularly spaced array of internal carbon walls [18]. Similarly, in the doped CNFs, more compartmentalization within the individual graphene cups is observed. The distortions created by such changes on the graphene layers can be clearly observed on a comparison of Figure 7.2(b) and (e), where N-doping induced narrow compartments compared to the undoped counterpart.

Morphologies of the N-doped CNF pyrolysed at 700 °C are also characterized by HRTEM analysis. Figure 7.3(a and b) show the representative images of CP-0.5-700 at different magnifications. On a comparison of the HRTEM images of CNF, CP-0.5-900 and CP-0.5-700 as given in Figure 7.2(c and f) and Figure 7.3(b) respectively, it can be deduced that the extent of disrupts and irregularities observed in the samples annealed at 700 °C is less as compared to that annealed at 900 °C. It is also important to note that the wavy pattern is observed only in the outer few graphene layers and the parallel stacking in the inner graphene layers is not disturbed much [Figure 7.3(b)]. This reveals a lesser degree of nitrogen incorporation in these samples. Moreover, we also observed an amorphous-like structure on the outer wall of the CP-0.5-700 as can be seen from Figure 7.3(a). We speculate that this amorphous-like material may be the partially burned polymer present in the sample. Based on the above observations, it can be concluded that a lower pyrolysis temperature (here 700 °C) is not sufficient for the complete decomposition of the PBI-BuI precursor into atomic nitrogen. As a result of this, the level of nitrogen incorporation will also be less. These results demonstrate that N-doping in CNF has strong temperature dependence. Similar kind of temperature effect for N-doping is observed in the case of other carbon morphologies as well [5b, 11].

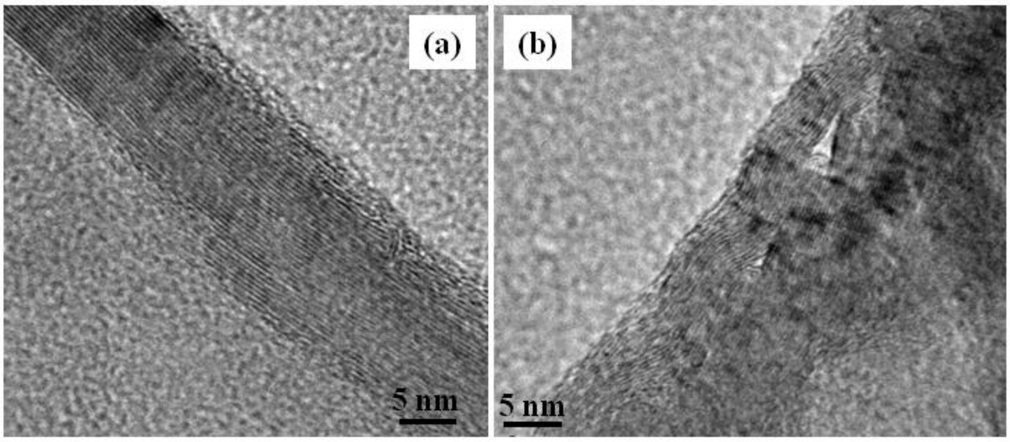

Figure 7.3. TEM images of CP-0.5-700 (a) indicating the presence of an amorphous layer on the outer wall and (b) the high magnification image showing the disorder induced in the outer few layers as a result of N-doping.

7.3.2. XRD Analysis

XRD analysis of the samples synthesized at different temperatures and polymer compositions is also conducted and the results are presented in Figure 7.4(a and b). Figure 7.4(a), the comparison of the XRD patterns of CNF, CP-0.25-700, CP-0.5-700, CP-1-700 and CP-2-700, exhibits an intense peak at 2θ = 26.4° for CNF, which can be attributed to the (002) plane diffractions from graphitic carbon [19]. The XRD profiles of CNF before and after N-doping appear almost similar. However, on a closer inspection, it can be observed that the diffraction peaks in the N-doped samples are slightly shifted to lower 2θ values as compared to that of CNF, with the (002) planes in the CNF, CP-0.25-700, CP-0.5-700, CP-1-700 and CP-2-700 systems observed at 26.5°, 26.34°, 26.13°, 26.25° and 26.27° respectively. Further, the *d*-spacing calculated from the (002) peaks of CNF, CP-0.25-700, CP-0.5-700, CP-1-700 and CP-2-700 are respectively 3.36, 3.38, 3.41, 3.39 and 3.39 Å. This slight shift in the (002) peak and the increased *d*-spacing observed in the N-doped samples imply a lower graphitic ordering in the samples. This can be attributed to the distortion in the CNF matrix as a result of the N-incorporation [19, 20]. From the shift in the peak position and the changes in the *d*-spacing obtained, it can be deduced that the highest N-doping is induced in the CP-0.5 system.

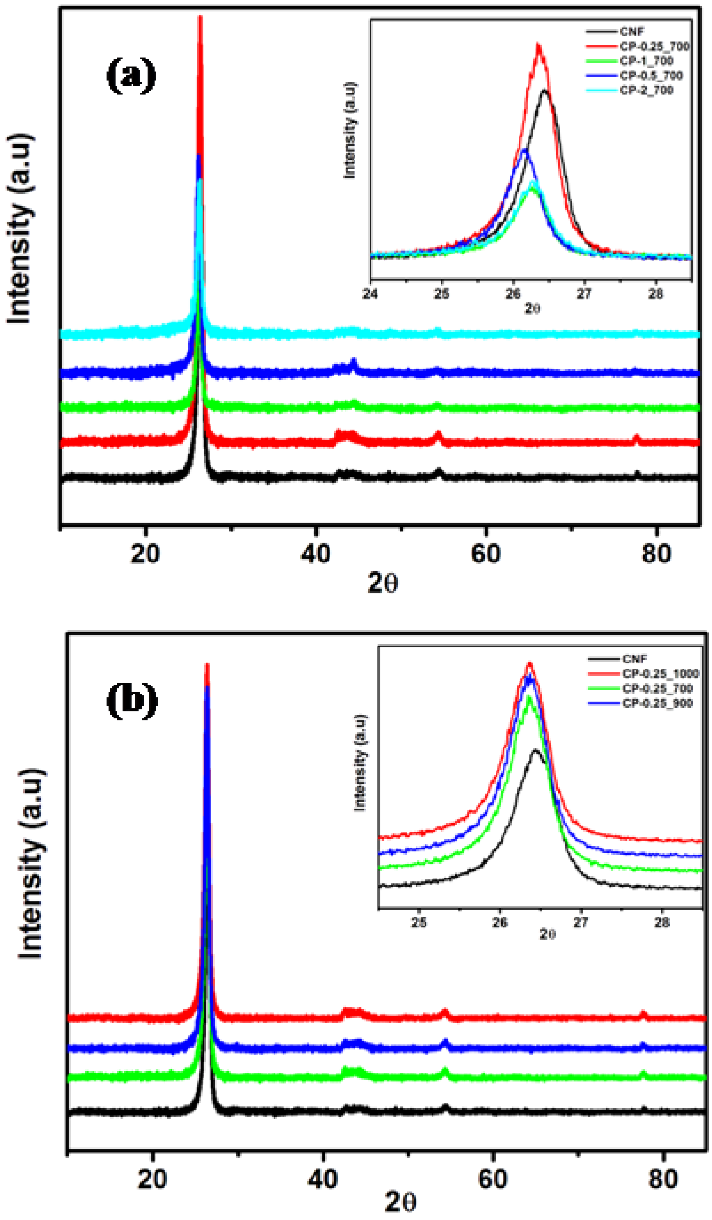

Figure 7.4. Powder XRD patterns obtained for (a) CNF, CP-0.25-700, CP-0.5-700, CP-1-700 and CP-2-700 and (b) CNF, CP-0.5-700, CP-0.5-900 and CP-0.5-1000; the inset shows the enlarged portion of the (002) planes.

The XRD analysis of the samples synthesized at various temperatures and at the P/C ratio of 0.5 is also carried out and the results are presented in Figure 7.4(b). The diffraction peak indexed to (002) plane shifts negatively as compared to that of CNF. It is evident from the XRD profiles that the highest shift in the peak position is observed in case of CP-0.25-900. Of interest, the peak position in CP-0.25-1000 retraces to a position close to CP-0.25-700. This can be explained based on the following facts. As the temperature increases from 700 to 900 °C, the total nitrogen content in the CNF matrix increases due to the high decomposition rate of the PBI-BuI precursor at high temperature [11]. This is evident from the TEM results also where a thin amorphous layer is clearly observed on the surface in CP-0.5-700 sample whereas this is completely absent in CP-0.5-900. At still higher temperature, the initial products can further decompose to molecular nitrogen which can escape from the reaction zone easily. Therefore, the nitrogen content decreases if the temperature exceeds an optimum level, which is in accordance with the earlier reports [21].

7.3.3. Raman Analysis

Raman spectroscopy is widely accepted as an excellent tool to characterize carbon based nanomaterials as it can provide precise information about the extent of defects, order/disorder in the structures and their graphitic nature [22]. Therefore, Raman spectroscopy is utilized to further characterize the CNF before and after N-doping. Figure 7.5 shows the comparison of the Raman spectra of the CNF with that of the N-doped samples. All of the samples exhibited similar patterns with the corresponding D, G and 2D bands at Raman shifts of 1325, 1570 and 2649 cm^{-1} respectively. The D band is indicative of the disordered graphite structure, whereas the G band indicates the presence of crystalline graphitic structure and the intensity ratio of D and G bands (I_D/I_G) can be used to estimate the extent of disorder within the samples [23]. The I_D/I_G ratio calculated for CNF is 0.33 whereas that obtained for CP-0.25-700, CP-0.5-700, CP-1-700, CP-2-700, CP-0.5-900 and CP-0.5-1000 systems are 0.36, 0.42, 0.42, 0.40, 0.60 and 0.45 respectively. The I_D/I_G ratio is higher in all the nitrogen incorporated systems as compared to that of CNF and the highest I_D/I_G ratio is obtained for CP-0.5-900 system. This indicates more defects which in turn indicate more nitrogen content in this system [24]. It is also evident from the Raman data that the I_D/I_G ratio increases when the pyrolysis temperature increases from 700 to 900 °C at the same polymer composition. A further increase in the temperature (900 to 1000 °C) results into a decrease in the (I_D/I_G) ratio. This also is in excellent agreement with the TEM and XRD results.

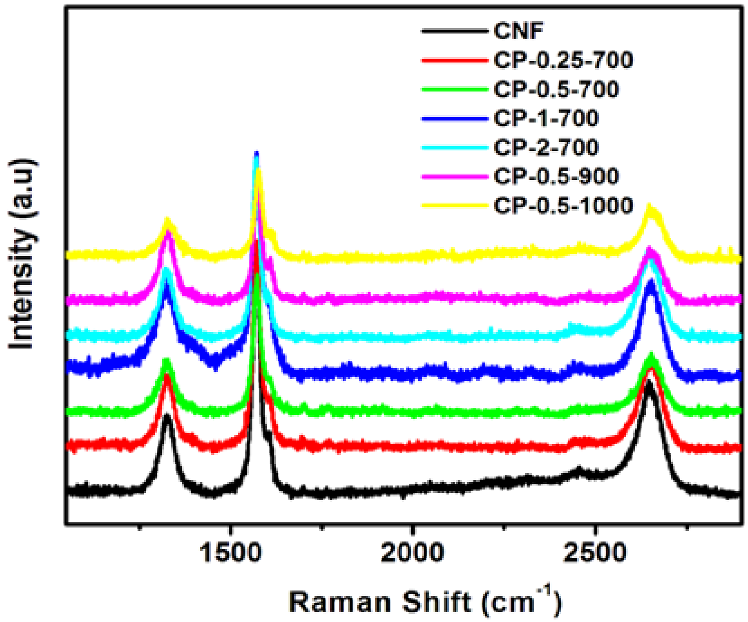

Figure 7.5. Comparison of the Raman spectra obtained for CNF, CP-0.25-700, CP-0.5-700, CP-1-700, CP-2-700, CP-0.5-900 and CP-0.5-1000.

7.3.4. TG Analysis

TG analysis of the CNF and the various N-doped samples is also performed in air from RT to 850 °C under identical conditions (e.g., analysis gas composition, flow rate and sample heating rate). Figure 7.6, the comparison of the TGA profile obtained for CNF, CP-0.5-700, CP-0.5-900 and CP-0.5-1000 samples, indicates that CP-0.5-700 exhibits a small weight loss followed by a continuous weight loss whereas CNF, CP-0.5-900 and CP-0.5-1000 show a single step weight loss. Moreover, it is important to note that the weight loss starts at different temperatures in all the samples which are indicative of their different thermal stability [11]. The weight loss occurs at the highest temperature in CNF which indicates its higher thermal stability. Interestingly, in CP-0.5-700, the weight loss is observed at a slightly lower temperature as compared to that of CNF. This can be attributed to the reduced thermal stability of the CNF as a result of N-incorporation. The weight loss in CP-0.5-900 occurs at the lowest temperature; however, from CP-0.5-900 to CP-0.5-1000, the thermal stability increases. The observed behavior can be ascribed to the following facts. It is reported that the N-doping in the carbon creates a higher number of deformations which makes them chemically more active toward thermal oxidation [17, 25]. Hence, once nitrogen is incorporated into the CNF matrix, its thermal stability decreases and gets oxidized at lower temperature. While moving from CP-0.5-700 to CP-0.5-900, the doping level increases and hence the thermal stability decreases further. Subsequently, from CP-0.5-900 to CP-0.5-1000, the doping level decreases and hence the thermal stability increases. These observations support HRTEM, Raman and XRD results as well. The additional, small weight loss observed in the TGA profile of CP-0.5-700 can be ascribed to the slight amount of partially burned polymer present in the sample, which is evident from the HRTEM results also.

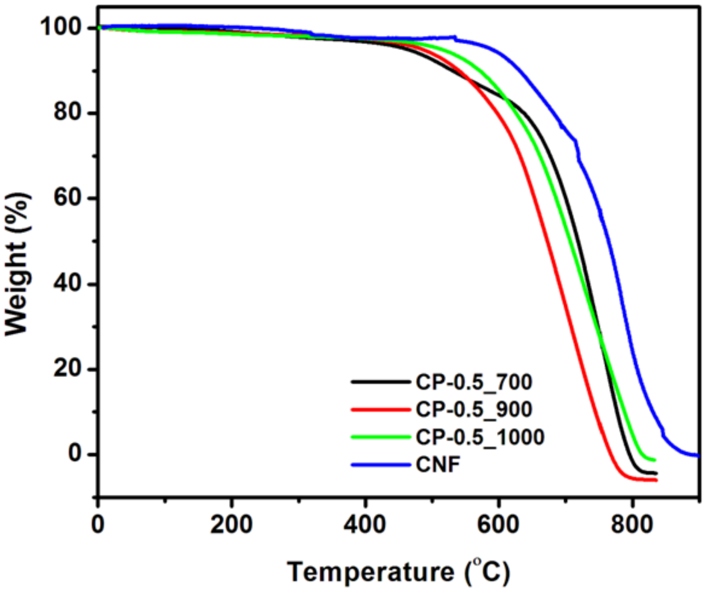

Figure 7.6. Comparison of the TGA profile obtained for CNF, CP-0.5-700, CP-0.5-900 and CP-0.5-1000 in air from RT to 1000 °C.

7.3.5. XPS Analysis

XPS analysis is carried out to investigate the elemental composition and the percentage of N-incorporation in CP-0.5-700, CP-0.5-900 and CP-0.5-1000 samples. In addition to this, as it is one of the best tools to identify the type of the nitrogen present in the samples based on their bonding interaction, XPS analysis is also used to quantify the amount of different types of nitrogen present in each sample. Accordingly, in the full survey XPS spectra of CP-0.5-700, CP-0.5-900 and CP-0.5-1000 given in Figure 7.7, peaks corresponding to C1s, O1s, N1s and Fe2p are observed. The most intense peak at 284.4 eV corresponds to the C1s sp^2 coordination [26]. The N1s and O1s peaks can be ascribed to those from the doped nitrogen and adsorbed oxygen and the Fe2p peak can be attributed to the catalyst used for the CNF synthesis [27].

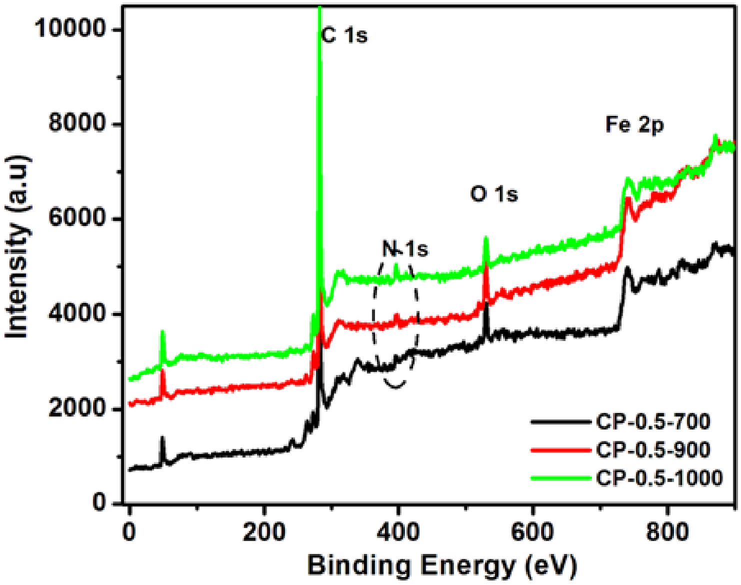

Figure 7.7. Comparison of the full survey XP spectra obtained for CP-0.5-700, CP-0.5-900 and CP-0.5-1000 showing the peaks corresponding to C1s, O1s, N1s and Fe2p.

The relative percentages of nitrogen in various samples are also calculated, which are 5.1, 8.4 and 7.4 atomic percentages, respectively in CP-0.5-700, CP-0.5-900 and CP-0.5-1000 (Table 7.1). The highest nitrogen atomic percentage is observed in CP-0.5-900. Apart from this, a slight decrease in the carbon atomic percentage is also observed with increase in the nitrogen percentage (Table 7.1). All these results authenticate the N-incorporation affected in the CNF.

Table 7.1. Atomic percentage calculated from the XPS data for Carbon, Nitrogen and Oxygen

	CP-0.5-700 (At%)	**CP-0.5-900 (At%)**	**CP-0.5-1000 (At%)**
Carbon	86.4	83.7	84.5
Nitrogen	5.1	8.4	7.4
Oxygen	8.5	7.9	8.1

Nitrogen atoms in carbon nanostructures exhibit a very broad range of structures such as graphitic, pyridinic, pyrrolic and oxidic type and each type of nitrogen sites is reported to contribute differently for ORR reaction [5b, 28]. As XPS is one of the best tools to identify the type of the elements present in the samples, based on their bonding interaction, the XPS spectra of C and N are deconvoluted to identify their bonding in the N-doped samples. Figure 7.8(a-f) shows the deconvoluted C1s and N1s peaks in CP-0.5-700, CP-0.5-900 and CP-0.5-1000 samples. The C1s part in all the three samples can be deconvoluted into three peaks. The most intense peak at 284.5 eV can be attributed to the graphite-like sp^2 C whereas the less intense peaks at 285.7 and 287.5-289.5 eV correspond to the N-sp^2 C and N-sp^3 C bonds [10b]. These peaks imply the different C-N bonding structures originated in the CNF as a result of the N-incorporation. It is also important to note that the highest intensity is for the peak at 284.5 eV even after the N-doping, indicating only a partial reconstruction of the graphene layers in the CNF during the process.

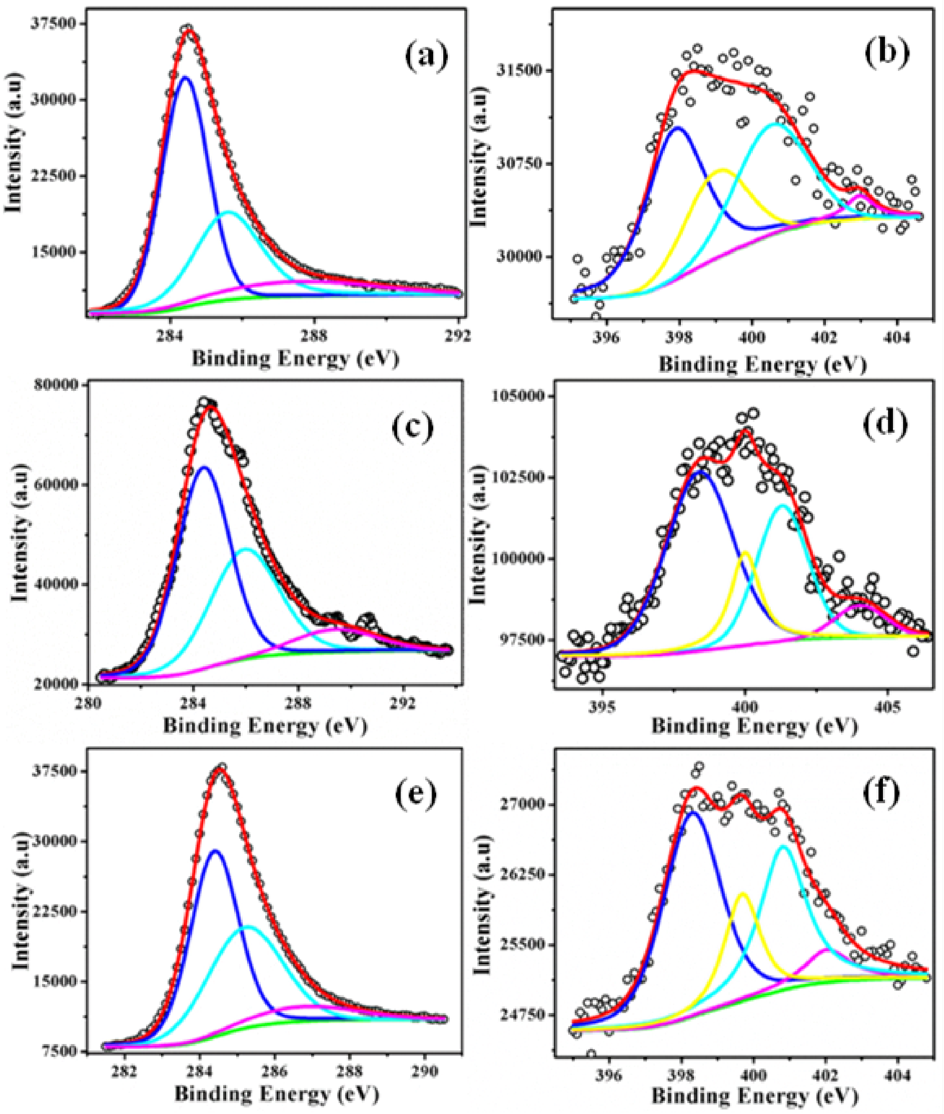

Figure 7.8. Deconvoluted C1s and N1s XP spectra of CP-0.5-700 (a and b), CP-0.5-900 (c and d) and CP-0.5-1000 (e and f). The circles represent the experimental data, the red line represents the fitting data for the overall signal, and the solid lines are the deconvoluted individual peaks for different species present in the sample.

Figure 7.8 (b, d and f) represents the deconvoluted N1s spectra of CP-0.5-700, CP-0.5-900 and CP-0.5-700 respectively. In CP-0.5-700, the peaks are located at BEs of 397.8. 399, 400.5 and 402.9 eV, which correspond to the pyridinic, pyrrolic, graphitic and oxidized nitrogen respectively [10b]. Among the various types of nitrogens, both pyridinic and pyrrolic nitrogen contribute to the conjugated π-system in the graphene layers. Graphitic type nitrogen is formed when the carbon atoms in the graphene layers are substituted by nitrogen atoms. Table 7.2 summarizes the relative percentages of various types of nitrogen present in different samples. It is evident from the XPS quantification that the pyridinic nitrogen is the major component in all the three samples with 41.52, 52.10 and 48.73 % of the total nitrogen content in CP-0.5-700, CP-0.5-900 and CP-0.5-1000 respectively (Figure 7.8 and Table 7.2). Interestingly, higher fraction of the pyridinic nitrogen as well as the total nitrogen content is displayed by CP-0.5-900 sample. Another important observation is that the chemical environment of nitrogen varies with temperature. The relative atomic percentage of oxidic type and pyrrolic type nitrogen decreases with increase in the annealing temperature. All these results demonstrate that the annealing temperature plays a key role in modulating the chemical state of nitrogen in CNF.

Table 7.2. Atomic percentage of various types of nitrogen present in N-doped CNF.

		CP-0.5-700 (At%)	**CP-0.5-900 (At%)**	**CP-0.5-1000 (At%)**
Nitrogen	Pyridinic	41.52	52.08	48.73
	Pyrrolic	21.19	15.14	15.91
	Graphitic	30.64	28.99	31.57
	Oxidic	6.65	3.80	3.78

7.3.6. Pore size Distribution Analysis

Furteher, nitrogen sorption analysis is carried out and the resulting nitrogen adsorption-desorption isotherms and the corresponding pore size distribution curves of the CP-0.5-700, CP-0.5-900 and CP-0.5-1000 are given in Figure 7.9(a-c). All the isotherms show Type IV charecteristics with absorptiton in between 0.4-0.9 relative pressure (P/P_o). These findings clearly indicate the presence of mesoporosity in these samples [5f]. BET surface area obtained for CP-0.5-700, CP-0.5-900 and CP-0.5-1000 are 85, 104 and 92 m^2/g respectively. It is evident from the above data that the BET surface area increases as the tempertaure increases from 700 to 900 °C. However, further increase in the temperature (1000 °C) decreases the surface area. The cumulative pore volumes obtained for CP-0.5-700, CP-0.5-900 and CP-0.5-1000 are 0.134, 0.157 and 0.172 cm^3/g respectively. Hence, the highest propotion of pore volume is displayed by CP-0.5-1000. This can be attributed to the loss of atomic nitrogen at elevated temperature, which results into the creation of mesopores.

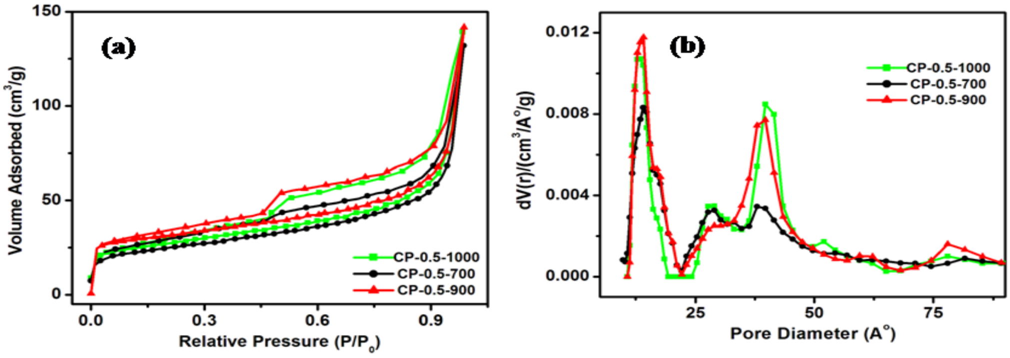

Figure 7.9. (a) Nitrogen adsorption-desorption isotherms and (b) the corresponding pore size distribution curves of CP-0.5-700, CP-0.5-900 and CP-0.5-1000.

7.3.7. Electrochemical Studies

7.3.7.1. CV Analysis

The electrocatalytic properties of the N-doped CNF for the ORR are initially evaluated by CV studies in Ar saturated 0.5 M aqueous KOH electrolyte at RT. For a fair comparison, the same amount of each catalyst by mass is loaded on the WE for all electrochemical studies and the geometrical area of the electrode is used to calculate the current density. In Figure 7.10(a), the CV obtained at a scan rate of 50 mV/s for CP-0.25-700, CP-0.5-700, CP-1-700 and CP-2-700 are compared with that of CNF. All the materials, including CNF show well resolved cathodic peak corresponding to ORR. The onset potential for the CNF is at -0.5 V with the ORR peak potential at -0.77 V. Upon N-incorporation, both the onset potential as well as the ORR peak potential move positively. These results clearly demonstrate a significant enhancement in the ORR activity after the N-incorporation. From the onset potential, the peak position and peak current density obtained for various samples as summarized in Table 7.3, it is evident that both the CP-0.25-700 and CP-0.5-700 samples exhibit better activity in terms of onset potential and ORR peak position. The highest peak current density is displayed by CP-1-700. However, with increase in the polymer content, the onset potential moves to more negative side as is observed in the case of the CP-1-700 and CP-2-700 samples. This shift in the onset potential may be due to diffusional limitations arising in the samples. As the polymer content increases, the excess polymer precursor may get converted into N-containing amorphous carbon, which can impede the diffusion of the reactants leading to a reduction in the activity.

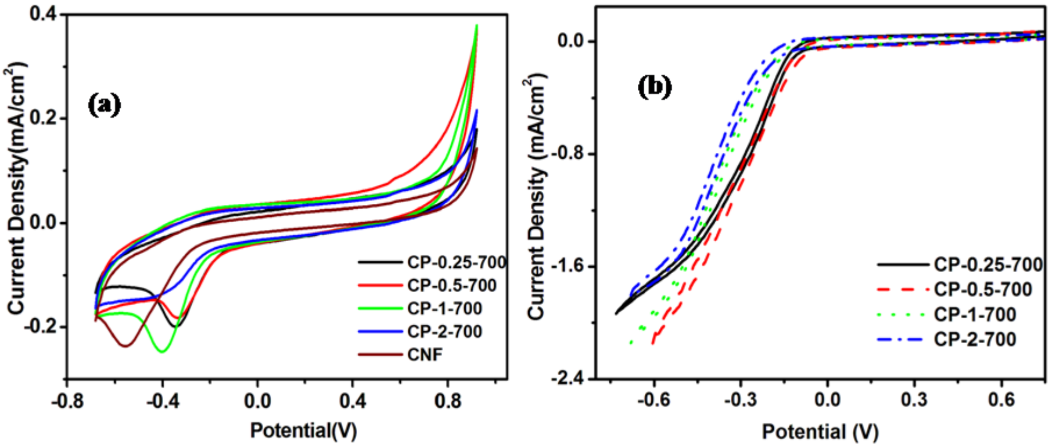

Figure 7.10. Comparison of the CVs obtained for CNF, CP-0.25-700, CP-0.5-700, CP-1-700 and CP-2-700 at a scan rate of 50 mV/s (a) in 0.1 M KOH and (b) in O_2 saturated 0.1 M KOH solution at 900 rpm; all potentials are quoted *vs.* MMS

In order to give additional evidence for the observed ORR activity of the N-doped CNF, CV is also recorded under O_2 saturated conditions at a rotation speed of 900 rpm. A significant improvement in the current density is observed in all the N-doped samples when the electrolyte solution is saturated with O_2 purging [Figure 7.10(b)]. Apart from this, a slight positive shift in the onset potential is also observed upon O_2 purging. This indicates the excellent ORR activity of these samples [5b, c]. Though the trend observed in the onset potential for the ORR is same before and after the O_2 purging, slight variations in the current density is observed after the O_2 purging (Table 7.3). The highest and almost similar current densities are obtained for CP-0.5-700 and CP-1-700 samples. These results clearly demonstrate a significant enhancement in the ORR activity for the N-doped CNF with respect to the pristine CNF. Hence, the best ORR activity is displayed by CP-0.5-700 in terms of the onset potential as well as the current density. This can be attributed to the more number of active sites present in this sample, which is in excellent agreement with the XPS results also.

Table 7.3. Comparison of the onset potential and current density obtained from CV studies for all the N-incorporated samples.

	Onset Potential (V)		**Current Density (mA/cm^2)**	
	Normal	**With O_2**	**Normal**	**With O_2**
CP-0.25-700	-0.14	-0.12	-0.18	-1.94
CP-0.5-700	-0.14	-0.08	-0.2	-2.15
CP-1-700	-0.19	-0.13	-0.25	-2.12
CP-2-700	-0.20	-0.16	-0.14	-1.8
CP-0.5-900	-0.08	-0.02	-0.22	-2.81
CP-0.5-1000	-0.14	-0.03	-0.25	-2.72

From the XPS quantification, it is apparent that the pyrolysis temperature plays a key role in determining the type of nitrogen sites as well as the total nitrogen content in the samples. Each type of nitrogen sites is reported to contribute differently for the ORR reaction [5b, 28]. Hence, the CV response of N-doped CNF prepared at different pyrolysis temperature is also investigated. Accordingly, Figure 7.11(a and b) show the CV response obtained for CP-0.5-700, CP-0.5-900 and CP-0.5-1000 samples in Ar and O_2 saturated 0.1 M KOH solutions respectively. From the CV trace presented in Figure 7.11(a), it is evident that there is a clear gain in the onset potential and the current density at temperatures higher than 700 °C. After O_2 purging, almost 10 times increase in the current density is obtained [Figure 7.11(b)], indicating that the current is obviously due to the reduction of O_2. Both CP-0.5-900 and CP-0.5-1000 samples display equal activity in terms of the onset potential. However, a slight enhancement in the limiting current is obtained in CP-0.5-900, which can be correlated to the improvement in the number of active sites present in this sample as evident from the XPS quantification.

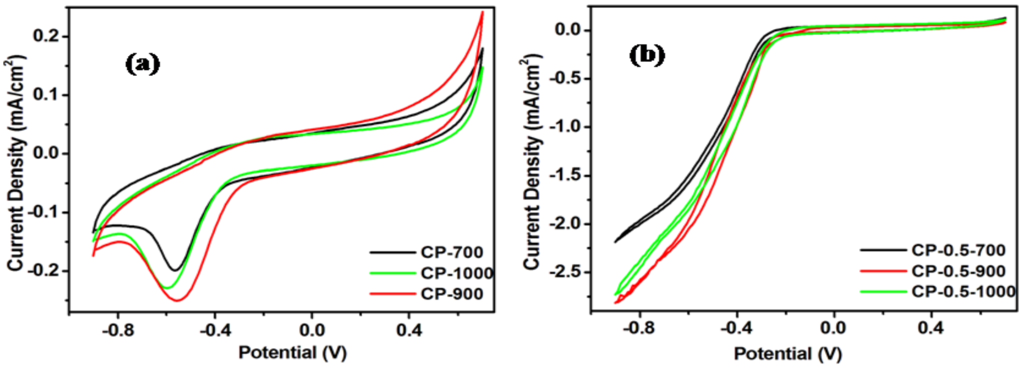

Figure 7.11. Superimposed CVs of CP-0.5-700, CP-0.5-900 and CP-0.25-1000 electrodes at a scan rate of 50 mV/s in (a) in Ar saturated 0.1M KOH and (b) O_2 saturated 0.1 M KOH solution; all potentials are quoted *vs*. MMS .

7.3.7.2. RDE Analysis

As linear sweep Voltammetry with RDE set-up can furnish significant amount of kinetic information on ORR such as the catalyst activity, selectivity of the ORR to H_2O *vs*. H_2O_2 and the electron transfer number of ORR etc., RDE studies of the various developed catalysts are also carried out to obtain a further insight into the mechanism of ORR in the N-doped CNF [29]. Figure 7.12 compares the RDE polarization curves for ORR of CP-0.5-700, CP-0.5-900 and CP-0.5-1000 with that of the commercial Pt/C electrocatalyst, at the same rotation rate of 1600 rpm. In all the three N-doped catalysts, the diffusion plateau is achieved slowly. This type of behavior is normally observed in the doped carbon materials prepared from high temperature pyrolysis [5b, 30, 31]. On a closer inspection, it can be observed that the CP-0.5-700 sample exhibits two oxygen reduction waves, whereas CP-0.5-900 and CP-0.5-1000 show a single reduction peak. The first wave in CP-0.5-700 corresponds to the two electron reduction of O_2 to H_2O_2 and the second wave corresponds to the reduction of peroxide to hydroxide [14, 32]. This indicates the different active sites present in this sample. It can also be observed that at a constant rotation speed of 1600 rpm, the onset potential and the limiting current density displayed by CP-0.5-900 is higher than that obtained for the samples pyrolysed at 700 and 1000 °C (Figure 7.12 and Table 7.4). This trend obtained is in exact agreement with the conclusions attained from the CV studies as well.

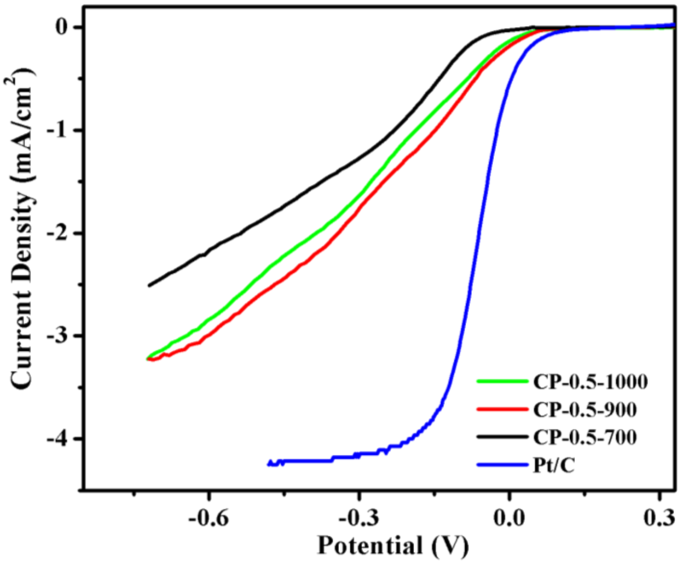

Figure 7.12. Comparison of RDE polarization curves for CP-0.5-700, CP-0.5-900 and CP-0.5-1000 in O_2 saturated 0.1 M KOH solution at a scan rate of 5 mV/s and at a rotation rate of 1600 rpm; all potentials are quoted *vs*. MMS.

It is also noted that the onset potential difference between the Pt/C and the CP-0.5-900 is 35 mV only (Figure 7.12). This gain in the onset potential for CP-0.5-900 catalyst is higher as compared to the ~ 50-150 mV difference in the onset potential reported for most of the N-containing carbon materials [5c-e, 7, 14, 28]. Nevertheless, the onset potential and current density obtained for CP-0.5-900 is less as compared to that of Pt/C catalyst and few state-of-the-art N-doped carbon materials [5b, 33]. This may be due to the low surface area of the CNF as compared to that of CNT and other conducting carbon supports. However, the possibility of blending this material with other high surface area carbon supports indicates the possibility of a significant improvement in the current density as well as the onset potential, as reported earlier [27].

Table 7.4. Comparison of the onset potential and current density obtained from RDE studies for all the N-incorporated samples

Sample	Onset Potential (V)	Limiting Current Density (mA/cm^2)
CP-0.5-700	-0.06	-2.5
CP-0.5-900	0.025	-3.3
CP-0.5-1000	0.02	-3.2
Pt/C	0.06	-4.1

In order to explore the ORR in a more quantitative manner, the number of electrons transferred per oxygen molecule in the ORR process is determined using Koutecky-Levich equation, which relates the inverse of the current density (1/j) and the inverse of the square root of the rotation speed ($1/\omega^{1/2}$) at different potential values [18]. The overall number of electrons transferred per O_2 (n) in the ORR can be calculated using the following equation,

$$1/j=1/j_k+1/B\omega^{1/2} \tag{7.1}$$

where, j_k is the kinetic current density, ω is the angular velocity and B is related to the diffusion limiting current density expressed by the following equation,

$$B = 0.62nF\,(D_{O2})^{2/3}\nu^{-1/6}\,C_{O2} \tag{7.2}$$

where, F is the Faraday constant (F= 96485 C/mol), C_{O2} is the bulk concentration of O_2 ($1.2x\ 10^{-3}$ mol/L), ν is the kinematic viscosity of the electrolyte (ν=0.1 m^2/s), and D_{O2} is the diffusion coefficient of O_2 in 0.1 M KOH ($1.9x10^{-5}$ cm^2/s). As shown in Figure 7.13(a-c), a linear 1/j to $1/\omega^{1/2}$ relationship is obtained for CP-0.5-700, CP-0.5-900 and CP-0.5-1000 in the potential range of -0.5 to -0.9 V. The slops obtained from the plots at different potentials are also approximately constant. Such linearity and parallelism in the K-L plots are considered to be an indication of the first order kinetics with respect to the oxygen concentration [34].

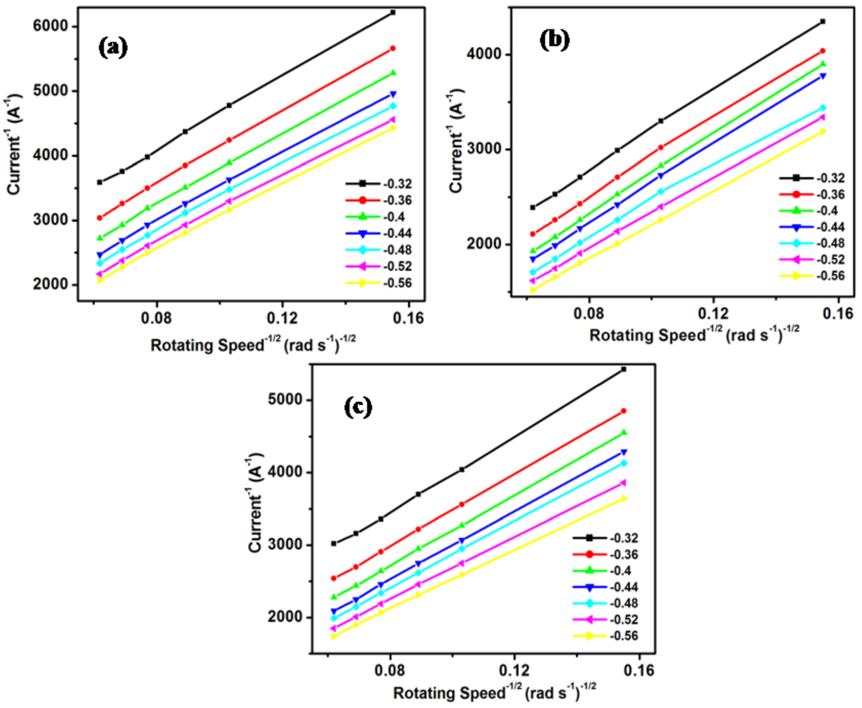

Figure 7.13. The K-L plots obtained for (a) CP-0.5-700, (b) CP-0.5-900, and (c) CP-0.5-1000 derived from the RDE polarization curves at different electrode potentials; all potentials are quoted *vs*. MMS.

In order to acquire a straightforward comparison in the mechanism followed by the samples prepared at different pyrolyzing temperatures, the K-L plots obtained at -0.86 V for CP-0.5-700, CP-0.5-900 and CP-0.5-1000 are also given in Figure 7.14(a). It shows that the slope obtained for CP-0.5-700 increases significantly, indicating a corresponding decrease in the number of electrons transferred in the ORR. However, the K-L plots obtained for CP-0.5-900 and CP-0.5-1000 are parallel, suggesting similar ORR mechanism in both the catalysts. The number of transferred electrons in the ORR is also calculated from the diffusion-limited current densities collected at different rotation rates in the potential range from -0.45 to -0.9 V. As shown in Figure 7.14(b), the electron transfer number varies with potential in all the three catalysts. The electron transfer number obtained for CP-0.5-900 and CP-0.5-1000 varies from 3.5 to 2.5, indicating a mixed two-electron and four-electron pathways followed in these materials [5d, 35]. In contrast to this, the CP-0.5-700 electrodes exhibit a typical two-electron transfer pathway for ORR with low current density, similar to that reported for other nitrogen containing carbon materials [36].This result suggests that the increase in the pyrolyzing temperature has resulted into a clear enhancement in the ORR activity with an improved ORR kinetics towards the preferred 4e- pathway.

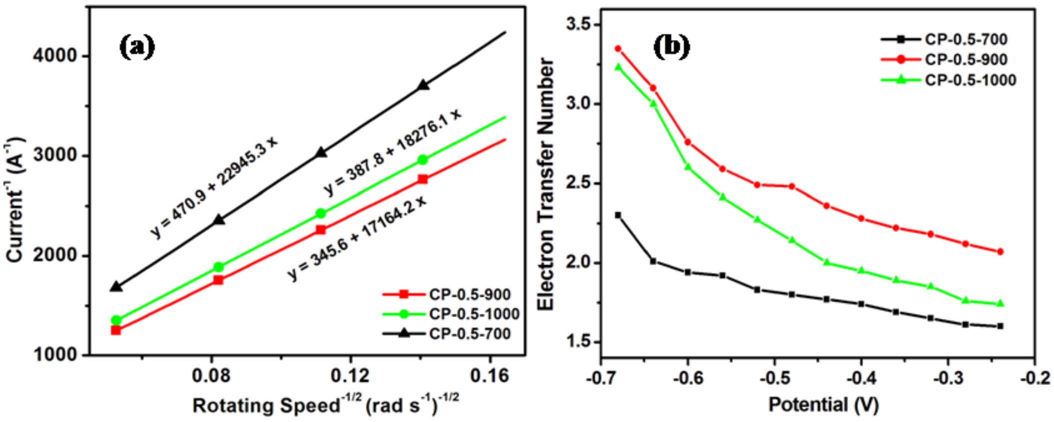

Figure 7.14. (a) K-L plots and (b) the electron transfer number calculated in the potential range of -0.7 to -0.25 V for CP-0.5-700, CP-0.5-900 and CP-0.5-1000; all potentials are quoted *vs*. MMS.

7.3.7.3. Durability Analysis

Since durability of the catalysts is another important concern in fuel cells, the durability of the CP-0.5-900 catalyst is also evaluated by chronoamperometric method. The analysis is conducted at a constant voltage of -0.1 V in O_2 saturated 0.1 M KOH solution at a rotation rate of 1600 rpm for 25000 s. The stability analysis of the commercial Pt/C catalyst is also performed under similar conditions. The current-time (i-t) response of CP-0.5-900 and Pt/C is compared in Figure 7.15. From the figure, it is evident that the CP-0.5-900 electrode shows a much slower decrease in the relative current than the electrode based on Pt/C. The CP-0.5-900 electrode retained a relative current of 83.4% after 25000 s whereas the Pt/C exhibited a relative current retention of only 56%. This result confirms the higher stability of CP-0.5-900 than the commercial Pt/C electrocatalyst.

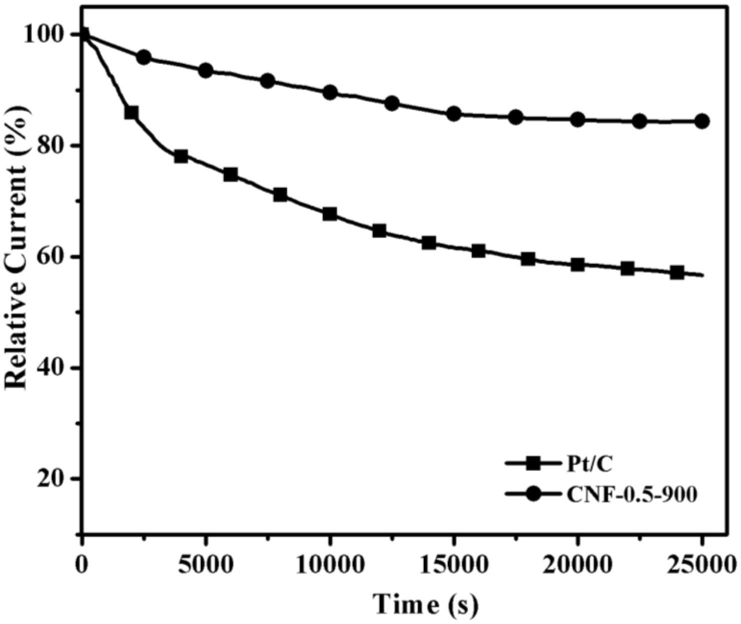

Figure7.15. Chronoamperometric current-time (i-t) response obtained for CP-0.5-900 and Pt/C electrodes in O_2-saturated 0.1M KOH at -0.1V; rotation rate is 1600 rpm; all potentials are quoted *vs*. MMS .

7.4. Conclusions

In summary, in this chapter, we discussed about a facile and cost-effective method for the fabrication of a noble ORR electrocatlyst by a polymer mediated thermal annealing strategy, using PBI-BuI as the nitrogen precursor. The resulting N-doped hollow CNF has displayed excellent electrocatalytic activity and durability for ORR. Our studies demonstrate that it is not the nitrogen content but the nitrogen bonding configuration, especially pyridinic and graphitic types, which plays the key role for the electrochemical oxygen reduction reaction. Thus, the ease with which this N-doped electrode material can be devised implies that the present strategy has far reaching potential in developing new cost effective electrocatalysts. Moreover, by rationally selecting the N-precursors with different chemical structure and nitrogen content, the nature and content of the N-centers in the doped materials can be tuned in a well defined manner. The present strategy can also be extended to dope other elements (such as B, Si, P, and S) if appropriate precursors are selected. Hence, a large variety of heteroatom-doped carbon materials can be designed with this synthetic approach, based on the large possible combinations of the carbon nanostructures and nitrogen or other precursors. These possibilities suggest that still there is considerable room for cost-effective preparation of various metal-free catalysts for ORR, and even new catalytic materials for applications beyond fuel cells.

7.5. References

1 B. C. H. Steele, A. Heinzel, *Nature* **2001**, *414*, 345. (b) W. Xiong , F. Du , Y. Liu , A. Perez Jr. , M. Supp , T. S. Ramakrishnan , L. M. Dai , L. Jiang, *J. Am. Chem. Soc.* **2010**, *132*, 15839.

2 (a) M. K. Debe, *Nature* **2012**, *486*, 43. (b) V. R. Stamenkovic, B. S. Mun, K. J. J. Mayrhofer, P. N. Ross, N. M. Markovic, *J. Am. Chem. Soc.* **2006**, *128*, 8813. (c) H. A. Gasteiger, S. S. Kocha, B. Sompalli, F. T. Wagner, *Appl. Catal. B.* **2005**, *56*, 9. (d) W. Chen, J. M. Kim, S. H. Sun, S. W. Chen, *J. Phys. Chem. C* **2008**, *112*, 3891.

3 (a) X. W. Yu, S. Y. Ye, *J. Power Sources* **2007**, *172*, 145. (b) W. Chen, S.W. Chen, *Angew. Chem. Int. Ed*. **2009**, *48*, 4386. (c) A. A. Gewirth, M. S. Thorum, *Inorg. Chem.* **2010**, *49*, 3557. (d) D. S. Yu, E. Nagelli, F. Du, L. M. Dai, *J. Phys. Chem. Lett.* **2010**, *1*, 2165. (e) M. Winter, R. J. Brodd, *Chem. Rev.* **2004**, *104*, 4245.

4 (a) G. Wu, K.L. More, C.M. Johnston, P. Zelenay, *Science* **2011**, *332*, 443. (b) J. P. Collman, N. K. Devaraj, R. A. Decreau, Y. Yang, Y. L. Yan, W. Ebina, T. A. Eberspacher, C. E. D. Chidsey, *Science* **2007**, *315*, 1565.(c) H. R. Byon, J. Suntivich, Y. Shao-Horn, *Chem. Mater.* **2011**, *23*, 3421. (d) S. Wang, D. Yu, L. Dai, *J. Am. Chem. Soc.* **2011**, *133*, 5182.

5 Y. Y. Shao, J. H. Sui, G. P. Yin, Y. Z. Gao, *Appl. Catal. B* **2008**, *79*, 89. (b) K. Gong, F. Du, Z. Xia, M. Durstock, L. Dai, *Science* **2009**, *323*, 760. (c) S. Yang, X. Feng, X. Wang, K. Müllen, *Angew. Chem. Int. Ed.* **2011**, *50*, 5339. (d) Y. Tang, B. L. Allen, D. R. Kauffman, A. Star, *J. Am. Chem. Soc.* **2009**, *131*, 13200. (e) A. Zamudio, A. L. Elias, J. A. Rodriguez-Manzo, F. Lopez-Urias, G.Rodriguez-Gattorno, F. Lupo, M. Ruhle, D. J. Smith, H. Terrones, D. Diaz, M. Terrones, *Small* **2006**, *2*, 346 (f) S. Chen, J. Bi, Y. Zhao, L.Yang, C. Zhang, Y. Ma , Q.Wu , X.Wang, Z. Hu, *Adv. Mater*. **2012**, DOI: 10.1002/adma.201202424.

6 S. Wang, D. Yu, L. Dai, D. W. Chang and J. B. Baek, *ACS Nano* **2011**, *5*, 6202.

7 J. Liang, Y. Zheng, J. Chen, J. Liu, D. Hulicova-Jurcakova, M. Jaroniec, S. Z. Qiao, *Angew. Chem. Int. Ed.* **2012**, 5*1*, 3892.

8 J. Liu, S. Webster and D. L. Carroll, *J. Phys.Chem. B* **2005**, *109*, 15769.

9 X. Li, H. Wang, J. T. Robinson, H. Sanchez, G. Diankov and H. Dai, *J. Am. Chem. Soc.* **2009**, *131*, 15939.

10 (a) Z. Wu, P. A. Webley and D. Zhao, *J. Mater. Chem.* **2012**, *22*, 11379. (b) Z. H. Sheng, L. Shao, J. J. Chen, W. J. Bao, F. B. Wang, X. H. Xia, *ACS Nano* **2011,** *5*, 4350.

11 K. Ghosh, M. Kumar, T. Maruyama, Y. Ando, *J. Mater.Chem.* **2010**, *20*, 4128.

12 T. Fujigaya, T. Uchinoumi, K. Kaneko, N. Nakashima, *Chem. Commun.* **2011**, *47*, 6843.

13 S. A. Wohlgemuth, F. Vilela, M. M. Titirici, M. Antonietti, *Green Chem.* **2012**, *14*, 741.

14 Y. Zhang, K. Fugane, T. Mori, L. Niu, J. Ye, *J. Mater. Chem.* **2012**, *22*, 6575.

15 M. Okamoto, T. Fujigaya , N. Nakashima, *Adv. Funct. Mater.* **2008**, *18*, 1776. (b) M. Okamoto, T. Fujigaya, N. Nakashima, *Small* **2009**, *5*, 735.

16 G. G. Tibbetts, G. L. Doll, D. W. Gorkiewicz, J. J. Moleski, T. A. Perry, C. J. Dasch, M. J. Balogh, *Carbon* **1993**, *31*, 1039. (b) J. H. Zhou, Z. J. Sui, P. Li, D. Chen, Y. C. Dai, W. K. Yuan, *Carbon* **2006**, *44*, 3255.

17 S. Maldonado, K. J. Stevenson, *J. Phys. Chem. B* **2005**, *109*, 4707.

18 C. P. Ewels, M. Glerup, *J. Nanosci. Nanotech.* **2005**, *5*, 1345.

19 S. Lim, S. H. Yoon, I. Mochida, D. H. Jung, *Langmuir* **2009,** *25*, 8268.

20 Y. Li, J. Wang, X. Li, J. Liu, D. Geng, J. Yang, R. Li, Sun, X. *Electrochem. Commun.* **2011,** *13*, 668.

21 H .Wang, T. Maiyalagan, X. Wang, *ACS catal.* **2012**, *2*, 781.

22 A. Das, S. Pisana, B. Chakraborty, S. Piscanec, S. K. Saha, U. V. Waghmare, K. S. Novoselov, H. R. Krishnamurthy, A. K. Geim, A. C. Ferrari, A. K. Sood, *Nat Nano.* **2008**, *3*, 210.

23 (a) A. C. Ferrari, *Solid State Commun.* **2007**, *143*, 47. (b) Y. Sun, C. Li, G. Shi. *J. Mater. Chem.* DOI: 10.1039/c0xx00000x.

24 J. Dong, X. Qu, L. Wang, C. Zhao, Xu, *J. Electroanalysis* **2008**, *20*, 1981.

25 L. S. Panchakarla, A. Govindaraj, C. N. R. Rao, *ACS Nano* **2007**, *1*, 494.

26 Y. Wang, Y. Shao, D. W. Matson, J. Li, Y. Lin, *ACS Nano* **2010**, *4*, 1790.

27 T. Palaniselvam, R. Kannan, S. Kurungot. *Chem. Commun*. **2011**, *47*, 2910.

28 L. Qu, Y. Liu, J. Baek, L.Dai, *ACS Nano* **2010**, *3*, 1321.

29 T. J. Schmidt, H. A. Gasteiger, G. D. Stab, P. M. Urban, D. M. Kolb, R. J. J. Behm, *Electrochem. Soc.* **1998**, *145*, 2354.

30 L. Yang, S. Jiang, Y. Zhao, L. Zhu, S. Chen, X. Wang, Q. Wu, J. Ma, Y. Ma, Z. Hu, *Angew. Chem. Int. Ed.* **2011**, *50*, 7132.

31 Z. W. Liu, F. Peng, H. J. Wang, H. Yu, W. X. Zheng and J. Yang, *Angew. Chem. Int. Ed.* **2011**, *50*, 3257.

32 M. Zhang, Y. Yan, K. Gong, L. Mao, Z. Guo, Y. Chen, *Langmuir* **2004**, *20*, 8781.

33 R. Liu, D. Wu, X. Feng, K. Mullen, *Angew. Chem. Int. Ed.* **2010**, *49*, 2565. (b) D. Geng, Y. Chen, Y. Chen, Y. Li, R. Li, X. Sun, S. Ye and S. Knights, *Energy Environ. Sci.* **2011**, *4*, 760.

34 C. Jeyabharathi, P. Venkateshkumar, M. S. Rao, J. Mathiyarasu, K. L. N. Phani, *Electrochim. Acta* **2012,** *74*, 171

35 Y. Q. Sun, C. Li, Y. X. Xu, H. Bai, Z. Y. Yao, G. Q. Shi, *Chem. Commun.* **2010**, *46*, 4740.

36 S. M. Lyth, Y. Nabae, S. Moriya, S. Kuroki, M. Kakimoto, J. Ozaki and S. Miyata, *J. Phys. Chem. C* **2009**, *113*, 20148.

Chapter 8

Conclusions

The present chapter gives an account of the important observations and conclusions of the work described in this thesis. The relevance of the strategy based on the potential utility of both the inner cavity as well as the outer wall of the hollow CNF support for the generation of active sites has been discussed. Several advantages of this approach such as the formation of thin electrode with the desired activity, better water management and lower mass transfer resistance are also demonstrated. Further, the significance of the hybrid electrocatalysts possessing multifunctional characteristics to address the challenges existing in the area of performance improvement is also discussed. Related promising developments and existing challenges in the area of catalyst support and active catalyst are also discussed to lay out the future scope pertain to this work.

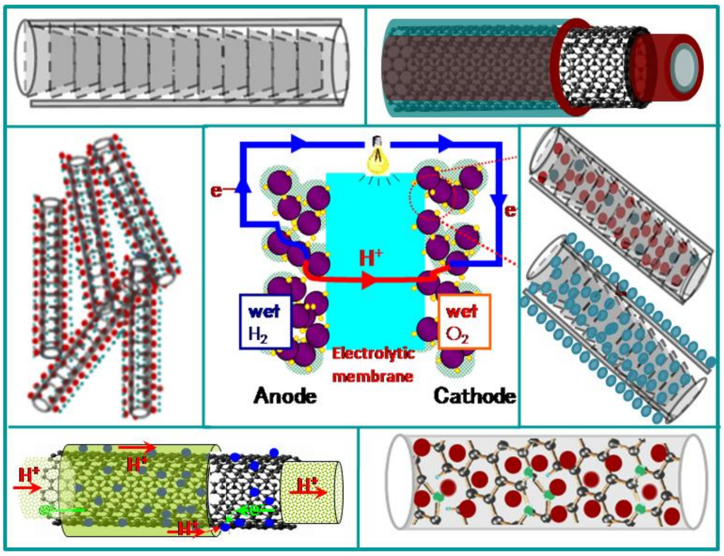

PEMFCs, because of their many fascinating features such as high efficiency, low pollution, wide development potential etc. offer the prospective to fulfill the future energy demands of the world. However, the development of commercially viable fuel cell systems faces a number of design, performance and cost related challenges. One of the main factors which hinder their widespread application is the cost, which mainly arises from the Pt based electrocatalysts. Thus, electrocatalysts, demand specific attention as they hold a pivotal role in the PEMFC performance. Hence, the main requirement for future is to develop innovative low-Pt or non-Pt materials as electrocatalyst for PEMFCs without impacting the performance and durability. Acquiring fundamental cognizance of the microstructure-to-property origins and engineering nanocatalysts at the atomic and molecular level, especially in the range of 1-10 nm, is particularly important to design novel electrocatalysts with improved performance to continue in the decades to follow. We have addressed some of these issues and the present thesis attempts to design novel Pt-based and non-Pt electrocatalysts for ORR by exploring the peculiar morphology characteristics of the hollow CNF as the support.

The major accomplishments of the present investigations could be summarized as follows:

1. Development of a novel electrocatalyst by utilizing both the inner cavity as well as the outer surface of CNF for Pt NP dispersion.

Till date, Pt nanoparticles supported on carbon substrates have been demonstrated as the best electrocatalysts for ORR. However, the performance of an electrocatalyst is determined by many factors like active catalyst size and shape, dispersion of catalyst on support material, surface area of support, catalyst-support interaction, proper mass transfer rate, balanced electron and proton conductivity, ionomer-catalyst-gas pore TPB etc. One dimensional carbon nanostructures such as CNTs and CNFs have triggered wide interest as catalyst support materials mainly due to their exciting features such as anisotropy, unique structure and surface properties. Nevertheless, the inherently low surface area possessed by these materials restricts the amount of active catalyst dispersible on these materials, resulting into a catalyst with higher carbon to Pt ratio. To circumvent this issue related to surface area, we have designed a novel electrocatalyst with excellent Pt dispersion on both the inner and outer walls of a hollow CNF support. This was achieved by a modified polyol process, wherein surface tension and polarity characteristics of the medium were tuned properly to promote solution entry into the tubular region by capillary filling. The pristine CNF, which possesses inherently active inner wall surface and inactive outer wall surface, led to selective Pt deposition along the inner wall, whereas activation of the outer wall with chemical functionalization resulted into excellent dispersion of Pt NPs along both the inner and outer walls. The electrochemical studies revealed enhanced methanol oxidation and ORR properties of the catalyst with Pt NPs on both the inner and outer walls as compared to the CNT supported catalyst. Thus, the enhanced electrocatalytic activity displayed by these materials opens up great scope in fuel cell electrode fabrication because appropriate Pt loadings can be achieved at significantly low carbon content in the system.

2. Enhancing the ORR activity by designing bimetallic sandwich type thin layer catalyst with improved Pt utilization.

It is well-known that the electronic structure and the surface geometric effects are directly reflected in the ORR activity of Pt. Hence, suitable bimetallic or multimetallic combinations with Pt can significantly enhance the ORR performance. Although, considerable efforts have been demonstrated in the synthesis and performance evaluation of bimetallic or multimetallic electrocatalysts, several important aspects related to the finite dispersion of catalyst NPs on the support material remain unaddressed. Accordingly, we have developed a high aspect ratio, Pt thin layer catalyst supported on an *in-situ* prepared ‘RuO_2-carbon-RuO_2’ sandwich type hybrid support. This was achieved based on the better affinity of oxygen containing functional groups on the functionalized CNF surface towards Ru ions, which resulted into the preferential adsorption of Ru ions from a mixture of Pt and Ru ions. This led to the to the *in-situ* renovation of FCNFs to form a hybrid ‘RuO_2-carbon-RuO_2’ sandwich type support followed by Pt NP decoration. The resultant material exhibited improved ORR and methanol oxidation activities as a result of the strong electronic perturbations and structural modifications effected in the catalyst and catalyst support phases. Thus, our study firmly establishes the role of hybrid support, catalyst and the synergistic contribution from individual components to address the future challenges in the area of utilization improvement.

3. Understanding the importance of surface functionalization in the bimetallic electrocatalyst design.

Following the studies on the Pt-RuO_2 bimetallic electrocatalysts for ORR, our next aim was to understand the role of surface functionalities in the design of bimetallic electrocatalysts. Although, different functionalization strategies have been reported for carbon nanomorphologies, functionalization dependent tuning of the property of hybrid systems is still at the infancy. Thus, we have carried out interesting manifestation on the role of surface functionalization in fine tuning the property of a Pt-RuO_2 bimetallic system from charge storage to electrocatalysts. When, pristine CNF was used to decorate Pt and RuO_2 NPs, mainly phase separated NPs with characteristic charge storage property of RuO_2 is obtained. In contrast to this, with functionalized CNF, a material rich in Pt features exhibiting ORR activity was obtained. Thus, with the same composition of Pt and RuO_2, two distinctly different distribution characteristics could be achieved. Hence, the present study demonstrated how important it is to have a clear understanding on the nature of surface functionalities in the processes involving dispersion of more than one component on various substrates including carbon nanomorphologies. Nevertheless, detailed understanding of the effect of other functional groups like -SH, -NH_2, -SO_3H etc. is required for the successful implementation of this concept for various applications.

4. Improving the ORR activity by designing multifunctional electrocatalysts with ideal interfacial structure.

After demonstrating the enhanced ORR activity of CNF supported catalyst

(F-Pt), where the fundamental concept was to utilize all the available surface area of the support material, the next goal was to impart multifunctional characteristics to this catalyst. Thus, a CNF-Pt-PBI hybrid electrocatalyst was developed by incorporating a low molecular weight polymer, PBI-BuI into the inner cavity and along the outer surfaces of F-Pt. Thus, the resulting multifunctional material with a unique combination of almost double surface area, high proton and electron conductivity, surface reactivity and effective pathways for reactant distribution and product dissipation, revealed the exceptionally high activity. The excellent perfoamrance displayed by the system offers intriguing possibilities of the present concept in effectively utilizing materials and creating new avenues in system developments.

5. Development of a non-Pt electrocatalyst by nitrogen doping along the inner and outer surfaces of CNF.

As nitrogen doped carbon nanostructures constitue a major class of Pt-free electrocatalysts with excellent electrocatalytic activity, selectivity and durabilty for ORR, our next focus was to develop a high performing nitrogen doped electrocatalyst by utilizing the plenty of exposed graphene edges present in CNF. As there has not been any attempt to introduce N-doping along the inner cavity as well as on the outer surfaces of hollow carbon morphologies, we have developed a facile polymer mediated, thermal annelaing strategy to induce nitrogen-doping on the exposed graphene edges present in the inner and outer surfaces of CNF. The resulting material displayed excellent electrocatalytic activity with improved durability for ORR. Thus, the present strategy offers far reaching potential in developing new cost-effective electrocatalysts, by rationally selecting different possible combinations of the carbon nanostructures and nitrogen precursors.

Overall, the present work combines the effect of nanoconfinement and multifunctional approach in the design of pure Pt and Pt-RuO_2 bimetallic electrocatalysts with high Pt utilization and activity and even in the design of non-Pt electrocatalyst with high activity and durability.

List of Publications

1. "*Effect of the Viscosity of Poly(benzimidazole) on the Performance of a Multifunctional Electrocatalyst with an Ideal Interfacial Structure*"
   Beena K Balan, Bipinlal Unni, Harshal D Chaudhari , Ulhas K Kharul and Sreekumar Kurungot, *J. Mater. Chem. A* **2013**, *1*, 4265 - 4276.

2. "*Carbon nanofiber-RuO_2-poly(benzimidazole) ternary hybrids for improved supercapacitor performance*"
   Beena K Balan, Harshal D Chaudhari, Ulhas K Kharul and Sreekumar Kurungot, *RSC Advances* **2013**, *3*, 2428 - 2436.

3. *"Polybenzimidazole Mediated N-Doping Along the Inner and Outer Surfaces of Carbon Nanofiber and Its Oxygen Reduction Properties"*
   Beena K Balan, Aiswarya Padinhare Manissery, Harshal D Chaudhari, Ulhas K Kharul and Sreekumar Kurungot, *J. Mater. Chem.* **2012**. *22*, 23668 - 23679.

4. *"Tuning the Functionality of a Carbon Nanofiber-Pt-RuO_2 System from Charge Storage to Electrocatalysis*"
   Beena K. Balan and Sreekumar Kurungot, *Inorg.Chem.* **2012**, *51*, 9766 - 9774.

5. *"One-dimensional Confinement of Nanosized Metal Organic Framework in Carbon Nanofibers for Improved Gas Adsorption*"
   Pradip Pachfule, **Beena K. Balan**, Sreekumar Kurungot and Rahul Banerjee, *Chem Commun*. **2012**, *48*, 2009 - 2011.

6. "Highly exposed and activity modulated sandwich type Pt thin layer catalyst with enhanced utilization"

Beena K. Balan and Sreekumar Kurungot, *J. Mater. Chem*. **2011**, *21*, 19039 -19048.

7. *"High Aspect Ratio Nanoscale Multifunctional Materials Derived from Hollow Carbon Nanofiber by Polymer Insertion and Metal Decoration"* **Beena K. Balan**, Pradnya P. Aher, Manjusha V. Shelke, Vijayamohanan K. Pillai and Sreekumar Kurungot, *Chem Commun*. **2010**, *46,* 5590 -5592.

8. "*Carbon Nanofiber with Selectively Decorated Pt Both on Inner and Outer Walls as an Efficient Electrocatalyst for Fuel Cell Applications*" **Beena K Balan**, Sreekuttan M Unni And Sreekumar Kurungot, *J. Phys. Chem. C*. **2010***, 113*, 11572-11578.

9. *"Significant Enhancement of Formic Acid Oxidation Using Rhodium Nanostructures*" **Beena K Balan** and Bhaskar R Sathe, *J. Nanosci. Nanotechnol*. **2012**, *12*, 8994-8998.

10. "*Carbon Nanofiber-MnO$_2$-Polybenzimidazole hybrids for high performance supercapacitors*" **Beena K Balan** and Sreekumar Kurungot, Manuscript submitted to *ACS Appl. Mater. Inter.*

11. "Enhanced electrocatalytic performance of interconnected Rh nano-chains towards formic acid oxidation", Bhaskar R Sathe, **Beena K Balan** and Vijayamohanan K Pillai, *Energy Environ. Sci*. **2011**,*4,* 1029-1036.

12. *"Tunable optical features from self-organized rhodium nanostructures"* Bhaskar R. Sathe, **Beena K. Balan**, and Vijayamohanan K. Pillai, *Appl. Phys. Lett.* **2010**, *96,* 233102-233104.

13. “*Template-Assisted Synthesis of Ruthenium Oxide Nanoneedles: Electrical and Electrochemical Properties*”

Mahima Subhramannia, **Beena K Balan**, Bhaskar R Sathe, Imtiaz S Mulla, Vijayamohanan K Pillai, *J. Phys. Chem. C*, **2007**, *111*, 16593-16600.

Erratum